DATING THE CENOZOIC INCISION HISTORY OF THE TENNESSEE AND SHENANDOAH RIVERS WITH COSMOGENIC NUCLIDES AND $^{40}AR/^{39}AR$ IN MANGANESE OXIDES

by

William E. Odom, III

A Dissertation

Submitted to the Faculty of Purdue University

In Partial Fulfillment of the Requirements for the degree of

Doctor of Philosophy

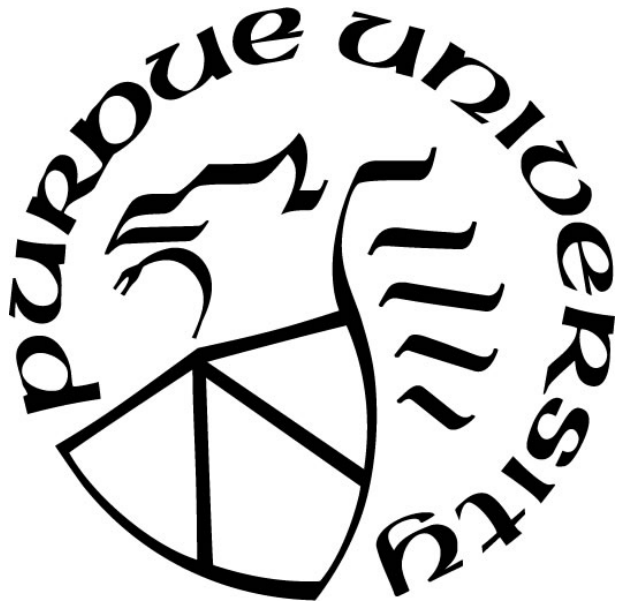

Department of Earth, Atmospheric, and Planetary Sciences

West Lafayette, Indiana

December 2020

THE PURDUE UNIVERSITY GRADUATE SCHOOL
STATEMENT OF COMMITTEE APPROVAL

Dr. Nathaniel A. Lifton, Chair

Department of Earth, Atmospheric, and Planetary Sciences

Dr. Darryl E. Granger

Department of Earth, Atmospheric, and Planetary Sciences

Dr. Christopher L. Andronicos

Department of Earth, Atmospheric, and Planetary Sciences

Dr. Marc W. Caffee

Department of Physics and Astronomy

Approved by:

Dr. Daniel Cziczo

"I have read as well as heard the statement by devotees of the concept that topography is a 'now thing.' I am philosophically in complete sympathy with this idea, but analysis of Appalachian landforms and the perfection of their adjustment compels the belief that these mountains have been around for a long time." – John Hack

ACKNOWLEDGMENTS

This thesis represents the culmination of many ideas, discussions, excursions, and experiments over the last five years. I would foremost like to thank Darryl Granger for guiding me through the development of this project and encouraging me to explore every idea and hypothesis along the way. His profound expertise, thought-provoking questions, and unending enthusiasm for understanding the big picture have continually inspired me and helped me mature from a student to a scientist. My committee members – Nat Lifton, Chris Andronicos, and Marc Caffee – have likewise played crucial roles in my graduate career. I would like to thank Nat for the thoughtful discussions and delicious coffee that he contributed to our office, Chris for forever changing the way I view fractures and cross-sections, and Marc for his thoughtful advice on cosmogenic nuclide and $^{40}Ar/^{39}Ar$ geochronology. Graduate school would have not been the same without Ken Ridgway, whose fascinating courses, professional advice, and friendly support have been immensely helpful along the way. I would like to thank Dan Doctor and Ryan McAleer for continually supporting my research, guiding me through both the Shenandoah Valley and the USGS building, and providing incredible professional opportunities.

The close friends I have made as a graduate student have immeasurably brightened my experience. I would like to thank Angus Moore for providing countless thought-provoking conversations, giving me helpful ideas when labwork went awry, and bringing me on fantastic field expeditions across the country. Likewise, I would like to thank Tom Clifton for teaching me the intricacies of mineral separation, Al/Be chemistry, and not taking myself too seriously while doing either activity. It was a pleasure to share an office with Sarah Sams, who provided oft-appreciated humor to the group. Outside of the PRIME Lab, I am especially thankful for the friendship of Zach Meyers, Noah Stewart-Maddox, and Yonah Sorin.

I owe everything to my family, especially my parents Alastair and Bill, for encouraging me to try everything and persist. My deepest appreciation goes to Carl Nyberg and Lee Capps for being great role models and friends. Finally, I am grateful to Mariah Romero for her kindness and support since our first semester at Purdue.

TABLE OF CONTENTS

LIST OF TABLES

LIST OF FIGURES

ABSTRACT

The post-orogenic history of the Appalachian Mountains, particularly the persistence of rough topography and the degree of river incision throughout the region, has been a longstanding focus of geomorphology studies. Numerous models have been developed to explain the evolution of this landscape, variously invoking episodic or continuous processes of uplift and erosion to drive the generation or reduction of topographic relief. Recently, late Cenozoic uplift has found favor as a mechanism for rejuvenating the topography of the southern and central Appalachians. This hypothesis has drawn on longitudinal river profiles, seismic tomography, and offshore sediment records as evidence of Neogene uplift.

Radiometric dating of surficial deposits provides a means to directly test models of episodic and continuous landscape evolution, as well as the Neogene uplift hypothesis. The research described in this thesis dates surficial sediments (river terraces, alluvial fans, and a filled sinkhole) and supergene manganese oxides using $^{26}Al/^{10}Be$ burial dating and $^{40}Ar/^{39}Ar$ geochronology, respectively. Our cosmogenic $^{26}Al/^{10}Be$ dating provides detailed histories of aggradation and incision along the Shenandoah and Tennessee Rivers since the early Pliocene. $^{40}Ar/^{39}Ar$ dating of manganese oxides permits estimates of surface preservation and denudation in the Shenandoah Valley and nearby watersheds throughout the Cenozoic.

The results of our work in the Shenandoah Valley, Tennessee River basin, and intervening areas indicate that the Appalachians experienced no significant pulse of uplift during the Cenozoic. Long-term preservation of supergene manganese oxides dates as far back as the Eocene, demonstrating minimal denudation and discontinuous formation that lend evidence to episodic landscape evolution models. Cosmogenic $^{26}Al/^{10}Be$ burial ages along the Shenandoah and Tennessee Rivers reveal Pliocene aggradation, with enhanced deposition in the Shenandoah Valley during the mid-Piacenzian Warm Period. Both rivers likely experienced incision during the Pleistocene, likely due to climatic fluctuations. These results demonstrate that while the Appalachian landscape has remained largely unchanged for tens of millions of years, rapid Pleistocene changes in base level recently triggered significant incision of major drainages.

CHAPTER 1. INTRODUCTION

1.1 Historical overview

The southern and central Appalachian Mountains have captured the interest of geologists for over a century, sparking numerous hypotheses regarding their growth and post-orogenic decay. Initial studies of the geomorphology of the Appalachian Mountains sought to better understand their downwasting through the lens of surface development and abandonment. William Morris Davis's seminal 1889 paper "The Rivers and Valleys of Pennsylvania" hypothesized that the accordant peaks of Kittatinny Mountain, NJ represented the preserved remnants of a Cretaceous relict surface. Davis (1891) designated a second, lower relict surface in the Appalachians in areas of low valleys that were deeply incised, assigning a Tertiary age to this surface. In Davis's model, the differences in elevations between these surfaces were caused by denudation that occurred between periods of baseleveling (Figure 1.1). Later publications throughout the nineteenth century and early twentieth century supported the episodic model, with numerous authors mapping various high-elevation, low-relief surfaces scattered throughout the mountain system (Figure 1.2). The Cretaceous surface, often referred to as the Kittatinny or Schooley peneplain, fell out of favor amongst many authors. However, the Tertiary surface, generally known as the Harrisburg or Valley Floor peneplain, found favor amongst supporters of the Davisian model (Thornbury, 1965). This surface is found within wide valley bottoms in the Valley and Ridge and Blue Ridge provinces, while in the Appalachian Plateau it is characterized by gently rolling hills. It has been deeply incised (up to ~100 m) by numerous rivers including the New, Cumberland, Tennessee, and Shenandoah Rivers. Karst-dominated drainages have contributed to the excellent preservation of deep weathering products that likely formed during extended base level stability.

The Tertiary surface found wider acceptance, thanks in part to the deep weathering deposits that lent support for its existence. These deposits include kaolinite and bauxite deposits in sinkholes, as well as manganese oxides frequently associated with the Tomstown/Shady dolomite. Bauxite deposits in the coastal plain have been stratigraphically dated to the Paleocene-Eocene, and Tennessean bauxites are generally associated with lignite that has been dated to the Paleocene-Eocene Thermal Maximum (PETM) using fossil flora (Bridge, 1950). During this time period, the climate of the southern Appalachian Mountains likely mirrored that of modern-day tropics

(Bárdossy and Aleva, 1990), supporting the hypothesis that the Valley Floor surface is at least early Cenozoic in age. However, the ages of bauxites cannot be directly measured, and it is possible that bauxites form over long durations of moderate weathering.

While bauxites cannot be directly dated, they are occasionally associated with manganese oxide deposits (Bridge, 1950) that can be precisely dated using $^{40}Ar/^{39}Ar$ geochronology (Figure 1.3) (Vasconcelos, 1999). Appalachian manganese oxides generally accumulate in the thick residuum that overlies the Cambrian Shady/Tomstown Dolomite units of the Valley and Ridge provinces (Miser, 1950) and are associated with warm and humid climates (Feng and Vasconcelos, 2007). Researchers in the mid-20th century noted that manganese oxide deposits occurred at specific elevations and used them in Virginia and Tennessee to reconstruct erosional surfaces, including the Valley Floor/Harrisburg surface (Hewett, 1916; King, 1949; 1950). The Paleogene formation age of this surface was largely uncontested until J.T. Hack introduced the continuous landscape evolution model of dynamic equilibrium (Hack, 1960).

Hack's model rejected the episodic concept of landscape evolution that had been embraced throughout the 20th century, arguing instead that topography develops continuously as a function of rock resistance to weathering and erosion (Figure 1.1) (Hack, 1960). Hack selected the Shenandoah Valley, VA, as a study area for demonstrating the concept of dynamic equilibrium. Rejecting Bridge (1950)'s interpretation that the valley represented the Valley Floor peneplain, Hack hypothesized that the entire Shenandoah Valley landscape is in a state of dynamic equilibrium, where all slopes are adjusted to each other such that erosion rates are constant throughout the landscape. To demonstrate this, Hack pointed to the hills underlain by resistant chert and valleys formed by erodible shales and carbonates. While the Davisian model would have designated different formation times for each landform, Hack instead argued that all were of the same age. Hack also rejected the hypothesis that valley gravels formed via channel incision, arguing instead that while Pleistocene climate fluctuations had likely enhanced mechanical weathering, gravels were continuously forming due to differences in gradient driven by lithology. Regarding the manganese oxides, Hack posited that manganese oxides form continuously when oxic groundwater interacts with carbonates and that such deposits are presently forming at all elevations. Similarly, Hack (1965) suggested that bauxite deposits are currently forming in the southern Appalachian Mountains and do not reflect any previous climatic regimes. While Hack's concept of dynamic equilibrium gained considerable traction in the late 20th century despite not

being mutually exclusive with the Davisian model (Bishop, 2007), neither model has been conclusively confirmed or refuted in the context of the southern and central Appalachian Mountains.

1.2 The Neogene uplift hypothesis

Episodic and continuous models of landscape evolution have both played major roles in models addressing the longevity of high relief in the Appalachian Mountains, particularly the Blue Ridge. The last major Appalachian orogeny ceased over 200 million years ago (Hatcher, 1989), and some authors have posited that the high Appalachian topography should have eroded down within tens of millions of years (e.g., Ahnert, 1970). To explain the rugged topography of the southern and central Appalachian Mountains, recent studies have invoked the mechanism of late Cenozoic topographic uplift (Hack, 1982; Wagner et al., 2012; Gallen et al., 2013; Miller et al., 2013; Biryol et al., 2016). Hack (1982) noted that convex longitudinal profiles in the central and southern Appalachians were potential evidence of a landscape in a state of disequilibrium. Similarly, Gallen et al. (2013) analyzed the longitudinal profiles of the Cullasaja River, NC, and its tributaries (Figure 1.4). The authors modeled knickpoint movement as a kinematic wave, invoked an onset of uplift during the early Miocene, and hypothesized a >150% increase in relief of the southern Appalachians since that time. Later work by Gallen (2018) alternatively proposed that Miocene incision of the upper Tennessee River basin may have been driven by drainage capture, as further discussed in Chapter 2 of this thesis. Miller et al. (2013) likewise modeled knickpoint propagation along the Susquehanna River, PA, and its tributaries to conclude that a 100-150 m decrease in base level occurred sometime during the Neogene (Figure 1.4).

These studies have drawn upon offshore sedimentary records in the Gulf of Mexico and along the East Coast. Galloway et al. (2011) described increased sedimentation rates during the Lower to Middle Miocene and Pleistocene in the Gulf of Mexico, which Gallen et al. (2013) pointed to as evidence for broad regional uplift and erosion. Poag and Sevon (1989) noted corresponding peaks in sediment accumulation rates during those same time periods in the Baltimore Canyon Trough, Hatteras Basin, and Salisbury Embayment. Pazzaglia and Brandon (1996) also noted accelerated sedimentation in the Miocene and hypothesized dynamic topography as a potential driver of enhanced erosion in the central Appalachians.

1.3 Evidence for Cenozoic tectonic quiescence

These observations do not necessitate Neogene uplift of the southern and central Appalachian Mountains. Knickzones identified by Gallen et al. (2013) and Miller et al. (2013) may have formed through stream capture or other mechanisms of drainage reorganization (Prince and Spotila, 2013; Gallen et al., 2018) rather than tectonic uplift. Modeling in the Tennessee River watershed (Gallen, 2018; Gallen and Thigpen, 2018) has recognized the potential of capture as a driver of incision and drawn upon aquatic biodiversity studies (i.e., Near and Keck, 2005) as evidence for capture of the upper Tennessee River near Chattanooga, TN during the Miocene. Such perturbations could also explain fluctuating sedimentation rates; the observed westward drainage divide propagation in the southern Appalachian Mountains would have increased drainage area of eastward flowing streams (including the Susquehanna River studied by Miller et al., 2013 and the Potomac River drainage) and led to a greater contribution of Appalachian sediments to the coastal plain and Atlantic Ocean (Naeser et al., 2016). In the Gulf of Mexico, Neogene pulses of sedimentation may have been due to accelerated erosion by global cooling, as opposed to uplift (Galloway et al., 2011). Similar deposodes have been noted during Pleistocene glaciations (Poag and Sevon, 1989; Galloway et al., 2011). Moreover, the models that invoke lower crustal foundering rely upon gravimetric and seismic data that have non-unique interpretations, and no geologic evidence – surficial or otherwise – of delamination has been noted.

The presence of deep weathering products further complicates the scenario. Bauxites in the coastal plain have been stratigraphically dated to the Paleocene-Eocene, and those in the Valley and Ridge are often associated with Paleocene-Eocene fossil flora (Bridge, 1950). Because the precursors to the bauxites must have been sourced from the Blue Ridge Mountains given their high aluminum content (Overstreet, 1964) and weathered within sinkholes that must have terminated above the water table (Ford and Williams, 2013), the elevations of bauxite deposits relative to modern river levels may be used to approximate river incision rates since the their inferred formation age, assuming that lowering by dissolution has been negligible. With this assumption, the proximity of bauxite deposits to modern channels in Chattanooga, TN and Elizabethton, TN (Finlayson et al., 1966; Wilson, 1989) suggests that incision rates have not exceeded *3 m/My* since the early Cenozoic. Such a low incision rate is incompatible with the recent rejuvenation hypothesized by Gallen et al. (2013) and Liu (2014). If the bauxite deposits indeed formed later in the Cenozoic, average incision rates would be slightly higher, but it is likely that they would not

be high enough to account for the incision hypothesized for Neogene uplift. Likewise, in the case that dissolution lowering significantly affected the bauxite deposits, the fact remains that near-surface deposits have likely been preserved for much of the Cenozoic and this lends evidence to gradual denudation near Chattanooga and Elizabethton.

In Highland and Pendleton Counties, VA, volcanic diatremes have been dated to ~47 Ma (Tso et al., 2004; Mazza et al., 2014). These volcanics are the youngest dated igneous rocks in the Appalachian Mountains and intrude Ordovician through Devonian-age rocks (Rader and Wilkes, 2001). Tso et al. (2004) stratigraphically estimated an emplacement depth of 198-335 m. On this basis, we can extrapolate a mean erosion rate of 4-7 m/My since the Eocene. This value is similar to erosion rate estimates derived for the Tennessee River watershed from the bauxites assuming a Paleocene-Eocene age.

These values are also generally consistent with modern erosion rates measured using cosmogenic ^{10}Be in catchments of the Valley and Ridge province. Granger et al. (1997) calculated modern erosion rates of 2-7 m/My in the New River basin, which has deeply incised into the Valley Floor surface (Fenneman, 1944). Along the Shenandoah River, Duxbury et al. (2015) calculated an average erosion rate of ~7 m/My for the entire watershed, noting that erosion rates vary depending on lithology and surficial geometry. Similarly, Hancock and Kirwan (2007) calculated an average erosion rate of 5.7 m/My at Dolly Sods, WV, a former periglacial plateau. In contrast, Matmon et al. (2003) demonstrated that the Great Smoky Mountains are uniformly eroding at ~30 m/My. It should be noted that cosmogenic erosion rate measurements average over only the past 10^4-10^5 yrs and do not reflect rates of erosional processes on Cenozoic timescales. In fact, long-term estimates of Appalachian erosion rates from other geochronometers have varied significantly from ^{10}Be-derived estimates (Figure 1.5). The spatial and temporal discrepancies in erosion rate estimates for the Appalachian Mountains lend evidence to a disequilibrium landscape.

1.4 Incision of the Valley Floor surface

The timing of river incision in response to disequilibrium can be constrained with cosmogenic ^{26}Al/^{10}Be burial dating of fluvial sediments. While overall erosion rates of the surface have remained extremely low since the Eocene, many Appalachian rivers underwent rapid, deep incision during the Pleistocene. This incision was first radiometrically dated along the Valley and Ridge by Granger et al. (1997), who obtained ≤1.5 My burial ages for fluvial sediments in caves

perched 12-35 m above the New River. They found that the New River was incising rapidly (27 ± 4.5 m/My) relative to modern erosion rates in the same watershed (<10 m/My). Terrace deposits along the edge of the Valley Floor surface near Pembroke, VA were also dated to 1.98 ± 0.20 My and 1.52 ± 0.19 My (Granger, unpublished data), suggesting that a significant perturbation <1.5 My ago drove incision along the New River.

A subsequent study along the Green River, KY dated the formation of multilevel passages at Mammoth Cave (Granger et al., 2001). Cosmogenic $^{26}Al/^{10}Be$ burial ages for samples from multiple levels of the cave revealed multiple discrete pulses of incision. Pliocene aggradation was followed by two Pleistocene incision events at ~2.4 My and ~1.5 My. The older incision event is coeval with an early Pleistocene glaciation dated by Balco and Rovey (2010) in till deposits, while the younger incision event is likely due to the same perturbation that drove incision along the New River.

Two pulses of incision at ~2 My and ~1.5 My were noted along the Cumberland River by Anthony and Granger (2004, 2006, 2007), who dated buried sediments in abandoned, high level trunk caves that formed during extended base level stability. It was previously thought that the ~1.5 My incision pulse shared by all three aforementioned rivers was driven by the same perturbation: the glacial reorganization of the Teays River and formation of the modern Ohio River. However, reassessment of the geochronologic data – including remeasurement of $^{26}Al/^{10}Be$ and recalculation of ages accounting for the updated half-life of ^{10}Be – has shown that incision likely predated the movement of the Laurentide Ice Sheet at 1.3 My (Granger et al., 2018). Prior to 1.3 My, many westward-flowing Appalachian rivers were tributaries of the Teays-Mahomet River, which flowed across the Midwest toward its confluence with the ancestral Mississippi River (Teller and Goldthwait, 1991). As the Laurentide Ice Sheet expanded southward ca. 1.3 My (Balco and Rovey, 2010), it buried the Teays-Mahomet River and dammed its tributaries at the ice front. Remnant gravels of the Teays-Mahomet River in Teays Valley, WV were dated by Granger (1999, unpublished) to 1.21 ± 0.30 My. This damming led to the formation of massive proglacial lakes south of the ice margin, as evidenced by lacustrine sediments. Granger (1999, unpublished) also dated lacustrine proglacial lake sediments in Warsaw, KY to 1.39 ± 0.14 My, demonstrating that the abandonment of Teays Valley, WV and formation of proglacial lakes occurred essentially simultaneously. The proglacial lakes eventually coalesced and overflowed, forming the Ohio River (Prince and Spotila, 2013). This rapid drop in base level likely triggered an incision pulse

that propagated up the tributaries of the Ohio River, but this would have occurred following the major incision pulse at ~1.5 My. While it appears that this incision pulse was localized to former tributaries of the Teays-Mahomet River, it is possible that the other pulses along the Cumberland and Green Rivers were also recorded by the Tennessee and Shenandoah Rivers.

1.5 Research plan

This study mainly focuses on two major rivers that drain the southern and central Appalachian Mountains: the Tennessee River and the Shenandoah River (Figure 1.6). The Tennessee River has its headwaters in the Blue Ridge Mountains; as such, any significant tectonic uplift signal should be recorded in the sedimentary record of the river. The Shenandoah River watershed has been central to the debate of Appalachian landscape evolution, from the mapping of peneplains in the early 20th century to Hack's development of dynamic equilibrium in the latter half of the century. Both of these watersheds contain alluvial fans, terrace deposits, and manganese oxides that provide ideal targets for cosmogenic nuclide and $^{40}Ar/^{39}Ar$ geochronology.

1.5.1 Cosmogenic nuclide geochronology

Cosmogenic nuclide burial dating is a powerful tool to constrain rates and dates of landscape incision and aggradation in response to climatic or tectonic drivers. This technique was previously limited to deeply buried deposits, such as those in caves, due to the deleterious effect of postburial cosmogenic nuclide production by deeply-penetrating muons. The development of an isochron burial dating technique (Balco and Rovey, 2008) removed the need for deep burial by measuring ^{26}Al and ^{10}Be in a suite of clasts and treating postburial production of those nuclides as a constant. In doing so, isochron burial dating enables precise dating of shallow deposits including fluvial terraces (Erlanger et al., 2012) and alluvial fans (Zhao et al., 2017). It also permits the computation of basin-averaged paleo-erosion rates from dated deposits, enabling us to track paleo-erosion trends through time.

This study employs isochron burial dating to constrain the ages of terrace deposits and alluvial fans along the Tennessee and Shenandoah Rivers. By obtaining burial ages for terraces, it is possible to identify episodes of aggradation that preceded incision. Where a single terrace is present, one can estimate an average incision rate through time and a paleo-erosion rate at the time

of terrace deposition. Where multilevel terraces are present, it is possible to constrain incision rates and paleo-erosion rates more precisely through time. Where alluvial fans are found, significant aggradation episodes may be dated and local paleo-erosion rates calculated. We utilize the isochron burial dating technique to examine these trends across the reliable limit of the $^{26}Al/^{10}Be$ dating technique.

1.5.2 $^{40}Ar/^{39}Ar$ geochronology

Dating manganese oxide deposits with $^{40}Ar/^{39}Ar$ allows a deeper temporal look at erosional trends in the Appalachian Mountains. Manganese oxides are supergene deposits that form during periods where chemical weathering outpaces removal of material by erosion (Vasconcelos and Carmo, 2018). They form in shallow environments through interactions between groundwater, bedrock, and the atmosphere. The vertical extent of weathering profiles is a function of numerous factors including climatic regime, bedrock lithology, and denudation rate; however, most evidence points to manganese oxides generally forming within 100 meters of the surface. Because some manganese oxides – namely, cryptomelane (KMn_8O_{16}) – incorporate potassium, the formation of weathering profiles can be dated using $^{40}Ar/^{39}Ar$ geochronology where mineralogy permits.

We have characterized and dated cryptomelane from manganese oxide mines and prospects scattered across the southern and central Appalachian Mountains. These sites represent the remnants of former landscapes that were largely dissected during the Cenozoic. We have demonstrated that, contrary to the Hackian model of continuous erosion, it is possible to preserve ancient surfaces over tens of millions of years even in relatively steep landscapes. The ages of these deposits provide a long-term constraint on downwasting rates in the field area.

1.5.3 Chapter 2: The Tennessee River watershed

Chapter 2 focuses on the Pliocene and Pleistocene history of the Tennessee River and provides a chronology of incision and erosion using cosmogenic nuclide geochronology. These results are used to examine models of drainage reorganization that have been debated for over a century. The results of this study have significant implications not only for landscape evolution histories, but also for evolutionary biology studies of freshwater fauna and sediment transport to the Gulf of Mexico.

The abundance of fluvial terraces along the lower Tennessee River and thick weathering deposits along the upper Tennessee River provide evidence that Late Neogene incision has been largely localized to the lowermost reaches. A major knickzone at Muscle Shoals, AL appears to represent the boundary between significant incision downstream and minimal incision upstream. This investigation revealed that incision downstream of the knickzone was gradual during the Pliocene (~6 m/My) and likely increased at the onset of the Pleistocene. The presence of metamorphic quartz in all dated terraces, generally accepted to be a marker of Blue Ridge provenance, demonstrated that the Tennessee River had incised through the 300-meter-deep Walden Gorge near Chattanooga, TN prior to the Early Pliocene. This indicates that the Tennessee River likely has maintained its modern course (or one close to it) for over 4.4 My, and probably since the Late Miocene. Later, it appears that during the Early Pleistocene the Tennessee River experienced the same incision event ca. 1.5 My that affected other tributaries of the paleo-Ohio River, followed by regional aggradation at 0.8 My that filled the bedrock channel. Additional geochronology is necessary to confirm this hypothesis. At present, the lower Tennessee River is still gradually incising through the Mississippian Fort Payne chert along the Muscle Shoals knickzone.

1.5.4 Chapter 3: The Shenandoah River watershed

Chapter 3 presents cosmogenic nuclide geochronology results for alluvial fan and fluvial terrace deposits in the Shenandoah Valley. These ages are examined in the context of the episodic (Davisian) and continuous (Hackian) models that were pioneered in the Valley and Ridge province of the southern Appalachian Mountains. Distributions of deposit ages and paleo-erosion rates in the Shenandoah Valley also provide evidence for disequilibrium in this landscape.

Ages for terraces and fans in the Shenandoah Valley span the Pliocene and Pleistocene. In multiple instances, deposits share common ages and paleo-erosion rates despite being located far from each other within the watershed. The older deposits are located far upstream on the north and south forks of the Shenandoah River, at Briery Branch and Timberville. These deposits date to the mid-Piacenzian Warm Period (mPWP) and reveal erosion rates that far exceed modern estimates by Duxbury et al. (2015), suggesting that climate fluctuations may have enhanced erosional processes during that time. This hypothesis is supported by the simulations of Yan et al. (2016), who demonstrated that tropical storm activity was likely enhanced during the mPWP.

Rapid Pleistocene incision along the lower reaches of the Shenandoah River, as inferred from a tentative terrace burial age at Tilthammer Mill Road, indicate that the lower river system has experienced base level fluctuations that had minimal effect on the upper Shenandoah Valley.

1.5.5 Chapter 4: Manganese oxide geochronology in the southern Appalachians

Chapter 4 details efforts to date weathering products throughout the Cenozoic using $^{40}Ar/^{39}Ar$ in manganese oxides. These supergene ore deposits are scattered throughout the Appalachian Mountains and have been thought to represent remnants of relict landscapes. They precipitate during periods of extended weathering and, given that they form within ~100 meters of the surface, can be used to estimate landscape lowering rates over longer time periods than possible with cosmogenic $^{26}Al/^{10}Be$ geochronology. We have also examined the rare-earth element and trace element distributions for a number of manganese oxides in order to better characterize their formation conditions and discern chemical signatures of different sample morphologies.

We obtained ages for manganese oxides that span nearly the entire Cenozoic. Ages of manganese oxides have no apparent correlation with long-term temperature trends. The long-term preservation of these ancient deposits in the supergene zone provides evidence that much of the southern and central Appalachians have been gradually eroding since at least the early Cenozoic. Rare earth element distributions illustrate the cycle of dissolution and reprecipitation that has driven the formation of different manganese oxide morphologies. In some instances, these processes have generated significant accumulations of REE in botryoidal samples relative to breccias and massive manganese oxides, revealing the evolution of different manganese oxide morphologies as weathering progresses.

1.5.6 Chapter 5: The Gray Fossil Site

Chapter 5 presents a new radiometric constraint on the age of the Gray Fossil Site (GFS) in Washington County, TN. Since its discovery in 2000, age estimates for the GFS have undergone continuous revision with improving biostratigraphic controls. Initial age estimates ranged from 4.5-7 My on the basis of rhinoceros and short-faced bear fossils (Wallace and Wang, 2004). Coring of the site and palynological analyses in 2011 yielded a Paleocene-Eocene age for portions of the deposit (Zobaa et al., 2011), though that age has come under scrutiny by more recent studies

and the results of this work. Samuels et al. (2018) concluded that the site dates to 4.5-4.9 My on the basis of rhinoceros, leporid, and cricetid fossils. This variance in age estimates motivated an independent constraint on the age of the sinkhole fill, which has important implications both for mammal emergence/migration patterns and the incision history of the nearby Watauga River, a major drainage in the Tennessee River watershed.

Measurements of ^{26}Al and ^{10}Be concentrations at eight depth increments along the core previously studied by Zobaa et al. (2011) demonstrate that the Gray Fossil Site sinkhole complex likely filled prior to the Blancan. Based on these measurements and the reversed paleomagnetic orientation of the cored sediments, we have estimated a most likely infilling age of 5.23-5.89 My for the Gray Fossil Site sinkhole complex. This age is slightly older than the most recent biostratigraphic estimates, possibly due to loosely constrained first appearance data for Neogene fauna at the site. The exponential relationship between depth and nuclide concentrations implies that the sinkhole complex filled relatively rapidly, as hypothesized by Shunk et al. (2009). Our work demonstrates that Hemphillian paleo-erosion rates were gradual (<10 m/My) and the modern surficial erosion rate at the site is even slower (~2 m/My).

1.5.7 Chapter 6: The Upland Complex

Chapter 6 focuses on constraining the age of the Upland Complex, a widespread group of terraces found along the Mississippi River. These terraces record an apparently long interval of base level stability along the Mississippi River and consequently its tributaries, including the Tennessee River. The terraces are found throughout the Mississippi drainage basin and have been variously linked to Pleistocene glaciations, ongoing seismicity in the New Madrid Seismic Zone, and Pleistocene sedimentation in the Gulf of Mexico. Despite these significant ties, the age of the Upland Complex terraces has been debated for decades. Previous age estimates have ranged from the Pleistocene to Miocene, with recent cosmogenic work pointing to either a Pleistocene or Pliocene age (Rovey and Spoering, 2020). Estimations of the deposit's true age have been hampered by significant post-burial production of cosmogenic nuclides, which we address by using a multi-chronometer approach in this chapter.

Fourteen cosmogenic $^{26}Al/^{10}Be$ burial ages at five terrace deposits in Kentucky, Arkansas, Tennessee, and Mississippi confirm the previously estimated Plio-Pleistocene age of the Upland Complex. We supplemented this age distribution with (U-Th)/He dating of post-depositional

goethite cements that frequently form horizons in the Upland Complex. In total, 84 fragments of goethite from four quarries in the Upland Complex yielded ages that span the Early Pliocene to Late Pleistocene. Given that these deposits form in-situ, the Pliocene ages at multiple locations point to a Pliocene minimum age for the Upland Complex. This result indicates that the Upland Complex is a preglacial gravel deposit that likely formed during a prolonged period of base level stability prior to the unstable Pleistocene. This chapter represents a collaboration between W. Odom, D. Granger, R. Van Arsdale (University of Memphis), and F. Hofmann (CalTech), and was published in *Geomorphology* in October 2020.

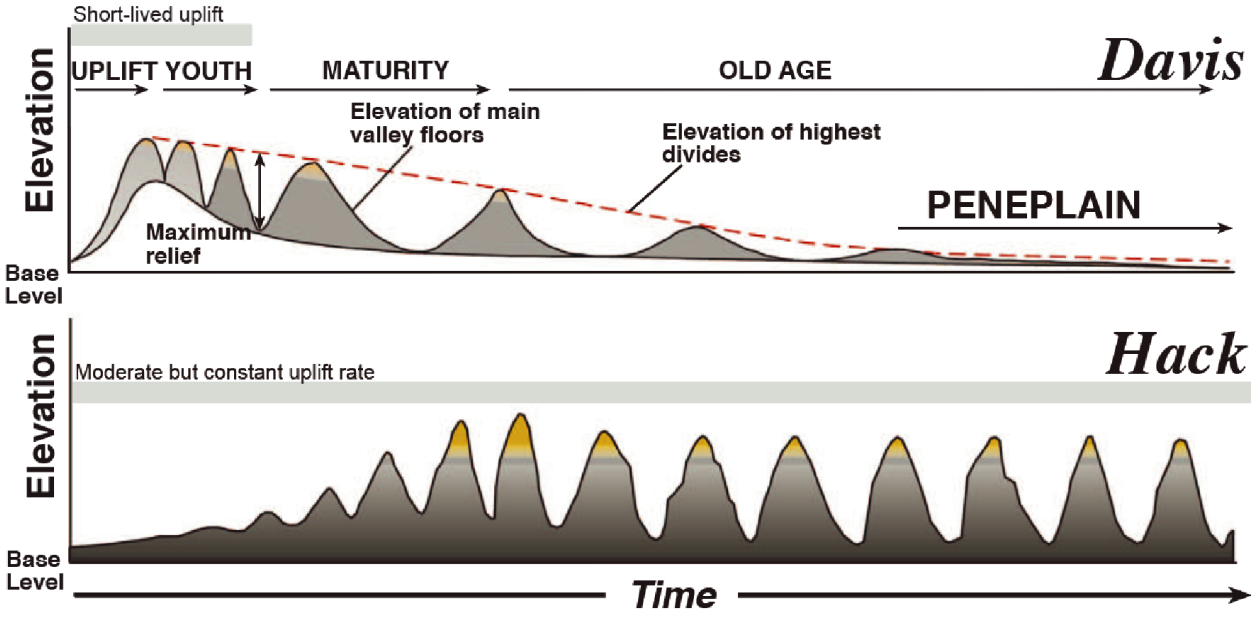

Figure 1.1. Schematic contrasting the Davisian and Hackian landscape paradigms. The Davisian model achieves low relief following a single pulse of uplift, while the Hackian model maintains relief during continuous uplift. Figure modified from Vasconcelos and Carmo (2018).

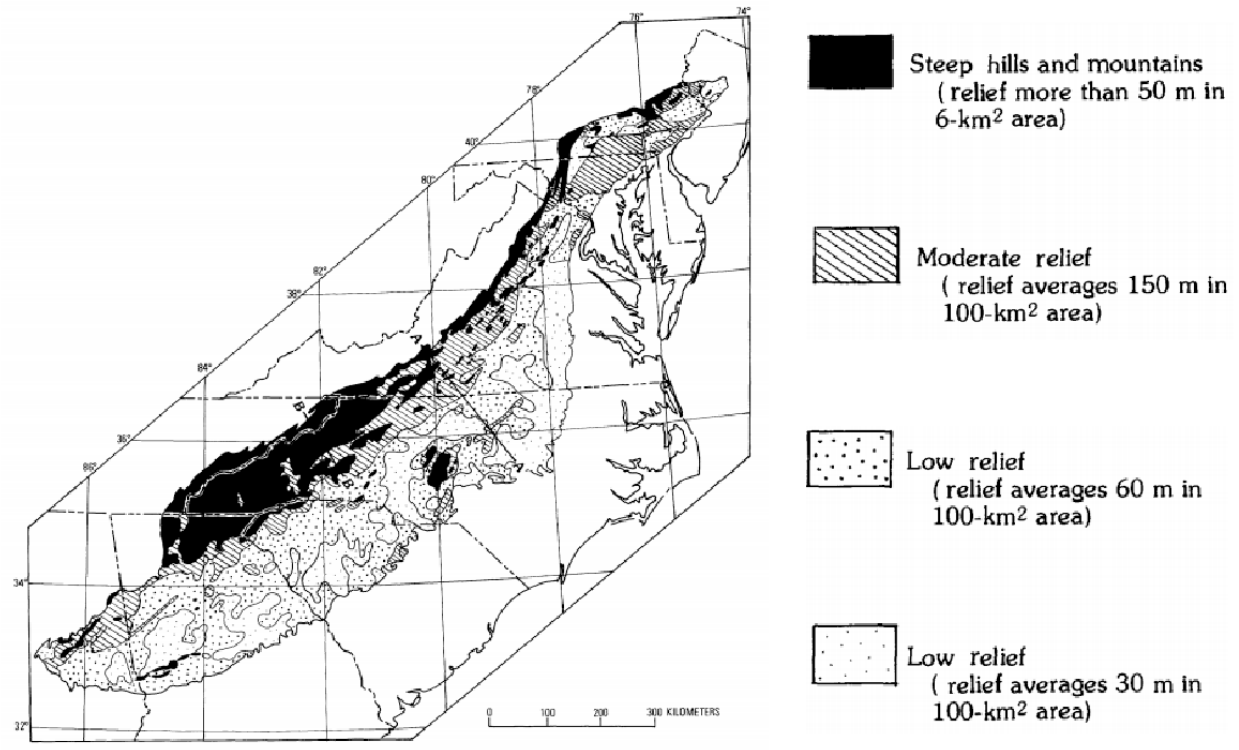

Figure 1.2. Relief map from Hack (1982) demonstrating that areas of low relief are scattered throughout the Appalachians, even within the high-relief Blue Ridge province. These zones were commonly interpreted to represent relict surfaces (i.e., peneplains) during the 19th and 20th centuries. See Chapter 4 for additional discussion and figures relating to this concept.

Figure 1.3. Field photos of common manganese oxide morphologies. Vein-filled botryoidal deposits (left) are common throughout Virginia. Manganese oxide-cemented breccias (right) are found both in Tennessee and Virginia, and frequently host dateable material. The botryoidal deposit was collected at the Silver Creek Mine, VA while the brecciated deposit was photographed at Gap Mountain, VA.

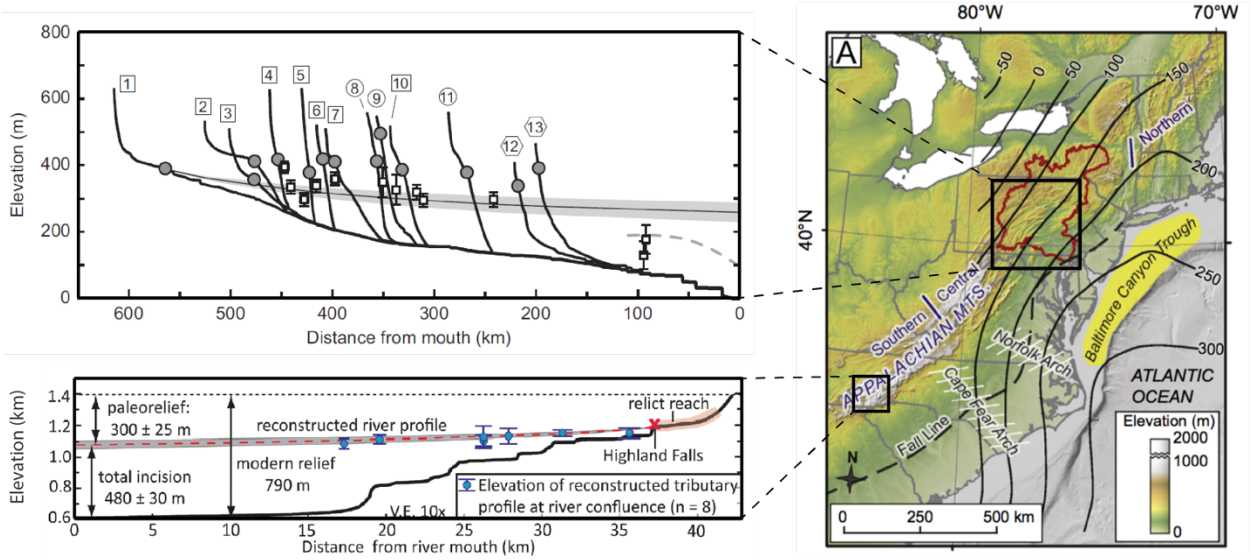

Figure 1.4. Longitudinal profiles of the Susquehanna (top) and Cullasaja (bottom) Rivers, both of which were used to invoke hundreds of meters of uplift during the Neogene. Note that the Susquehanna River basin is immediately north of the Shenandoah River basin, while the Cullasaja River is a tributary to the Tennessee River. Figures modified from Gallen et al. (2013) and Miller et al. (2013).

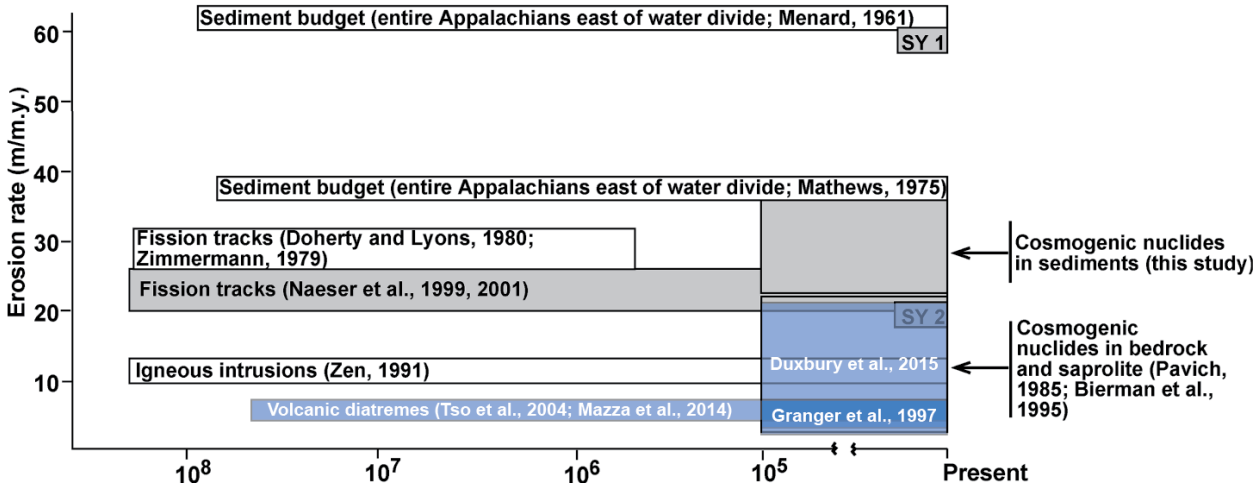

Figure 1.5. Modern erosion rates from ^{10}Be and long-term erosion rates derived from other geochronometers demonstrate disparities in Appalachian erosion rates through time. Figure modified from Matmon et al. (2003).

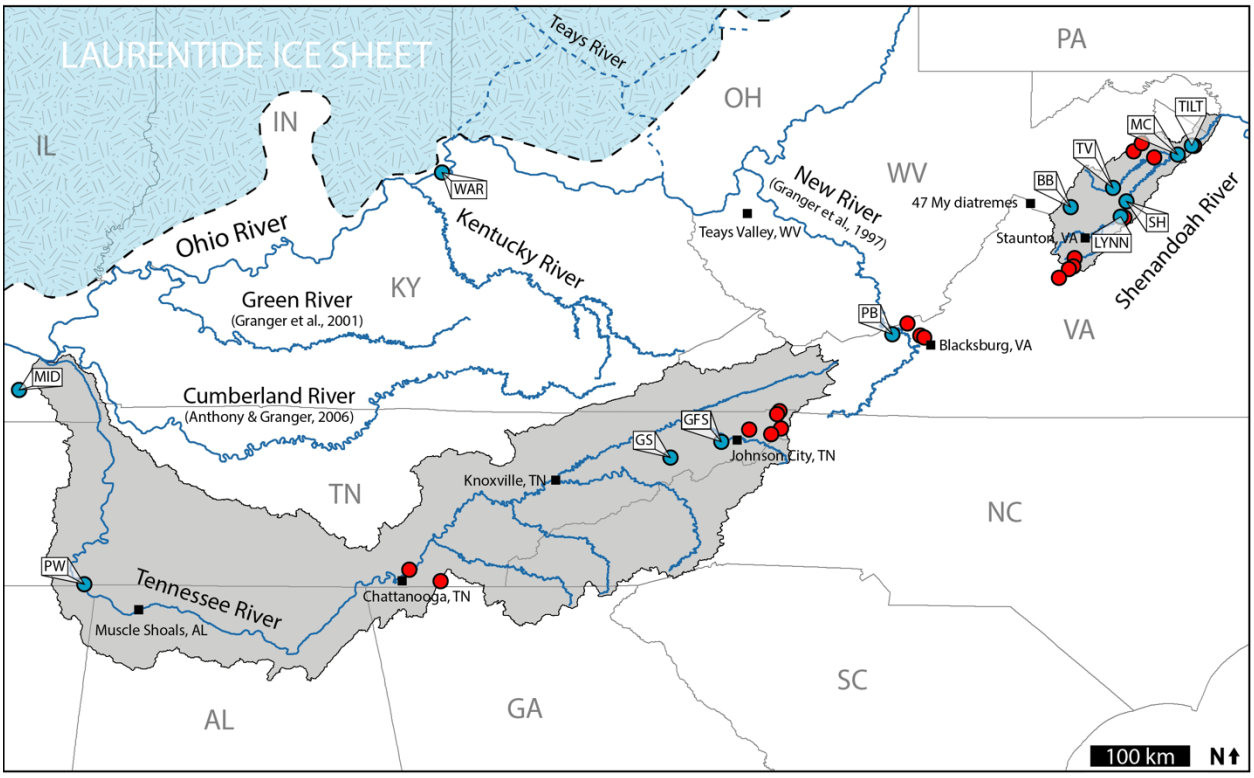

Figure 1.6. Overview of primary study area. The Tennessee and Shenandoah River basins are shaded, and previously studied rivers are labeled. Blue circles denote areas dated using cosmogenic nuclides, while red circles represent areas where manganese oxides were collected for $^{40}Ar/^{39}Ar$ geochronology. The Upland Complex is not shown due to the widespread nature of the deposits and emphasis placed on the Tennessee and Shenandoah River basins in this thesis.

1.6 References

Ahnert, F., (1970). Functional relationships between denudation, relief, and uplift in large, mid-latitude drainage basins. American Journal of Science, 268 (3), 243-263.

Anthony, D. M., & Granger, D. E., (2004). A late Tertiary origin for multilevel caves along the western escarpment of the Cumberland Plateau, Tennessee and Kentucky, established by cosmogenic ^{26}Al and ^{10}Be. Journal of Cave and Karst Studies, 66(2), 46-55.

Anthony, D. M., & Granger, D. E., (2006). Five million years of Appalachian landscape evolution preserved in cave sediments. Geological Society of America Special Papers, 404, 39-50.

Anthony, D. M., & Granger, D. E., (2007). A new chronology for the age of Appalachian erosional surfaces determined by cosmogenic nuclides in cave sediments. Earth Surface Processes and Landforms, 32(6), 874-887.

Balco, G., & Rovey, C. W., (2008). An isochron method for cosmogenic-nuclide dating of buried soils and sediments. American Journal of Science, 308(10), 1083-1114.

Balco, G., & Rovey, C. W., (2010). Absolute chronology for major Pleistocene advances of the Laurentide Ice Sheet. Geology, 38(9), 795-798.

Bárdossy, G., & Aleva, G. J. J., (1990). Lateritic bauxites (Vol. 27). Elsevier Science Ltd.

Biryol, C. B., Wagner, L. S., Fischer, K. M., & Hawman, R. B., (2016). Relationship between observed upper mantle structures and recent tectonic activity across the Southeastern United States. Journal of Geophysical Research: Solid Earth.

Bishop, P., (2007). Long term landscape evolution: linking tectonics and surface processes. Earth Surface Processes and Landforms, 32(3), 329-365.

Bridge, J., (1950). Bauxite deposits of the southeastern United States. Snyder, FG.

Davis, W. M., (1889). The rivers and valleys of Pennsylvania. National Geographic Society.

Davis, W. M., (1891). The Geological Dates of Origin of Certain Topographic Forms on the Atlantic Slope of the United States, Geological Society of American Bulletin, 2, 545-584.

Duxbury, J., Bierman, P. R., Portenga, E. W., Pavich, M. J., Southworth, S., & Freeman, S. P., (2015). Erosion rates in and around Shenandoah National Park, Virginia, determined using analysis of cosmogenic ^{10}Be. American Journal of Science, 315(1), 46-76.

Erlanger, E. D., Granger, D. E., & Gibbon, R. J., (2012). Rock uplift rates in South Africa from isochron burial dating of fluvial and marine terraces. Geology, 40(11), 1019-1022.

Feng, Y. X., & Vasconcelos, P., (2007). Chronology of Pleistocene weathering processes, southeast Queensland, Australia. Earth and Planetary Science Letters, 263(3), 275-287.

Fenneman, N. M., (1944). Physiography of the eastern United States. McGraw-Hill Book Co., New York.

Finlayson, C. P., Barnes, R. H., Colvin, J. M., & Luther, E. T., (1966). Geologic map and mineral resources summary of the Chattanooga quadrangle (including the Tennessee portion of the Oglethorpe quadrangle, GA-TN). Tennessee Division of Geology, geologic quadrangle map 105 SE.

Ford, D., & Williams, P. D., (2013). Karst hydrogeology and geomorphology. John Wiley & Sons.

Gallen, S. F. (2018). Lithologic controls on landscape dynamics and aquatic species evolution in post-orogenic mountains. Earth and Planetary Science Letters, 493, 150-160.

Gallen, S. F., Wegmann, K. W., & Bohnenstiehl, D. R., (2013). Miocene rejuvenation of topographic relief in the southern Appalachians. GSA Today, 23(2), 4-10.

Galloway, W. E., Whiteaker, T. L., & Ganey-Curry, P., (2011). History of Cenozoic North American drainage basin evolution, sediment yield, and accumulation in the Gulf of Mexico basin. Geosphere, 7(4), 938-973.

Granger, D. E., Kirchner, J. W., & Finkel, R. C., (1997). Quaternary downcutting rate of the New River, Virginia, measured from differential decay of cosmogenic ^{26}Al and ^{10}Be in cave-deposited alluvium. Geology, 25(2), 107-110.

Granger, D. E., Fabel, D., & Palmer, A. N., (2001). Pliocene-Pleistocene incision of the Green River, Kentucky, determined from radioactive decay of cosmogenic ^{26}Al and ^{10}Be in Mammoth Cave sediments. Geological Society of America Bulletin, 113(7), 825-836.

Granger, D. E., Odom, W. E., & Fabel, D., (2018). A re-evaluation of the timing of Mammoth Cave development and formation of the Ohio River. In GSA Annual Meeting in Indianapolis, Indiana, USA. GSA.

Hack, J. T., (1960). Interpretation of erosional topography in humid temperate regions. Bobbs-Merrill.

Hack, J. T., (1965). Geomorphology of the Shenandoah Valley, Virginia and West Virginia, and origin of the residual ore deposits (No. 484). US Govt. Print. Off.

Hack, J. T., (1982). Physiographic divisions and differential uplift in the Piedmont and Blue Ridge (No. 1265). US Govt. Print. Off.

Hancock, G., & Kirwan, M., (2007). Summit erosion rates deduced from ^{10}Be: Implications for relief production in the central Appalachians. Geology,35(1), 89-92.

Hatcher, R. D., (1989). Tectonic synthesis of the U.S. Appalachians, in Hatcher R. D., Thomas, W. A., and Viele, G. W., eds., The Appalachian-Ouachita Orogen in the United States: Boulder, Colorado, USA Geological Society of America Decade of North American Geology, v. F-2, p. 511-531.

Hewett, D. F., (1916). Some manganese mines in Virginia and Maryland, in Ransome, F. L., and Gale, H. S., Contributions to economic geology, 1916, Part. 1: U.S. Geol. Survey Bull. 640, p. 37-71.

King, P. B., (1949). The floor of the Shenandoah Valley [Virginia]. American Journal of Science, 247(2), 73-93.

King, P. B., (1950). Geology of the Elkton area, Virginia. U.S. Geol. Survey Prof. Paper 230.

Liu, L., (2014). Rejuvenation of Appalachian topography caused by subsidence-induced differential erosion. Nature Geoscience, 7(7), 518-523.

Matmon, A., Bierman, P., Larsen, J., Southworth, S., & Caffee, M., (2003). Temporally and spatially uniform rates of erosion in the southern Appalachian Great Smoky Mountains. Geology, 31(2), 155-158.

Mazza, S. E., Gazel, E., Johnson, E. A., Kunk, M. J., McAleer, R., Spotila, J. A., Bizimis, M., & Coleman, D. S., (2014). Volcanoes of the passive margin: The youngest magmatic event in eastern North America. Geology, 42(6), 483-486.

Miller, S. R., Sak, P. B., Kirby, E., & Bierman, P. R., (2013). Neogene rejuvenation of central Appalachian topography: Evidence for differential rock uplift from stream profiles and erosion rates. Earth and Planetary Science Letters, 369, 1-12.

Miser, H. D., (1950). Manganese deposits of the southeastern states. In Proc. Symposium on Mineral Resources of the Southeastern United States, Univ. Tennessee (pp. 152-69).

Naeser, C. W., Naeser, N. D., Newell, W. L., Southworth, S., Edwards, L. E., & Weems, R. E., (2016). Erosional and depositional history of the Atlantic passive margin as recorded in detrital zircon fission-track ages and lithic detritus in Atlantic Coastal plain sediments. American Journal of Science, 316(2), 110-168.

Near, T. J., & Keck, B. P. (2005). Dispersal, vicariance, and timing of diversification in Nothonotus darters. Molecular Ecology, 14(11), 3485-3496.

Overstreet, E. C. F., (1964). Geology of the southeastern bauxite deposits (No. 1199-A). US Govt. Print. Off.

Pazzaglia, F. J., & Brandon, M. T., (1996). Macrogeomorphic evolution of the post-Triassic Appalachian Mountains determined by deconvolution of the offshore basin sedimentary record. Basin Research, 8(3), 255-278.

Poag, C. W., & Sevon, W. D., (1989). A record of Appalachian denudation in postrift Mesozoic and Cenozoic sedimentary deposits of the US middle Atlantic continental margin. Geomorphology, 2(1), 119-157.

Prince, P. S., & Spotila, J. A., (2013). Evidence of transient topographic disequilibrium in a landward passive margin river system: knickpoints and paleo landscapes of the New River basin, southern Appalachians. Earth Surface Processes and Landforms, 38(14), 1685-1699.

Rader, E. K., and Wilkes, G. P., (2001). Geolgic map of the Virginia portion of the Staunton 30x60 minute quadrangle. Virginia Division of Mineral Resources, Publication 163.

Rovey, C. W., Spoering, G., 2020. Age and provenance of upland gravels in Missouri, USA, and their relationship to Early Pleistocene glaciation. Boreas 49(2), 333-349.

Samuels, J. X., Bredehoeft, K. E., & Wallace, S. C., (2018). A new species of Gulo from the Early Pliocene Gray Fossil Site (Eastern United States); rethinking the evolution of wolverines. PeerJ, 6, e4648.

Shunk, A. J., Driese, S. G., & Dunbar, J. A., (2009). Late Tertiary paleoclimatic interpretation from lacustrine rhythmites in the Gray Fossil Site, northeastern Tennessee, USA. *Journal of Paleolimnology*, *42*(1), 11-24.

Teller, J. T., & Goldthwait, R. P., (1991). The old Kentucky River; a major tributary to the Teays River. Geology and hydrogeology of the Teays-Mahomet bedrock valley system: Geological Society of America Special Paper, 258, 29-41.

Thornbury, W. D., (1965). Regional geomorphology of the United States. Soil Science, 100(2), 148.

Tso, J. L., McDowell, R. R., Avary, K. L., Matchen, D. L., & Wilkes, G. P., (2004). Middle Eocene igneous rocks in the Valley and Ridge of Virginia and West Virginia. US Geological Survey Circular, 1624, 137-157.

Vasconcelos, P. M., (1999). K-Ar and $^{40}Ar/^{39}Ar$ geochronology of weathering processes. Annual Review of Earth and Planetary Sciences, 27(1), 183-229.

Vasconcelos, P. M., & Carmo, I. D. O., (2018). Calibrating denudation chronology through $^{40}Ar/^{39}Ar$ weathering geochronology. *Earth-science reviews*, *179*, 411-435.

Wagner, L. S., Stewart, K., & Metcalf, K., (2012). Crustal-scale shortening structures beneath the Blue Ridge Mountains, North Carolina, USA. Lithosphere, 4(3), 242-256.

Wallace, S. C., & Wang, X., (2004). Two new carnivores from an unusual late Tertiary forest biota in eastern North America. Nature, 431(7008), 556.

Whitelaw, J. L., Mickus, K., Whitelaw, M. J., & Nave, J., (2008). High-resolution gravity study of the Gray Fossil Site. Geophysics, 73(2), B25-B32.

Wilson, R. L., (1989). Geologic map and mineral resources summary of the East Chattanooga quadrangle. Tennessee Division of Geologic, Geologic Quadrangle Map 112 SW.

Yan, Q., Wei, T., Korty, R. L., Kossin, J. P., Zhang, Z., & Wang, H., (2016). Enhanced intensity of global tropical cyclones during the mid-Pliocene warm period. Proceedings of the National Academy of Sciences, 113(46), 12963-12967.

Zhao, Z., Granger, D. E., Chen, Y., Shu, Q., Liu, G., Zhang, M., ... & Yan, Y., (2017). Cosmogenic nuclide burial dating of an alluvial conglomerate sequence: an example from the Hexi Corridor, NE Tibetan Plateau. Quaternary Geochronology, 39, 68-78.

Zobaa, M. K., Zavada, M. S., Whitelaw, M. J., Shunk, A. J., & Oboh-Ikuenobe, F. E., (2011). Palynology and palynofacies analyses of the Gray Fossil Site, eastern Tennessee: their role in understanding the basin-fill history. Palaeogeography, Palaeoclimatology, Palaeoecology, 308(3-4), 433-444.

CHAPTER 2. AGGRADATION, INCISION, AND DRAINAGE EVOLUTION OF THE LATE NEOGENE TENNESSEE RIVER FROM COSMOGENIC ^{26}AL/^{10}BE ISOCHRON BURIAL DATING

2.1 The Tennessee River watershed

The Tennessee River follows an unusually indirect path to its outlet (Figure 2.1). Originating in the Valley and Ridge province at Knoxville, Tennessee, at the confluence of rivers draining the Valley and Ridge and the Blue Ridge Mountains, the river flows southwest along the strike of the fold-and-thrust belt for >200 km before abruptly turning northwest at Chattanooga. There, the river cuts a 300 m deep gorge through resistant sandstones of the Cumberland Plateau at Walden Ridge. After exiting the Valley and Ridge, the river flows west across northern Alabama, skirting the southern flank of the Nashville Dome on a topographic surface developed atop the resistant Mississippian Fort Payne chert. The Fort Payne chert primarily crops out to the north of the Tennessee River and is responsible for the generally steeper tributaries along the north side of the river. Beneath Wheeler Lake, Alabama, the Fort Payne directly underlies the Tennessee River (Rindsberg, 2004a). Shortly downstream, the river breaks through the Fort Payne chert at a ~50 m high knickzone at Muscle Shoals that marks the most significant convexity along the Tennessee River (Figures 2.1, 2.2) and soon encounters younger, more erodible Cretaceous and Paleogene rocks of the Mississippi Embayment near Pickwick, Tennessee. It turns and follows the strike of the younger rocks north, directly away from the Gulf of Mexico and 180 degrees opposite of the Mississippi River less than 200 km to the west. It continues a northern course for ~300 km, joins the Ohio River, and executes a hairpin bend to join the Mississippi River, ultimately draining to the Gulf of Mexico.

Why the Tennessee River turns northward, away from its eventual outlet in the Gulf, when it encounters the Cretaceous sediments near Pickwick, TN has stimulated discussion for over a century. It would seem far more efficient for the river to cut across the highly erodible sediments directly to the Mississippi River, or to drain southwards directly to the Gulf. In fact, the present drainage divide to the Gulf of Mexico through the Tombigbee River near Holcut, Mississippi lies only ~50 meters above the modern Tennessee River and is occupied by a canal linking the two rivers. Many authors have hypothesized that the course of the Tennessee River evolved from one or more drainage captures, potentially here and/or at the westward bend through Walden Ridge.

There is good evidence from sedimentary records in the Gulf of Mexico, as well as from the distribution of freshwater fish and other riverine animals, that the Tennessee River did drain more directly to the Gulf of Mexico until the Late Cenozoic, although its exact path remains debated.

Sedimentary evidence of a paleo-Tennessee River connection to the Gulf comes from Late Cretaceous to Eocene terrestrial fluvial sediments and basin-floor deposits near the inferred outlet near Mobile, AL (Blum et al., 2017). Xu et al. (2017) also identified Grenville (950-1300 Ma) and Appalachian-Ouachita (280-500 Ma) U-Pb age signatures in terrestrial Miocene outcrops that they attributed to an ancestral Tennessee River that carried sediment from the southern Appalachian Mountains to the Mobile Basin. Sediment accumulation rates near Mobile Bay, attributed to a paleo-Tennessee River, accelerated drastically during the middle Miocene (Galloway et al., 2011) and have been interpreted as evidence for Miocene uplift and erosion of the southern Appalachians (Gallen et al., 2013; Xu et al., 2017). Accumulation rates then diminished during the Late Miocene - Early Pliocene, which has been interpreted as being due to the basin's capture by the Mississippi River system (Galloway et al., 2011; Ewing and Galloway, 2019). Age estimates for the capture of the Tennessee River away from its direct course to Mobile Bay range from Eocene-Oligocene (Blum et al., 2017) to Pleistocene (Galloway et al., 2011).

Additional evidence for a former linkage between the Tennessee River and the Mobile Basin comes from the similarity of aquatic species in these rivers that now drain separately to the Gulf. Hayes and Campbell (1894; 1900) first suggested such a link based on geomorphic reconstructions and on the distribution of molluscs. Their evidence has been heavily debated, with some suggesting that the molluscs could have been carried between the watersheds on the feet of birds (Johnson, 1905). More recently, Mayden (1988) and Hoagstrom (2014) examined similarities in the fish fauna across the southeastern United States and found some similarities between the Mobile Basin and other rivers. However, the Mobile Basin shows the fewest affinities with the other rivers and occupies the basal node on their cladograms. They interpreted that the Mobile Basin was likely connected to the Tennessee River in the past, but that the connection was severed early in the drainage history, far prior to known Pleistocene drainage reorganizations due to the Laurentide ice sheet. Examining DNA differences from related darter species, Near and Keck (2005) used a molecular clock to determine that separation of the Mobile Basin from the Tennessee River likely occurred at 9.0 ± 1.7 Ma. On the younger end of the spectrum, Niemiller et al. (2016) used the distribution of cavefishes on either side of Walden Ridge to hypothesize that

the Tennessee River was captured into its western course across Alabama much more recently, in the Late Pliocene. As such, biological evidence does not provide an unambiguous age for the course of the modern Tennessee River.

It is worth noting that the distribution of fish and riverine species alone may not be sufficient to distinguish whether the entire Tennessee River flowed to Mobile Bay or whether there were smaller drainage captures along the margins (Figure 2.1). For example, using phylogenetic analyses of darter species, Persons (2010) interpreted the capture of Bear Creek from the Tombigbee River into the Tennessee River drainage. Mills et al. (2005) noted high-level gravels indicating a former connection between the Ocoee River (of the modern Tennessee River basin) and the Conasauga River (of the modern Coosa River basin that drains to the Gulf), that could have exchanged fish species across the drainage divide. Nonetheless, the marked decrease in sediment delivery to the Gulf in the Late Miocene-Early Pliocene and the molecular clock estimate of vicariance at 9.0 ± 1.7 Ma both point to the loss of a significant former connection between the Tennessee River and Mobile Bay in the Late Miocene.

Significant evidence exists for the formation of the modern Tennessee River by at least one major drainage capture during the late Cenozoic, but precisely reconstructing the prior courses of the Tennessee River remains challenging. The most common proposed capture point is the 90 degree turn where the river cuts across strike through Walden Ridge near Chattanooga, Tennessee. Hayes and Campbell (1894) proposed that the paleo-Tennessee River had previously continued down strike, flowing southwestward from Chattanooga via the Coosa River, a major tributary of the Mobile Basin (Figure 2.1). Recent geomorphic modeling by Gallen (2018) showed that knickzones in the upper Tennessee River basin are consistent with a pulse of Late Cenozoic incision driven by capture of the upper Tennessee River through Walden Ridge during the Late Miocene. However, this drainage capture has been questioned by others on the grounds that there are no known gravel deposits in the area of the preserved Coosa-Tennessee linkage (Mills et al., 2005; Persons, 2010). Based on the distribution of vein quartz pebbles in Cretaceous conglomerates, Adams (1928) suggested that the Tennessee River has flowed west across northern Alabama since the Cretaceous and that the connection across Walden Ridge was superposed from that time.

Another possible drainage capture point is where the Tennessee River turns north at Pickwick, Tennessee, away from the Gulf of Mexico, to follow the strike of the Cretaceous

sediments. Self (2000) mapped quartz gravels and hypothesized that the Tennessee River continued west to the Mississippi River through the Hatchie River valley until the Late Miocene-Early Pliocene. Mills and Kaye (2001) mapped and compiled the presence of distinctive vein quartz pebbles preserved in ancient fluvial deposits as potential evidence for the course of the Tennessee River. They found several areas with scattered high-level pebbles indicating possible connections between the Tennessee River and the Mobile Basin, notably along the Sipsey, Black Warrior, and Tombigbee Rivers, but there was little clear evidence of a major channel. In particular, the gravels along the Tombigbee River are lower than those along the Tennessee River but appear similar in age, which Russell and Schmitz (2003) interpreted as evidence against a former connection. Mills and Kaye (2001) instead proposed that the gravels along the Tombigbee may reflect (1) reworking of Tennessee River terraces by the Tombigbee River or (2) genuine terraces of the ancestral Tennessee River that have been lowered by dissolution of underlying bedrock. Given these potential scenarios, along with the antiquity of the Tennessee River and generally poor preservation of fluvial deposits (Mills and Kaye, 2001), many of these hypotheses are difficult to test conclusively.

Constraints on the former course of the Tennessee River have been difficult to test primarily because there are so few deposits that are datable or contain unambiguous Tennessee River sediments. The lower Tennessee River, downstream of Walden Gorge, has remarkably few terraces and high-level gravel deposits are rare and thin, often a mere scattering of rounded quartz pebbles. The notable exception is where the river encounters the erodible Cretaceous rocks downstream of Muscle Shoals, where its valley widens and a flight of well-developed terraces has been preserved. These terraces are very near the point where the Tennessee River turns north, away from the Gulf, and can help constrain the minimum age of the river's anomalous turn.

2.2 Site descriptions

At its northward turn near Pickwick, the Tennessee River flows over the Mississippian Fort Payne chert into a highly dissected zone of onlapping poorly consolidated Cretaceous sands (Russell, 1968; Russell et al., 1972; Parks and Russell, 1975). This area hosts terraces that represent the most complete fluvial archive of incision in the Tennessee River watershed. The presence of quartzite clasts in each terrace level provides evidence of a paleo-drainage that included the Blue Ridge province, given that no significant outcrops of quartzite are found in the

Valley and Ridge or Cumberland Plateau. These terraces have never been directly dated, though geologic maps in the area suggest Pliocene-Pleistocene ages.

Self (2003) divided the terraces into five levels (QFL^1-QFL^5), with bases ranging in elevation from 128 to 213 m above sea level (asl) (Figures 2.2, 2.3). We have revised this nomenclature to Nt_1-Nt_5, given that not all terraces are necessarily Quaternary in age. Nt_5 is the highest terrace, with remnants described by Self (2003) at ≥ 213 m asl to the east of the Tennessee River near Pickwick, TN. It is the most quartzite-rich terrace, with rounded quartzite clasts comprising 84% of the deposits. Self (2003) hypothesized that this terrace level corresponded with the terraces along the nearby Hatchie River and inferred a prior connection, but a sizable discrepancy in terrace elevations between the two watersheds (Mills and Kaye, 2001) and a potential source for quartzite gravels in the Hatchie River area (Parks, 1992) suggest that no such connection existed. Along with its high quartzite content, Nt_5 features no chert clasts, indicating that the upstream Fort Payne chert had likely not been incised by that time (Figure 2.3) (Self, 2003). The terraces below feature complementary opposite lithological compositions, with an average 75% chert and 13% quartzite content. Self (2003) noted that the chert in the Tennessee River terraces was likely predominantly derived from the Mississippian Fort Payne formation, implying that the Tennessee River began incising through the Fort Payne chert sometime between the deposition of Nt_5 and Nt_4 (Self, 2003).

Nt_4 is the second highest terrace, located at ≥ 183 m asl and featuring centimeter-sized rounded quartzites within a chert-rich, iron-cemented sandstone (Figure 2.3) (Self, 2003). The deposit is substantially eroded, with only about 50 cm of iron-cemented gravels remaining at visited locations. Nt_3 is the third-highest terrace, located at ≥ 171 m asl. It consists of predominantly subrounded to rounded chert with some quartz and rounded quartzite clasts (Figure 2.3). Nt_2 is the second lowest terrace and is located at ≥ 152 m asl. It features iron-oxide cements, small (<5 cm) chert gravels, and occasional rounded quartzite clasts within a quartz-rich sand (Figure 2.3) (Self, 2003). Nt_1 is the lowest terrace, located at ≥ 128 m asl and featuring abundant iron-oxide cements and replacements (Figure 2.3) (Self, 2003). Most gravels are <5 cm in diameter and cherty, with occasional rounded quartzite clasts.

The thickness of sand and gravel deposits varies significantly between different terrace levels, ranging from 0.5 m in Nt_4 to 6-10 m in the lowest three terraces. Higher terraces are generally more dissected; fieldwork revealed scant evidence of Nt_5, while Nt_4 was substantially

eroded and insufficiently thick for cosmogenic nuclide burial dating. We sampled terrace levels Nt_1- Nt_3 for $^{26}Al/^{10}Be$ burial dating. Sample locations are provided in Table 2.1 and Figure 2.4. At each site, we collected quartzite cobbles for $^{26}Al/^{10}Be$ burial isochrons (Figure 2.5a-2.5f). Sands were also collected for isochrons and estimates of paleo-erosion rates.

2.3 Methods

2.3.1 Cosmogenic nuclide production and decay

The concentration of a given cosmogenic nuclide in rock or sediment reflects the balance between decay of already-present (i.e., inherited) nuclides and ongoing production of additional nuclides via secondary cosmic ray interactions. For a cosmogenic nuclide *i*, this balance is represented by the equation:

$$N_i(z,t) = N(z,0)e^{-t/\tau_i} + \frac{P_i e^{-\rho z/\Lambda}}{\frac{1}{\tau_i} + \frac{\rho E}{\Lambda}}\left(1 - e^{-\left(\frac{1}{\tau_i} + \frac{\rho E}{\Lambda}\right)t}\right) \qquad [\mathbf{1}]$$

Where z is depth below the surface, t is time spent at that depth, τ_i is nuclide mean-life, P_i is the nuclide's surficial production rate, ρ is the density of overlying material, and Λ is the penetration length of cosmic radiation (Lal, 1991). The first term on the right side of the equation represents the inherited component of the cosmogenic nuclide inventory and its decay across time t, while the second term on the right side of the equation represents the ongoing production and decay of additional cosmogenic nuclides as a function of depth. This equation may be modified to account for production of cosmogenic nuclides by multiple pathways including neutrons, fast muons, and negative muons. Because these particles have significantly different penetration lengths, it is useful to use a parameterized approach for calculating production at depth and sum the different components of production:

$$N_i(z,t) = N(z,0)e^{-t/\tau_i} + \sum_j \frac{A_{i,j} e^{-\rho z/L_j}}{\frac{1}{\tau_i} + \frac{\rho E}{L_j}}\left(1 - e^{-\left(\frac{1}{\tau_i} + \frac{\rho E}{L_j}\right)t}\right) \qquad [\mathbf{2}]$$

Where j is the production pathway of nuclide i, $A_{i,j}$ is the production rate factor, and L_j is the penetration length factor used for parameterizing production via neutrons and muons at depth (Granger, 2014). This equation is useful for modeling the concentrations of ^{26}Al and ^{10}Be throughout a rock's journey from eroding bedrock to deep burial in a terrace downstream.

2.3.2 Modelling erosion and burial

For rocks in an eroding landscape, such as the Appalachian Mountains, it is reasonable to assume that there is no inherited component in either the ^{26}Al or ^{10}Be inventories. As such, for the case of steady-state erosion equation [2] simplifies to:

$$N_i(z) = \sum_j \frac{A_{i,j} e^{-\rho z / L_j}}{\frac{1}{\tau_i} + \frac{\rho E}{L_j}} \qquad [3]$$

For material that has arrived at the surface (z = 0), the concentration of a given nuclide is purely a function of local production and erosion rates. In most cases the transport time between erosion and burial is short relative to the mean-lives of ^{26}Al and ^{10}Be, and is not a significant consideration for burial dating. Once a rock is buried – in this case, within a fluvial terrace – production rates are reduced as a function of shielding and the cosmogenic nuclide component produced during erosion, equation [3] becomes the inherited component. We treat postburial production as a scenario of constant exposure, where E = 0. In this case, equation [2] becomes:

$$N_i(z,t) = e^{-t/\tau_i} \sum_j \frac{A_{i,j}}{\frac{1}{\tau_i} + \frac{\rho E}{L_j}} + P_{i,post}\tau_i\left(1 - e^{-t/\tau_i}\right) \qquad [4]$$

Where $P_{i,post}$ is the postburial production rate for nuclide *i* at a given depth and *t* is burial time. Equation (4) is used to date sediment burial. For very deeply buried sediments, such as in caves, postburial production is nearly zero and can be ignored. However, for sediments buried by only several meters, postburial production remains significant. In this case, isochron burial dating of a suite of samples can be used to solve simultaneously for the burial age and the postburial component. The isochron approach applies equation (4) to multiple ^{26}Al/^{10}Be measurements, treating postburial production as a constant among all samples. It fits a line to the ^{26}Al vs. ^{10}Be plot defined by $N_{26}(z,t)/N_{10}(z,t)$ that can be used to estimate postburial production, burial age, and inherited N_{26} and N_{10} concentrations which depend paleo-erosion rates.

2.3.3 Identifying reworked samples in isochrons

Most rocks experience a single episode of exposure followed by a single episode of burial, and their measured ^{26}Al and ^{10}Be concentrations will all fall along the isochron line. A sample that has experienced prior burial and reworking, however, will have ^{26}Al and ^{10}Be concentrations that record its cumulative burial histories and will fall below the isochron line. Such reworked

samples must be eliminated from isochron calculations, as they will yield deceptively old burial ages.

Given the scatter inherent in some isochrons, whether or not a clast is reworked can be ambiguous. To address this issue, we applied an iterative modification of the Chauvenet criterion to test isochron fits, identify outliers, remove them, and calculate revised isochrons. The approach is as follows:

1) Examine the MSWD of the isochron. If MSWD >> 1, proceed to step 2. Otherwise, incorporate all measurements into the isochron age calculation.
2) Plot all ^{26}Al and ^{10}Be measurements and find each sample's weighted deviation from the isochron line defined by a York regression (York et al., 2004).
3) Use the weighted deviation of each sample to calculate the probability, according to a t-distribution, that it belongs to the same parent population as the isochron line. If $p < 0.05$ and the sample falls below the isochron line, it has likely been reworked.
4) Remove reworked clast(s). Calculate a new isochron line, repeating steps 1-3.
5) Once an isochron line has been defined for which all samples feature $p \geq 0.05$, note MSWD of the isochron. If MSWD $\gg$ 1 and one or more clasts have relatively low p values, consider eliminating them if it significantly improves MSWD.

This approach is preferable over visual selection of reworked clasts, given that mild or moderate reworking can be difficult to identify yet may have profound implications for calculated age. We applied this approach to each ^{26}Al/^{10}Be isochron collected along the Tennessee River.

2.3.4 Sample processing

Collected quartzite clasts and sand fractions were rinsed, dried, and weighed prior to mineral separation. Sufficiently large clasts ($\geq$ 4 g) for individual dating were crushed manually to minimize loss of material, while sand fractions were ground to 250-500 μm fractions with a disk mill. Finer grain sizes were subsequently rinsed away with deionized water, and the sands were run through magnetic separation and heavy liquid (lithium heteropolytungstate) treatments to reduce magnetic and heavy mineral contaminants. Sands featuring significant amounts of contaminant minerals also underwent froth flotation to further isolate pure quartz. All samples

received multiple selective dissolution treatments in heated 1-5% HF/HNO_3 solution to remove excess meteoric ^{10}Be and aid in dissolution of contaminant minerals. In most cases, quartzites received 3-4 days of dissolution treatment, while sands required additional leaching in HF/HNO_3 to remove contaminants. Prior to total sample dissolution and Al/Be chemistry, each sample's elemental contents were assayed via inductively coupled optical emission spectrometry (ICP-OES) to ensure sufficient purity.

Samples that featured low aluminum contents (<200 ppm) were deemed ready for chemical analysis, and received ~270 μg of Be carrier. If the total aluminum content was < 1 mg, an additional ~1 mg of Al carrier was added. The samples were then dissolved in heated concentrated hydrofluoric and nitric acids. An ICP-OES aliquot was taken following dissolution to measure total Al content. Concentrated sulfuric acid (~1 ml) was added to each sample, which was then uncapped to permit evaporation of HF/HNO_3. Remaining sulfuric acid was diluted and mixed with sodium hydroxide to precipitate and remove excess Fe/Ti oxides at pH 14. The resultant Al/Be hydroxides were subsequently rinsed and separated via anion and cation exchange chromatography. Following chromatography, the Al and Be were dissolved in hydrochloric and nitric acids, evaporated, and converted to oxides using a torch. The resultant residues were mixed with niobium powder, transferred to stainless steel AMS cathodes, and delivered to PRIME Lab for measurement. There, $^{26}Al/^{27}Al$ and $^{10}Be/^{9}Be$ ratios were measured alongside the standards of Nishiizumi (2004) and Nishiizumi et al. (2007). Measured ratios are available in Appendix A and detailed methods are available in Appendix B.

2.4 Results

Isochron burial dating of the Pickwick terraces yields Early Pliocene to Late Pliocene/Early Pleistocene burial ages. Burial isochrons, ages, and their analytical uncertainties are shown in Figures 2.6a-2.6c and Tables 2.1 and 2.2. Our iterative approach to identifying outlier samples shows reworked materials in the isochrons of the lower two terraces, Nt_2 and Nt_1. The highest dated terrace, Nt_3, features no reworked clasts (Figure 2.6a). Its five $^{26}Al/^{10}Be$ measurements yield a burial age of 4.36 ± 0.41 My (MSWD = 1.24). Below it, the Nt_2 terrace yields a burial age of 2.78 ± 0.08 My (MSWD = 1.49) after excluding one clearly reworked clast (Figure 2.6b). The lowest dated terrace, Nt_1, initially yielded a burial age of 2.88 ± 0.13 My (MSWD = 3.19) after excluding reworked clast PW4-4 (Figure 2.6c). Despite the fact that all remaining clasts featured

$p \geq 0.05$, removal of clast PW4-18 ($p = 0.08$) substantially improves the MSWD value. As such, the preferred isochron age for Nt_1 is 2.63 ± 0.11 My (MSWD = 2.37). Notably, the sand fraction for the Nt_1 isochron has elevated concentrations of ^{26}Al and ^{10}Be relative to other isochrons. It is possible that the gravels within the Nt_1 terrace experienced brief, mild reworking during transport, while the sand fraction is dominantly non-reworked grains.

The paleo-erosion rates from sands and clasts, calculated by subtracting post-burial production of ^{10}Be and backtracking the decay of inherited ^{10}Be, are variable. Paleo-erosion rates from sands slowed somewhat since the early Pliocene, with median values of 9.8 $^{+0.4}/_{-0.4}$ m/My for Nt_3, 5.9 $^{+0.7}/_{-0.6}$ m/My for Nt_2, and 6.9 $^{+0.3}/_{-0.2}$ m/My for Nt_1 (Figure 2.7). Individual cobbles showed much greater variation in localized paleo-erosion rates, with median values ranging from 1.7 $^{+0.1}/_{-0.1}$ m/My to 32.0 $^{+3.3}/_{-2.7}$ m/My. These values are likely minima, given that the ^{10}Be production rate used for these calculations is based on the median elevation of the Tennessee River watershed (627 m asl) and cobbles from the Blue Ridge may have eroded from higher elevations with higher ^{10}Be production rates.

2.5 Discussion

Our isochron burial ages for the terraces of the lower Tennessee River provide new insight into its behavior and course since the Early Pliocene, and allow us to refine previous reconstructions of its course that date to the Early Miocene. The existing Miocene reconstruction by Xu et al. (2017) describes a "paleo-Tombigbee River" that incorporates the upper watershed of the modern Tennessee River and drains southwest across Alabama to the Gulf of Mexico (Figure 2.8). This hypothesis is supported by high-level metamorphic quartz gravels mapped along the Tombigbee and Sipsey Rivers by Mills and Kaye (2001) that indicate a previous course of a Blue Ridge-draining river, and is bolstered by Blum et al. (2017)'s terrestrial and basin floor evidence for a paleo-Tennessee River that flowed to the Gulf of Mexico. Russell and Schmitz (2003) questioned this model due to poor correlation between the terraces of the Tennessee and Tombigbee Rivers in eastern Mississippi. Given that there are no major sources of metamorphic quartz gravels west of the Cumberland Plateau, the Tennessee River must have incised through Walden Ridge at Chattanooga, TN by this time. The exact course of the lower Tennessee River, however, remains unclear; it may have connected to the Mobile Basin via the Tombigbee River,

the Sipsey River, or both. Regardless of its exact lower course, this connection was likely severed at 9.0 ± 1.7 My, as shown by Near and Keck (2005)'s modeling of darter vicariance.

The severing of the Tennessee-Mobile basin connection was likely accompanied by the Tennessee River assuming its modern course through Pickwick and to the north (Figure 2.8). Self (2003) proposed that the Tennessee River originally flowed through the Hatchie River valley during the Late Miocene; however, discrepancies in terrace levels between the two rivers imply that there was no connection (Mills and Kaye, 2001) and instead favor a direct path north from Pickwick. We hypothesize that the deposition of terrace level Nt_5 occurred at 9.0 ± 1.7 My (Near and Keck, 2005), supported by Self (2003)'s assertion that Nt_5 was deposited prior to the breaching of the Fort Payne chert that occurred ca. 5 My (Reesman and Stearns, 1989). That incision would have triggered an influx of chert to the river gravels as reflected by the higher chert contents in terraces Nt_4-Nt_1 and reconstructions of the Fort Payne chert outcrops that show the Tennessee River likely began incising the formation at the same time Nt_4 was being deposited (Figures 2.2, 2.3). Given our isochron age for Nt_3 and the inferred 9.0 ± 1.7 My age for Nt_5, we may interpolate an approximate age of 5.2-7.0 My for Nt_4, consistent with the hypotheses of Self (2003) (Figure 2.8).

Following the deposition of Nt_4, our isochron ages for Nt_3 and Nt_2 reveal gradual incision of the lower Tennessee River throughout much of the Pliocene (Figure 2.7). This interval corresponds to the formation of the Upland Complex downstream, as shown by recent $^{26}Al/^{10}Be$ and (U-Th)/He dating of terrace deposits (Odom et al., 2020); however, the terraces are not directly correlated. Self (2003) noted that the Upland Complex (therein referred to as the Lafayette gravels) featured coarse gravel and honey-colored chert, while chert in the Tennessee River terraces is predominantly white, reflecting its origin in the Fort Payne chert. During the Pliocene, the basin-averaged erosion rate upstream of Pickwick decreased slightly from $9.8\ ^{+0.4}/_{-0.4}$ m/My in the sand fraction of Nt_3 to $5.9\ ^{+0.7}/_{-0.6}$ m/My in the sand fraction of Nt_2 (Figure 2.7). No major drainage reorganizations likely occurred during the quiescent period leading up to the Pleistocene.

Our Latest Pliocene/Earliest Pleistocene age for Nt_1 reflects a drop in the base level of the Tennessee River and consequent incision. Basin-averaged erosion rates remained virtually constant, changing from $5.9\ ^{+0.7}/_{-0.6}$ m/My in Nt_2 to $6.9\ ^{+0.3}/_{-0.2}$ m/My in Nt_1. Cosmogenic $^{26}Al/^{10}Be$ burial ages of fluvial sediments in perched caves along the Green and Cumberland Rivers, also tributaries of the preglacial Ohio River, demonstrate that those rivers incised to bedrock near 1.5

My and 2.0 My, respectively (Granger et al., 2001; Anthony and Granger, 2006). Extrapolating the range of potential incision rates between Nt_2 and Nt_1 shows that the Tennessee River may have incised down to bedrock by either of these times; however, it is impossible to directly test this hypothesis without samples of the submerged Pleistocene fill. Given the widespread incision at 1.5 My, we have assigned an approximate age of 1.5 My to the bedrock level of the Tennessee River (Figure 2.8). This age is consistent with deep incision along the Mississippi River between 2.5-0.8 My (Wickert et al., 2019) and along the Ohio River sometime prior to the glaciation at 1.3 My that deposited valley trains in the area (Ray, 1974; Balco and Rovey, 2010). Despite the significant incision occurring during the Pleistocene, the Tennessee River was not able to completely cut through the Fort Payne chert and likely featured steep lower reaches during that time.

Following the Tennessee River's incision to bedrock during the Early Pleistocene, the preglacial Ohio River watershed experienced a major drainage reorganization. The Teays River drainage, including some modern tributaries of the Ohio River, was mostly overridden by the Laurentide Ice Sheet, damming its tributaries and forming the modern Ohio River. Independent constraints on the age of Pleistocene glaciations indicate that this reorganization likely occurred at ~1.3 My (Balco and Rovey, 2010), consistent with burial ages of proglacial lacustrine sediments in Kentucky (Granger, unpublished data from 1999). While the effect that the Ohio River's reorganization had on the Tennessee River is difficult to quantify, it is an important step in the Pleistocene history of the Ohio River drainage network. This reorganization was followed by widespread aggradation in the Mississippi River drainage network at ~0.8 My (Granger et al., 2001; Anthony and Granger, 2006; Keen-Zerbert et al., 2016). We hypothesize that this aggradation also occurred on the Tennessee River, and propose an ~0.8 My age for the submerged Pleistocene fill that appears downstream of Pickwick. Further fluctuations in base level likely occurred due to glaciations near 0.8 My and 0.4-0.2 My (Balco and Rovey, 2010).

2.6 Conclusions

The course and incision behavior of the Tennessee River exerted primary controls on faunal distribution patterns, landscape evolution, and sediment transport in the southern Appalachians throughout the Neogene. Previous interpretations provided reasonable reconstructions of the drainage through time, but testing these hypotheses proved difficult due to limited age controls on

the river's behavior and sparse well-preserved deposits. Our $^{26}Al/^{10}Be$ isochron ages for the terraces near Pickwick, TN confirm that the Tennessee River has existed in its modern configuration for at least four million years, and likely since the Late Miocene. Since that time, the lower Tennessee River has been responding to Pliocene and Pleistocene base level fluctuations similarly to other tributaries of the preglacial Ohio River, while the upper Tennessee River gradually erodes and remains insulated from these changes by the Muscle Shoals knickpoint.

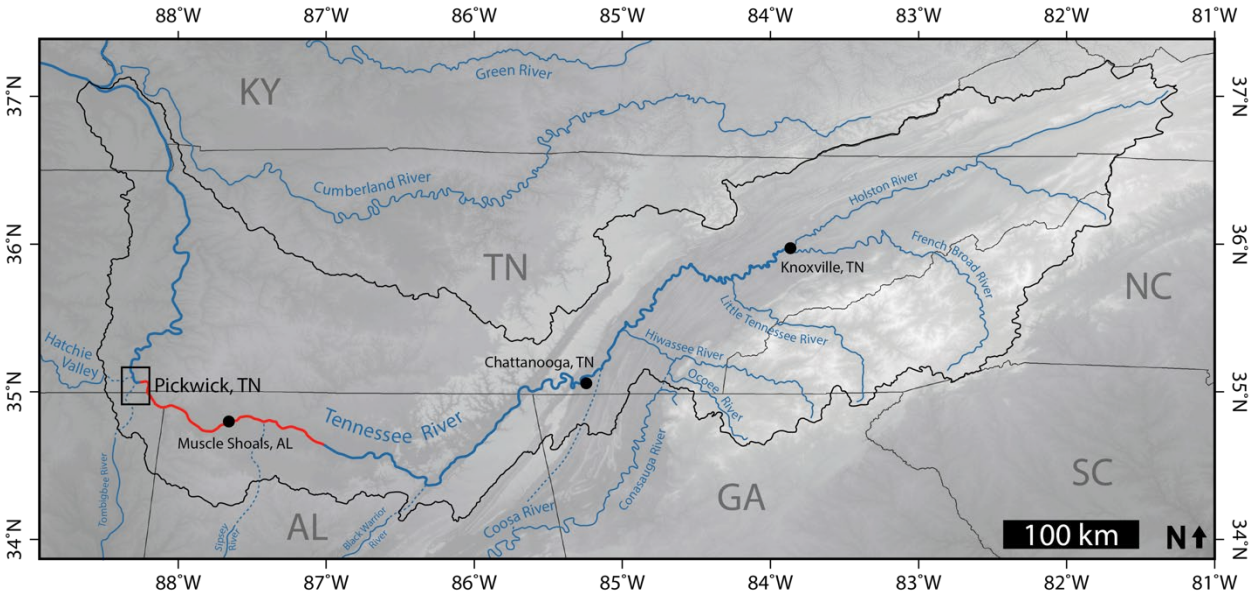

Figure 2.1. The Tennessee River watershed (outlined in black) and select major tributaries. Neighboring rivers and tributaries of the Ohio River are also shown. Several previously hypothesized paths of the paleo-Tennessee River are indicated by dashed blue lines. The length of the Tennessee River that is immediately underlain by the Fort Payne chert is denoted by a solid red line. Extent of Figure 2.4 is indicated near Pickwick, TN.

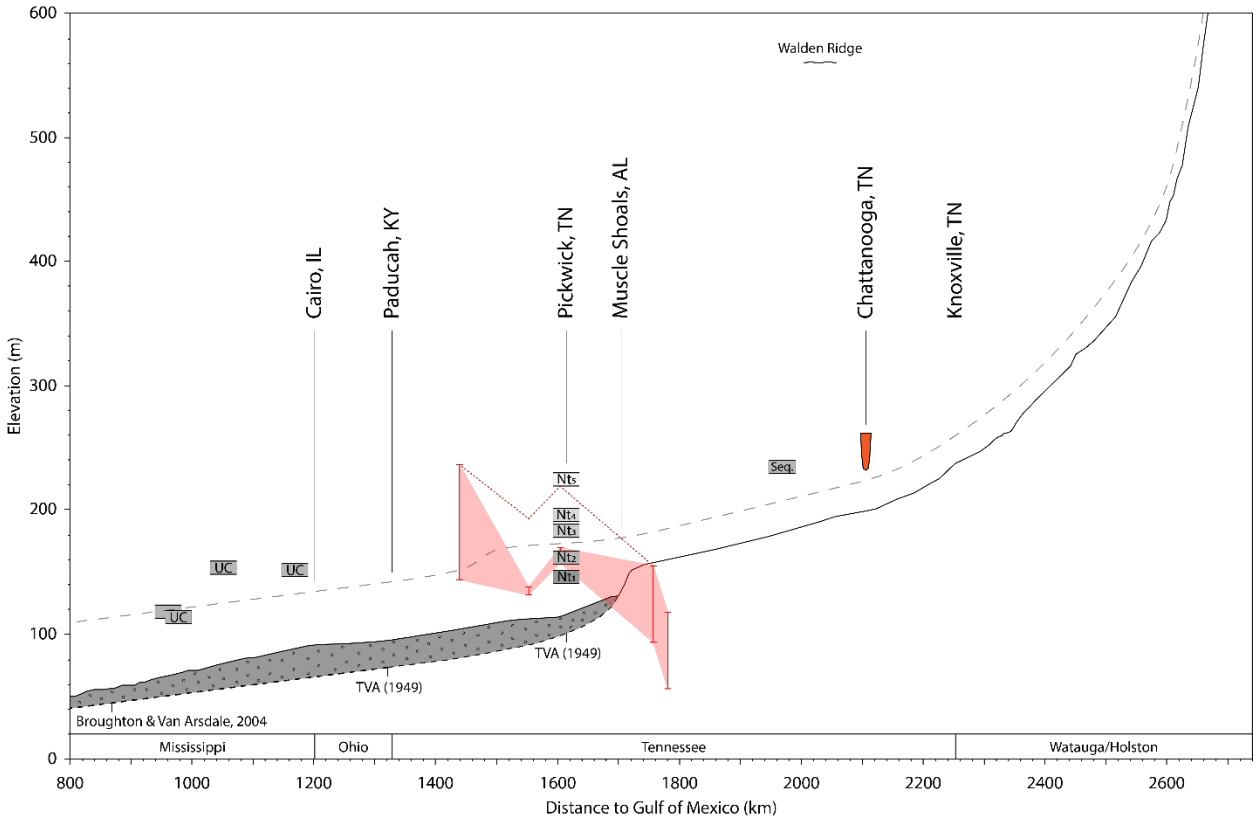

Figure 2.2. Longitudinal profile of the Tennessee River, beginning with the Watauga River in northeastern Tennessee and ending with the Mississippi River. An interpreted profile of the Tennessee River during the middle Pliocene is shown as a dashed line; note the prominent knickzone. The modern mapped extent of the Fort Payne chert in quadrangles along the Tennessee River is shaded in red (Barnes and Larson, 1967; Raymond, 2005; Rindsberg, 2004a; Rindsberg, 2004b; Russell and Wilson, 1970; Russell et al., 1972). Its thickness is highly variable due to extensive erosion, but inferring an initially 60 m-thick formation in the Pickwick area (dashed line) yields a formation geometry that agrees with chert distributions in the terrace levels (i.e., a chert-free Nt_5 and chert-rich Nt_1-Nt_4). Terraces mapped by Self (2003) are shown at Pickwick, Tennessee. The presence of deep gravels beneath the modern Tennessee River is indicated by gray alluvium; these gravels were interpolated using core data from TVA (1949) and Broughton and Van Arsdale (2004). Locations of the Pliocene Upland Complex (Odom et al., 2020) are also displayed along the Mississippi River. Gravels near the Sequatchie Valley, initially described by Johnson (1905), are indicated. The approximate location and depth of bauxite sinkholes in Chattanooga, TN is shown in orange (Dunlap et al., 1965).

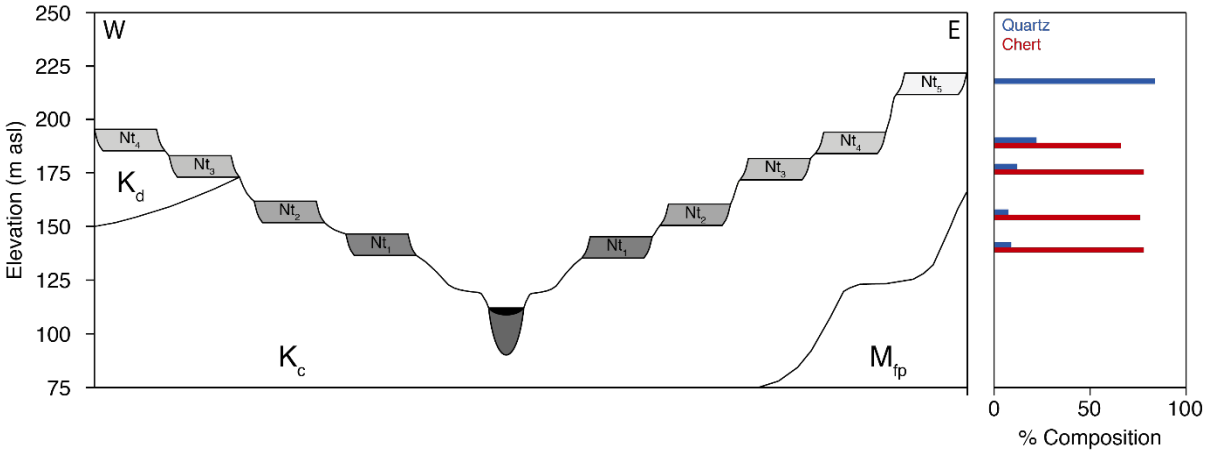

Figure 2.3. Cross-sectional diagram of the major terrace levels at Pickwick, Tennessee and corresponding quartz/chert compositions for individual levels. The terraces (Nt_1-Nt_5) directly overlie unconsolidated Cretaceous deposits (K_c, K_d) that generally dip westward. Quaternary fill beneath the modern Tennessee River is indicated. Figures modified from Self (2003).

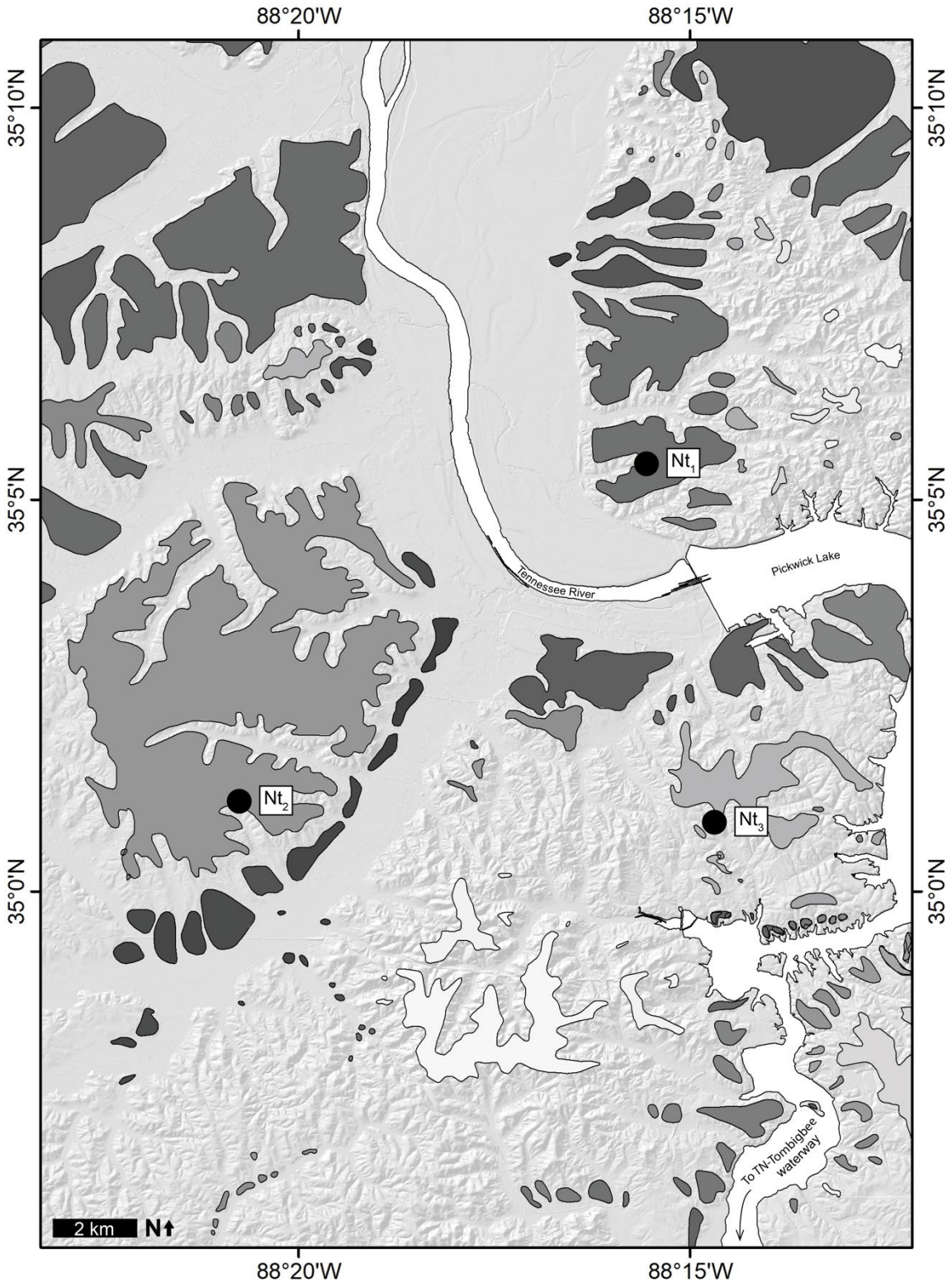

Figure 2.4. Overview of the Pickwick, TN area. Mapped terraces are shaded according to elevation, with higher terraces being lighter (Merrill, 1988a; 1988b; Parks and Russell, 1975). Sampling sites are indicated by black dots.

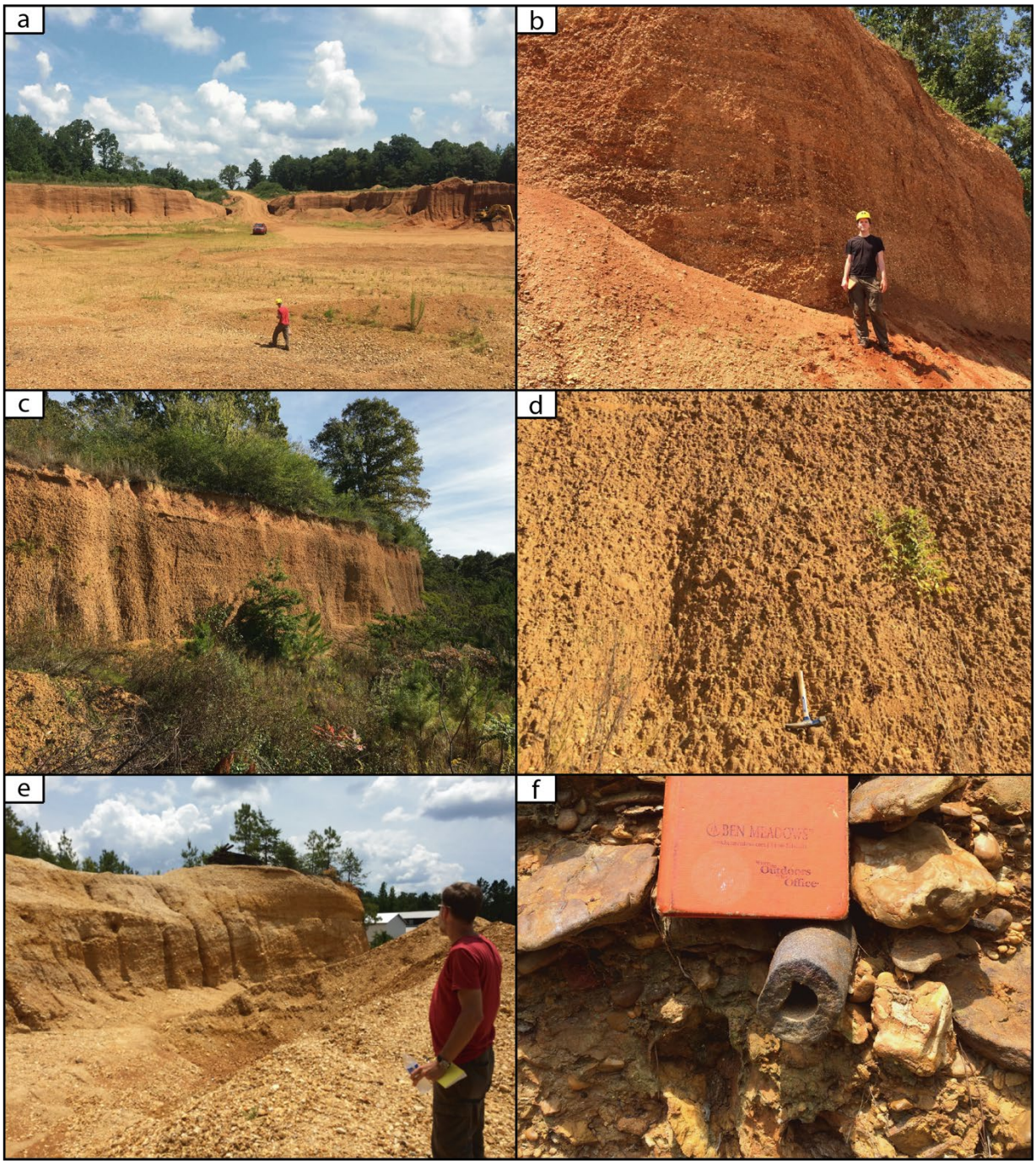

Figure 2.5. (a) Gravel pit where samples for Nt_3 were collected for dating. (b) Cross-bedded sands and gravels in the Nt_3 terrace deposit. (c) Overview of Nt_2 gravel pit on Dr. Williams Drive. (d) Close-up image of Nt_2 outcrop. Hammer indicates location where samples were collected for isochron burial dating. (e) Overview of Nt_1 gravel pit with D. Granger for scale. Note the large (2 m) cross-beds in the deposit. (f) Iron-cemented sandstone tube at Nt_1 gravel pit.

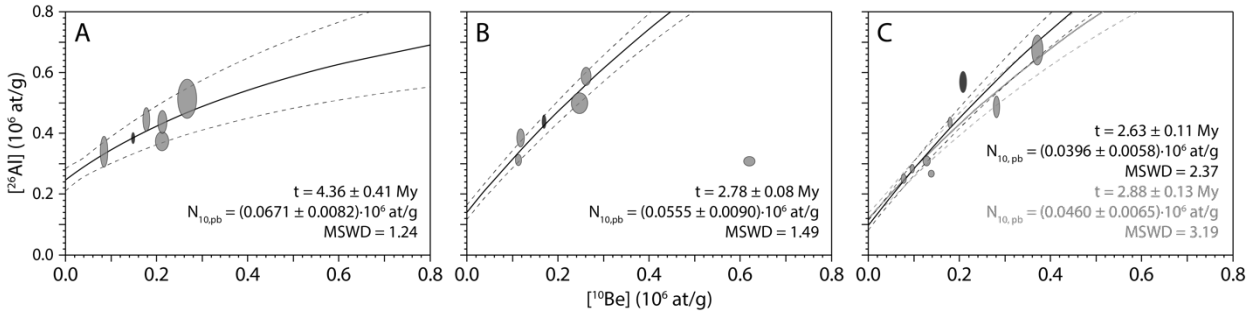

Figure 2.6. Burial isochrons for the three dated terraces. Each oval represents a clast (gray oval) or sand fraction (black oval) that was used for age calculations. Dashed lines represent 1σ uncertainty. (A) The burial isochron for Nt_3 contains no reworked clasts and yields an age of 4.36 ± 0.41 My (MSWD = 1.24). (B) The burial isochron for Nt_2 contains one reworked clast, QFL4-7, that features a significantly lower $^{26}Al/^{10}Be$ than other samples. It yields an age of 2.78 ± 0.08 My (MSWD = 1.49). (C) The burial isochron for Nt_1 contains at least one reworked clast, PW4-4, and yields an age of 2.88 ± 0.13 My (MSWD = 3.19) upon removal of the clast (see gray isochron line). It is likely that a second clast, PW4-18, is also reworked. Removal of this clast yields an age of 2.63 ± 0.11 My (MSWD = 2.37), as shown by the black isochron line. This isochron is preferred. Its sand fraction has a notably high $^{26}Al/^{10}Be$ ratio and elevated concentrations, pointing to a more gradual erosion rate than most clasts and suggesting that some individual clasts may be slightly reworked.

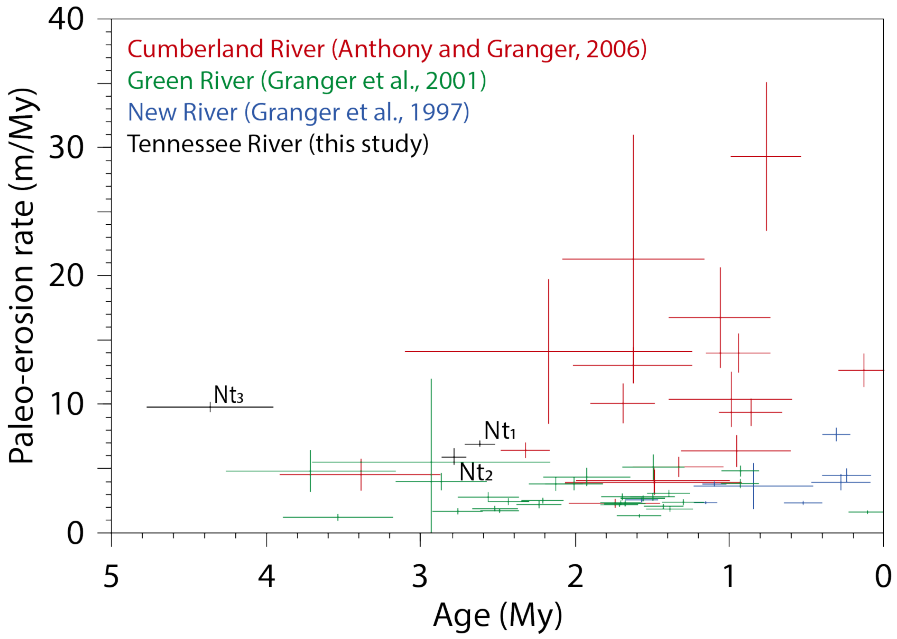

Figure 2.7. Paleo-erosion rates for the Tennessee River (black), Cumberland River (red), Green River (green), and New River (blue). The age and paleo-erosion rates from Granger et al. (1997), Granger et al. (2001), and Anthony and Granger (2006) have been recalculated to account for refinements in the half-life of ^{10}Be (Chmeleff et al., 2010; Korschinek et al., 2010).

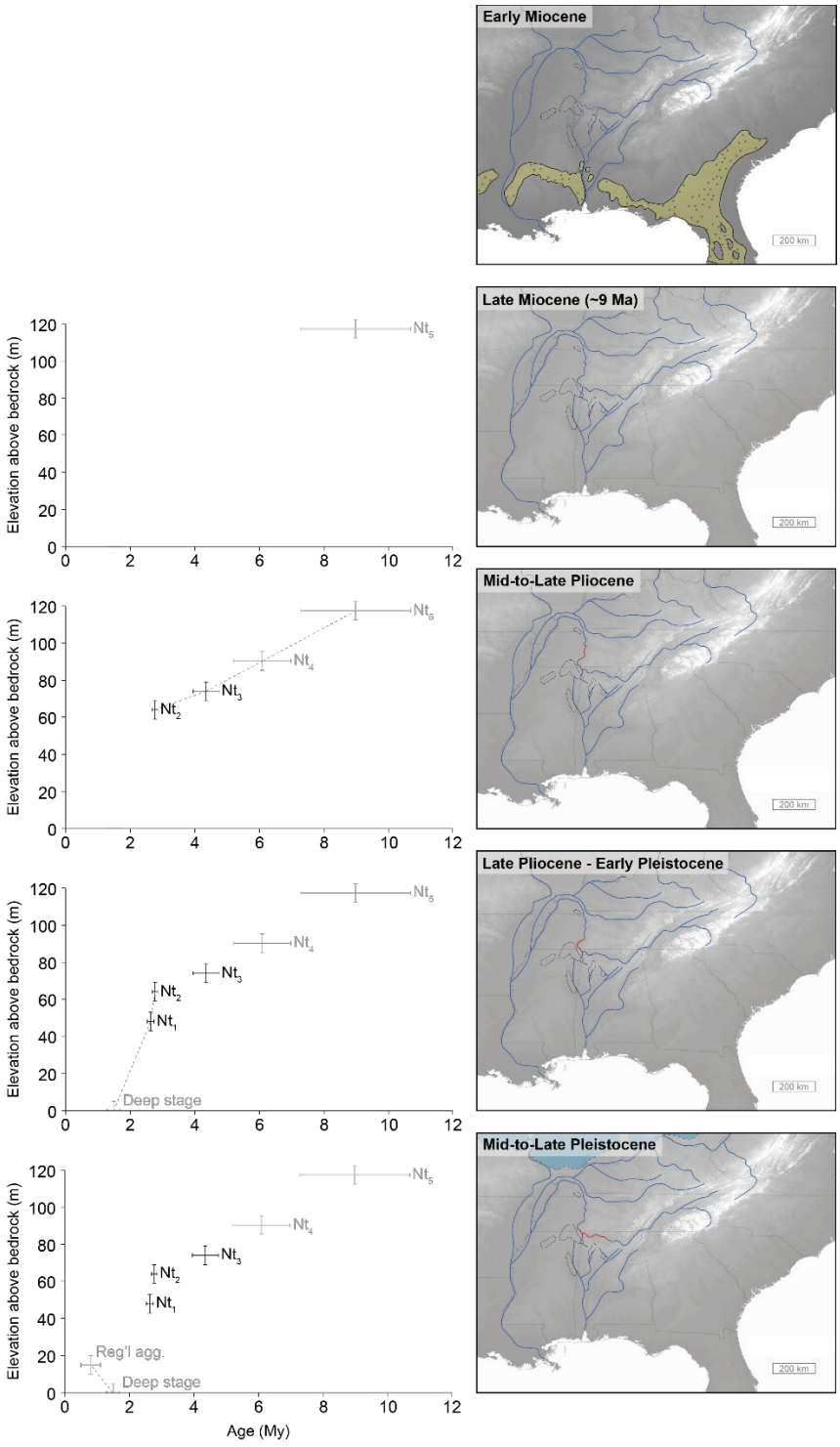

Figure 2.8. Terrace deposition (left) and drainage reconstructions (right) of the Tennessee River since the Early Miocene. Hypothesized courses of the Tennessee River are shown as blue lines, which are dashed where inferred. Metamorphic quartz deposits mapped by Mills and Kaye (2001) are outlined in Alabama, Kentucky, Mississippi, and Tennessee. Miocene terrestrial sediments highlighted in yellow from Ipshording and Flowers (1983). Laurentide Ice Sheet indicated by blue shading in Mid-to-Late Pleistocene reconstruction.

Table 2.1. Sample masses and blank-corrected $^{26}Al/^{10}Be$ data. Paleo-erosion rates were not calculated for reworked samples.

Terrace	Sample	Mass (g)	[^{26}Al] (10^6 at/g)	[^{10}Be] (10^6 at/g)	$^{26}Al/^{10}Be$	Min age (My)	Paleo-E (m/My)
Nt_1	PW4-1	16.954	0.2512 ± 0.0150	0.0776 ± 0.0057	3.24 ± 0.31	1.50 ± 0.16	$32.0\ ^{+3.3}/_{-2.7}$
	PW4-2	41.443	0.4352 ± 0.0178	0.1792 ± 0.0047	2.43 ± 0.12	2.04 ± 0.10	$8.5\ ^{+0.3}/_{-0.3}$
	PW4-3	33.432	0.2841 ± 0.0150	0.0970 ± 0.0048	2.93 ± 0.21	1.70 ± 0.14	$20.9\ ^{+1.3}/_{-1.3}$
	PW4-4	32.207	0.2674 ± 0.0116	0.1380 ± 0.0066	1.94 ± 0.12	2.52 ± 0.13	---
	PW4-5	22.526	0.3102 ± 0.0164	0.1281 ± 0.0076	2.42 ± 0.19	2.08 ± 0.15	$13.5\ ^{+0.8}/_{-0.7}$
	PW4-13	13.241	0.6746 ± 0.0491	0.3704 ± 0.0123	1.82 ± 0.15	2.49 ± 0.14	$3.4\ ^{+0.1}/_{-0.1}$
	PW4-18	16.135	0.4878 ± 0.0357	0.2809 ± 0.0070	1.74 ± 0.13	2.63 ± 0.15	---
	PW4-S	11.906	0.5699 ± 0.0351	0.2078 ± 0.0077	2.74 ± 0.20	1.78 ± 0.14	$6.9\ ^{+0.3}/_{-0.2}$
Nt_2	QFl4-1	18.232	0.3127 ± 0.0189	0.1131 ± 0.0066	2.76 ± 0.23	1.82 ± 0.15	$3.2\ ^{+0.4}/_{-0.3}$
	QFl4-3	14.893	0.5874 ± 0.0292	0.2616 ± 0.0106	2.25 ± 0.14	2.15 ± 0.12	$4.3\ ^{+0.5}/_{-0.4}$
	QFl4-4	9.277	0.3850 ± 0.0295	0.1177 ± 0.0088	3.27 ± 0.35	1.48 ± 0.23	$26.8\ ^{+8.9}/_{-6.8}$
	QFL4-6	9.861	0.4990 ± 0.0341	0.2469 ± 0.0183	2.02 ± 0.20	2.39 ± 0.19	$2.2\ ^{+0.3}/_{-0.2}$
	QFL4-7	19.760	0.3077 ± 0.0156	0.6193 ± 0.0123	0.50 ± 0.03	4.51 ± 0.08	---
	QFL4-S	35.012	0.4389 ± 0.0211	0.1693 ± 0.0040	2.59 ± 0.14	1.91 ± 0.11	$5.9\ ^{+0.7}/_{-0.6}$
Nt_3	PW1-1	10.830	0.4381 ± 0.0381	0.2121 ± 0.0100	2.07 ± 0.20	2.37 ± 0.23	$19.3\ ^{+1.9}/_{-1.6}$
	PW1-2	8.202	0.4462 ± 0.0388	0.1771 ± 0.0077	2.52 ± 0.24	1.98 ± 0.23	$5.3\ ^{+0.2}/_{-0.2}$
	PW1-3	4.511	0.3398 ± 0.0510	0.0840 ± 0.0087	4.05 ± 0.74	1.13 ± 0.34	$17.9\ ^{+1.8}/_{-1.4}$
	PW1-4	2.962	0.5146 ± 0.0642	0.2666 ± 0.0209	1.93 ± 0.28	2.44 ± 0.29	$5.7\ ^{+0.3}/_{-0.3}$
	PW1-10	5.519	0.3746 ± 0.0313	0.2098 ± 0.0163	1.79 ± 0.20	2.60 ± 0.23	$1.7\ ^{+0.1}/_{-0.1}$
	PW1-S	29.716	0.3854 ± 0.0179	0.1482 ± 0.0040	2.60 ± 0.14	1.92 ± 0.10	$9.8\ ^{+0.4}/_{-0.4}$

Table 2.2. Locations of isochrons and calculated values. Terrace level elevations (m abr) refer to site elevation above the bedrock channel of the Tennessee River.

Terrace	Location	m abr	Isochron age (My)	MSWD	Postburial ^{10}Be (10^6 at/g)
Nt_1	35.0908°N, 88.2592°W	48	2.63 ± 0.11	2.37	0.0396 ± 0.0058
Nt_2	35.0201°N, 88.3457°W	64	2.78 ± 0.08	1.49	0.0555 ± 0.0090
Nt_3	35.0146°N, 88.2442°W	74	4.36 ± 0.41	1.24	0.0671 ± 0.0082

2.7 References

Adams, G. I. (1928). The course of the Tennessee River and the physiography of the southern Appalachian region. The Journal of Geology, 36(6), 481-493.

Anthony, D. M., & Granger, D. E. (2006). Five million years of Appalachian landscape evolution preserved in cave sediments. Special papers - Geological Society of America, 404, 39.

Balco, G., & Rovey, C. W. (2010). Absolute chronology for major Pleistocene advances of the Laurentide Ice Sheet. Geology, 38(9), 795-798.

Barnes, R. H., & Larson, L. T. (1967). Geologic map and mineral resources summary of the Hustburg quadrangle. Tennessee Division of Geology, Geologic Quadrangle Map 31 NW.

Blum, M. D., Milliken, K. T., Pecha, M. A., Snedden, J. W., Frederick, B. C., & Galloway, W. E. (2017). Detrital-zircon records of Cenomanian, Paleocene, and Oligocene Gulf of Mexico drainage integration and sediment routing: Implications for scales of basin-floor fans. Geosphere, 13(6), 2169-2205.

Broughton, J., & Van Arsdale, R. (2004). Surficial geologic map of the Northwest Memphis quadrangle, Shelby County, Tennessee, and Crittenden County, Arkansas (No. 2838).

Chmeleff, J., von Blanckenburg, F., Kossert, K., Jakob, D. Determination of the ^{10}Be half-life by multicollector ICP-MS and liquid scintillation counting. Nucl. Instrum. Methods Phys. Res. Sect. B Beam Interact. Mater. Atoms, 268 (2010), pp. 192-199.

Dunlap, J. C., Bergquist, H. R., Craig, L. C., & Overstreet, E. F. (1965). Bauxite deposits of Tennessee. US Govt. Print. Off., No. 1199-L.

Ewing, T. E., & Galloway, W. E. (2019). Evolution of the Northern Gulf of Mexico Sedimentary Basin. The Sedimentary Basins of the United States and Canada (pp. 627-694). Elsevier.

Gallen, S. F. (2018). Lithologic controls on landscape dynamics and aquatic species evolution in post-orogenic mountains. Earth and Planetary Science Letters, 493, 150-160.

Gallen, S. F., Wegmann, K. W., & Bohnenstiehl, D. R. (2013). Miocene rejuvenation of topographic relief in the southern Appalachians. GSA Today, 23(2), 4-10.

Galloway, W. E., Whiteaker, T. L., & Ganey-Curry, P. (2011). History of Cenozoic North American drainage basin evolution, sediment yield, and accumulation in the Gulf of Mexico basin. Geosphere, 7(4), 938-973.

Granger, D.E., 2014, Cosmogenic nuclide burial dating in archaeology and paleoanthropology, in Cerling. T.E., ed., Archaeology and Anthropology: Treatise on Geochemistry, v. 12, Chapter 8, 17 pages. : Oxford, UK, Elsevier- Pergamon, doi:10.1016/B978-0-08-095975-7.01208-0

Granger, D. E., Kirchner, J. W., & Finkel, R. C. (1997). Quaternary downcutting rate of the New River, Virginia, measured from differential decay of cosmogenic ^{26}Al and ^{10}Be in cave-deposited alluvium. Geology, 25(2), 107-110.

Granger, D. E., Fabel, D., & Palmer, A. N. (2001). Pliocene− Pleistocene incision of the Green River, Kentucky, determined from radioactive decay of cosmogenic ^{26}Al and ^{10}Be in Mammoth Cave sediments. Geological Society of America Bulletin, 113(7), 825-836.

Hayes, C. W., & Campbell, M. R. (1894). Geomorphology of the southern Appalachians. National Geographic Society.

Hayes, C. W., & Campbell, M. R. (1900). The relation of biology to physiography. Science, 12(291), 131-133.

Hoagstrom, C. W., Ung, V., & Taylor, K. (2014). Miocene rivers and taxon cycles clarify the comparative biogeography of North American highland fishes. Journal of Biogeography, 41(4), 644-658.

Isphording, W. C., & Flowers, G. C. (1983). Differentiation of Unfossiliferous Clastic Sediments: Solutions from the Southern Portion of the Alabama-Mississippi Costal Plain. Tulane Studies in Geology and Paleontology, 17(3).

Johnson, D. W. (1905). The tertiary history of the Tennessee River. The Journal of Geology, 13(3), 194-231.

Keen-Zebert, A., Granger, D. E., Paces, J. B., Hudson, M. R., & Bitting, C. (2016). Combined use of cosmogenic nuclide, U-series disequilibrium, paleomagnetism, and optically stimulated luminescence within Fitton Cave to evaluate the landscape evolution of the Buffalo National River, Arkansas (abs.). Geological Society of America Abstracts with Programs (Vol. 48, No. 7).

Korschinek, G., Bergmaier, A., Faestermann, T., Gerstmann, U.C., Knie, K., Rugel, G., Wallner, A., Dillmann, I., Dollinger, G., Von Gostomski, C.L., Kossert, K., 2010. A new value for the half-life of ^{10}Be by heavy-ion elastic recoil detection and liquid scintillation counting. Nucl. Instrum. Methods Phys. Res. Sect. B Beam Interact. Mater. Atoms 268, 187-191.

Lal, D. (1991). Cosmic ray labeling of erosion surfaces: in situ nuclide production rates and erosion models. Earth and Planetary Science Letters, 104(2-4), 424-439.

Mayden, R. L. (1988). Vicariance biogeography, parsimony, and evolution in North American freshwater fishes. Systematic Biology, 37(4), 329-355.

Merrill, R. K. (1988a). Geologic map of Mississippi portions of the Yellow Creek (Mississippi - Alabama - Tennessee) and Waterloo (Mississippi - Alabama) quadrangles, Mississippi Department of Environmental Quality, Office of Geology, Open-File Report OF-9.

Merrill, R. K. (1988b). Geologic map of the Doskie quadrangle (Mississippi portion), Mississippi – Tennessee, Mississippi Department of Environmental Quality, Office of Geology, Open-File Report OF-9.

Mills, H. H., & Kaye, J. M. (2001). Drainage history of the Tennessee River: review and new metamorphic quartz gravel locations. Southeastern Geology, 40(2), 75-97.

Mills, H. H., Sumners, D. N., Hart, E. A., & Li, P. (2005). Distribution of high-level alluvial deposits in the Valley and Ridge of Polk County, southeastern Tennessee: implications for river history and drainage evolution. Southeastern Geol, 44, 37-44.

Near, T. J., & Keck, B. P. (2005). Dispersal, vicariance, and timing of diversification in Nothonotus darters. Molecular Ecology, 14(11), 3485-3496.

Niemiller, M. L., Zigler, K. S., Hart, P. B., Kuhajda, B. R., Armbruster, J. W., Ayala, B. N., & Engel, A. S. (2016). First definitive record of a stygobiotic fish (Percopsiformes, Amblyopsidae, Typhlichthys) from the Appalachians karst region in the eastern United States. Subterranean Biology, 20, 39.

Nishiizumi, K. (2004). Preparation of ^{26}Al AMS standards. Nuclear Instruments and Methods in Physics Research Section B: Beam Interactions with Materials and Atoms, 223, 388-392.

Nishiizumi, K., Imamura, M., Caffee, M. W., Southon, J. R., Finkel, R. C., & McAninch, J. (2007). Absolute calibration of ^{10}Be AMS standards. Nuclear Instruments and Methods in Physics Research Section B: Beam Interactions with Materials and Atoms, 258(2), 403-413.

Odom, W. E., Hofmann, F., Van Arsdale, R. B., Granger, D. E. (2020). New ^{26}Al/^{10}Be and (U-Th)/He constraints on the age of the Upland Complex, central Mississippi River Valley. Geomorphology. https://doi.org/10.1016/j.geomorph.2020.107448

Parks, W. & Russell, E. (1975). Geologic map showing upper Cretaceous, Paleocene, and Lower and Middle Eocene units and distribution of younger fluvial deposits in western Tennessee. U.S. Geological Survey, Miscellaneous Investigations Series Map I-916.

Persons, A. K. (2010). Geological and Ichthyological Investigations into Palaeodrainage Hypothesis for the Tennessee River. Masters Thesis.

Ray, L. L. (1974). Geomorphology and Quaternary geology of the glaciated Ohio River Valley – a reconnaissance study. United States Geological Survey, Professional Paper 826.

Raymond, D. E. (2005). Geology of the Mason Ridge 7.5-minute quadrangle, Limestone, Morgan, and Madison Counties, Alabama. Geological Survey of Alabama, Quadrangle Series 41.

Reesman, A. L., & Stearns, R. G. (1989). The Nashville dome, an isostatically induced erosional structure and the Cumberland Plateau Dome, an isostatically suppressed late Paleozoic extension of the Jessamine dome. Southeastern Geology, 30, 147-174.

Rindsberg, A. K. (2004a). Geology of the Jones Crossroads 7.5-minute quadrangle, Limestone, Morgan, and Lawrence Counties, Alabama. Geological Survey of Alabama, Quadrangle Series 131.

Rindsberg, A. K. (2004b). Geology of the Decatur 7.5-minute quadrangle, Morgan and Limestone Counties, Alabama. Geological Survey of Alabama, Quadrangle Series 35.

Russell, E. (1968). Geologic map and mineral resources summary of the Counce quadrangle (including the Tennessee portion of the Doskie quadrangle, Mississippi-Tennessee). Tennessee Division of Geology, Geologic Quadrangle Map 13 SE.

Russell, E., & Schmitz, D. (2003). Implications of comparisons of Tennessee with Tombigbee River depositional systems. Geological Society of America Southeastern Section, Abstracts with Programs.

Russell, E., & Wilson, C. (1970). Geologic map and mineral resources summary of the Thurman quadrangle. Tennessee Division of Geology, Geologic Quadrangle Map 23 NW.

Russell, E., Wilson, C., & Jewell, J. (1972). Geologic map and mineral resources summary of the Pickwick quadrangle. Tennessee Division of Geology, Geologic Quadrangle Map 24 SW.

Self, R. P. (2000). The pre-Pliocene course of the lower Tennessee River as deduced from river terrace gravels in southwest Tennessee. Southeastern Geology, 39(2), 61-70.

Self, R. P. (2003). The Cretaceous to late Tertiary gravel deposits in the western Tennessee River valley. Field trip guidebook, joint meeting of the south-central and southeastern sections of the Geological Society of America.

Wickert, A. D., Anderson, R. S., Mitrovica, J. X., Naylor, S., & Carson, E. C. (2019). The Mississippi River records glacial-isostatic deformation of North America. Science advances, 5(1), eaav2366.

Xu, J., Snedden, J. W., Stockli, D. F., Fulthorpe, C. S., & Galloway, W. E. (2017b). Early Miocene continental-scale sediment supply to the Gulf of Mexico Basin based on detrital zircon analysis. GSA Bulletin, 129(1-2), 3-22.

York, D., Evensen, N. M., Martinez, M. L., & De Basabe Delgado, J. (2004). Unified equations for the slope, intercept, and standard errors of the best straight line. American Journal of Physics, 72(3), 367-375.

CHAPTER 3. PLIO-PLEISTOCENE AGGRADATION IN THE SHENANDOAH VALLEY, VA DATED WITH COSMOGENIC ^{26}AL/^{10}BE

3.1 Introduction

The Shenandoah Valley has long served as a natural laboratory for geomorphologists, and was pivotal in the development of both the episodic Davisian model of erosion and uplift and the continuous Hackian model of dynamic equilibrium. Its numerous landscape markers include fluvial terraces, alluvial fans, caverns, volcanic plugs, and surficial weathering deposits that have been used as evidence in conflicting hypotheses regarding the evolution of the valley throughout the Cenozoic. A paucity of radiometric age constraints on nearly all surficial deposits has rendered these hypotheses difficult to evaluate. Cosmogenic nuclide geochronology applied to alluvial fans and fluvial terraces provides an opportunity to constrain the ages of widespread surficial deposits, providing insight into erosional processes at the time of their deposition. As such, it is now possible to quantitatively test existing hypotheses regarding the erosional decay of this post-orogenic landscape. This technique also allows us to identify significant aggradation and incision events in the Pliocene and Pleistocene in order to consider what climatic or tectonic drivers may have triggered these responses.

3.2 Background

3.2.1 Bedrock geology and surficial deposits

The Shenandoah Valley is located within the Valley and Ridge Province of Virginia and West Virginia (Figure 3.1). Its eastern limit is located along the western flank of the Blue Ridge, where Blue Ridge crystalline rock has been thrust over the sedimentary formations of the Valley and Ridge. This deformation is responsible for the synclinal geometry of the Shenandoah Valley that is most obviously expressed in the form of Massanutten Mountain, a ~75-kilometer-long NE-SW striking sandstone-dominated syncline that divides the valley and separates the north and south forks of the Shenandoah River. The topography of the valley floor is influenced by underlying Ordovician limestones, cherts, and shales (Hack, 1965). Numerous caves have developed within the limestone bedrock, some of which are thought to have deep phreatic origin (Doctor and Orndorff, 2017).

Most bedrock in the Shenandoah Valley is overlain by thick alluvial deposits that have been generally inferred to be Neogene in age. Slopes along the western Blue Ridge feature angular talus that Hack (1965) hypothesized to be Pleistocene in age. Along the boundary of the Blue Ridge and Valley and Ridge provinces, large alluvial fans blanket the landscape and reach the banks of the south fork of the Shenandoah River. These fans were estimated to be Miocene in age by Heller et al. (2014) using cosmogenic $^{26}Al/^{10}Be$ burial dating. Terrace deposits along the Shenandoah River and its tributaries were alternatively estimated to be Pleistocene by King (1950) and continuously forming by Hack (1965).

The widespread, largely undated surficial deposits and the variety of topographic features on which they lie inspired multiple models to explain their formation. Early geomorphologists working in the area interpreted the accordant summits and alluvial surfaces of the Shenandoah Valley area as peneplains dating to the Early Cenozoic. Stose et al. (1919) interpreted the Blue Ridge mountain peaks as being remnants of the Schooley peneplain, while the crests of the Massanutten Mountain syncline represented another former peneplain (Keith, 1894; Spencer, 1897). The floor of the Shenandoah Valley was widely interpreted as the Harrisburg/Valley Floor peneplain by numerous authors (Keith, 1894; Stose et al., 1919; Wright, 1934). This assertion was countered by King (1949), who hypothesized that the gravels were deposited due to Pleistocene climate fluctuations driving alternating cycles of aggradation and erosion. The age of deposits filling the valley remains an unresolved question, but existing ages for igneous intrusions and surficial weathering deposits provide insight into the erosional processes driving the Cenozoic evolution of the Shenandoah Valley.

3.2.2 Radiometric constraints on Cenozoic erosion

Geochronology of weathering deposits and volcanic intrusions in the Shenandoah Valley and surrounding area indicates that denudation has been generally gradual (<10 m/My) since the early Cenozoic. An igneous complex in Highland County, VA and Pendleton County, WV hosts dikes, sills, and diatremes that provide valuable markers of denudation since the Eocene. Fullagar and Botino (1969) initially dated the intrusions to ~47 My using K-Ar geochronology; this date was later revised to 47.9-47.0 My by Mazza et al. (2014) with $^{40}Ar/^{39}Ar$ dating. Because these intrusions contained rocks from stratigraphically higher units that collapsed into the diatremes and showed evidence of interactions with groundwater, Tso et al. (2004) hypothesized that the

diatremes in Highland County formed at depths of at least 198-335 m. Coupled with the $^{40}Ar/^{39}Ar$ ages by Mazza et al. (2014), this can be used to infer an average denudation rate of 4-7 m/My since the early Eocene.

Recent $^{40}Ar/^{39}Ar$ dating of manganese oxide deposits in the Shenandoah Valley (Doctor et al., 2018; Chapter 4, this thesis) also provides evidence of gradual landscape lowering during much of the Cenozoic. Manganese oxide deposits form in the shallow environment at depths of approximately 0-100 m, and as such may be used to approximate denudation rates since their formation. Manganese oxide geochronology has been used to constrain weathering, climate, and incision in a variety of settings worldwide (Vasconcelos and Carmo, 2018). The deposits dated by Doctor et al. (2018) ranged in age from Eocene to Oligocene, while the deposits dated in this thesis ranged in age from Eocene to Miocene. Though the deposits were likely formed by a weathering front that extended tens of meters below the surface (and thus, do not reflect exact geomorphic surfaces), they can be used to approximate maximum denudation rates that do not exceed 5 m/My in several locations throughout the valley. These estimates are generally consistent with the denudation rate inferred from the Eocene volcanic complex, as well as modern and paleo-erosion rate trends that have been directly measured using cosmogenic nuclides.

Modern erosion rates and paleo-erosion rates have been measured in the Shenandoah Valley and other Appalachian drainages using in-situ ^{10}Be. Duxbury et al. (2015) calculated modern erosion rates in the Shenandoah River and smaller tributaries and estimated an average erosion rate of 6.6 ± 0.5 m/My for the south fork of the Shenandoah River. Erosion rates in contributing catchments varied from 3-21 m/My, with variations likely controlled by slope and lithology; more rapidly eroding catchments are generally smaller and located in the steeper Blue Ridge province. These estimates are consistent with paleo-erosion rates measured on the nearby New River by Granger et al. (1997), who dated fluvial sands in riverside caves using $^{26}Al/^{10}Be$ burial dating and estimated paleo-erosion rates of 2-6 m/My.

River incision rates, paleo-erosion rates, and aggradation dates are less constrained in the Shenandoah Valley area, but data exist downstream and in neighboring drainages. Bierman (2015) used ^{10}Be exposure dating of strath terraces along the Potomac River to date the Late Pleistocene propagation of the Great Falls, VA knickpoint, providing a potential minimum age for non-lithologic upstream knickzones. Hancock and Harbor (2002) dated terraces along the James River immediately south of the Shenandoah Valley to 1.1 and 1.3 My and inferred mean local incision

rates of ~50 m/My. However, these burial ages appear to be minima (and consequently, incision rates are maxima). Hancock et al. (2004) proposed base level fluctuations due to drainage capture or climate, rather than tectonic activity, as potential drivers for incision. The primary objective of this study is to examine depositional and erosional processes operating in the Shenandoah River watershed during the Pliocene and Pleistocene and identify the primary driving force(s) behind these processes.

3.2.3 The Potomac and Shenandoah Rivers

Longitudinal profiles of the Potomac River and its tributaries, including the Shenandoah River, feature several knickpoints that imply response to significant perturbations in base level (Figure 3.2). The most apparent knickpoint in the Shenandoah River watershed is visible on Passage Creek (~225 m asl). A reconstruction of the relict profile upstream of this knickpoint using TopoToolbox (Schwanghart and Scherler, 2014) and assuming that river concavity (θ) has a typical value of 0.45 (Kirby and Whipple, 2012) directly intersects terraces mapped at Tysons Corner, VA, thought to be Mio-Pliocene in age (Drake and Froelich, 1997). As such, it appears that a Mio-Pliocene relict landscape may be preserved in the Shenandoah Valley within the watershed of Passage Creek, the core of the Massanutten Mountain syncline. Alternatively, the knickpoint along Passage Creek may be intransient and reflect the channel's adjustment to underlying lithology. If the former is true, slope-area plots of these drainages reveal that Passage Creek has uniquely responded to base level fluctuations relative to its neighboring watersheds, likely as a consequence of its structural isolation from the larger Shenandoah Valley drainage system by the highly resistant Massanutten Sandstone (Figure 3.3). Given the low erodibility of this sandstone, the hypothesized Mio-Pliocene base level responsible for creating the graded profile upstream of the knickzone was likely extremely stable given that base level fluctuations during the Pleistocene have not yet affected the upper reaches of Passage Creek.

A longitudinal profile of the South Fork of the Shenandoah River appears to show a minor convexity (Figure 3.2); however, its slope-area diagram is nearly identical to that of the apparently concave North Fork (Figure 3.3). The location of the South Fork of the Shenandoah River along the western flank of the Blue Ridge Mountains may influence its behavior, as the area is subject to significant deposition of alluvial material shed off the Blue Ridge. In contrast, the North Fork is a concave-up stream that appears to have reached a graded state. The variance in the erosional

responses of the various forks may be a consequence of underlying lithology; the steepest reaches are found on Passage Creek, which is located along the highly resistant Massanutten Sandstone, while less sandstone is found beneath the South Fork and even less along the North Fork (Rader and Gathright, 2001b). To identify any potential disequilibrium between the tributaries of the Shenandoah River, test the hypothesis of continuous deposition and erosion proposed by Hack (1965), and identify potential drivers of Neogene landscape change in the Shenandoah Valley, we dated multiple alluvial fans and fluvial terraces in the valley using $^{26}Al/^{10}Be$ burial dating.

3.3 Methods

Most cosmogenic nuclides are produced when high-energy cosmic rays interact with atmospheric particles and trigger a cascade of nuclear reactions, producing neutrons and muons that can reach rocks at the Earth's surface. When the neutrons interact with silicon and oxygen in quartz, they produce the radionuclides ^{26}Al and ^{10}Be, respectively, through spallation. Because neutron flux is rapidly attenuated with depth, production via spallation reaches about 1% of its surficial value at ~3 m depth in rock. Below this depth, production by muons dominates. While rocks are eroding and transiting through this zone of production, they accumulate ^{10}Be and ^{26}Al as a function of erosion rate. Quickly eroding rock will transit the production zone rapidly and accumulate a small inventory of cosmogenic nuclides, while slowly eroding rock will transit slowly and accumulate a higher concentration of cosmogenic nuclides. The $^{26}Al/^{10}Be$ ratio in rock as a function of erosion rate is generally modeled using the equation:

$$\textbf{(1)} \quad \left(\frac{N_{26}}{N_{10}}\right)_{inh} = \frac{P_{26}}{P_{10}} \frac{\frac{1}{\tau_{10}} + \frac{\rho E}{\Lambda}}{\frac{1}{\tau_{26}} + \frac{\rho E}{\Lambda}}$$

where N_{26} and N_{10} are the concentrations of ^{26}Al and ^{10}Be (at/g), P_{26} and P_{10} are the production rates of ^{26}Al and ^{10}Be (at/g·yr), τ_{26} and τ_{10} are the mean lives of ^{26}Al ($1.020 \cdot 10^6$ yr) and ^{10}Be ($2.005 \cdot 10^6$ yr), ρ is the density of eroding rock (g/cm^3), and Λ is the attenuation length (160 g/cm^2) (Granger et al., 1997; Nishiizumi, 2004; Chmeleff et al., 2010; Korschinek et al., 2010). This ratio is assumed to be the inherited (pre-burial) $^{26}Al/^{10}Be$ ratio when calculating a burial age and increases with pre-burial erosion rate.

3.3.1 Minimum burial ages

The most straightforward way to calculate a burial age is to assume that no postburial production of ^{26}Al or ^{10}Be has occurred, and that the measured ^{26}Al/^{10}Be ratio is solely a function of preburial exposure and radioactive decay following burial. This relationship is represented by the equation

$$\textbf{(2)} \quad \frac{N_{26}}{N_{10}} = \left(\frac{N_{26}}{N_{10}}\right)_{inh} e^{-t/\tau_{bur}}$$

where t is burial age (yr) and $\tau_{bur} = (\tau_{26}^{-1}\text{-}\tau_{10}^{-1})^{-1} = 2.076$ My. This is a valid assumption for rapidly, deeply buried deposits such as those in caves; however, shallower deposits such as alluvial fans and fluvial terraces often experience substantial postburial production of cosmogenic nuclides by deeply penetrating muons. Muogenic production is extremely slow compared to spallation but dominates production at depth and can dramatically influence ^{26}Al and ^{10}Be concentrations over millions of years of burial. Postburial production raises the ^{26}Al/^{10}Be ratio, yielding a younger apparent age if not accounted for (Granger, 2006). As such, this number represents a minimum burial age. Minimum ages for all samples are included in Table 3.1.

3.3.2 Maximum burial ages

It is possible to account for the effects of postburial production by modeling cosmogenic nuclide production by muons at depth. This study estimated production rates of ^{26}Al and ^{10}Be at depth using MATLAB code from Balco (2017). Those rates were input to the equations

$$\textbf{(3)} \quad N_{10,pb} = P_{10,z}\tau_{10}\left(1 - e^{-t/\tau_{10}}\right)$$

$$\textbf{(4)} \quad N_{26,pb} = P_{26,z}\tau_{26}\left(1 - e^{-t/\tau_{26}}\right)$$

to solve for the postburial component $N_{i,pb}$ (at/g) as a function of postburial production rate $P_{i,z}$ (at/g·yr) and guessed burial age t. The resultant postburial components were input into the equation:

$$\textbf{(5)} \quad t = \ln\left[\frac{(R_{inh})(N_{10} - N_{10,pb})}{(N_{26} - N_{26,pb})}\right]\tau_{bur}$$

where R_{inh} is the initial ^{26}Al/^{10}Be ratio (Granger, 2014). The equations were then iterated until convergence to solve for a maximum burial age. Maximum burial age calculations in this study assumed no postburial erosion of overlying material, and thus incorporate the maximum possible postburial production of ^{26}Al and ^{10}Be. In many instances, postburial production is so significant

that calculating a maximum burial age is impossible. Such cases may benefit from isochron burial dating, which provides an alternative approach to dealing with postburial production of ^{26}Al and ^{10}Be.

3.3.3 Isochron burial ages

The isochron approach provides an advantage over minimum-maximum burial age dating in that it allows the user to explicitly solve for burial age without requiring rapid, deep burial or constraints on burial depth and density of overlying material. By measuring ^{26}Al and ^{10}Be concentrations in a suite of clasts from the same depth, it is possible to treat postburial production as a constant between samples and solve for burial age via regression. On a plot of ^{26}Al vs. ^{10}Be, the clasts will fall on a line represented by the equation:

$$\textbf{(6)} \quad N_{26} = \left(N_{10} - N_{10,pb}\right)(R_{inh})e^{-t/\tau_{bur}} + N_{26,pb}$$

By calculating both burial age and postburial production, the isochron method makes it possible to estimate the preburial concentrations of ^{26}Al and ^{10}Be in the isochron's constituent clasts and sand. The preburial concentrations in sand are useful for estimating basin-averaged erosion rates at the time of burial (paleo-erosion rates) which are useful for identifying erosional trends through time. This study calculated paleo-erosion rates using ^{10}Be production rates derived from digital elevation models that were clipped to only include quartz-bearing lithologies (sandstone, arenite, igneous intrusions, etc.) according to digitized state maps from the U.S. Geological Survey (https://mrdata.usgs.gov/ geology/state/state.php). Estimated paleo-erosion rates are provided for sand and cobbles in Tables 3.1. See methods section of Chapter 2 and Appendix B for details of sample preparation and chemistry.

3.4 Sample locations

3.4.1 Tilthammer Mill Road cut (TILT) – Clarke County, VA

The Tilthammer Mill Road site is a roadcut located 1.6 kilometers northwest of Berrys, VA (Figure 3.4a). It is a ~10 m thick terrace exposure, with its base perched at 145 m asl, approximately 21 m above the modern Shenandoah River. This site is of particular interest because it is the only known dateable exposure of a Shenandoah River terrace along its main branch. Furthermore, it is located on the west side of the Shenandoah River and should not be influenced

by deposition of fans along the western edge of the Blue Ridge. Sandstone clasts and sand fractions were collected from the site for $^{26}Al/^{10}Be$ isochron burial dating at 39.0488°N, 78.0092°W.

3.4.2 Timberville gravel pit (TV) – Rockingham County, VA

The Timberville gravel pit is located 2.6 km ENE of Timberville, VA at 310 m asl, approximately 10 m above the modern level of the north fork of the Shenandoah River (Figure 3.4b). It is interpreted as a fluvial terrace deposit that overlies the Ordovician Conococheague Formation. The sample site at 38.6343°N, 78.7443°W features a seven-meter-thick exposed section of fluvial gravels consisting primarily of sandstones and sands. Sandstone clasts and sand fractions were collected from the site for cosmogenic isochron burial dating.

3.4.3 Briery Branch (BB) – Rockingham County, VA

Briery Branch is a tributary of the North River that has incised through several generations of fan deposits 19 km west of Harrisonburg, VA (Figure 3.4c). The deposits primarily consist of gravels sourced from the Catoctin greenstone, Chilhowee quartzites, Tuscarora and Massanutten sandstones, and the Pocono sandstone (Hack, 1965). Fan deposits in the Shenandoah Valley were initially described by King (1949), who proposed that the gravels were produced during discrete periods of deposition during the Pleistocene as a function of colder climate and enhanced scree formation. Focusing on the fans near Briery Branch, Hack (1965) asserted that the variation in erodibility between the bedrock upstream (sandstones, quartzites, and shales) and the bedrock downstream (carbonates and shales) led to the development of transitional deposits at the boundaries between the two lithologies. Consequently, Hack (1965) argued for continuous deposition of the aprons.

The roadcut exposes a mid-level fan along Briery Branch and is perched at 462 m asl, approximately 10 m above the modern channel. Clasts range in diameter from <10 cm to ~50 cm, with larger clasts being more angular than the smaller clasts. Kaolinite is present throughout the deposit, and many clasts have weathered to saprolite. More resistant clasts, such as sandstones and quartzites, have remained lithified. The matrix is predominantly sand. This site is of interest due to its unknown age since King's (1949) discussion and its pivotal role in Hack's model of dynamic equilibrium. In addition to providing a test of episodic versus continuous weathering, it

also reveals an average incision rate for the tributary of the Shenandoah River that has cut through it. We sampled the base of the exposure at 38.4230°N, 79.0828°W for gravels and sands.

3.4.4 Lynnwood alluvial fan (LYNN) – Rockingham County, VA

The alluvial fan deposit near Lynnwood, VA is located at 350 m asl, 7 km northeast of Grottoes, VA along the South Fork of the Shenandoah River (Figure 3.4d). This area hosts abundant alluvial fans sourced from the nearby Blue Ridge and is geomorphically similar to the Shenandoah, VA sampling site described in section 3.4.6. Quarrying has exposed ~10 m sections of one of the fans, which shows layers indicative of episodic deposition. This fan covers the Cambrian Waynesboro Formation and is sourced primarily from the Cambrian Harpers and Antietam Formations (Rader and Gathright, 2001a). Grains ranged in diameter from sand to boulders. We sampled sands at the base of the pit at 38.3087°N, 78.7517°W at a depth of approximately 9 meters for a minimum-maximum burial age calculation.

3.4.5 McCarty Pit #1 (MC) – Warren County, VA

Nine kilometers northeast of Front Royal, VA, a large gravel pit is situated at 165 m asl near the intersection of Howellsville Road and Morgans Ridge Road. A 10 m-thick layer of fan gravels is perched 30 m above the nearby Shenandoah River. Excavations at this pit have removed most overlying gravels and continued into the underlying Cambrian Harpers Formation, which in this location has weathered to saprolite (Lukert and Nuckols, 1976). While no exposed fan deposits remain in the pit itself, a small stream immediately southeast of the pit has deeply incised into a remnant of the fan and exposed the gravel-saprolite contact (Figure 3.4e). The gravels are subrounded to rounded, generally smaller than 15 cm in diameter, and lie within a sandy matrix. Near the contact between the fan and the Harpers Formation, gravels are cemented by a crumbly iron oxide crust. We sampled the fan-saprolite contact at 38.9540°N, 78.1060°W.

3.4.6 Shenandoah alluvial fan cut (S12) – Page County, VA

The area near Shenandoah, VA features broad, gently sloping alluvial fans sourced from the nearby Blue Ridge Mountains (Figure 3.4f). The fans terminate along the eastern banks of the South Fork of the Shenandoah River; to the west of the river, steeper fans have formed on the

slopes of Massanutten Mountain. Alluvium in the eastern fans is highly oxidized and features coarse cobbles with high quartz contents. Thickness to bedrock is not known. A similarly situated fan deposit approximately 65 kilometers southeast of Shenandoah, VA was reportedly dated to 6.9-7.9 My using cosmogenic $^{26}Al/^{10}Be$ burial dating by Heller et al. (2014).

This site is located at 38.4958°N, 78.6206°W, only 0.8 km from the modern Shenandoah River and perched at 307 m asl, 30 m above the river. It exposes six meters of alluvial sands and cobbles, generally <20 cm in diameter. Unlike the Briery Branch fan deposit, no kaolinite is apparent and the clasts themselves are not deeply weathered, suggesting a relatively young deposit in contrast to the upstream BB site. Imbrication of the clasts suggests a roughly northern flow direction. For this study, quartzites and sandstones were collected and analyzed.

3.5 Results

The cosmogenic nuclide concentrations and burial ages for deposits in the Shenandoah Valley exhibited a wide range of values (Figure 3.5). Fans and terraces in the uppermost reaches of the north and south forks of the Shenandoah River were oldest (Pliocene), while those along the main branch of the Shenandoah River dated to the Pleistocene. The highest paleo-erosion rates (>10 m/My) were measured in the western Shenandoah Valley despite generally lower slopes, while paleo-erosion rates in the eastern Valley were closer to modern basin-averaged values (<10 m/My) estimated by Duxbury et al. (2015). Taken together, the deposits illustrate an upstream history of rapid Pliocene aggradation followed by subsequent gradual incision and erosion. The Pleistocene history of the lower Shenandoah Valley remains less clear due to an abundance of reworked materials in burial isochrons.

3.5.1 Tilthammer Mill Road cut – Clarke County, VA

An isochron burial age could not be calculated using all four $^{26}Al/^{10}Be$ measurements from the Tilthammer Mill Road terrace, yet no clasts were obviously reworked relative to the sand fraction (Figure 3.5). To identify the problematic measurement(s), we calculated burial age likelihood functions for all samples following the methodology of Odom et al. (2020) (see Figure 3.6 and Chapter 6 of this thesis). The likelihood function for TILT-4 shows an apparently younger age than the sand fraction and all other clasts, indicating that it experienced more postburial

production of ^{26}Al and ^{10}Be than the other samples and was potentially sourced from higher in the deposit. Given that the samples were collected from a roadcut, it is possible that TILT-4 was dislodged during excavation of the area. It is also possible that laboratory error contributed to TILT-4's anomalous measurement. Sample TILT-2 features a burial age likelihood function that is apparently older than the sand fraction, indicating that the sample likely experienced prior burial and reworking. Considering the abundance of alluvial fans upstream of the site, it is plausible that TILT-2 eroded out of a riverside fan and was reburied in the terrace. A two-point isochron from the remaining samples, TILT-8 and TILT-SAND, yields a potential burial age of 0.87 ± 0.05 My and no postburial production of $^{26}Al/^{10}Be$. This corresponds to a sand paleo-erosion rate of 6.6 $^{+0.1}/_{-0.1}$ m/My, indistinguishable from the modern erosion rate measurements by Duxbury et al. (2015) in the upper watershed of the South Fork of the Shenandoah River.

Alternatively, it is possible that all samples *except* TILT-4 experienced some degree of prior burial, given its high $^{26}Al/^{10}Be$ ratio and concentrations relative to the others. In this case, the deposit would have a minimum burial age of 0.44 ± 0.06 My (Figure 3.6). The reworked material would have likely originated in the alluvial fans across the Shenandoah River, as no significantly higher terraces are evident in the immediate vicinity of the Tilthammer Mill Road terrace. While this is a plausible explanation for the $^{26}Al/^{10}Be$ measurements of TILT-2 and TILT-8, it is unlikely that the sand fraction draining most of the Shenandoah Valley would feature a significant reworked component. Given the improbability of the sand hosting enough reworked material to skew its burial age by ≥ 0.5 My, this alternative is not favored, but it nonetheless remains a possibility. As such, we assign a low degree of confidence to our two-point isochron burial age of 0.87 ± 0.05 My and would require additional measurements to test its veracity.

While uncertain, this tentative age provides some constraints on the Pleistocene behavior of the Shenandoah River. From TILT-4, it is clear that the deposit is at least 0.44 ± 0.06 My, providing a maximum incision rate of 42-55 m/My at the site. From the two-point isochron, it appears likely that the true average incision rate of the Shenandoah River is closer to 23-26 m/My; however, this estimate is subject to change pending additional $^{26}Al/^{10}Be$ measurements. Given the present results, it appears that the Shenandoah River is incising rapidly relative to the basin-averaged erosion rate.

3.5.2 Timberville gravel pit – Rockingham County, VA

The terrace at Timberville, VA yielded an isochron age of 3.29 ± 0.14 My and postburial ^{10}Be production of 4.91 ± 0.86·10^4 at/g (Figure 3.5). The MSWD was 0.56. No clasts were interpreted as reworked. The inherited ^{10}Be concentration in the sand fraction was 32.89 ± 8.06·10^4 at/g, providing an estimated paleo-erosion rate of 14.3 $^{+1.6}/_{-1.4}$ m/My. The average incision rate of the North Fork of the Shenandoah River was only 2.9-3.2 m/My at this location, indicating that no significant incision has occurred at this location since at least the Middle Pliocene. This contrasts with the (potentially) high Pleistocene incision rates measured downstream at the Tilthammer Mill Road terrace. The lack of a significant knickpoint between the two locations suggests that the difference in incision rates may have been accommodated by a decrease in the river's concavity during the Plio-Pleistocene, but a firmer constraint on the age of the TILT terrace would be necessary to test this inference.

3.5.3 Briery Branch – Rockingham County, VA

The fan at Briery Branch yielded an isochron age of 3.19 ± 0.40 My (MSWD = 1.88) and an estimated 4.43 ± 0.43·10^4 at/g of postburial ^{10}Be production (Figure 3.5). No clasts were interpreted as reworked or excluded from age and paleo-erosion rate calculations. The estimated inherited ^{10}Be concentration was 28.47 ± 6.48·10^4 at/g, corresponding to a paleo-erosion rate of 17.8 $^{+2.1}/_{-1.9}$ m/My. Briery Branch has incised approximately 10 meters through the fan deposit at the sampling location, corresponding to an average incision rate of 2.8-3.6 m/My at this location. Within analytical uncertainty, the age, erosion rate, and local incision rate for this deposit are identical to that of the Timberville, VA terrace despite its location in a different watershed, suggesting that the entire western Shenandoah Valley underwent substantial aggradation during the Mid-to-Late Pliocene. Since that time, the western valley has undergone minimal incision.

3.5.4 Lynnwood alluvial fan – Rockingham County, VA

Sand from the LYNN site yielded a minimum burial age of 1.68 ± 0.11 My and an approximate paleo-erosion rate of 14.0 $^{+0.9}/_{-0.6}$ m/My (Figure 3.5). Note that this paleo-erosion rate does not account for postburial production and is thus a maximum bound on the true paleo-

erosion rate. A maximum burial age could not be calculated, likely due to significant postburial production of ^{26}Al and ^{10}Be following burial.

3.5.5 McCarty Pit #1 – Warren County, VA

The isochron constructed from samples at the McCarty Pit #1 alluvial fan showed evidence of reworking in samples MC-2, MC-5, and MC-11 (Figure 3.5). Sample MC-2 was the most obviously reworked, with a minimum burial age of 1.80 ± 0.17 My relative to the sand fraction's minimum burial age of 1.17 ± 0.11 My. Samples MC-5 and MC-11 had minimum burial ages of 1.30 ± 0.12 My and 1.47 ± 0.12 My, respectively. While these minimum ages did not preclude them from inclusion on the isochron, they featured potential maximum burial ages that far exceeded those of the sand fraction (Figure 3.7). More importantly, their exclusion from the isochron significantly improved its MSWD from 5.0 to 0.66. These clasts were probably locally sourced from an older, higher alluvial fan in the area immediately south of the sample location that has been eroding into lower fan deposits and the Shenandoah River itself.

With the three reworked samples excluded, the fan at McCarty Pit #1 had an age of 1.51 ± 0.19 My (MSWD = 0.66) and estimated $11.52 \pm 0.84 \cdot 10^4$ at/g of postburial ^{10}Be production (Figure 3.5). The estimated inherited ^{10}Be concentration was $66.15 \pm 7.04 \cdot 10^4$ at/g, corresponding to a paleo-erosion rate of $4.9\ ^{+0.2}/_{-0.2}$ m/My. This low paleo-erosion rate is similar to modern basin-averaged erosion rates in the Shenandoah Valley (Duxbury et al., 2015).

3.5.6 Shenandoah alluvial fan cut – Page County, VA

The alluvial fan near Shenandoah, VA had similar concentrations of ^{26}Al in each clast, indicating that significant postburial production had occurred (Figure 3.5). Concentrations of ^{10}Be varied, indicating that burial time was insufficient to decay the inherited component of ^{10}Be and implying that the fan is probably no older than Late Miocene. Overlapping ^{26}Al concentrations made an isochron calculation impossible, but each clast yielded a minimum burial age of the deposit. Minimum ages ranged from 0.58 ± 0.17 My to 1.49 ± 0.11 My. The oldest minimum age is taken to be the minimum age of the deposit, assuming no reworking of previously buried material. Maximum ages could not be calculated for this site due to the shallow burial (4 m) and significant postburial production of ^{26}Al.

3.6 Discussion

3.6.1 Preservation of Late Cenozoic deposits

The Pliocene through Pleistocene ages for terrace and fan deposits demonstrate that Late Cenozoic erosion rates in the Shenandoah Valley were sufficiently low and/or discontinuous to preserve unconsolidated materials over extended periods. This contrasts with the model of dynamic equilibrium, which was used to infer a Late Pleistocene or younger age for gravels in the Shenandoah Valley with the assumption of constant erosion (Hack, 1965). The clustering of burial ages at different times also implies that erosion and deposition occurred episodically in the area, during which times erosion rates also fluctuated. Paleo-erosion rates derived from isochrons show that erosion rates also varied from >10 m/My in the Middle Pliocene to <5 m/My in the Middle Pleistocene. This episodic nature of deposition is partially consistent with King (1949)'s hypothesis that the alluvial gravels of the Shenandoah Valley were emplaced at discrete intervals, though the Pliocene gravels are somewhat older than predicted by King (1949).

3.6.2 Rapid Pliocene aggradation in a warmer climate

Fan and terrace deposits at Briery Branch, VA and Timberville, VA both date to ~3.3 My, despite being located in hydrologically distant tributary watersheds of the Shenandoah River. They exhibit similar, relatively rapid erosion rates that significantly outpace the subsequent local incision rates, modern average erosion rates in the upper South Fork (Duxbury et al., 2015), and long-term denudation rates estimated from manganese oxide geochronology (Chapter 4, this thesis). This points to rapid aggradation in the Late Pliocene that apparently corresponds to the mid-Piacenzian Warm Period (mPWP) that lasted from 3.26-3.03 My (Raymo et al., 1996; Haywood et al., 2016). The mPWP was marked by a higher sea level (Lisiecki and Raymo, 2005) and a global increase in surface temperature (Robinson et al., 2018). Paleoclimate modeling by Fedorov et al. (2010) indicates that a positive feedback between tropical cyclones and the upper ocean circulation system in the Pacific Ocean may have driven sustained El Niño-like conditions from approximately 5-3 Ma, leading to intensified storm activity. Recent modeling by Yan et al. (2016, 2019) supports these conclusions, noting that warmer sea surface temperatures directly contributed to greater storm intensity and hypothesizing that the Late Miocene to Late Pliocene restrictions of the Panama and Indonesian seaways significantly influenced the genesis potential

of tropical cyclones in the northern hemisphere. It is likely that increased storm intensity in the mPWP was a primary driver of sedimentation in the Shenandoah Valley, leading the coeval formation of the Briery Branch and Timberville deposits despite the differences between their local geomorphology and drainages. This interpretation differs from King (1949)'s hypothesis that the gravel deposits were formed during cold intervals and lends support to Butts (1940)'s proposal that the gravels were deposited during periods of increased rainfall.

3.6.3 Gradual erosion and potential rapid incision in the Pleistocene

Pleistocene paleo-erosion rates were markedly lower than in the mPWP (Figure 3.8), yet there is moderate evidence for increased incision rates during the mid to late Pleistocene. The McCarty alluvial fan showed gradual local erosion rates of $4.9\ ^{+0.2}/_{-0.2}$ m/My near 1.5 My, despite being located in a steeper area than either the Briery Branch or Timberville sites. Similarly, the basin averaged erosion rate for the Tilthammer terrace – assuming the two-point isochron constructed from the sand fraction and TILT-8 is valid – was $6.6\ ^{+0.1}/_{-0.1}$ m/My for the combined North and South Fork watersheds. If the isochron burial age of 0.87 ± 0.05 My is indeed accurate, it corresponds to rapid incision (23-26 m/My) of the main branch of the Shenandoah River during the Pleistocene that exceeds paleo- and modern erosion rates (Duxbury et al., 2015) by more than threefold.

This discrepancy would appear to indicate that the landscape is not in a state of dynamic equilibrium, wherein incision rates should be approximately equal to erosion rates (e.g., Cyr and Granger, 2008). In such a scenario, however, one would expect to see one or more knickpoints developed between the supposedly rapidly incising area near the Tilthammer terrace and the gradually incising area near the Timberville terrace. The remarkably concave profile of the North Fork (Figure 3.2) shows no such knickpoints, indicating that either (a) the concavity of the North Fork decreased following the deposition of the Timberville terrace, permitting increased incision along the river's lower reaches without generating knickpoints, or (b) the ~0.9 My age inferred for the Tilthammer terrace is too young. Given the low confidence in the TILT isochron, additional measurements would be necessary to evaluate these hypotheses and better constrain Pleistocene incision along the Shenandoah River.

3.6.4 Potential influence of dynamic topography

Our interpretations of alluvial fan and terrace burial ages indicate climate as a primary driver of late Cenozoic landscape change, given the episodic nature of aggradation and low magnitude of river incision. Climate records reflect geologically short-term fluctuations in temperature and sea level in the Pliocene and especially the Pleistocene (Zachos et al., 2001; Robinson et al., 2018) that readily explain the episodic nature of Pliocene aggradation and potential Pleistocene incision indicated by our dataset. This is highlighted by the close alignment of Pliocene burial ages with the mid-Piacenzian Warm Period (Figures 3.5, 3.8). However, while climate appears to be the primary driver of landscape evolution in the late Cenozoic Appalachians, it is likely not the only factor influencing long-term aggradation and incision.

Dynamic topography driven by asthenospheric flow has the potential to drive uplift and subsidence over long timescales. Its influence on the east coast of North America is evident in the Orangeburg scarp, a Pliocene wave-cut shoreline that has been deformed tens of meters since its formation. Rowley et al. (2013) examined the shoreline and estimated that up to 60 m of warping has occurring along the coastline. Offshore, Rovere et al. (2014) similarly estimated up to 55 m of N-S tilting since the Pliocene. Given the Shenandoah Valley's proximity to the coast, it likely has experienced some degree of asthenosphere-driven uplift; Rowley et al. (2013) interpolated 0-40 m of uplift affecting the Shenandoah Valley since the Pliocene. The exact magnitude and timing of dynamic topography – and its effect on the behavior of the Shenandoah landscape – is difficult to constrain, but it likely played long-term roles in the evolution of the watershed. Given the discrete nature of terrace and fan deposition, it appears that climate remains the driving force of major landscape changes in the valley, while dynamic topography exerts a more subtle, long-term effect.

3.7 Conclusions

The Shenandoah Valley features a robust Plio-Pleistocene sedimentary record. It is particularly sensitive to fluctuations in climate and sea level given its proximity to the river system's outlet, the Atlantic Ocean. This work has demonstrated that the Shenandoah Valley is a geomorphically complex system that shows elements of both Hackian and Davisian erosional styles. Topography and sedimentation are continuously influenced by lithology, but episodic

drivers – most notably the mid-Piacenzian Warm Period – exert a clear influence on erosional processes. Our results indicate that climate, rather than tectonism, is the primary driving force of topographic change in the Virginia Valley and Ridge province that has caused both immense aggradation and incision.

This chronology improves upon the current understanding of the Shenandoah Valley's evolution during the Late Cenozoic, but several questions arise from these results. For one, the potential discrepancy in incision response between the North Fork and South Forks of the Shenandoah River remains an unresolved issue that could be verified by additional dating of terraces. Another important – and unanswered – question is that of the relict landscape within Massanutten Mountain. Given that the lower landscapes surrounding the mountain are Pliocene and Pleistocene in age, it is conceivable that the landscape within Massanutten Mountain is Miocene-Pliocene or older. This is supported by the hypothesized Miocene-Pliocene age for the Tysons Corner terrace deposits that correspond to the reconstruction of the Passage Creek longitudinal profile, but those deposits have not yet been radiometrically dated. It is also possible that the Passage Creek knickpoint instead represents an equilibrium stream that has adjusted to the underlying lithology, a hypothesis that could be tested by measuring erosion rates above and below the convexity. Beyond the Shenandoah Valley, dating other terrace and/or cave deposits perched above the Potomac River and its tributaries may also provide valuable insight into the late Cenozoic history of this iconic landscape.

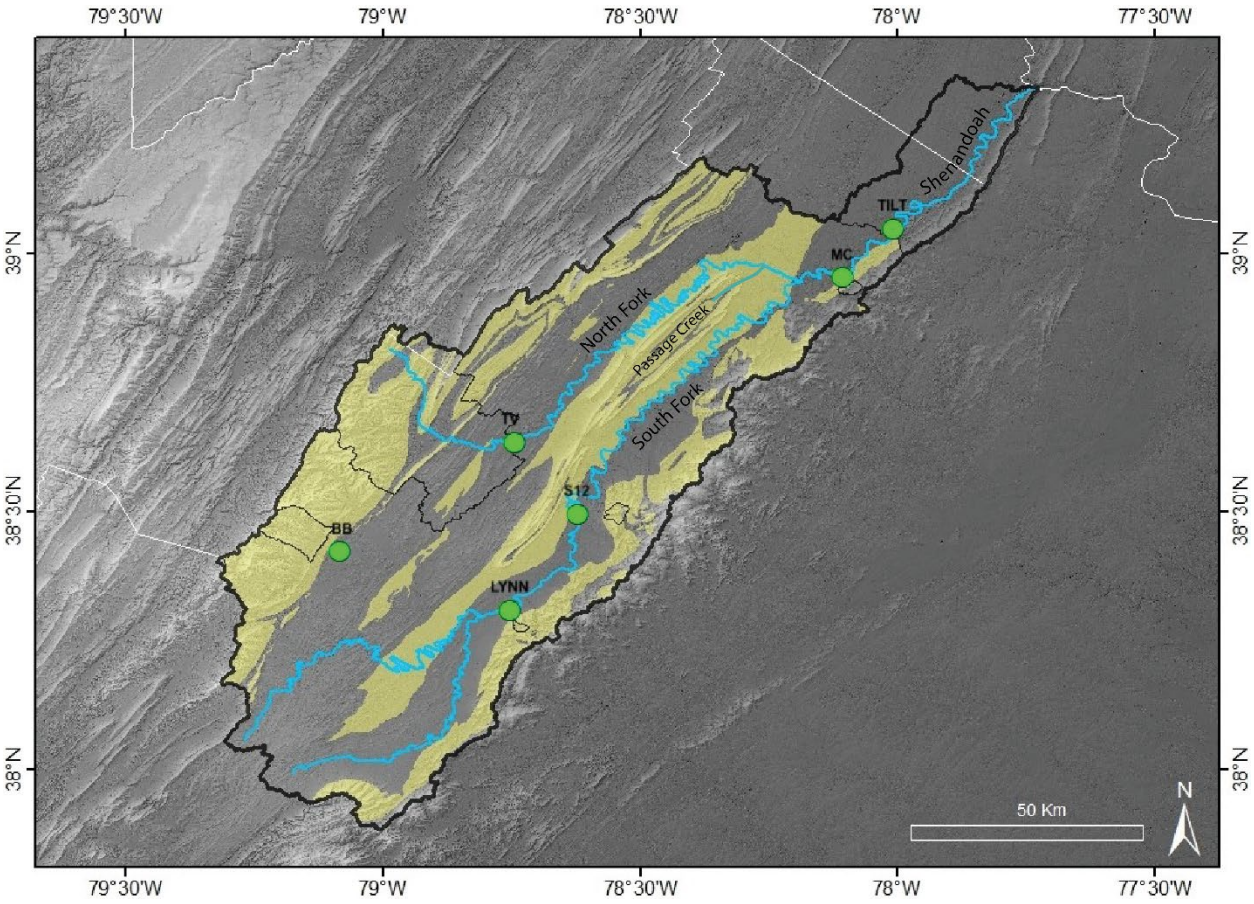

Figure 3.1. Overview of study area. The watershed of the Shenandoah River is outlined in solid black, and major tributaries are shown in blue. Drainage areas of individual sample sites are signified by thin black lines, and green dots represent sample sites. Note that the TILT terrace watershed includes each of the other studied watersheds and nearly all of the Shenandoah Valley. Quartz-rich rocks within watersheds of sample sites are indicated by yellow shading.

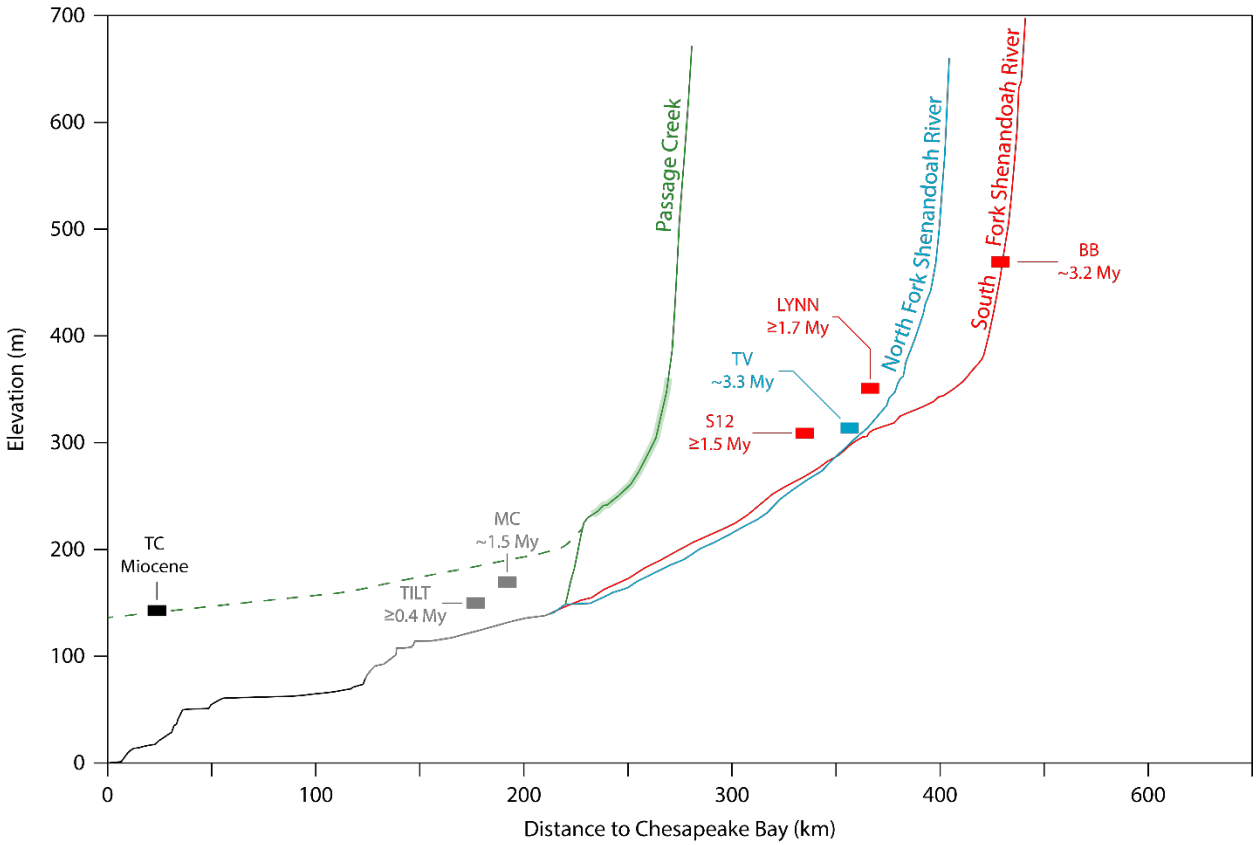

Figure 3.2. Longitudinal profiles of the Shenandoah and Potomac Rivers. Individual rivers are color coded, as are relevant deposits. TC – Tysons Corner, VA terrace; TILT – Tilthammer Mill Road terrace; MC – McCarty Pit fan; S12 – Shenandoah, VA fan; TV – Timberville, VA terrace; BB – Briery Branch, VA fan, LYNN – Lynnwood, VA fan. The reconstructed profile (dashed line) of Passage Creek was produced using the highlighted area upstream of the knickpoint and setting $\theta = 0.45$. Profiles and reconstructions were generated from 1-arcsecond digital elevation models using MATLAB and the Topotoolbox attachment (Schwanghart and Scherler, 2014).

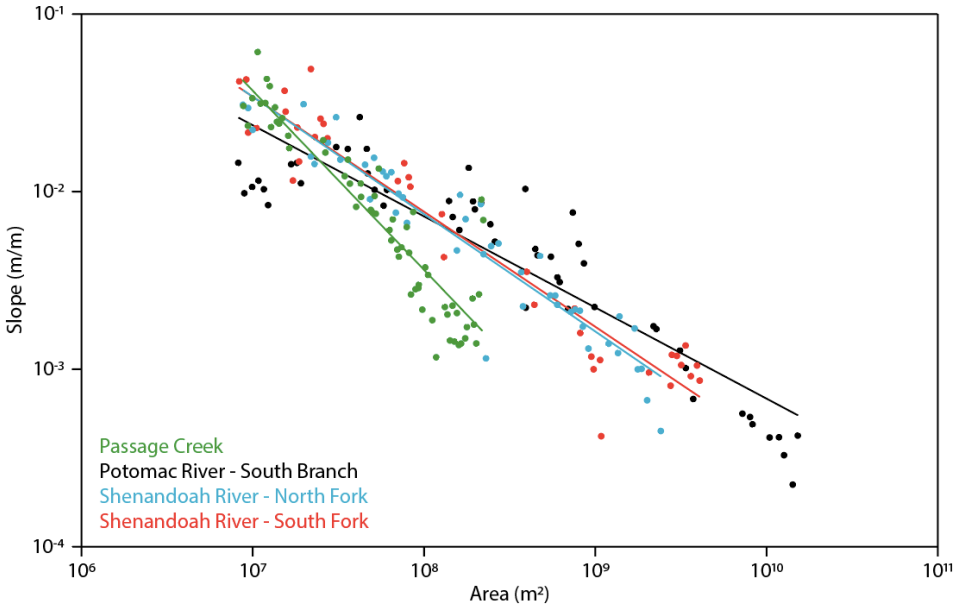

Figure 3.3. The unique behavior of Passage Creek in relation to other tributaries of the Shenandoah and Potomac Rivers is evident in slope-area plots. Both forks of the Shenandoah River feature nearly identical slope-area relationships, despite the knickpoint along the North Fork of the Shenandoah River. These relationships demonstrate similar incision behavior to the South Branch of the Potomac River, though the South Branch shows evidence of a low-relief landscape in its upper reaches. Passage Creek conversely features a high concavity and steepness index, suggesting that it responds to base level perturbations independent of the surrounding landscape. Slope-area plots were generated from 1-arcsecond digital elevation models using MATLAB and the Topotoolbox attachment (Schwanghart and Scherler, 2014).

Figure 3.4. (a) Tilthammer Mill Road terrace exposure (TILT). Shovel is located at sampling depth. (b) Timberville, VA terrace exposure (TV). D. Doctor is standing at the sampled depth. (c) Briery Branch, VA fan (BB). Approximately 10 m of fan deposits overlie this location. (d) Lynnwood, VA fan deposit (LYNN). Odom is sampling base of deposit; 9 m high wall is visible in background. (e) McCarty Pit #1 fan deposit (MC). Shovel is located at sampling depth, where fan gravels directly overlie saprolite. (f) Shenandoah, VA fan deposit (S12). Granger and Odom collected gravels at a depth of ~4 m.

Figure 3.5. (below) ^{26}Al-^{10}Be burial isochrons for terraces and fans in the study area. Gray ellipses represent individual clasts that were included in age calculations; empty ellipses represent clasts that were interpreted as reworked and excluded from age calculations. Black ellipses represent sand fractions. Mean isochron curves and 1σ uncertainties are shown, as are postburial production lines. (a) The Timberville terrace yielded a Pliocene age with some postburial production. Its good overall fit lends confidence to this age estimate; the low MSWD indicates that analytical uncertainty is high relative to natural scatter. (b) The Tilthammer Mill Road terrace near Berrys, VA yielded an ambiguous age. It is possible to form an isochron from samples TILT-8 and TILT-SAND (shown above) if sample TILT-4 is regarded as reworked from higher in the deposit. In contrast, assuming that TILT-4 is a valid sample would necessitate prior burial of all other clasts including sand, an unlikely yet possible occurrence. (c) The Briery Branch alluvial fan yielded virtually identical results to the Timberville terrace, within uncertainty. The somewhat higher MSWD value points to minor potential reworking of one clast, but not to a degree sufficient to merit removal from the isochron. (d) The McCarty alluvial fan showed numerous reworked clasts indicative of previous burial, likely in an older alluvial fan. Removal of these clasts yielded an isochron with a large spread in ^{10}Be concentrations and low MSWD value. (e) The Shenandoah, VA alluvial fan showed evidence of substantial postburial production. No maximum valid ages could be calculated for the samples, as all inherited ^{26}Al has decayed and/or been overprinted by postburial production.

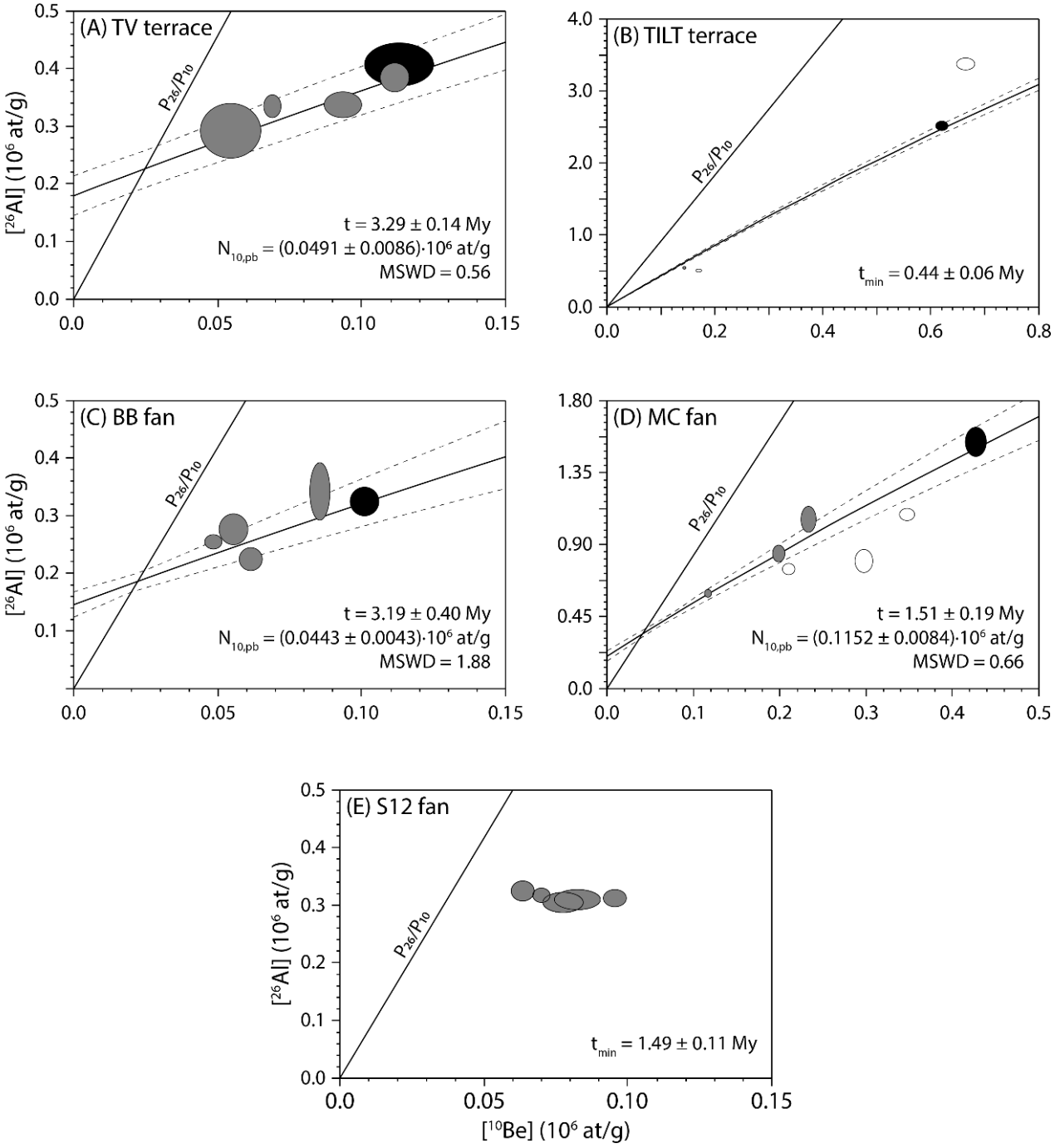
(A) TV terrace
P26/P10
t = 3.29 ± 0.14 My
N10,pb = (0.0491 ± 0.0086)·10⁶ at/g
MSWD = 0.56
(B) TILT terrace
P26/P10
tmin = 0.44 ± 0.06 My
(C) BB fan
P26/P10
t = 3.19 ± 0.40 My
N10,pb = (0.0443 ± 0.0043)·10⁶ at/g
MSWD = 1.88
(D) MC fan
P26/P10
t = 1.51 ± 0.19 My
N10,pb = (0.1152 ± 0.0084)·10⁶ at/g
MSWD = 0.66
(E) S12 fan
P26/P10
tmin = 1.49 ± 0.11 My
[26Al] (10⁶ at/g)
[10Be] (10⁶ at/g)

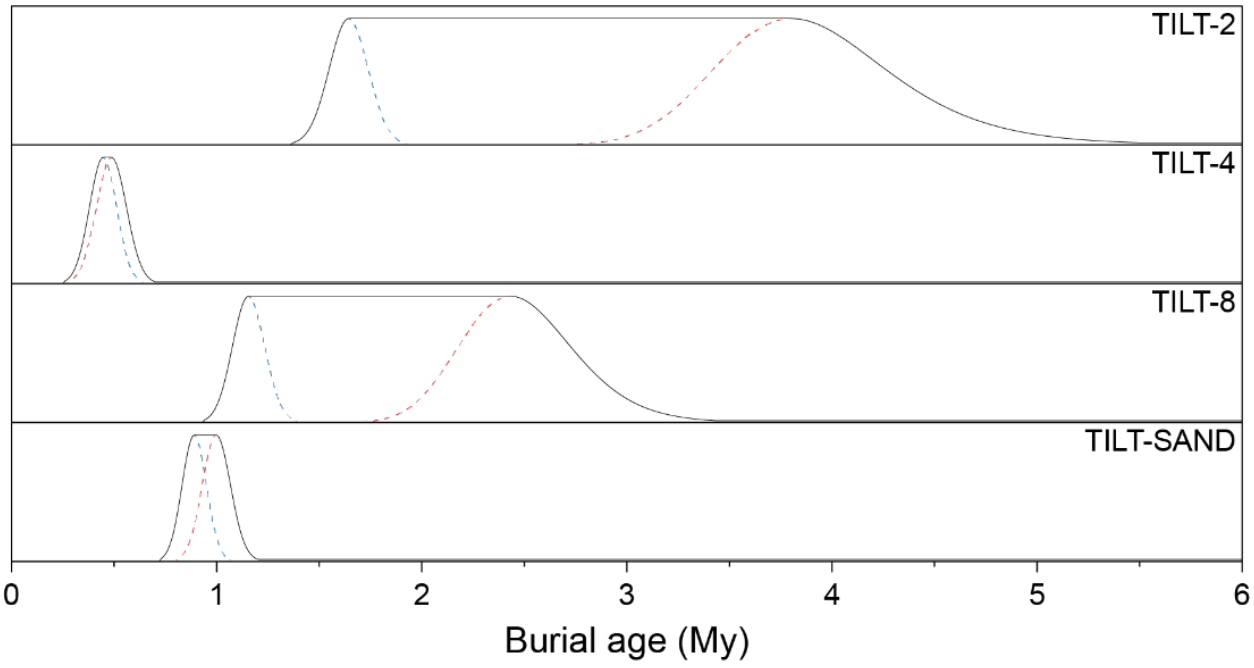

Figure 3.6. Minimum-maximum burial age likelihood functions for all samples measured in the Tilthammer Mill Road terrace. Minimum burial ages are indicated by blue dashed lines, while maximum burial ages are indicated by red dashed lines. Likelihood functions calculated using the code of Odom et al. (2020).

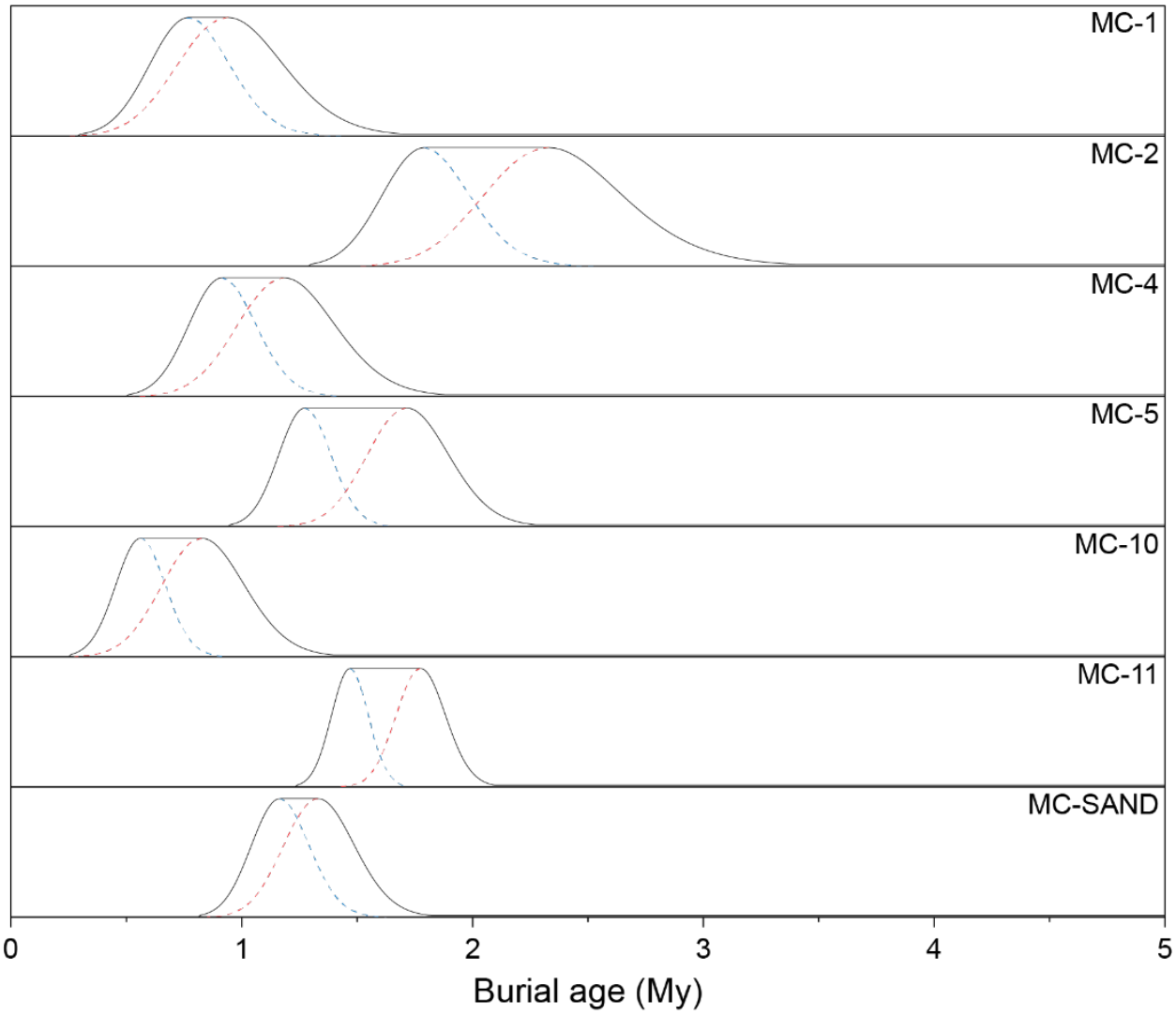

Figure 3.7. Minimum-maximum burial age likelihood functions for all samples measured in the McCarty Pit #1 alluvial fan. Minimum burial ages are indicated by blue dashed lines, while maximum burial ages are indicated by red dashed lines. Note that while all samples have overlapping likelihood functions with MC-SAND, reworked samples MC-2, MC-5, and MC-11 have likelihood functions that extend beyond that of MC-SAND. Likelihood functions calculated using the code of Odom et al. (2020).

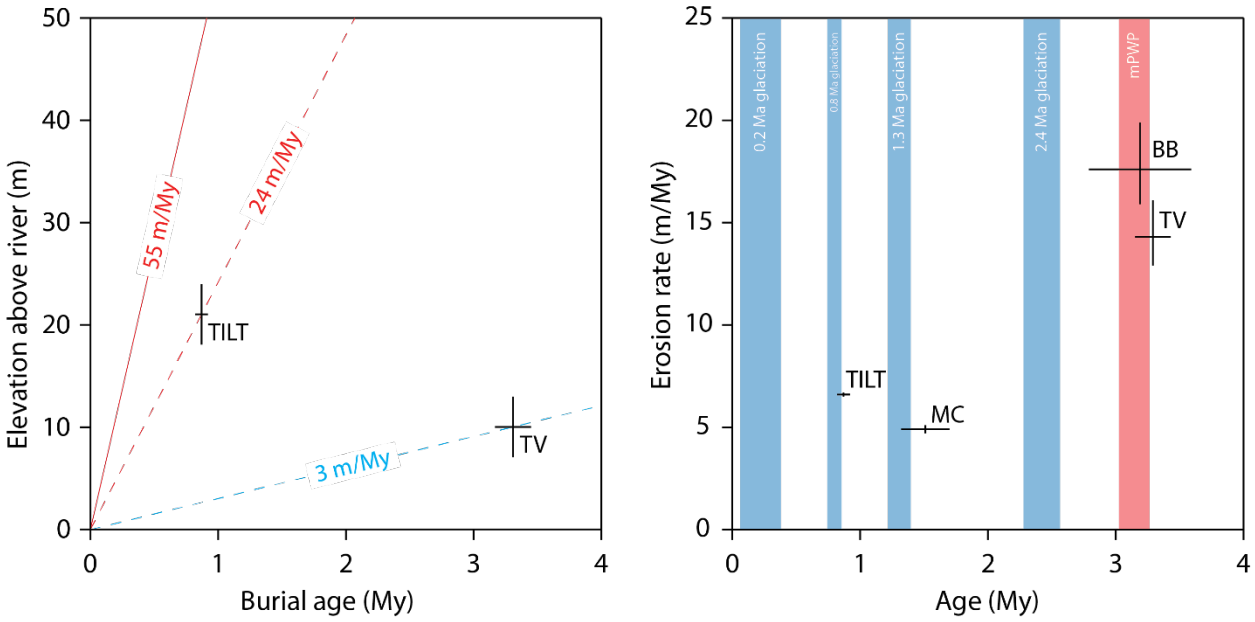

Figure 3.8. Left: Elevation vs. age relationships for dated deposits. The Timberville terrace, located in the upper watershed of the North Fork of the Shenandoah River, shows gradual incision at ~3 m/My since the Pliocene. Our ~0.9 My burial age inferred from a two-point isochron at the Tilthammer Mill Road terrace shows significantly faster incision during the Pleistocene, as indicated by a red dashed line. The maximum incision rate for the TILT site, calculated from sample TILT-4, is indicated by a solid red line. Right: Paleo-erosion rates vs. time for deposits with successful isochrons. Glaciations dated by Balco and Rovey (2010 are shown in blue and the mid-Piacenzian Warm Period is shown in red. Note that the BB and TV deposits correspond with the mid-Piacenzian Warm Period and have elevated paleo-erosion rates relative to the Pleistocene TILT and MC deposits. Again, the age provided for TILT here is derived from the two-point isochron and is approximate.

Table 3.1. $^{26}Al/^{10}Be$ data, minimum ages, and paleo-erosion rates.

Sample	Mass(g)	[^{26}Al] (10^6 at/g)	[^{10}Be] (10^6 at/g)	$^{26}Al/^{10}Be$	Min. age (My)	E (m/My)
BB-6	15.571	0.2761 ± 0.0240	0.0555 ± 0.0050	4.98 ± 0.62	0.62 ± 0.22	$83.3\ ^{+26.1}/_{-16.2}$
BB-7	16.923	0.2250 ± 0.0203	0.0616 ± 0.0039	3.65 ± 0.40	1.30 ± 0.25	$59.0\ ^{+11.8}/_{-8.80}$
BB-8	25.193	0.3413 ± 0.0492	0.0856 ± 0.0035	3.99 ± 0.60	1.12 ± 0.33	$24.9\ ^{+3.0}/_{-2.6}$
BB-10	30.863	0.2548 ± 0.0137	0.0487 ± 0.0028	5.23 ± 0.41	0.53 ± 0.16	$141.3\ ^{+67.3}/_{-46.4}$
BB-S	22.263	0.3250 ± 0.0238	0.1011 ± 0.0048	3.21 ± 0.28	1.50 ± 0.16	$17.8\ ^{+2.1}/_{-1.9}$
LYNN-S	46.707	0.2745 ± 0.0136	0.0927 ± 0.0024	2.96 ± 0.16	1.68 ± 0.11	-
MC-1	15.558	1.0589 ± 0.0820	0.2331 ± 0.0089	4.54 ± 0.39	0.76 ± 0.17	$13.3\ ^{+1.0}/_{-0.7}$
MC-2	17.551	0.7974 ± 0.0724	0.2974 ± 0.0103	2.68 ± 0.26	1.77 ± 0.20	-
MC-4	27.099	0.8440 ± 0.0529	0.1986 ± 0.0073	4.25 ± 0.31	0.90 ± 0.12	$19.3\ ^{+1.4}/_{-1.4}$
MC-5	21.095	0.7467 ± 0.0349	0.2105 ± 0.0071	3.55 ± 0.20	1.27 ± 0.11	-
MC-10	27.560	0.5961 ± 0.0241	0.1166 ± 0.0040	5.11 ± 0.27	0.55 ± 0.10	$96.8\ ^{+91.7}/_{-256.2}$
MC-11	44.123	1.0885 ± 0.0374	0.3474 ± 0.0085	3.13 ± 0.13	1.47 ± 0.08	-
MC-S	18.782	1.5440 ± 0.0911	0.4273 ± 0.0122	3.61 ± 0.24	1.16 ± 0.13	$4.9\ ^{+0.2}/_{-0.2}$
S12-3	31.365	0.3183 ± 0.0132	0.0698 ± 0.0032	4.56 ± 0.28	0.81 ± 0.14	-
S12-4	20.610	0.3040 ± 0.0176	0.0773 ± 0.0071	3.93 ± 0.43	1.11 ± 0.23	-
S12-6	15.280	0.3239 ± 0.0178	0.0636 ± 0.0041	5.09 ± 0.43	0.58 ± 0.17	-
S12-8	19.020	0.3103 ± 0.0170	0.0824 ± 0.0080	3.77 ± 0.42	1.21 ± 0.21	-
S12-9	23.983	0.3128 ± 0.0151	0.0957 ± 0.0039	3.27 ± 0.21	1.49 ± 0.11	-
TILT-2	50.545	0.5050 ± 0.0179	0.1699 ± 0.0055	2.97 ± 0.14	1.63 ± 0.10	-
TILT-4	28.938	3.3750 ± 0.0837	0.6647 ± 0.0172	5.08 ± 0.18	0.44 ± 0.06	-
TILT-8	55.314	0.5445 ± 0.0179	0.1431 ± 0.0030	3.80 ± 0.15	1.15 ± 0.07	$29.8\ ^{+0.3}/_{-0.3}$
TILT-S	29.814	2.5138 ± 0.0659	0.6206 ± 0.0113	4.05 ± 0.13	0.89 ± 0.06	$6.6\ ^{+0.1}/_{-0.1}$
TV-1	29.946	0.3353 ± 0.0210	0.0692 ± 0.0028	4.85 ± 0.36	0.69 ± 0.15	$46.2\ ^{+10.9}/_{-7.7}$
TV-2	4.575	0.2934 ± 0.0484	0.0547 ± 0.0107	5.36 ± 1.37	0.53 ± 0.52	$47.1\ ^{+23.5}/_{-76.6}$
TV-3	21.227	0.3370 ± 0.0234	0.0933 ± 0.0064	3.61 ± 0.35	1.27 ± 0.21	$20.8\ ^{+2.5}/_{-2.0}$
TV-5	14.192	0.3843 ± 0.0249	0.1117 ± 0.0052	3.44 ± 0.27	1.37 ± 0.17	$14.5\ ^{+1.3}/_{-1.0}$
TV-S	5.389	0.4067 ± 0.0376	0.1130 ± 0.0119	3.60 ± 0.51	1.27 ± 0.27	$14.3\ ^{+1.6}/_{-1.4}$

"E" refers to erosion rates calculated by subtracting postburial production and accounting for decay. Paleo-erosion rates were not calculated for reworked samples or samples without isochron ages.

Table 3.2. Sampling locations, isochron results, and basin-averaged ^{10}Be production rates.

Site	Location	Elev. (m)	Isochron age (My)	MSWD	P_{10} (at/g/yr)
BB	38.4230°N, 79.7440°W	450	3.19 ± 0.40	1.88	8.1
MC	38.9540°N, 79.0830°W	160	1.51 ± 0.19	0.66	5.6
TILT	39.0488°N, 78.0092°W	145	0.87 ± 0.05	-	7.0
TV	38.6340°N, 78.7440°W	310	3.29 ± 0.14	0.56	7.8

3.8 References

Balco, G. (2017). Production rate calculations for cosmic-ray-muon-produced ^{10}Be and ^{26}Al benchmarked against geological calibration data. Quaternary Geochronology, 39, 150-173.

Balco, G., & Rovey, C. W. (2010). Absolute chronology for major Pleistocene advances of the Laurentide Ice Sheet. Geology, 38(9), 795-798.

Bierman, P. (2015, September). The incision history of the Great Falls of the Potomac River—The Kirk Bryan field trip. In Tripping from the Fall Line: Field Excursions for the GSA Annual Meeting, Baltimore (pp. 1-10).

Butts, C. (1940). Geology of the Appalachian Valley in Virginia. Virginia Geological Survey, Bulletin 52.

Chmeleff, J., von Blanckenburg, F., Kossert, K., Jakob, D. Determination of the ^{10}Be half-life by multicollector ICP-MS and liquid scintillation counting. Nucl. Instrum. Methods Phys. Res. Sect. B Beam Interact. Mater. Atoms, 268 (2010), pp. 192-199.

Cyr, A. J., & Granger, D. E. (2008). Dynamic equilibrium among erosion, river incision, and coastal uplift in the northern and central Apennines, Italy. *Geology*, *36*(2), 103-106.

Doctor, D. H., & Orndorff, W. (2017). Hypogene Caves of the Central Appalachian Shenandoah Valley in Virginia. In Hypogene Karst Regions and Caves of the World (pp. 691-707). Springer, Cham.

Doctor, D. H., McAleer, R. M., Carmichael, S. K., & Kunk, M. J. (2018). ^{40}Ar/^{39}Ar ages of manganese oxide ores in surficial and bedrock deposits of the central Appalachian Mountains. Geological Society of America Abstracts with Programs, Vol. 40, No. 3.

Drake, A. A., Jr., & Froelich, A. J. (1997). Geologic map of the Falls Church quadrangle, Fairfax and Arlington Counties and the City of Falls Church, Virginia, and Montgomery County, Maryland. U.S. Geological Survey, Geologic Quadrangle Map GQ-1734.

Duxbury, J., Bierman, P. R., Portenga, E. W., Pavich, M. J., Southworth, S., & Freeman, S. P. (2015). Erosion rates in and around Shenandoah National Park, Virginia, determined using analysis of cosmogenic ^{10}Be. American Journal of Science, 315(1), 46-76.

Fedorov, A. V., Brierley, C. M., & Emanuel, K. (2010). Tropical cyclones and permanent El Niño in the early Pliocene epoch. Nature, 463(7284), 1066.

Fullagar, P. D., & Bottino, M. L., (1969). Tertiary felsite intrusions in the Valley and Ridge province, Virginia. Geological Society of America Bulletin, v. 80, no. 9, p. 1853-1858.

Granger, D. E., Kirchner, J. W., & Finkel, R. C. (1997). Quaternary downcutting rate of the New River, Virginia, measured from differential decay of cosmogenic ^{26}Al and ^{10}Be in cave-deposited alluvium. Geology, 25(2), 107-110.

Granger, D. E., Fabel, D., & Palmer, A. N. (2001). Pliocene− Pleistocene incision of the Green River, Kentucky, determined from radioactive decay of cosmogenic ^{26}Al and ^{10}Be in Mammoth Cave sediments. Geological Society of America Bulletin, 113(7), 825-836.

Granger, D.E., 2006, A review of burial dating methods using ^{26}Al and ^{10}Be, in Siame, L.L., Bourlès, D.L., and Brown, E.T., eds., In Situ–Produced Cosmogenic Nuclides and Quantification of Geological Processes: Geological Society of America Special Paper 415, 1–16.

Granger, D. E. (2014). Cosmogenic nuclide burial dating in archaeology and paleoanthropology.

Granger, D. E., Odom, W.E., Fabel, D., (2018). A re-evaluation of the timing of Mammoth Cave development and formation of the Ohio River. GSA Abstracts with Programs, Vol. 50, No. 6.

Hack, J. T. (1965). Geomorphology of the Shenandoah Valley, Virginia and West Virginia, and origin of the residual ore deposits (p. 84). US Government Printing Office.

Hancock, G. S., & Harbor, D. (2002). Cosmogenic isotope dating of rapid, disequilibrium incision of the James River in central Virginia. In Abstracts with Programs-Geological Society of America (Vol. 34).

Hancock, G. S., Harbor, D. J., Felis, J., & Turcotte, J. (2004, March). ^{10}Be dating of river terraces reveals Piedmont landscape disequilibrium in the central James River basin, Virginia. In GSA Abstracts with Programs (Vol. 36, No. 2, p. 95).

Haywood, A. M., Dowsett, H. J., & Dolan, A. M. (2016). Integrating geological archives and climate models for the mid-Pliocene warm period. Nature communications, 7, 10646.

Heller, M. J., Hancock, G. S., & Carter, M. W. (2014). Structure and geomorphology at the Blue Ridge-Valley and Ridge boundary near Big Levels, Virginia. Geological Society of America Abstracts with Programs, Vol. 46, No. 3.

Keith, A. (1894). Geology of the Catoctin Belt. US geol. Surv., Ann. Rept, 14, 285-295.

King, P. B. (1949). The floor of the Shenandoah Valley [Virginia]. American Journal of Science, 247(2), 73-93.

King, P. B. (1950). Geology of the Elkton area, Virginia. U.S. Geological Survey, Professional Paper 230.

Kirby, E., & Whipple, K. X. (2012). Expression of active tectonics in erosional landscapes. Journal of Structural Geology, 44, 54-75.

Korschinek, G., Bergmaier, A., Faestermann, T., Gerstmann, U.C., Knie, K., Rugel, G., Wallner, A., Dillmann, I., Dollinger, G., Von Gostomski, C.L., Kossert, K., 2010. A new value for the half-life of ^{10}Be by heavy-ion elastic recoil detection and liquid scintillation counting. Nucl. Instrum. Methods Phys. Res. Sect. B Beam Interact. Mater. Atoms 268, 187-191.

Lisiecki, L. E., & Raymo, M. E. (2005). A Pliocene-Pleistocene stack of 57 globally distributed benthic δ^{18}O records. Paleoceanography, 20(1).

Lukert, M.L., III & Nuckols, E.B., II. (1976). Geology of the Linden and Flint Hill quadrangles, Virginia. Virginia Division of Mineral Resources, Report of Investigations 44.

Mazza, S. E., Gazel, E., Johnson, E. A., Kunk, M. J., McAleer, R., Spotila, J. A., ... & Coleman, D. S. (2014). Volcanoes of the passive margin: The youngest magmatic event in eastern North America. Geology, 42(6), 483-486.

Naish, T. R., & Wilson, G. S. (2008). Constraints on the amplitude of Mid-Pliocene (3.6–2.4 Ma) eustatic sea-level fluctuations from the New Zealand shallow-marine sediment record. Philosophical Transactions of the Royal Society A: Mathematical, Physical and Engineering Sciences, 367(1886), 169-187.

Nishiizumi, K. (2004). Preparation of ^{26}Al AMS standards. Nucl. Instrum. Methods B 223, 388–392.

Rader, E.K., & Gathright, T.M., II. (2001a). Geologic map of the Augusta, Page, and Rockingham Counties portion of the Charlottesville 30x60 minute quadrangle, Virginia Division of Mineral Resources, Publication 159.

Rader, E.K., & Gathright, T.M., II. (2001b). Geologic map of the Front Royal 30 X 60 minute quadrangle: portions of Clarke, Page, Rockingham, Shenandoah, and Warren counties, Virginia, Virginia Division of Mineral Resources, Publication 162.

Raymo, M. E., Grant, B., Horowitz, M., & Rau, G. H. (1996). Mid-Pliocene warmth: stronger greenhouse and stronger conveyor. Marine Micropaleontology, 27(1-4), 313-326.

Robinson, M. M., Dowsett, H. J., Foley, K. M., & Riesselman, C. R. (2018). PRISM marine sites—The history of PRISM sea surface temperature estimation (No. 2018-1148). US Geological Survey.

Rovere, A., Raymo, M. E., Mitrovica, J. X., Hearty, P. J., O'Leary, M. J., & Inglis, J. D. (2014). The Mid-Pliocene sea-level conundrum: Glacial isostasy, eustasy and dynamic topography. Earth and Planetary Science Letters, 387, 27-33.

Rowley, D. B., Forte, A. M., Moucha, R., Mitrovica, J. X., Simmons, N. A., & Grand, S. P. (2013). Dynamic topography change of the eastern United States since 3 million years ago. Science, 340(6140), 1560-1563.

Schwanghart, W., & Scherler, D. (2014). TopoToolbox 2-MATLAB-based software for topographic analysis and modeling in Earth surface sciences. Earth Surface Dynamics, 2(1), 1.

Spencer, A. C. (1897). The Geology of Massanutten Mountain in Virginia. The Author.

Stose, G. W., Miser, H. D., Katz, F. J., & Hewett, D. F. (1919). Manganese deposits of the west foot of the Blue Ridge, Virginia (No. 17). University of Virginia.

Tso, J. L., McDowell, R. R., Avary, K. L., Matchen, D. L., & Wilkes, G. P. (2004). Middle Eocene igneous rocks in the Valley and Ridge of Virginia and West Virginia. US Geological Survey Circular, 1624, 137-157.

Vasconcelos, P. M., & Carmo, I. D. O. (2018). Calibrating denudation chronology through $^{40}Ar/^{39}Ar$ weathering geochronology. Earth-science reviews, 179, 411-435.

Wright, F. J. (1934). The newer Appalachians of the South (Part I). Between the Potomac and New Rivers. Dension Univ. Bull. J. Sci. Lab, 29, 1-105.

Yan, Q., Wei, T., Korty, R. L., Kossin, J. P., Zhang, Z., & Wang, H. (2016). Enhanced intensity of global tropical cyclones during the mid-Pliocene warm period. Proceedings of the National Academy of Sciences, 113(46), 12963-12967.

Yan, Q., Korty, R., Zhang, Z., & Wang, H. (2019). Evolution of tropical cyclone genesis regions during the Cenozoic era. Nature communications, 10(1), 1-9.

Zachos, J., Pagani, M., Sloan, L., Thomas, E., & Billups, K. (2001). Trends, rhythms, and aberrations in global climate 65 Ma to present. Science, 292(5517), 686-693.

CHAPTER 4. CHARACTERIZING AND DATING SUPERGENE MANGANESE OXIDE DEPOSITS IN THE SOUTHERN AND CENTRAL APPALACHIANS WITH RARE-EARTH ELEMENT GEOCHEMISTRY AND $^{40}AR/^{39}AR$ GEOCHRONOLOGY

4.1 Introduction

The post-orogenic history of the Appalachian Mountains, namely the persistence of high relief throughout the area despite hundreds of millions of years of erosion (Hack, 1982), has inspired numerous models seeking to understand the mechanism through which topographic relief can survive in ancient landscapes. Recently, Neogene uplift has been proposed as a potential mechanism for generating zones of high relief in the southern and central Appalachians (Gallen et al., 2013; Miller et al., 2013). These studies modeled the propagation of knickpoints along Appalachian rivers and proposed that uplift sometime in the past ~23 Ma triggered river incision that has rejuvenated relief in once-subdued relict landscapes. The Neogene uplift hypothesis has appeared in a variety of disciplines, with discussions of Appalachian crustal structures (Wagner et al., 2012; Biryol et al., 2016), North American geodynamics (Liu, 2014), and accelerated offshore Miocene sedimentation (Poag and Sevon, 1989; Galloway et al., 2011; Bentley et al., 2016) all invoking Neogene uplift as a potential driver or consequence of their findings. While the precise timing, underlying mechanism, and indeed existence of this hypothesized uplift remain unclear, the overall concept shares core similarities with historic episodic models of landscape evolution that envisioned gradual downwasting of landscapes punctuated by uplift as a means to maintain relief.

Davis (1899)'s geographic cycle was perhaps the most well-known episodic model of landscape evolution applied to the Appalachian Mountains, and was broadly used to explain the apparent "levels" of topography observed in the region (see Chapter 1). Low-relief surfaces were interpreted as remnants of peneplains, relict landscapes that had been erosionally flattened during long periods of base-level stability and subsequently incised during brief episodes of uplift. Most of these surfaces were highly controversial due to sparse evidence, but one surface – commonly known as the Harrisburg or Valley Floor peneplain – was widely accepted (Figure 4.1). This generally low-relief surface includes the floor of the Shenandoah Valley, which played a crucial

role in arguments for and against episodic landscape evolution that focused on its abundant gravel and manganese oxide deposits.

Manganese oxides were mined through the Valley Floor area and were commonly used to argue for the antiquity of the surface (Hewett, 1916; King, 1949; King 1950). Hewett (1916) proposed an early Tertiary age for the deposits and the Valley Floor surface that found continued support in later studies (King, 1949). Most manganese oxide accumulations are found not within bedrock but suspended in thick residuum, which King (1949) inferred as evidence for their formation in a warm period marked by extremely low erosion rates, corresponding to a peneplain. This hypothesis concurs with the work of earlier authors (Harder, 1910; Hewett, 1916), who recognized that manganese oxides likely form through supergene weathering processes that require oxygenated groundwater in a low-relief area. Evidence for the importance of oxygenated water lay in vertical manganese oxide mines, which generally extended no deeper than ~100 m. Hewett (1916) described Mn oxide deposits in Virginian mines that terminated in the supergene zone (Niesswaner shaft at 79 m, Kendall and Flick Mine at 78 m, Piedmont Mine at 63 m, Crimora Mine at 60 m, and Dargan Mine at 125 m) and inferred that Mn oxides should generally form down to maximum depths of 90 m. Below this depth, water is too anoxic to permit Mn to precipitate, as has been observed in other settings (P. Vasconcelos, pers. comm., Nov. 2018). The manganese oxide deposits therefore reflect a former land surface and, if their ages can be determined, can be used to test hypotheses of landscape stability punctuated by uplift.

4.1.1 Formation

Modern understanding of supergene ore formation generally supports the notion that manganese oxides form during weathering of stable surfaces and require groundwater interactions, and has been used to characterize multilevel landscapes that experienced deep weathering (Vasconcelos and Carmo, 2018). While numerous mechanisms have been proposed for the formation of Mn oxides, including hydrothermal activity (Chan et al., 2001), here we focus on chemical weathering as the primary formation mechanism for Appalachian manganese oxides given that the area over which they are found is likely too large to invoke hydrothermal activity (Hack, 1965) and there is abundant evidence for long-term weathering in the form of residuum and deep weathering deposits, including bauxite (Bridge, 1950). It is worth noting, however, that localized hydrothermal activity may have played a role in the genesis of some manganese oxide

deposits (Carmichael et al., 2017). We present a conceptual model to address the source of manganese, its mechanism of movement, and subsequent accumulation in manganese oxide deposits.

Most Appalachian manganese oxide deposits are found near contacts between carbonates and siliceous units. These contacts are typically marked by thrust faults or fractured zones that likely facilitate interactions between deep groundwater and surface waters. In Virginia, the formations involved are usually the Cambrian Shady Dolomite and the Cambrian Antietam Quartzite, while in Tennessee the equivalent units are known as the Tomstown Dolomite and Erwin Quartzite. Early authors recognized that the Shady/Tomstown dolomite was enriched in manganese (Rodgers, 1945), which has led to several hypotheses regarding it as a potential original source for manganese (Force and Cox, 1991).

While the units involved are typically the Shady/Tomstown Dolomite and Antietam/Erwin Quartzite, some exceptions are present. Within Massanutten Mountain, the Little Fort Valley Pit is located in a syncline developed in the Devonian Oriskany Sandstone and Needmore Shale/Siltstone, both of which are locally described as having calcareous zones (Rader et al., 2013). The Capola Mountain Mine near Zepp, VA is situated at the contact between the Devonian Ridgeley (Oriskany) Sandstone and Helderberg Limestones (Young et al., 2014). A roadcut along Gap Mountain north of Blacksburg, VA features manganese oxides near a contact between undivided Devonian sandstones and cherts, some of which are manganiferous, and the Devonian Millboro Formation, which features limestone beds (Prince et al., 2019). West of Gap Mountain, the Stange Mine and nearby mines feature large accumulations of manganese oxides in the Devonian Becraft Sandstone that is underlain by the residual clay of the Tonoloway Limestone (Ladd et al., 1944; Schultz et al., 1991). Other sites feature variable underlying rock, as detailed in Table 4.1. These variations demonstrate that while the involved formations are may differ, the presence of carbonate-bearing units and siliceous units is a requisite for the formation of Appalachian manganese oxide deposits. Considering the strong correlation between dolomites/limestones and manganese oxide deposits, we accept the hypothesis that the dolomites are the likely primary source of manganese while providing a model for enrichment via supergene weathering and fluid flow.

The flow of slightly acidic rain and surficial waters through carbonates is sufficient to gradually dissolve bedrock and transport manganese, as recognized by Hack (1965). Once

liberated from bedrock, dissolved manganese can persist in anoxic conditions at depth and enter groundwater flowpaths, given that pH is sufficiently low (Kiracofe et al., 2017) (Figure 4.2). If groundwater-carbonate interactions in anoxic conditions persist and sufficiently raise pH, manganese carbonate (rhodochrosite) may form. While rhodochrosite has been noted in multiple large manganese oxide accumulations (Parc et al., 1989; Varentsov, 1996), its absence in the Appalachians suggests that most, if not all, manganese remains dissolved at depth. We hypothesize that the fractured zones and faults along which most Appalachian manganese oxide deposits are found represent zones of high permeability that facilitated discharge of deep groundwater. This upwelling fosters the interaction of anoxic, Mn-rich groundwater with oxidizing surficial waters that promote the formation of manganese oxides, a hypothesis explored in detail by Kiracofe et al. (2017). In the case that any rhodochrosite did accumulate at depth, its absence at the surface could be explained by its replacement by manganese oxides upon reaching the lower pH, higher Eh conditions near the surface. Whether or not rhodochrosite formed as an intermediate protore, it is clear that surficial conditions in our field area promote the formation of manganese oxides (Hack, 1965).

These manganese oxides are subject to additional dissolution from acidic rain and surficial waters carrying organic acids followed by reprecipitation, a cycle that typically generates a sequence of mineral deposits (Carmichael et al., 2017). Parc et al. (1989) described sequences of manganese oxide minerals that formed from rhodochrosite protores in Brazil and closely resemble the mineral assemblages observed in the Appalachians (Figure 4.2). Rhodochrosite [$MnCO_3$] is initially weathered to form manganite [MnO(OH)]. Subsequent weathering in the presence of K-bearing clays – and in the Appalachians, K-bearing micas and feldspars – promotes the formation of cryptomelane [KMn_8O_{16}]. These micas and feldspars are often visible at the surface, but the dissolution of detrital K-bearing minerals from siliceous units at depth is also likely contributing K to the formation of cryptomelane breccias. Further dissolution and reprecipitation alongside Al-rich minerals such as feldspars, micas, and clays can form lithiophorite [$(Al,Li)MnO_2(OH)_2$], a commonly occurring mineral in Appalachian manganese oxide deposits. Some variations exist between this model and the minerals observed in the Appalachians, likely due to variations in parent materials and surrounding lithologies. However, the sequences of manganese oxide mineral formations described in sedimentary landscapes around the world (Parc et al., 1989; Varentsov, 1996) provide a basis for understanding the formation of Appalachian manganese oxide deposits.

4.2 Setting

4.2.1 Structural features associated with manganese oxide accumulations

Manganese oxide deposits sampled for this study were located in a variety of structural/geomorphic settings. Synclines were the most commonly sampled sites, with 10/32 mines being located either along the hinge or within the core of a syncline, most notably the Mine Bank Mine (Werner, 1965). Alluvial fans hosted numerous deposits as well, with 8/32 mines being located within an alluvial fan; however, it is worth noting that alluvial fans were typically underlain by faults, as in the case of the Kelly Bank/Dixie Mine (Werner, 1965). Hack (1965) noted the correlation between synclines, alluvial fans, and manganese oxide accumulations, hypothesizing that the cores of synclines and gravels of alluvial fans constituted mechanical traps that hindered erosion and permitted the accumulation of residuum and manganese oxides. Reverse faults without substantial alluvial cover accounted for 7/32 sites, and in some cases the faults were exposed at the surface. The Hogpen Hollow Mine is developed on a thrust fault plane, with numerous slickensides present on local rocks (Werner, 1965). Other accumulations (5/32) were developed in thrust sheets, a phenomenon that was particularly evident near Chattanooga, TN (Rodgers, 1953; Swingle et al., 1964; Wilson, 1983). Unique sites included the Gap Mountain roadcut, developed in a wind gap (Bartholomew and Mills, 1991; Prince et al., 2019) and the Stange Mine that formed along the hinge of an anticline (Ladd et al., 1944; Schultz et al., 1991). Thrust faults have been mapped discontinuously along Gap Mountain (Prince et al., 2019), though none are apparent in the immediate vicinity of the deposit. The majority of these mines are developed in residuum, with few deposits forming within bedrock.

In this study, only the following sites showed evidence of manganese oxide accumulation within bedrock: Capola Mountain Mine, VA, D.A.M. Mine, TN, Gap Mountain, VA, Hogpen Hollow Mine, VA, Larry's Place, VA, Stange Mine, VA, and TN-421 roadcut, TN. Capola Mountain Mine and Stange Mine are located along ridges, Hogpen Hollow Mine and Larry's Place are situated near deeply incised rivers, and the TN-421 roadcut and D.A.M. Mine are near low-relief valleys. Gap Mountain, on the other hand, is located near a wind gap hosting rounded gravels (Houser, 1981) that were used to interpret a former course of the New River (Bartholomew and Mills, 1991). Beyond the presence of bedrock, the one common feature between these sites is the presence of breccia and/or massive manganese oxides devoid of detrital minerals. The occurrence

of these two morphologies in association with bedrock points to their presence near the beginning of the weathering sequence.

4.2.2 Manganese oxide morphologies

Manganese oxide deposits can be characterized by the morphologies of the rocks they host, which reflect the evolution of a deposit through repeated dissolution and reprecipitation. We observed five distinct morphologies in the field: massive manganese oxides, breccias with manganese oxide matrices, manganese-coated quartzites, manganese-cemented sandstones, and botryoidal manganese oxides (also referred to as nodules) (Figure 4.3). The mineralogy and occurrence of these various deposits provide clues to their formation. The fact that breccias or massive manganese oxides are found at all bedrock sites indicates that they likely form in-place, concurring with our model that postulates initial manganese oxide formation in fractured, permeable zones. This is further supported by the mineralogical simplicity of the massive manganese oxides and breccias, which are free of detrital minerals other than quartz and typically only incorporate pure manganese oxides, indicating that they have not yet undergone dissolution and reprecipitation in the presence of weathered rock. Manganese-covered quartzites and manganese-cemented sandstones may represent different steps in the formation process or could simply reflect textural heterogeneities in the brecciated zone, while botryoidal samples (nodules) are clearly among the last to form. They have been found on the surfaces of breccias at multiple locations including the Gap Mountain roadcut and TN-421 roadcut, indicating that they post-date breccia formation. Moreover, the incorporation of abundant detrital materials, including micas, into botryoidal samples supports the notion that they form via the dissolution of brecciated material and its reprecipitation in residuum. Our model predicts that ongoing denudation will foster the generation of nodular deposits through ongoing precipitation and dissolution of other manganese oxides and their reprecipitation as nodules, as later discussed section 4.5.3.

4.3 Methods

Characterizing and dating manganese oxides has the potential to test numerous hypotheses regarding their formation and the erosional history of the Appalachian Mountains. By dating the formation of manganese oxides, we can test the hypotheses of continuous (Hack, 1965) and

discontinuous formation (King, 1949; 1950). Identifying the mineralogical and REE signatures of different manganese oxide morphologies allows us to test our model of their formation through time, and identify what elements enriched or depleted as the weathering process proceeds. Furthermore, the $^{40}Ar/^{39}Ar$ dates of manganese oxide formation from this study provide the opportunity to identify any rapidly eroding locations and evaluate the possibility of late Cenozoic uplift.

4.3.1 Sample collection

We located manganese oxide mines and prospects using geologic maps, historic publications, and the Virginia DMME database (Figure 4.4). Prior to sampling, sites were evaluated using high resolution digital elevation models (LiDAR available through the National Map website https://viewer.nationalmap.gov/basic) where possible. Emphasis was placed on sampling a broad selection of landforms, geologic structures, and elevations. Sites were primarily located within the watersheds of the Tennessee and Shenandoah Rivers, but several other watersheds of Virginia/West Virginia were also sampled to improve spatial continuity between the main study areas. In the unusual case that manganese oxides were located in bedrock, the bedrock was sampled (Figure 4.5A). When a visited site hosted appreciable manganese oxides, care was taken to collect multiple morphologies including sandstones (Figure 4.5B), breccias (Figures 4.5C, 4.5E), massive manganese oxides, Mn-covered quartzites, and botryoidal/nodular clasts (Figure 4.5F, 4.5G). Occurrence of multiple morphologies was commonly limited to larger mines. Most mines featured scattered deposits around mined zones and tailings piles (Figure 4.5D). As such, many samples lacked geologic context and may have been previously located tens of meters from their collection point.

4.3.2 $^{40}Ar/^{39}Ar$ geochronology

4.3.2.1 Theory

The formation of the K-bearing manganese oxide cryptomelane can be directly dated using K-Ar or $^{40}Ar/^{39}Ar$ geochronology, with the latter having been applied to deposits around the world for over 25 years (Vasconcelos et al., 1992; Chan et al., 2001; Jordan et al., 2007; Vasconcelos et al., 2015). Most dated deposits are interpreted as the result of deep weathering processes over

millions of years; as such, it is common to observe a spread of ages at any given site that reflects long-term processes of dissolution and reprecipitation (e.g., Vasconcelos and Carmo, 2018). Generally, the global distribution of manganese oxide ages has been linked warmer intervals (Vasconcelos, 1999; Vasconcelos et al., 2015).

All interpretations of $^{40}Ar/^{39}Ar$ data from cryptomelane and associated minerals are predicated on the assumption that the $^{40}Ar/^{39}Ar$ spectra derived from stepwise heating represent the true ages of mineralization. The pioneering work of Vasconcelos et al. (1992) addressed many concerns regarding the application of this versatile geochronometer to manganese oxides. Regarding the potential incorporation of excess Ar from groundwater during weathering, they noted that the $^{36}Ar/^{40}Ar$ intercepts of $^{36}Ar/^{40}Ar$-$^{39}Ar/^{40}Ar$ isochrons would reveal deviations from the expected atmospheric value. Regarding the presence of contaminant phases, they advised that rigorous chemical interrogation of all dated samples be performed (including optical microscopy and scanning electron microscopy) to identify potential unwanted phases. Such unwanted phases (e.g., K-bearing micas or feldspars) could yield spuriously old ages that reflected their $^{40}Ar/^{39}Ar$ ages, rather than the ages of the manganese oxide deposits.

One of the most common concerns regarding $^{40}Ar/^{39}Ar$ dating of cryptomelane is the potential for recoil of ^{39}Ar during irradiation, given the generally fine-grained nature of cryptomelane (Figure 4.6). To directly test for recoil effects, Vasconcelos et al. (1992) dated fragments of the same rock using K-Ar (which does not require irradiation) and $^{40}Ar/^{39}Ar$ geochronology. The matching ages yielded by both techniques indicated that recoil effects, if present, are minimal and do not significantly impact the calculated ages of most samples. Additional research on potential recoil has determined that it is not typically a problem when dating manganese oxides (Vasconcelos et al., 1994; Ruffet et al., 1996; Vasconcelos et al.,1996). It appears that despite its fine-grained nature, cryptomelane is relatively unaffected by recoil due to its overall high density. While recoil does occur internally, most ^{39}Ar that is displaced in the process ends up in neighboring crystals and does not exit the sample in question (Vasconcelos et al., 1994; Ren and Vasconcelos, 2019). As such, this study primarily focused on the concern of identifying contaminant minerals and ensuring that dated samples were devoid of K-bearing minerals besides cryptomelane. Contaminants that go undetected by SEM analysis can often be detected in age ideograms, which will feature multiple age peaks that are tens to hundreds of millions of years apart and have a high MSWD value.

4.3.2.2 Sampling, mineral preparation, and dating

Following collection, a 1-2 cm thick slab was cut from each sample using a water-cooled saw. The slab was then polished using a rotating polishing machine and cryptomelane-rich zones were verified visually by their characteristic bluish luster. Using a water-cooled 2.75 mm (inner diameter) diamond corer, cryptomelane-bearing zones were precisely sampled. The core was then crushed manually with a mortar and pestle to <2 mm diameter fragments. The fragments were placed in bottles with deionized water and submerged in an ultrasonic bath for up to one week. Most non-cryptomelane minerals were destroyed by the ultrasonic action, leaving behind cryptomelane and other resistant minerals including quartz or iron oxides. Each sample was then sonicated in acetone followed by ethanol for one hour each to aid in removing any additional contaminants. No acids were used in sample preparation for $^{40}Ar/^{39}Ar$ dating, as acids can partially dissolve cryptomelane and other manganese oxides (Vasconcelos, 1999). Following ultrasonic treatment, samples were rinsed, dried, and examined for purity with a low-magnification hand sample microscope. Those that contained suitable accumulations of cryptomelane/hollandite were prepared for analysis via scanning electron microscopy.

Most samples were characterized at Purdue University using FEI Quanta 3D field emission gun dual beam and/or FEI Quanta 650 field emission scanning electron microscopes equipped with backscatter electron (BSE) imaging and energy-dispersive X-Ray (EDX) spectroscopy capabilities. Several samples were also analyzed at the US Geological Survey in Reston, VA using a Hitachi SU-5000 field emission SEM with EDX capabilities. Due to their high conductivity, the samples did not require any carbon coating and were simply mounted on aluminum pins with carbon tape. Most analyzed sample fragments were 1-2 mm in diameter. In most instances, a beam current of 20 kV was employed while spot size was varied based on desired resolution. BSE imaging was performed to identify chemical homogeneity of samples and locate unwanted K-bearing minerals such as muscovite and potassium feldspar (Figures 4.6, 4.8). EDX analysis was performed on suspect minerals and at random throughout samples to identify constituent elements and characterize the bulk composition of the sample (Figures 4.7, 4.8). Samples that were sufficiently K-rich and devoid of contaminants for $^{40}Ar/^{39}Ar$ dating were submitted to collaborators at the United States Geological Survey and University of Queensland, AU for packaging, irradiation, and analysis.

Irradiation took place at the Oregon State TRIGA Reactor (OSTR) facility in Corvallis, OR. Samples received 10 megawatt-hour radiation doses and were returned to $^{40}Ar/^{39}Ar$ geochronology laboratories at the USGS Reston office and University of Queensland. $^{40}Ar/^{39}Ar$ dating at the USGS laboratory was performed using stepwise heating with a CO_2 laser. In many cases, larger samples were split into duplicates for multiple measurements. This proved useful in cases where samples yielded ambiguous age plateaus, most likely due to undetected contaminant minerals. For some samples, multiple aliquots were measured if contaminants were detected, but occasionally contamination was too substantial to yield useful dates. The results of $^{40}Ar/^{39}Ar$ dating are provided in Figure 4.9, Figure 4.10, and Table 4.2. See Appendix D for detailed methods.

4.3.3 Trace and rare-earth element analyses

We sampled 32 manganese oxides for rare-earth element, trace element, and bulk geochemical analyses, including samples from sites that were not suitable for dating with $^{40}Ar/^{39}Ar$ geochronology. Samples were photographed, characterized, and cut to ~100 g aliquots prior to analysis by Activation Laboratories, Ltd. Each sample was milled to <75 μm and underwent sodium peroxide fusion. Bulk chemistry, trace elements, and rare-earths were measured via inductively coupled plasma optical emission spectrometry (ICP-OES) and inductively coupled plasma mass spectrometry (ICP-MS). Because numerous samples contained significant quantities of relatively pure quartz, all measurements were adjusted with the assumption that all measured rare-earth and trace elements were from manganese oxides. Adjusted concentrations of REE are available in Table 4.3. Correlations of different element concentrations are available in Table 4.4. To facilitate comparisons of REE concentrations, the measured REE values were also normalized with respect to the chondrite values of Boynton (1984). Total REE concentrations for samples from each site are shown in Figure 4.11 and normalized chondrite values are plotted in Figure 4.12.

4.3.4 In-situ ^{10}Be measurements

Manganese oxide breccias hosting abundant sandstones or quartzites provide an opportunity to measure local erosion rates over ~10^4-10^5 years using ^{10}Be in quartz, providing a comparatively short-term estimate of denudation rates to compliment long-term rates from

$^{40}Ar/^{39}Ar$ ages. We selected five large breccia samples that were successfully dated with $^{40}Ar/^{39}Ar$ geochronology for erosion rate measurements. Each rock was crushed manually and placed in warm hydrochloric acid to dissolve its manganese oxide cement. Most samples required several cycles of hydrochloric acid treatment to effect complete dissolution of manganese oxides. Once the bulk quartz was retrieved, the samples underwent magnetic separation and subsequent heated leaching in a 1% nitric acid/hydrofluoric acid solution to eliminate potential meteoric ^{10}Be. A pre-chemistry assay was performed via inductively coupled plasma optical emission spectrometry (ICP-OES) to identify potential contaminants. Sufficiently pure quartz was then spiked with ~310 μg of ^{9}Be carrier and dissolved in concentrated nitric acid/hydrofluoric acid on heat. Excess titanium and iron oxides were removed by precipitation at high pH, followed by precipitation of Be hydroxide at pH ~7. The Be hydroxide was then dissolved in oxalic acid, run through cation exchange columns, and isolated. It was converted to beryllium nitrate and dried overnight via hotplate. The remaining residue was decomposed by propane torch, and the resultant Be oxides were mixed with niobium. All samples were loaded into stainless steel cathodes and delivered to PRIME Lab for AMS measurement. Beryllium measurements were performed against the standards of Nishiizumi et al. (2007).

Time-averaged local production rates of ^{10}Be in quartz for the last 10^5 years were estimated based on Lifton et al., (2014). These production rates were corrected for the influence of terrain on cosmic radiation following Li (2013). The resultant production rates were combined with the measured ^{10}Be concentrations in a Monte Carlo model that calculated 10^4 potential erosion rates based on the input parameters. The results of this model are provided in Table 4.5.

4.4 Results

4.4.1 Scanning electron microscopy – textures and compositions

Secondary electron (SE) and backscatter electron (BSE) imaging of manganese oxides prior to ultrasonic treatment provided insight into the diverse assemblages of manganese oxides located in the field area. In most instances, the purest cryptomelane/hollandite mixtures were generally found in manganese oxide-cemented breccias. They were easily identifiable in BSE mode, appearing bright in contrast with other mineralogies and often featuring acicular crystals within void spaces (Figure 4.6A). These breccias showed textural evidence of the Mn oxide

cements being secondary features, as evidenced by cryptomelane/hollandite "needles" surrounding euhedral quartz grains (Figure 4.6B). The needle-like grains eventually coalesce to form acicular grains, and occasionally both morphologies were present on the same sample (Figure 4.6C). This coalescence of extremely fine grains into dense, acicular grains may provide a mechanism for Ar retention as previously noted.

Sandstones commonly featured similar mineralogical and textural patterns to breccia, with typically homogenous cements (Figure 4.6D). SEM imaging of other non-breccias, however, typically revealed more heterogeneous mineralogies and textures. A common accessory mineral in many morphologies was lithiophorite, characterized by dark coloration in BSE relative to cryptomelane/hollandite (Figure 4.6E). Within botryoidal samples, numerous mineralogies were commonly present that complicated dating with $^{40}Ar/^{39}Ar$ techniques. Due to their incorporation of surrounding minerals, most botryoidal samples featured a range of mineralogies visible in BSE, often crosscut by cryptomelane-hollandite veins (Figure 4.6F). SE imaging of botryoidal samples revealed that layer thicknesses were highly variable but generally on the order of ~10 μm (Figures 4.6G, 4.6H).

Energy-dispersive X-Ray spectroscopy (EDX) provided critical information when evaluating samples for $^{40}Ar/^{39}Ar$ geochronology. While numerous lithologies were revealed by EDX analysis during the course of this investigation, several common types occurred frequently whose representative spectra are given in Figure 4.7. One of the most common spectra featured prominent O, Al, Si, K, and Mn peaks (Figure 4.7A), which was commonly interpreted to represent a manganese oxide containing detrital aluminosilicates. BSE verification of contaminant lithologies usually confirmed the presence of micas and/or feldspars in such samples, which were deemed ineligible for geochronology. Nearly all morphologies also incorporated the most basic manganese oxide, pyrolusite [MnO_2], as revealed by well-defined peaks for O and Mn (Figure 4.7B). A less ubiquitous, yet common, accessory mineral was lithiophorite (Figure 4.7C). In addition to its BSE-dark appearance, it could easily be identified in EDX spectra by characteristic peaks of O, Al, and Mn. Very rarely, other elemental spectra – such as Co – appeared alongside these peaks. For geochronology purposes, pure cryptomelane could be readily identified by peaks for O, K, and Mn (Figure 4.7D). More frequently, samples with mixtures of cryptomelane, hollandite, and lithiophorite were identified in EDX (Figure 4.7E). These samples, when devoid of K-bearing contaminants such as micas or feldspars, were also deemed dateable. The only

exception was the pure hollandite, as evidenced only by O, Ba, and Mn peaks (Figure 4.7F). Because measurable K is necessary for $^{40}Ar/^{39}Ar$ dating, pure hollandite samples were excluded.

These examples of manganese oxide textures and compositions represent a small, yet representative fraction of the data collected during sample preparation and analysis. Hundreds of SE/BSE images and thousands of EDX analyses were collected during the characterization of these samples from 2017-2020, and these results reflect the broad patterns observed during this process. BSE images of each sample dated using $^{40}Ar/^{39}Ar$ geochronology are provided in Figure 4.8.

4.4.2 $^{40}Ar/^{39}Ar$ geochronology

Gap Mountain exposure

Two separate aliquots of a breccia (12-11-17A) with variable Pb content from the Gap Mountain roadcut were dated. Both aliquots primarily consisted of cryptomelane breccia cement, with trace pyrolusite but no detectable hollandite. The most robust data were obtained from a Pb-free aliquot, which featured an integrated age of 8.1 ± 0.6 Ma and a plateau age of 8.0 ± 0.3 Ma (MSWD = 0.47). Its $^{36}Ar/^{40}Ar$-$^{39}Ar/^{40}Ar$ isochron had an intercept of 296 ± 7, consistent with no incorporation of excess Ar during formation, and its ideogram age featured one prominent age peak at 7.9 ± 0.3 Ma (MSWD = 1.28).

An aliquot that showed trace Pb contents on 4/10 EDX spectra yielded an integrated age of 7.9 ± 0.9 Ma and a forced plateau age of 9.0 ± 1.0 Ma (MSWD = 4.90). Its ideogram age shows a broad age distribution at 9 ± 4 Ma (MSWD = 18.88), indicating a poorly constrained age. While the $^{36}Ar/^{40}Ar$-$^{39}Ar/^{40}Ar$ isochron had a less constrained intercept than the Pb-free sample at 300 ± 20, it implies that negligible Ar contamination – if any – has occurred. It appears likely that the uncertainty in this measurement was due to the presence of minor quartz in the dated sample and/or minor contamination by Pb. The plateau age gleaned from the Pb-free sample was taken as the true age of the cryptomelane at Gap Mountain.

Kendall-Flick Mine

Two aliquots of a vein extracted from a botryoidal sample (12-18-17C) were dated, with varying levels of purity. Both samples primarily consisted of cryptomelane. One sample contained micaceous minerals, as confirmed by BSE imaging and EDX analysis that revealed Mg, Al, and Si in addition to the constituent elements of cryptomelane. That aliquot featured a saddle-

shaped plateau and yielded an integrated age of 25.09 ± 0.18 Ma. It was difficult to evaluate for potential Ar contamination on the $^{36}Ar/^{40}Ar$-$^{39}Ar/^{40}Ar$ isochron given its imprecise intercept of 1800 ± 2000 (MSWD = 1100). The ideogram age featured numerous discrete peaks indicative of contamination as suspected from BSE analysis; the presence of ages extending back to 220 Ma is consistent with the incorporation of older Appalachian grains.

The second aliquot was almost entirely pure cryptomelane, with 2/10 EDX spectra also showing trace Na, Si, and Cl. It yielded a slightly flatter spectrum, with an integrated age of 18.51 ± 0.14 Ma. The $^{36}Ar/^{40}Ar$-$^{39}Ar/^{40}Ar$ isochron again yielded a vague intercept of 600 ± 300; as such, it is difficult to evaluate whether Ar contamination occurred in this aliquot. The numerous age peaks in the sample's ideogram span the Cenozoic suggest contamination by other mineral phases, while exposed acicular cryptomelane (Figure 4.8D) raises the possibility of recoil. Given these poor results, no plateau ages were interpreted for either aliquot. We estimate a minimum age of ~13 Ma for the cryptomelane in this sample as that represents the base of the "saddle" formed by stepwise heating of these fragments.

Mine Bank Mine

One fragment of a Mn-cemented breccia (02-12-18D) was dated for the Mine Bank Mine. The sample primarily consisted of cryptomelane, with trace amounts of lithiophorite inferred from the presence of Al in some EDX spectra. Stepwise heating yielded an integrated age of 8.7 ± 0.4 Ma and a plateau age of 8.74 ± 0.13 Ma (MSWD = 0.94). Its $^{36}Ar/^{40}Ar$-$^{39}Ar/^{40}Ar$ isochron had an intercept of 299 ± 5, consistent with no incorporation of excess Ar during formation. Its ideogram plot yielded an age of 8.6 ± 0.4 M (MSWD = 2.18), consistent with the integrated and plateau ages. The plateau age was taken to be the true age of the sample.

Fork Ridge Mine

One fragment of an Mn-cemented breccia (02-16-18A) was dated for the Fork Ridge Mine. It consisted largely of cryptomelane, with minor hollandite inferred from Ba peaks on several EDX spectra. BSE and EDX analysis revealed minor SiO_2. The sample yielded an integrated age of 28.8 ± 0.3 Ma and a plateau age of 30.38 ± 0.17 Ma (MSWD = 0.34). Its $^{36}Ar/^{40}Ar$-$^{39}Ar/^{40}Ar$ isochron featured a low intercept of 246 ±11. The ideogram for the sample yields one prominent

peak at 30.1 Ma, and a minor peak at ~18 Ma. Given the excellent fit of the plateau age, we interpreted 30.38 ± 0.17 Ma as the formation age of this sample.

Big Levels Mine #1

One breccia sample from Big Levels Mine #1 (05-21-18B-1) was dated. SEM analysis revealed a cryptomelane-dominated cement with minor hollandite; trace lithiophorite was inferred from Al peaks on several EDX spectra. Minor Fe-oxides and SiO_2 grains were also present in the sample. It yielded an integrated age of 29.9 ± 0.2 Ma and a plateau age of 31.6 ± 0.3 Ma (MSWD = 0.94). The $^{36}Ar/^{40}Ar$-$^{39}Ar/^{40}Ar$ isochron yielded an ambiguous intercept of 300 ± 200. The sample's ideogram featured a broad peak at 30 ± 2 Ma (MSWD = 53.72) that generally corresponds with the interpreted plateau age. Its plateau age was taken to be the sample's true age.

Adams Peak Mine

A single breccia sample from the Adams Peak Mine (09-24-18B-1) was dated. The Mn oxide cement was comprised of roughly equivalent parts cryptomelane and hollandite. As one of the older deposits in this study, it yielded an integrated age of 37.7 ± 1.0 Ma and a plateau age of 39.6 ± 0.5 Ma (MSWD = 2.59). This slightly high MSWD may be due to trace quartz within the sample. Its $^{36}Ar/^{40}Ar$-$^{39}Ar/^{40}Ar$ isochron was consistent with no Ar contamination during formation, with an intercept of 293 ± 12. The ideogram age was predominantly bimodal, with peaks at ~33 and ~39 Ma. Given the acceptable fit of the plateau age, it was taken as the sample's formation age.

Hogpen Hollow Mine

Two samples from a single hand sample of Mn oxide-cemented breccia (09-25-18A-2 and 09-25-18A-3) were dated for the Hogpen Hollow Mine. The 09-25-18A-2 sample contained abundant cryptomelane with minor amounts of lithiophorite (inferred from Al peaks) and hollandite. Trace amounts of P were also present in the sample. Sample 09-25-18A-2 yielded an integrated age of 21.5 ± 0.3 Ma and a forced plateau age of 22.1 ± 0.5 Ma (MSWD = 27.58). Its $^{36}Ar/^{40}Ar$-$^{39}Ar/^{40}Ar$ isochron had an intercept of 288 ± 15, indicating no significant Ar excess. The ideogram showed broad peaks from 0-18 Ma and four sharp peaks from 20-24 Ma. These scattered ages may be the consequence of the sample's multiphase mineralogy. Sample 09-25-18A-3 also

yielded a predominantly cryptomelane matrix with some lithiophorite and trace P; however, no hollandite was detected during EDX analyses. The sample was split into two fragments that were analyzed separately.

Sample 09-25-18A-3 (1/2) yielded an integrated age of 21.7 ± 0.2 Ma and a vastly improved plateau age of 22.14 ± 0.12 Ma (MSWD = 0.93). It featured an $^{36}Ar/^{40}Ar$-$^{39}Ar/^{40}Ar$ isochron intercept of 286 ± 11, consistent with little or no excess Ar. The sample's ideogram showed two minor peaks and one major peak at 21.9 ± 0.6 Ma, consistent with the plateau age. Sample 09-25-18A-3 (2/2) yielded an integrated age of 25.6 ± 0.8 Ma and a plateau age of 24.6 ± 0.6 Ma (MSWD = 2.07). Its $^{36}Ar/^{40}Ar$-$^{39}Ar/^{40}Ar$ isochron had an intercept of 500 ± 200; as such, it is possible that the sample features excess Ar. The ideogram for this sample featured a high peak at 25 ± 2 Ma, consistent with the plateau age, and minor peaks before the Cenozoic. These peaks likely reflect trace micas that were incorporated during formation; however, the plateau age is satisfactory and likely represents cryptomelane formation. As such, the two fractions of 09-25-18A-3 demonstrate ongoing weathering during the Early Miocene in the Shenandoah Valley.

Kelly Bank/Dixie Mine

Several samples of Mn oxide-cemented breccias (09-25-18D-2, 09-25-18D-3, 11-08-18A-1, 11-08-18A-S2 (1/2), and 11-08-18A-S2 (2/2)) were dated from the Kelly Bank/Dixie Mine. Sample 09-25-18D-2 consisted of mostly cryptomelane with trace amounts of hollandite and lithiophorite, as inferred from Ba and Al peaks on several EDX spectra. It yielded an integrated age of 15.79 ± 0.20 Ma and a forced plateau age of 15.9 ± 0.7 Ma (MSWD = 69.31). The sample's $^{36}Ar/^{40}Ar$-$^{39}Ar/^{40}Ar$ isochron had an intercept of 310 ± 30, consistent with little or no excess Ar at formation. Its ideogram featured numerous peaks between 10-25 Ma, potentially reflecting minor contributions from multiple phases of cryptomelane or perhaps recoil effects due to hidden microstructures.

A second fragment from the same hand sample, 09-25-18D-3, had analytically similar mineralogy but yielded more robust age data. It featured an integrated age of 15.2 ± 0.6 Ma and a plateau age of 15.1 ± 0.4 Ma (MSWD = 1.33). As with the previous sample, its $^{36}Ar/^{40}Ar$-$^{39}Ar/^{40}Ar$ isochron had an intercept (300 ± 30) that did not necessitate excess Ar. Its ideogram featured a minor peak near 12 Ma and one major peak at 15 ± 3 Ma, consistent with the plateau and integrated ages.

Sample 11-08-18A-1 was analytically pure cryptomelane cement with substantial amounts of SiO_2 incorporated into the matrix. Despite the excellent quality of the cement, it yielded no plateau age. The integrated age was 137.6 ± 1.7 Ma. Its $^{36}Ar/^{40}Ar$-$^{39}Ar/^{40}Ar$ isochron had an intercept of 300 ± 140 (MSWD = 750), providing no clear information regarding initial Ar. The ideogram plot featured a range of ages extending back to the Devonian, suggesting that detrital K-bearing minerals were incorporated into the sample and not detected during SEM/EDX analysis.

Sample 11-08-18A-S2 (1/2) contained equal parts cryptomelane and hollandite, with minor amounts of lithiophorite (inferred from Al peaks in EDX spectra) and SiO_2 fragments. It yielded an integrated age of 60.1 ± 0.6 Ma, with an apparent minimum age near 40 Ma. No plateau age was interpretable. Its $^{36}Ar/^{40}Ar$-$^{39}Ar/^{40}Ar$ isochron had an intercept of 1600 ± 1700, consistent with potential incorporation of excess Ar during formation. Its ideogram yielded a poorly constrained age of 50 ± 20 Ma (MSWD = 1771.79).

Given this unsatisfactory result, a duplicate of the sample (11-08-18A-S2 (2/2) was also dated. It contained identical mineralogies and was run at smaller laser power steps to aid in plateau identification. It yielded an integrated age of 54.9 ± 0.4 Ma, but no satisfactory plateau age could be interpreted. Its $^{36}Ar/^{40}Ar$-$^{39}Ar/^{40}Ar$ isochron had an intercept of 2000 ± 3000, consistent with potential incorporation of excess Ar during formation. Its ideogram yielded a very poorly constrained age of 40 ± 20 Ma (MSWD = 8782.61). Inferring that K-rich micas or other unidentified minerals were present beneath the grain surfaces of this sample, we inferred a maximum age of ~32 Ma for these manganese oxide phases based on the saddle-shaped heating spectra.

Capola Mountain Mine

Six aliquots of Mn oxide-cemented breccias (11-09-18D-S1-1, 11-09-18D-S2-3 (1/2), 11-09-18D-S2-3 (2/2), 11-09-18F-1 (1/2), 11-09-18F-1 (2/2), and 11-09-18F-3) were dated from the Capola Mountain Mine. Sample 11-09-18D-S1-1 consisted of coarse sandstone grains (likely of the Oriskany Sandstone) suspended in a cryptomelane-hollandite matrix. It yielded a slightly saddle-shaped age spectrum with an integrated age of 221 ± 13 Ma and no discernible plateau age. The sample's $^{36}Ar/^{40}Ar$-$^{39}Ar/^{40}Ar$ isochron featured an intercept of 380 ± 70, indicated potential excess Ar. Significantly, the ideogram reveals numerous age peaks from 0-600 Ma and a broad

peak near 1500 Ma. It appears highly likely that detrital minerals from the underlying bedrock were incorporated into this deposit.

Sample 11-09-18D-S2-3 primarily consisted of hollandite, with minor amounts of cryptomelane and trace lithiophorite inferred from Al peaks on EDX analyses. The first aliquot, 11-09-18D-S2-3 (1/2), yielded an integrated age of 40 ± 6 Ma and a forced plateau age of 33 ± 2 Ma (MSWD = 7.18) due to its low radiogenic yield. Its $^{36}Ar/^{40}Ar$-$^{39}Ar/^{40}Ar$ isochron had an intercept of 304 ± 5, consistent with little to no excess Ar. The ideogram age was generally unimodal with a minor peak; the overall ideogram age was 33 ± 5 Ma (MSWD = 7.23). Given the presence of abundant voids and exposed acicular cryptomelane in this sample (see Figure 4.8P), it is possible that it was affected by substantial recoil during irradiation.

The second aliquot of the sample, 11-09-18D-S2-3 (2/2), was of similar mineralogy and yielded more problematic results. Its integrated age was 102 ± 12 Ma; no plateau age could be interpreted. The sample's $^{36}Ar/^{40}Ar$-$^{39}Ar/^{40}Ar$ isochron intercept was 303 ± 16, indicating little to no excess Ar. However, the ideogram featured four broad peaks ranging from the Miocene to Early Mesozoic. It appears likely that, in addition to possible recoil, this fragment hosted older Appalachian minerals – likely micas – that contributed to the older ages.

Sample 11-09-18F-1 (1/2) consisted of hollandite-dominated cement with some cryptomelane and yielded an integrated age of 33.5 ± 1.0 Ma. No valid plateau could be interpreted. Its $^{36}Ar/^{40}Ar$-$^{39}Ar/^{40}Ar$ isochron had an intercept of 310 ± 70, showing poor precision and inconclusive data regarding potential incorporation of excess Ar during formation. Its ideogram yielded a poorly constrained age of 37 ± 13 Ma (MSWD = 150.34).

Given this result, a second fragment 11-09-18F-1 (2/2) was analyzed. It was mineralogically identical to the first and but was run at smaller laser power steps. It yielded an integrated age of 33.6 ± 1.0 Ma, but no interpretable plateau age. Its $^{36}Ar/^{40}Ar$-$^{39}Ar/^{40}Ar$ isochron had a similarly loosely constrained intercept of 300 ± 40, hindering our ability to detect potential excess Ar. Its ideogram also yielded a poorly constrained age of 38 ± 11 My (MSWD = 88.1). The scattered ages do not appear to be due to older K-bearing minerals given their Cenozoic range. Rather, it appears that both fragments of 11-09-18F-1 yielded poorly defined ages due to the relative dominance of hollandite and low K concentrations. Moreover, the presence of exposed acicular cryptomelane (Figure 4.8Q) indicates that recoil may have influenced the results for both fragments.

An additional fragment (11-09-18F-3) from the same hand sample as the above aliquots was also dated. It consisted of a hollandite-dominated matrix containing minor amounts of cryptomelane and hollandite; however, EDX spectra also revealed trace amounts of Co in the sample. Despite this heterogeneity, it yielded a preferable age to the aforementioned 11-09-18F-1 samples. The sample had an integrated age of 38.9 ± 0.6 Ma and a forced plateau age of 40.3 ± 0.9 Ma (MSWD = 13.51). Its $^{36}Ar/^{40}Ar$-$^{39}Ar/^{40}Ar$ isochron had an intercept of 291 ± 11, consistent with little or no excess Ar. The ideogram featured multiple peaks between 35-45 Ma, again likely due to the intermingling phases of hollandite/cryptomelane and corresponding low K content.

Larry's Place (top)

Two breccia samples with slightly varying compositions (11-09-18J-2 and 11-09-18J-3) were dated from a single hand sample collected at Larry's Place. Sample 11-09-18J-2 consisted of equal parts cryptomelane and hollandite, with minor amounts of lithiophorite and SiO_2 incorporated into the matrix. It yielded an integrated age of 51.9 ± 0.4 Ma and a plateau age of 43.90 ± 0.19 Ma (MSWD = 0.70). The $^{36}Ar/^{40}Ar$-$^{39}Ar/^{40}Ar$ isochron had a loosely constrained intercept of 440 ± 90, indicating – but not necessitating – that some excess Ar may have been incorporated during formation. Its ideogram featured numerous ages > 100 Ma, extending as far back as the Proterozoic, indicative of the incorporation of detrital minerals from local bedrock.

Sample 11-09-18J-3 also contained equal parts cryptomelane and hollandite, but no detectable lithiophorite. It yielded an integrated age of 48.0 ± 0.4 Ma, but no plateau age could be interpreted. The minimum age step was ~42.3 Ma. Its $^{36}Ar/^{40}Ar$-$^{39}Ar/^{40}Ar$ isochron yielded an intercept of 450 ± 120, leaving open the possibility of excess Ar. The ideogram showed ages ranging from 45 Ma to >340 Ma, again implying the presence of detrital minerals from the Appalachian bedrock.

4.4.3 Bulk geochemistry and rare-earth elements

Trace and rare-earth element analysis of 32 samples revealed trends in the geochemical content of different manganese oxide morphologies. While these data do not typically reveal unambiguous information about the genesis of manganese oxides (Varentsov, 1996; Carmichael et al., 2017), they do provide useful clues regarding the origin of various morphologies and potential weathering sequences. All morphologies had generally poor correlations between Mg

and La, Tm, and Lu, consistent with a nonmarine origin (Franceschelli et al., 1996). Total REE content varied from 26-3967 ppm (Figure 4.11), with mean REE contents being higher in nodules (948 ppm) than sandstones (641 ppm), breccias (430 ppm, excluding one outlier), quartzites (383 ppm), or massive manganese oxides (92 ppm). The general slope of the chondrite normalized REE concentrations reveals the progressive enrichment of lighter rare-earth elements in supergene deposits (Figure 4.12). The most uniform concentrations belong to the massive deposits, which feature nearly uniform concentrations of light and heavy REE. Sandstones are slightly more enriched in light REEs, followed by breccias and subsequently quartzites. Enrichment of light REEs is most significant in the nodular deposits, supporting the potential sequence of weathering and reprecipitation that initiates with the dissolution of massive manganese oxides and quartz-rich manganese oxides and terminates with the precipitation of nodular deposits. Nodules also feature relatively high Ce anomalies when normalized to the chondrite values of Boynton (1984), which Feng (2010) associated with chemical weathering of carbonates. The nodules also feature strong correlations between Al and Ti, Nb, Sn, Ta, Hf, and Th content which Franceschelli et al. (1996) associated with the incorporation of detrital material into manganese oxides (Table 4.4). This detrital nature, along with the overall enrichment of REE and particularly high Ce contents of the nodular deposits, supports the hypothesis that they formed in a near-surface environment through the weathering, dissolution, and reprecipitation of older manganese oxide deposits.

The source of the initial accumulations of manganese oxides – namely those in breccias and massive deposits – is less clear. Our trace element and REE measurements provide some evidence that those deposits may be hydrothermal in nature (Table 4.4). The As/Zr ratio exceeds the typical value of ~0.601 for dolomite for 6/13 measured breccias and 5/5 measured massive deposits, indicating a potential hydrothermal source (Varentsov, 1996). In contrast, none of the nodular deposits featured As/Zr ratios that exceeded 0.601. Furthermore, 6/13 breccias and 2/5 massive deposits had hydrothermal-range Eu/Sm ratios above the typical value for dolomite (~0.601) in contrast with only 1/8 measured nodules (Varentsov, 1996). These data are further supported by the minimal Ce enrichment of non-nodular deposits and poor evidence for detrital components, as demonstrated by SEM imaging and the poor correlations of Al with Ti, Nb, Sn, Ta, Hf, and Th. However, it should be noted that the correlation between Mn and As, inferred by Nicholson (1992) as a marker for hydrothermal activity, is generally poor for all morphologies. It

is evident, however, that the breccias and massive manganese oxides do not have a detrital origin and that their formation or diagenesis may have hydrothermal components.

4.4.4 Erosion rates from ^{10}Be in quartz

Modern erosion rates derived from ^{10}Be in quartz-bearing manganese oxides varied widely between locations. The two locations where samples were collected directly from exposed bedrock, Capola Mountain Mine and Larry's Place, are taken to yield the most reliable erosion rates. The sample at Capola Mountain Mine yielded a modern erosion rate of 11.9 $^{+0.4}/_{-0.4}$ m/My, consistent with some modern catchment-averaged erosion rates measured by Duxbury et al. (2015) on the eastern edge of the Shenandoah Valley. Along the main branch of the Shenandoah River, the local bedrock erosion rate at Larry's Place is 41.9 $^{+1.7}/_{-1.8}$ m/My. This value exceeds our estimate for the river's average incision rate of 23-26 My since ~0.9 My, based on a tentative isochron age for the nearby Tilthammer Mill Road terrace (Chapter 3, this thesis).

The remaining erosion rates were derived from scattered samples with unknown exposure histories, and so they represent maximum erosion rates due to the likelihood that they were originally buried below the ground surface. At the Fork Ridge Mine, the local erosion rate was 43.4 $^{+2.3}/_{-2.2}$ m/My. The nearby Gap Mountain roadcut yielded a local erosion rate of 50.2 $^{+2.5}/_{-2.3}$ m/My. In the southern Shenandoah Valley, the Hogpen Hollow Mine featured a significantly higher erosion rate of 66.5 $^{+3.2}/_{-3.1}$ m/My. These relatively high erosion rates compared to those derived from nearby detrital measurements (e.g., Duxbury et al., 2015) suggest that the low ^{10}Be concentrations measured may reflect burial prior to excavation by manganese mining operations. The shielding provided by soil and dense manganese oxides would have attenuated cosmic radiation at depth, yielding falsely high erosion rates for samples that were presumed to have been at the surface but were actually recently mined. The immense contrast between erosion rates from in-place bedrock samples and scattered samples highlights potential pitfalls of using individual clasts with poorly constrained exposure histories to measure local erosion rates.

4.5 Discussion

Our SEM characterizations and geochemical analyses have shown that manganese oxide deposits frequently host diverse assemblages of mineralogies and morphologies that reflect long-

term processes of dissolution and reprecipitation. This process appears to begin with the formation of massive manganese oxides and breccias, commonly with low REE concentrations and minimal detrital components, that undergo chemical weathering and are reprecipitated as REE-enriched sandstones and nodules. Given that the age ranges between samples at any given location can vary by several million years, the presence of multiple generations of manganese deposits at a site implies that extensive chemical weathering (and minimal denudation) likely occurred at that site since the deposits formed. It follows, then, the manganese oxide deposits scattered throughout the Appalachian Mountains indeed represent remnants of former low-relief, gradually eroding surfaces.

4.5.1 $^{40}Ar/^{39}Ar$ dating considerations

Efforts to date these surfaces were largely successful, but careful consideration of the $^{40}Ar/^{39}Ar$ data reveals potentially problematic Ar contents in some samples. The $^{40}Ar/^{36}Ar$ intercepts of $^{36}Ar/^{40}Ar$-$^{39}Ar/^{40}Ar$ isochrons occasionally exceeded the expected atmospheric value of 298.56 ± 0.17 (Lee et al., 2006), indicating that excess Ar may have been incorporated during the precipitation of the dated phases (Vasconcelos et al., 1992). Eight samples featured intercepts that did not agree within one standard deviation of analytical uncertainty, though five of those were minor differences (~1). Three samples, 11-09-18D-S1-1 from Capola Mountain Mine, 11-09-18J-2 from Larry's Place, and 11-09-18J-3 from Larry's Place, yielded intercepts that far exceeded the expected value. Out of those samples, only 11-09-18J-2 yielded a valid plateau age. All of these samples showed unexpectedly old ages consistent with incorporation of pre-Cenozoic Appalachian detritus, and thus their ages likely represent maximum bounds on the ages of manganese oxides.

The often-multiphasic nature of manganese oxides renders them potentially susceptible to recoil effects during irradiation. Work by Vasconcelos et al. (1994) implied that recoil can occur within pure cryptomelane samples but displaced ^{39}Ar is typically trapped interstitially, rather than ejected from the sample. However, the potential for recoil due to microstructures (Reiners et al, 2018) remains. We identified potential recoil in sample 11-9-18D-S2-3(1/2), which featured a forced plateau age of 33 ± 2 Ma (MSWD = 7.18). The dated sample appeared sufficiently mineralogically pure for geochronology, but close inspection of its mineral structures via SEM revealed zones of exposed acicular cryptomelane (Figure 4.8P). It is possible that these

microstructures dispersed across the sample led to measurable recoil effects, and similar hidden structures may be responsible for age discrepancies in other samples. In particular, samples 11-09-18F-1 (Capola Mountain Mine) and 12-18-17C (Kendall-Flick Mine) also featured zones of exposed acicular cryptomelane that could have enhanced recoil effects (Figures 4.8D, 4.8Q). These results highlight the importance of rigorous SEM characterization and suggest that samples featuring zones of exposed cryptomelane "needles" are less suitable for dating than those with uniform textures.

Despite rigorous visual, SEM, and EDX analyses prior to irradiation and $^{40}Ar/^{39}Ar$ dating, several samples also showed evidence of contaminant phases that skewed age distributions. This problem was particularly severe at the Kelly Bank/Dixie Mine, for which 3/5 age ideograms (samples 11-8-18A-1, 11-8-18A-S2 (1/2), and 11-8-18A-S2 (2/2)) showed numerous age peaks that extended from the Cenozoic through the Proterozoic. It appears likely that these samples, despite being apparently contaminant-free cryptomelane-hollandite/lithiophorite breccias, hosted bedrock minerals that skewed their age distributions. These minerals were likely obscured beneath the surfaces of the analyzed grains and thus evaded detection during SEM/EDX characterization. At the Capola Mountain Mine, 2/6 samples (11-9-18D-S1-1 and 11-9-18D-S2-3(2/2)) showed strong evidence of contamination, as inferred from Cenozoic through Proterozoic age peaks on their age ideograms. It is also possible that sample 11-9-18J-3 from Larry's Place, in addition to hosting excess Ar, may have contained some contaminant minerals as evidenced by minor age ideogram peaks ca. 100 Ma, 215 Ma, and 345 Ma.

These problematic age spectra are difficult to avoid, particularly when dating such fine-grained and mineralogically complex materials such as manganese oxides. However, they highlight the utility of stepwise heating, $^{36}Ar/^{40}Ar$-$^{39}Ar/^{40}Ar$ isochrons, and age ideograms to interpret the reliability of $^{40}Ar/^{39}Ar$ age data. Furthermore, the frequency of contamination by pre-Cenozoic detritus demonstrates that while REE data indicate detrital material is primarily incorporated into nodules, small yet significant amounts of detritus are commonly found in breccias as well. By identifying the age distributions and stepwise heating spectra associated with these contaminants, it is possible to refine our dataset of $^{40}Ar/^{39}Ar$ ages that truly reflect the formation of cryptomelane-hollandite phases through chemical weathering.

The viable plateau ages from our dataset span most of the Cenozoic, with younger samples yielding more viable spectra as indicated by robust plateau ages and concurring replicate ages. Of

the fourteen plateau ages calculated, three were Eocene, four were Oligocene, and seven were Miocene. As has been noted with iron oxide geochronology (Odom et al., 2020), it is conceivable that the dataset is biased toward younger samples due to ongoing dissolution and reprecipitation processes destroying older materials. However, it is also worth noting that the deposits dated by Doctor et al. (2018) in Virginia and Tennessee were all Eocene in age, so the presence or lack of a survivorship bias is difficult to evaluate. The existing age spectra from this study show little correlation with temperature, in contrast with the general global correlations noted by Vasconcelos (1999) and Vasconcelos et al. (2015) (Figure 4.10). Globally, manganese oxide ages are regularly distributed across warmer and colder intervals of the Cenozoic, with the exception of the Pliocene and Pleistocene. Given that the last 5 Ma were cooler than the preceding periods of the Cenozoic (Zachos et al., 2001), it is conceivable that the Plio-Pleistocene Appalachians were too cold to maintain the extended chemical weathering processes required to form appreciable manganese oxide deposits.

4.5.2 Evidence for prolonged chemical weathering

Within individual mines, we observed variable $^{40}Ar/^{39}Ar$ ages that reflected the precipitation, dissolution, and reprecipitation of manganese oxides during prolonged chemical weathering. At the Hogpen Hollow Mine, one hand sample yielded three plateau ages that ranged from 22.1 ± 0.5 Ma to 24.6 ± 0.6 Ma, a maximum 1σ span of 3.6 Ma. While the Kelly Bank/Dixie Mine samples yielded few plateau ages, one hand sample produced two plateau ages of 15.9 ± 0.7 Ma and 15.1 ± 0.4 Ma, a maximum 1σ age span of 1.9 Ma. These variations between ages within individual samples highlight the fact that $^{40}Ar/^{39}Ar$ geochronology applied to manganese oxides can yield numerous ages due to the heterogeneity induced by partial dissolution and reprecipitation of deposits over millions of years. As such, it is generally advisable to date numerous samples per location to produce a suite of ages, as illustrated by Vasconcelos and Carmo (2018). In practice, locating dateable cryptomelane can be extremely challenging and was a limiting factor in this study.

Dating multiple in-place samples from vertical transects of bedrock outcrops permits additional constraints on weathering by directly dating the downward progression of manganese oxide formation. Our samples from the outcrop at Larry's Place only yielded one plateau age (43.9 ± 0.19 Ma), but prior geochronology from Doctor et al. (2018) showed that the deposit hosted materials as young as 37.3 ± 0.5 Ma, a potential 1σ span of 7.29 Ma. Given that the samples

collected by Doctor et al. (2018) were located approximately 5 m below our sample location, the local downward propagation of Eocene weathering occurred at approximately 0.8 m/My. The presence of iron oxides at the top of the outcrop precluded a complete transect of $^{40}Ar/^{39}Ar$ ages but demonstrated the formation of a chemically stratified weathering profile. Similarly, two separate hand samples taken from the Capola Mountain Mine provided longer-term evidence of this trend and illustrated the downward progression of the weathering front responsible for manganese oxide formation. Sample 11-09-18F-3 was taken from bedrock at the top of a ~10 m high outcrop and yielded a forced plateau age of 40.3 ± 0.9 Ma. In contrast, sample 11-09-18D-S2-3 (1/2) was collected from the base of the outcrop and yielded a forced plateau age of 33 ± 2 Ma. While the variable age ranges within hand samples at other sites only varied 2-4 Ma at most, these samples have a potential 1σ age difference of 10.2 Ma. As such, it appears that these ages reflect the downward progression of an Eocene weathering front that occurred at an approximate rate of 1.4 m/My.

4.5.3 Geomorphological insights

4.5.3.1 Denudation and incision

The longevity of supergene manganese oxide deposits has profound implications for the landscape stability of the Cenozoic Appalachians. Given that manganese oxides typically form within ~100 meters of the surface (Hewett, 1916), their $^{40}Ar/^{39}Ar$ ages may be used to approximate maximum local denudation rates since their formation (Figure 4.13). We calculated maximum denudation rates for all samples with plateau ages using the formula:

$$D_{max} = \frac{100\ m}{t}$$

Where t is the $^{40}Ar/^{39}Ar$ plateau age. The resultant values ranged from 2.3 ± 0.1 m/My at Larry's Place to 12.5 ± 0.5 m/My at the Gap Mountain Roadcut, with an average value of 5.6 m/My (Table 4.6) (Figure 4.14). This rate is similar to modern basin-averaged erosion rates in the nearby New River watershed (Granger et al., 1997) as well as modern basin-averaged erosion rates in many parts of the Shenandoah Valley (Duxbury et al., 2015). The consistency between modern basin-averaged erosion rates and our long-term denudation rate estimates from the Miocene through Eocene demonstrates that the Appalachian Mountains of Virginia have been gradually eroding since at least the middle Eocene.

These estimates of denudation may be further contextualized by considering their relation to the nearby streams and rivers driving landscape evolution. Assuming that manganese oxides generally form at or below the level of nearby rivers and again inferring a maximum formation depth of 100 m, we can place broad constraints on the incision rates of Appalachian rivers over tens of millions of years (Figure 4.13). Minimum incision rates may be estimated by assuming that manganese oxides formed near the surface, at river level. Maximum incision rates, on the other hand, can be inferred by assuming that formation occurred at 100 m below the surface. These approximations were calculated using the formulae:

$$I_{min} = \frac{\text{m arl}}{t} \qquad I_{max} = \frac{100\text{ m} + \text{m arl}}{t}$$

Where m arl is the deposit's modern elevation above river level. Minimum river incision rates ranged from 1.6 ± 0.1 m/My at Capola Mountain Mine to 11.8 ± 0.2 m/My at Mine Bank Mine, while maximum river incision rates varied from 4.0 ± 0.1 m/My at Capola Mountain Mine to 41.1 ± 1.5 m/My at the Gap Mountain Roadcut (Table 4.6) (Figure 4.14). These incision rates demonstrate that while rapid incision has occurred along Appalachian rivers during the Pleistocene (e.g., Anthony and Granger, 2006; Granger et al., 1997; Granger et al., 2001; Chapters 2 and 3, this thesis) the average Cenozoic incision rates in this area have remained gradual.

4.5.3.2 Neogene river incision and topographic rejuvenation in the Appalachians

Arguments put forth for Neogene topographic rejuvenation necessitate that hundreds of meters of river incision occurred during the Miocene. This has been hypothesized for the Cullasaja River basin southwest of Shenandoah Valley (Gallen et al., 2013) and the Susquehanna River basin north of Shenandoah Valley (Miller et al., 2013). It follows, then, that the Shenandoah River basin would be correspondingly affected by any significant topographic rejuvenation of the southern and central Appalachians. The preservation of supergene deposits since the Miocene, Oligocene, and even Eocene provides a compelling argument that erosion rates remained minimal during this time of hypothesized uplift. Given that local maximum denudation rates do not exceed 5 m/My at nearly all dated locations and that most maximum river incision rates are correspondingly low, it is evident that the Appalachians have remained tectonically quiescent throughout most, if not all of the Cenozoic. Despite this quiescence, substantial incision has nonetheless occurred along numerous rivers throughout the region, namely the New River and the St. Marys River.

4.5.3.3 Gap Mountain and the New River

The formation ages and ranges of potential incision rates derived from the manganese oxide deposits at Gap Mountain complement existing studies that examined the behavior of the New River during the late Neogene. Houser (1981) initially interpreted rounded gravels located atop Gap Mountain, near the manganese oxide deposits, as remnants of a former tributary of the New River that dated to the late Cenozoic. Alternatively, Bartholomew and Mills (1991) suggested that the gravels represented an older course of the New River itself, given that no gravels were observed on the nearby Fort Lewis Mountain to support Houser (1981)'s hypothesis. Both of these studies sought to constrain the downcutting rate of the New River, with Houser (1981) inferring a rate of ~40 m/My and Bartholomew and Mills (1991) hypothesizing rates ranging from 40-100 m/My (Granger et al., 1997; references therein).

One way to directly test these hypotheses is through cosmogenic burial dating of New River sediments, as first done by Granger et al. (1997). While the gravel accumulations on Gap Mountain are poorly preserved and likely insufficiently thick for burial dating, Granger et al. (1997) demonstrated that fluvial gravels in nearby abandoned caves perched above rivers are ideal targets for $^{26}Al/^{10}Be$ dating. They dated quartz gravels in five caves above the New River to the Pleistocene, and demonstrated that the New River has been constantly incising at 27 ± 5 m/My since approximately 1.5 My. The oldest cave dated, Benton Williams #1, had a burial age of 1.47 ± 0.22 My and was perched 29 meters above the modern river (Figure 4.15).

The manganese oxide deposits on Gap Mountain are located 90 meters above the closest section of the modern New River, providing a way to not only date a former course of the river, but also constrain its incision rate since the Miocene. Accepting the assertion of Bartholomew and Mills (1991) that the Gap Mountain wind gap reflects a former course of the New River, we used the ages of the manganese oxides to estimate a minimum incision rate of 28.6 ± 1.1 m/My and a maximum incision rate of 41.1 ± 1.5 m/My. The minimum incision rate is strikingly close to the overall incision rate estimated by Granger et al. (1997), and combining both datasets yields an average incision rate for the New River of 27.3 ± 0.8 m/My since ~9 My (Figure 4.15). It appears that New River has been constantly incising since the late Miocene, but further dating of higher perched caves is needed to confirm this hypothesis.

4.5.3.4 Mine Bank Mine and capture of the St. Marys River

Another anomalous site is the Mine Bank Mine, located near the St. Marys River of the James River watershed. Like the Gap Mountain site, Mine Bank Mine hosted Late Miocene manganese oxides (8.74 ± 0.13 Ma) that revealed potentially rapid denudation rates (11.4 ± 0.2 m/My) and unusually rapid river incision rates (11.8 ± 0.2 to 23.2 ± 0.3 m/My). Unlike the Gap Mountain site, however, the Mine Bank Mine is located <5 km from the headwaters of the Shenandoah River in an area featuring abundant evidence of recent capture by the James River watershed. Examining the broad alluvial valleys of the upper Shenandoah River watershed and the steep headwaters of the upper James River watershed, Bank et al. (1999) hypothesized that ongoing capture of the Shenandoah River's headwaters by those of the James River has driven rapid local incision. This hypothesis is bolstered by χ analysis of the pair of watersheds (Willett et al., 2014) that uses high-resolution digital elevation models to illustrate the discrepancies in steepness – and thus, direction of ongoing captures – between the two watersheds (Figure 4.16). Our Miocene age for the Mine Bank manganese oxide deposit and corresponding rapid incision rate estimates, as well as our χ analysis, provide strong evidence for Bank et al. (1999)'s argument and provide a clear example of drainage capture as a mechanism for local topographic rejuvenation.

4.5.3.5 Modern erosion rates from ^{10}Be

The modern bedrock erosion rates derived from in-situ ^{10}Be from Capola Mountain Mine and Larry's Place are significantly faster than our long-term estimates of denudation from ^{40}Ar/^{39}Ar dating of the same manganese oxides. Quartz from bedrock atop the Capola Mountain Mine provided an erosion rate of 11.9 $^{+0.4}/_{-0.4}$ m/My that exceeds the long-term maximum denudation rate by four- to fivefold. Even more remarkably, the modern erosion rate at Larry's Place (41.9 $^{+1.7}/_{-1.8}$ m/My) outpaced the long-term maximum denudation rate by twentyfold.

These discrepancies likely reflect short-term erosional regimes in the Pleistocene that led to enhanced erosion during the Late Pleistocene. While there is no substantial evidence for Pleistocene glaciations reaching the Shenandoah Valley, it has been demonstrated that periglacial processes (e.g., enhanced frost weathering) can lead to increased erosion rates in nonglaciated landscapes (Marshall et al., 2015). This mechanism may be particularly responsible for increased

erosion at the Capola Mountain Mine, which is not located near any large rivers that could respond rapidly to base level changes.

In contrast, Larry's Place is located along the main branch of the Shenandoah River and is more susceptible to base level fluctuations. Burial dating of a fluvial terrace near Larry's Place (Chapter 3, this thesis) has revealed relatively rapid incision of the Shenandoah River watershed since at least ~0.9 My. On the basis of this tentative age, we have estimated that the Shenandoah River has been incising at 23-26 m/My since that time in response to base level fluctuations affecting the entire Potomac River basin. The fact that the ^{10}Be-derived erosion rate is approximately double that of the river incision rate may reflect accelerated erosion during the last glacial interval, while the river incision rate is averaged over glacial and interglacial cycles.

4.5.3.6 Dynamic topography considerations

While climate appears to play a primary role in the Late Cenozoic history of the Shenandoah Valley and neighboring watersheds, it is likely that mantle behavior has exerted some forcing on the evolution of this landscape. Models of dynamic topography in the Appalachian Mountains have pointed to the potential of asthenospheric flow to drive uplift in the Late Cenozoic (Pazzaglia and Brandon, 1996; Rowley et al., 2013), thus triggering rapid sedimentation in Gulf of Mexico (Galloway et al., 2011) and along the Atlantic coast (Poag and Sevon, 1989) as well as subsequent Pliocene deformation of onshore and offshore rocks (Rovere et al., 2014; Rowley et al., 2013). These models have notably differed in their estimates of uplift/subsidence magnitudes and locations, primarily driven by varying considerations of mantle characteristics and plate-mantle interactions (Rovere et al., 2014). Recent work focusing on the deformed Pliocene shoreline of eastern North America has demonstrated that up to 60 m of warping have occurred in the area since approximately 3 Ma, as a result of negative buoyancy driven by the Farallon slab, west-flowing warm mantle, and glacial isostatic adjustment (Rowley et al., 2013; Rovere et al., 2014). In the Shenandoah Valley, Rowley et al. (2013) hypothesized that 0-40 m of uplift had affected the area since the Pliocene, with the greatest amount of uplift having occurred along the eastern side of the Valley. In contrast, Liu (2014) modeled dynamic subsidence driven by the eastward-moving Farallon slab from 60 Ma – present and estimated that over 400 m of relief were generated in the central Appalachians during the past 20 Ma.

Our manganese oxide formation ages and derived denudation rates indicate that no denudation associated with topographic rejuvenation occurred on the magnitude hypothesized by Liu (2014). However, the warped Pliocene shoreline along the eastern coast of North America is relatively consistent with the predictions of Rowley et al. (2013), lending credence to their modeled uplift in the area east of the Shenandoah Valley. It is difficult to directly and precisely evaluate this model in the Shenandoah Valley and neighboring basins, but there is a distinct likelihood that dynamic topography has affected the area in the geologically recent past. It is therefore important to consider that while climate likely exerted a direct force on landscape evolution through weathering processes (Marshall et al., 2015) and an indirect force through influencing glacial retreat and consequent rebound, the Cenozoic behavior of the mantle likely drove some portion of denudation during this time.

4.6 Conclusions

This work provides fresh insights into the formation of Appalachian manganese oxide deposits and their implications for the Cenozoic erosional history of this ancient mountain range. Scanning electron microscopy, energy-dispersive X-Ray spectroscopy, and rare earth element analyses have demonstrated that manganese oxide deposits are typically comprised of multigenerational, mineralogically and texturally complex materials. We have provided a modified model for the formation of these deposits that can account for the mineralogical diversity of these deposits as well as the range of ages observed within individual sites. $^{40}Ar/^{39}Ar$ geochronology applied to manganese oxides has shown that the chemical weathering responsible for forming these deposits has been occurring over extended intervals throughout the Cenozoic, generally regardless of long-term temperature trends. As such, these deposits broadly support elements of both continuous and episodic landscape evolution models, which are not mutually exclusive. These manganese oxides furthermore provide compelling evidence that the Appalachians experienced no substantial uplift since at least the Early Cenozoic. Short-term estimates of erosion rates from cosmogenic ^{10}Be reveal increases in erosion of the Shenandoah Valley, likely due to Pleistocene climate fluctuations that may have been accompanied by asthenospheric forcing since the Pliocene. Over timescales of tens of millions of years, however, manganese oxide deposits show the southern and central Appalachian Mountains to be a stable, gradually eroding orogen.

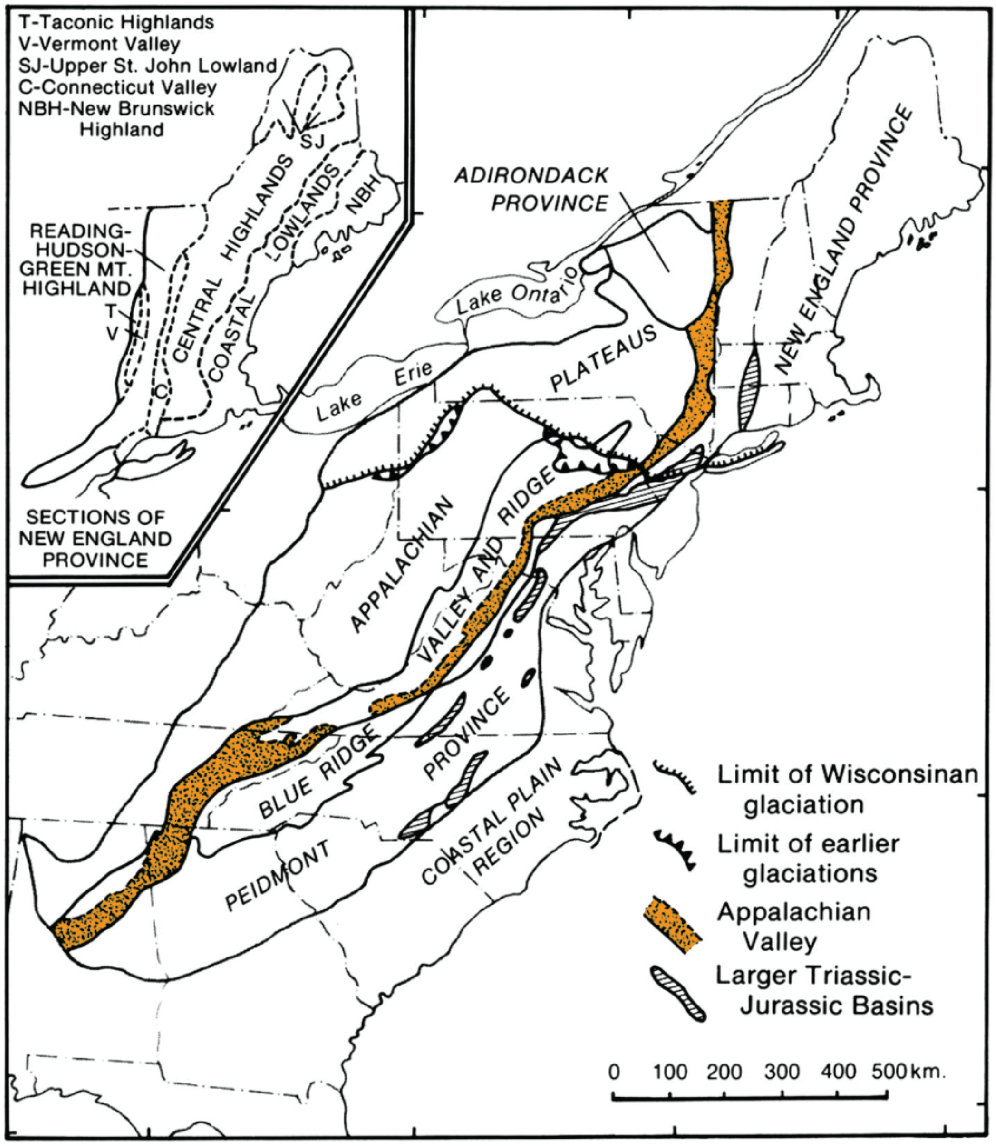

Figure 4.1. Major provinces of the Appalachian Mountains with the extent of the Appalachian Valley, which generally corresponds to the Valley Floor peneplain, highlighted in orange. Figure modified from Hack (1989).

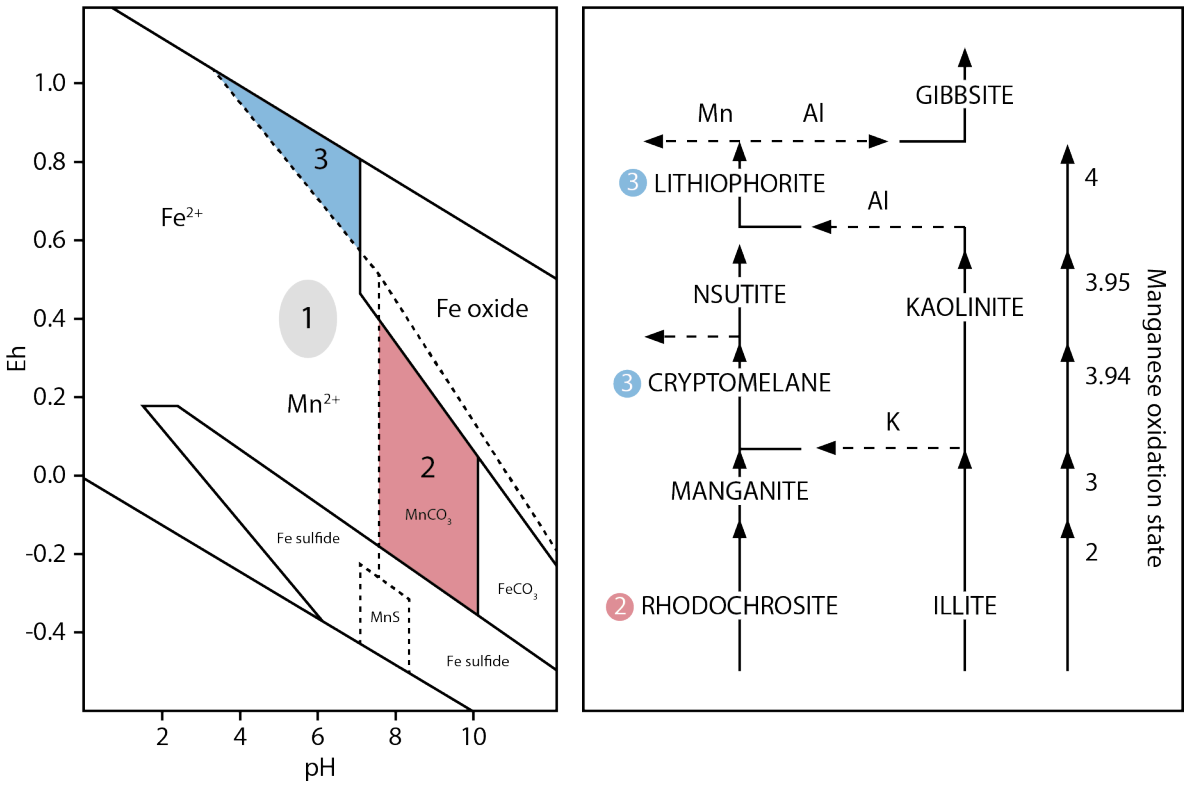

Figure 4.2. Left: Stability fields for dissolved manganese (1), rhodochrosite (2), and manganese oxides (3) modified from Maynard (2005). Right: Weathering sequence of manganese oxides from rhodochrosite with common Appalachian minerals indicated. Figure modified from Parc et al. (1989).

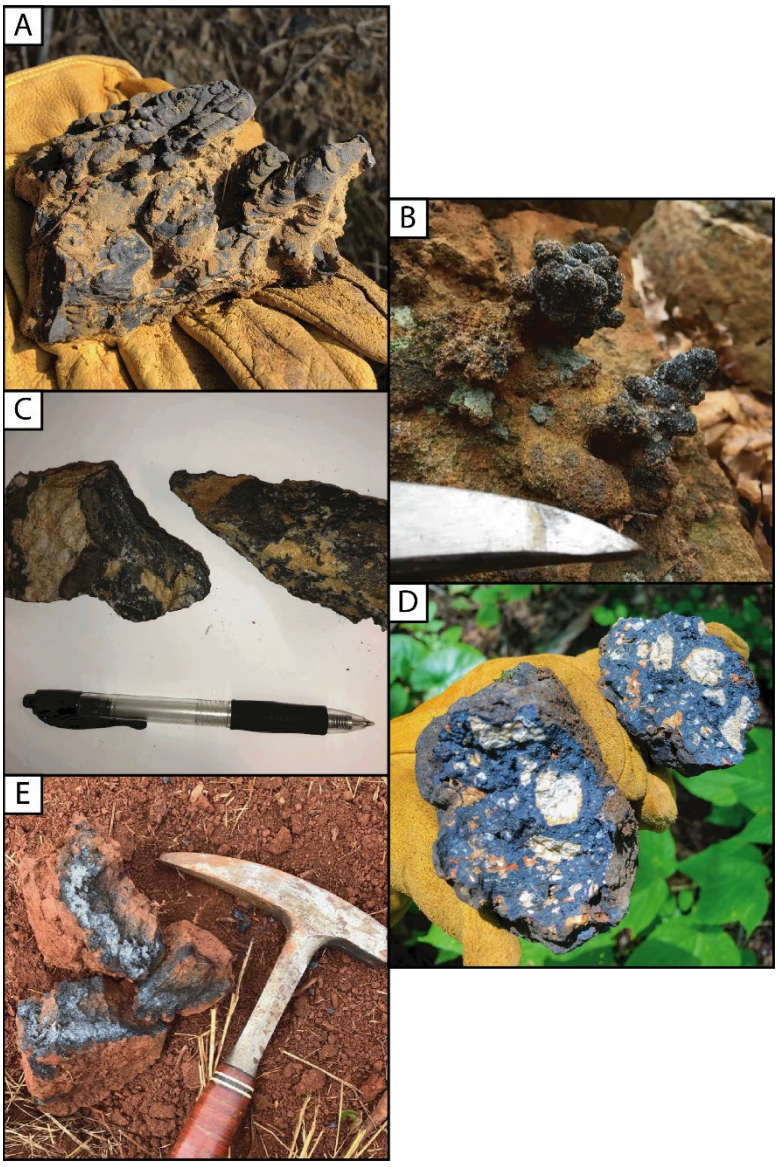

Figure 4.3. Common manganese oxide morphologies found at Appalachian mines. (A) Botryoidal/nodular sample from Gap Mountain roadcut, VA. Photo by D. Doctor. (B) Mn-cemented sandstone at Capola Mountain Mine, VA. (C) Mn-covered quartzites from Little Fort Valley Pit, VA. (D) Breccia with manganese oxide (hollandite-cryptomelane) cement at Silver Creek Mine, VA. Photo by D. Doctor. (E) Massive manganese oxide devoid of detrital minerals from Hambright Mine, TN.

Figure 4.4. Overview of field area and individual sub-areas included in this study. Geologic units from USGS Mineral Resources database (https://mrdata.usgs.gov/geology/state/). Digital elevation data from The National Map (https://viewer.nationalmap.gov/basic/). (A) The Cleveland, TN area northeast of Chattanooga, TN hosts several manganese mines. We sampled mines along both sides of the Tennessee River and on the flanks of Whiteoak Mountain. (B) Northeast Tennessee features dozens of manganese mines and prospects, many of which are located in the synclinal valleys immediately northeast of Elizabethton, TN. (C) The landscape of southwest Virginia immediately north of Blacksburg, VA has been deeply incised by the New River. In addition to hosting numerous caves, it features several large manganese oxide deposits including the well-preserved Gap Mountain roadcut. (D) The Shenandoah Valley of Virginia was most intensely studied and dated during this investigation. Most geochronology was performed on samples collected near the Big Levels area in the southwestern valley.

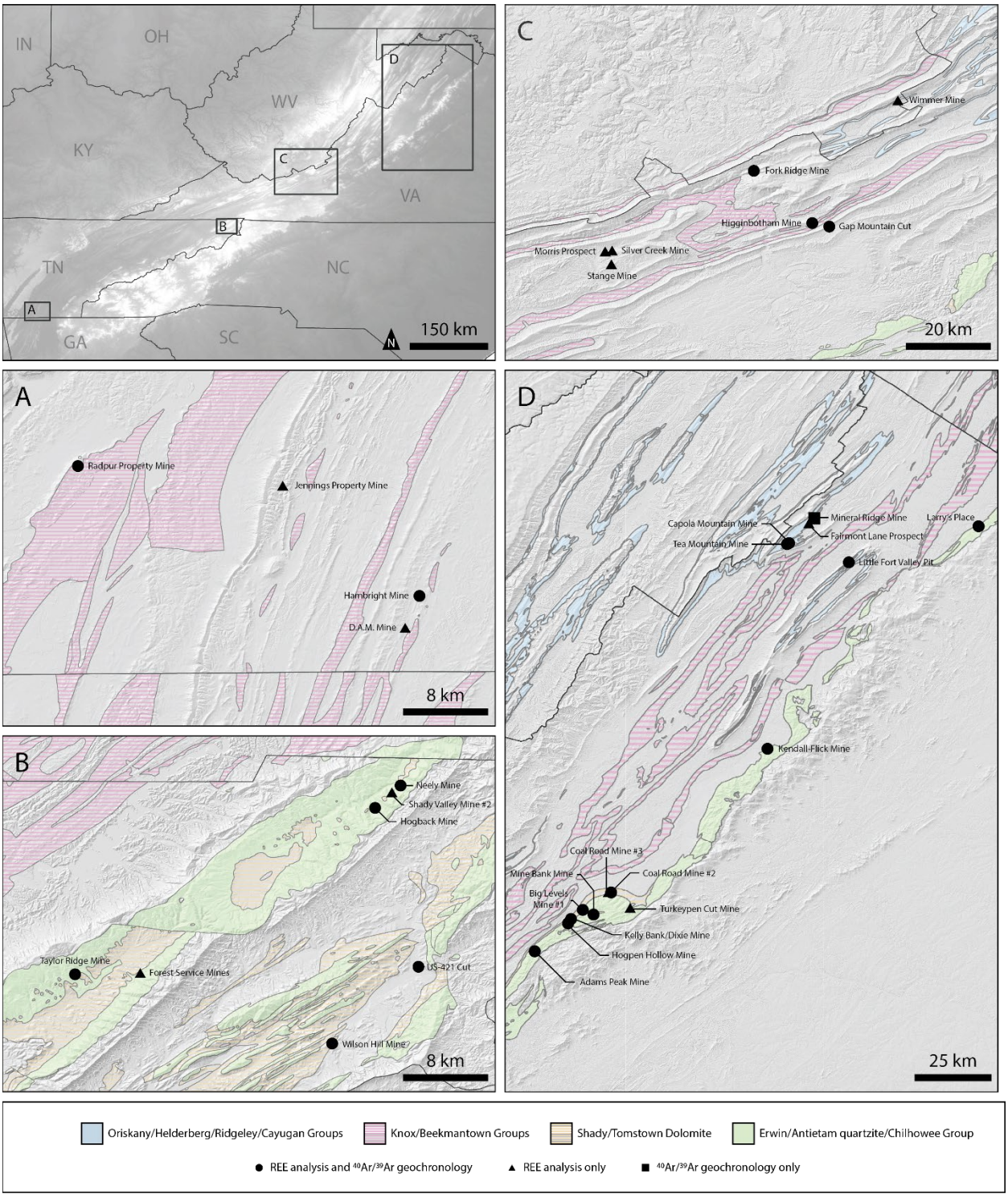
IN
OH
WV
KY
VA
TN
NC
GA
SC
A
B
C
D
150 km
N
Wimmer Mine
Fork Ridge Mine
Higginbotham Mine
Gap Mountain Cut
Morris Prospect
Silver Creek Mine
Stange Mine
20 km
Radpur Property Mine
Jennings Property Mine
Hambright Mine
D.A.M. Mine
8 km
Neely Mine
Shady Valley Mine #2
Hogback Mine
Taylor Ridge Mine
Forest Service Mines
US-421 Cut
Wilson Hill Mine
8 km
Capola Mountain Mine
Mineral Ridge Mine
Larry's Place
Fairmont Lane Prospect
Tea Mountain Mine
Little Fort Valley Pit
Kendall-Flick Mine
Coal Road Mine #3
Mine Bank Mine
Coal Road Mine #2
Big Levels Mine #1
Turkeypen Cut Mine
Kelly Bank/Dixie Mine
Hogpen Hollow Mine
Adams Peak Mine
25 km
Oriskany/Helderberg/Ridgeley/Cayugan Groups
Knox/Beekmantown Groups
Shady/Tomstown Dolomite
Erwin/Antietam quartzite/Chilhowee Group
REE analysis and 40Ar/39Ar geochronology
REE analysis only
40Ar/39Ar geochronology only

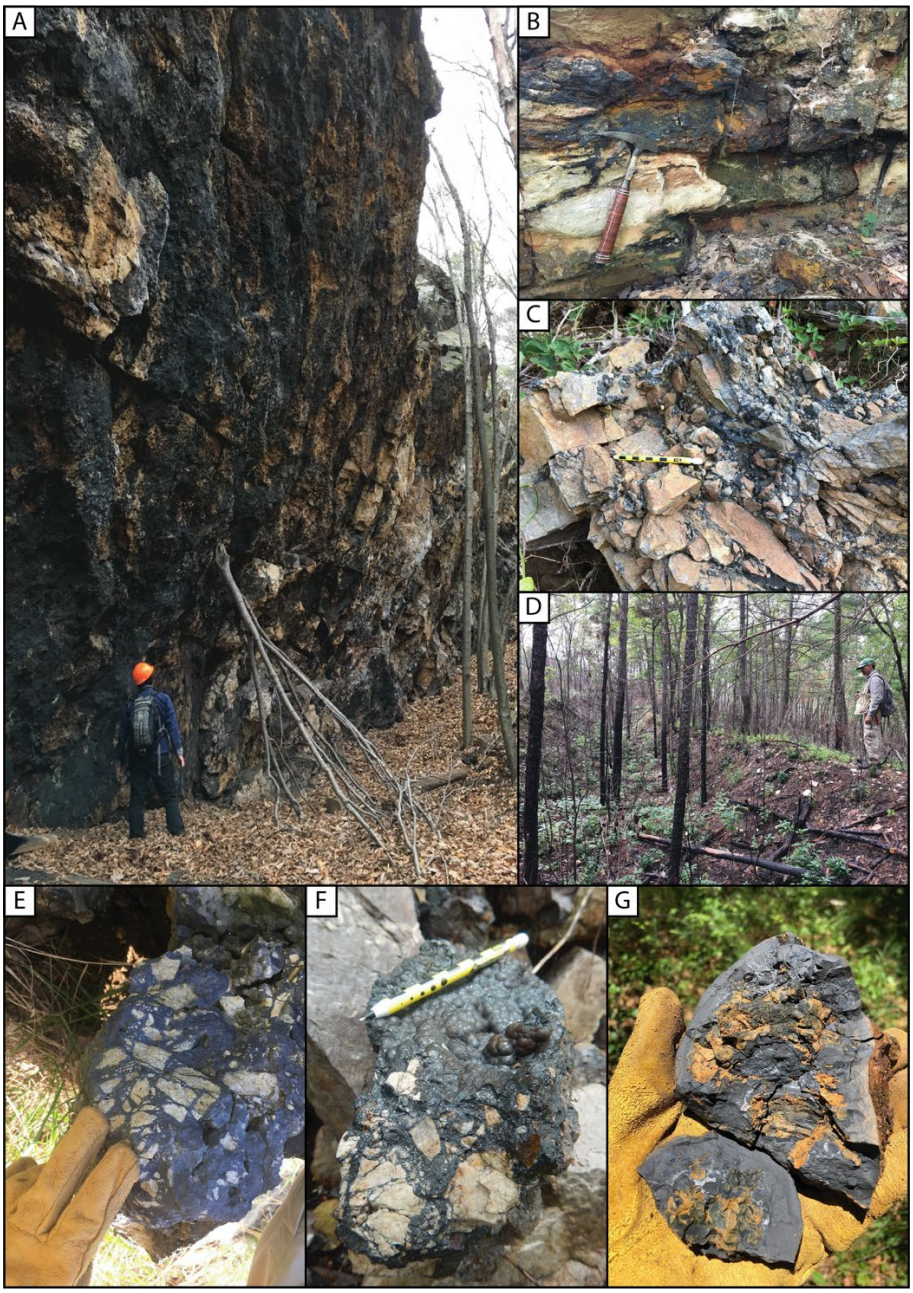

Figure 4.5. (A) Manganese oxides, primarily pyrolusite, in Oriskany Sandstone at Capola Mountain Mine, VA. R. McAleer in foreground for scale. (B) Iron and manganese oxides replacing crossbedded Becraft Sandstone at Stange-Arms Mine, VA. To the right, a fracture has been filled with hollandite. (C) In-place cryptomelane-hollandite deposit at Gap Mountain, VA. This is one of the locations where breccia appears with botryoidal material in the same samples. (D) D. Doctor surveys a typical site, Kelly Bank Mine, VA, where iron and manganese oxides appear as scattered materials. (E) Sandstone breccia with cryptomelane-hollandite cement at Gap Mountain, VA. Note bluish hue indicative of cryptomelane and fact that clasts do not contact one another. (F) Hollandite-rich breccia featuring iron-rich botryoidal exterior. This sample was collected along a fault at Hogpen Hollow Mine, VA. (G) Botryoidal sample containing iron and manganese oxides. Cryptomelane is visible in veins.

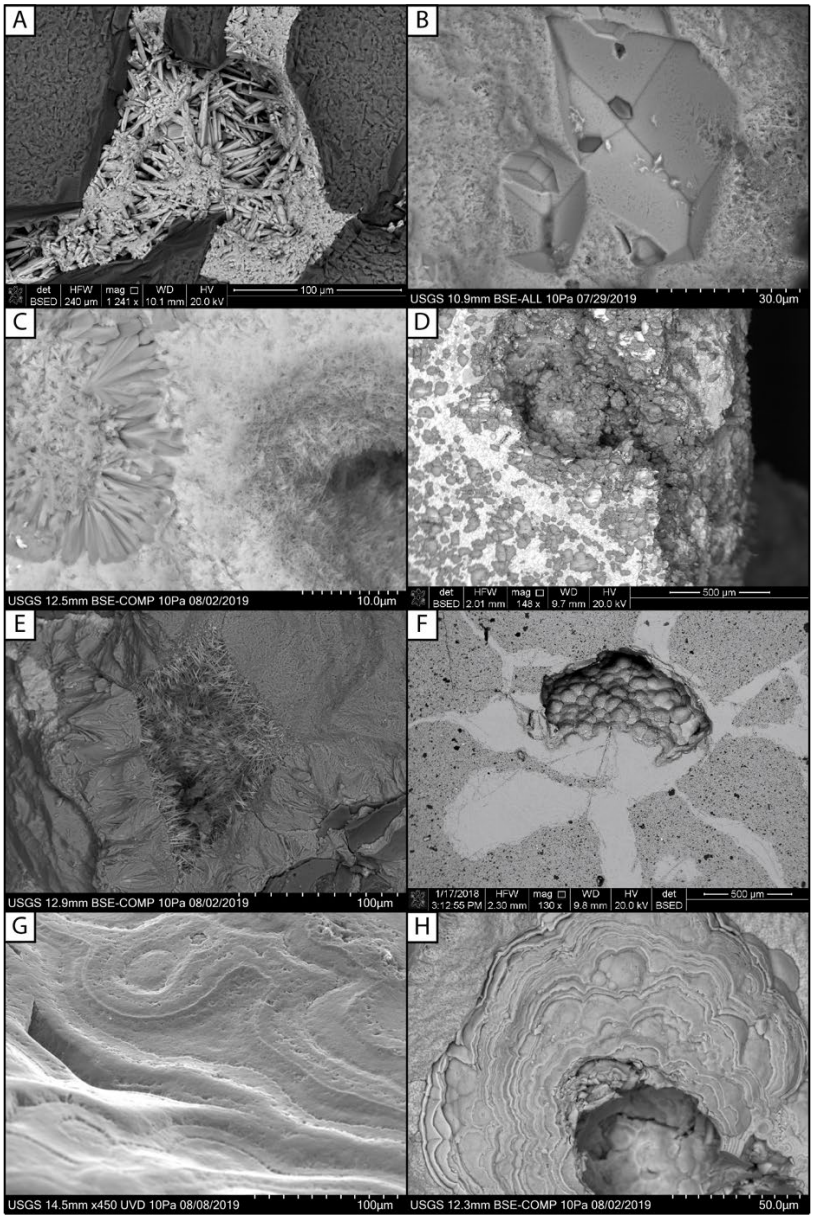

Figure 4.6. (A) Quartz grains (dark) cemented by cryptomelane/hollandite matrix in a breccia sample collected from Neely Mine, TN (sample 08-22-18A). (B) Euhedral quartz grain impression in hollandite/cryptomelane/lithiophorite matrix collected from an undocumented mine on Coal Road, VA (sample 07-06-19B-2). (C) Intergrown acicular grains (left) and needles (right) composed of hollandite/cryptomelane collected from Mineral Ridge Mine, VA (sample 06-26-19A-3). (D) Cryptomelane/hollandite-cemented sandstone collected from Black Shaft Mine in Big Levels, VA. (E) Lithiophorite with cryptomelane-rich needles in sample collected from Tea Mountain Mine, VA (sample 06-26-19C-3). (F) Veins of pure cryptomelane/hollandite filling cracks in a matrix of detrital material. Note botryoidal textures in void space. Material collected at Turkeypen Cut Mine, VA (sample 11-14-17B). (G) Banded lithiophorite collected at Higginbotham Mine near Gap Mountain, VA (sample 07-25-19A-1). (H) Botryoidal cryptomelane/lithiophorite collected by D. Doctor from Kelly Bank Mine, VA (sample DR092518F1B).

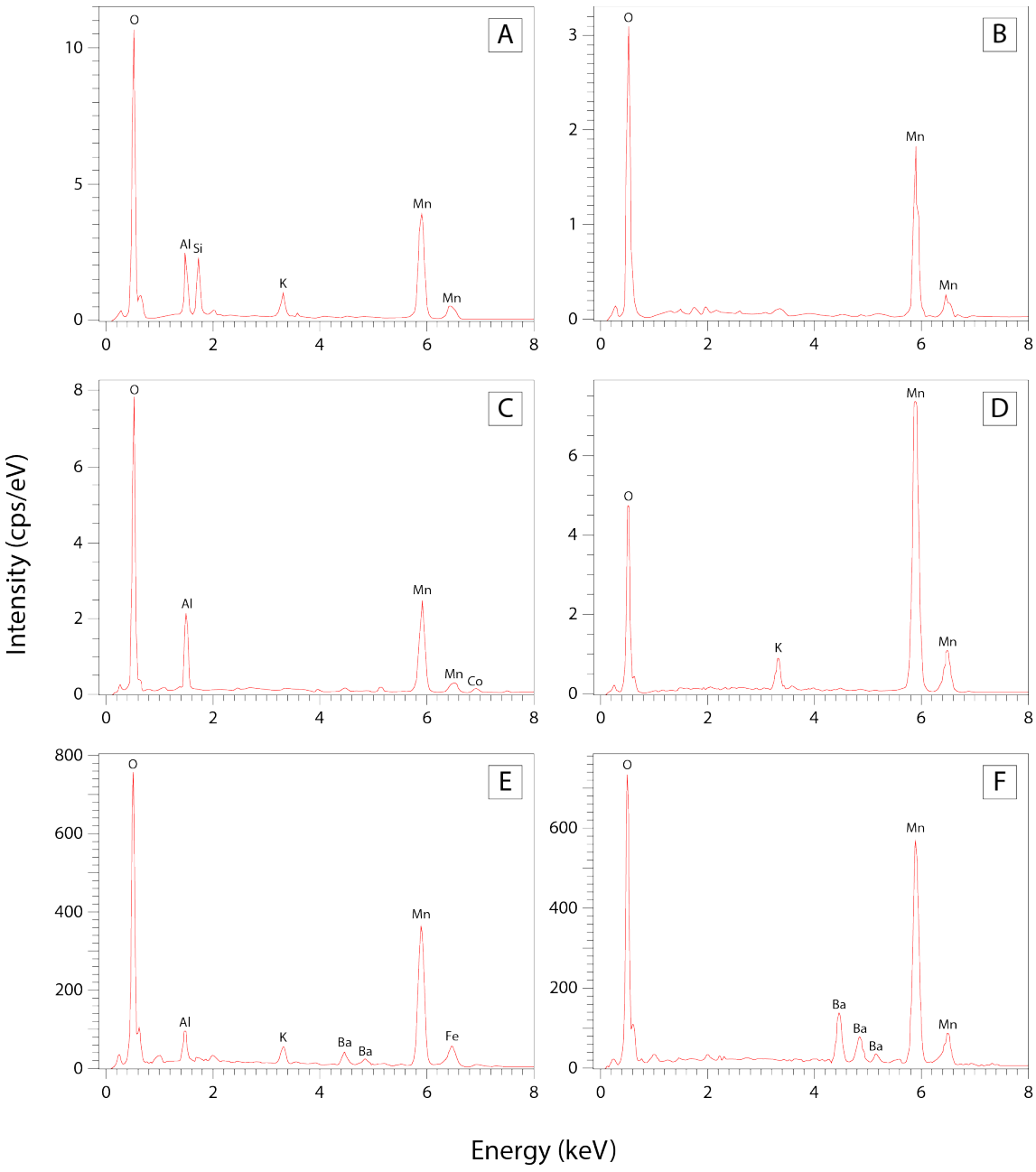

Figure 4.7. (A) Typical manganese oxide containing detrital aluminosilicates, as indicated by Al/Si peaks. Sample 08-23-18H was collected at Taylor Ridge Mine, TN. (B) Pyrolusite (MnO_2) is an abundant mineral at many manganese oxide mines. Sample 08-22-18D was collected at Hogback Mine, TN. (C) Lithiophorite [$(Al,Li)MnO_2(OH)_2$] frequently occurs in conjunction with cryptomelane and hollandite. Sample 08-23-18C was collected at Wilson Hill Mine, TN. (D) Analytically pure cryptomelane (KMn_8O_{16}) is less common than the cryptomelane-hollandite solid solution. Sample 09-25-18D was collected at Kelly Bank Mine, VA. (E) Solid solution of lithiophorite, cryptomelane, and hollandite suitable for dating. Sample 09-25-18A was collected at Hogpen Hollow Mine, VA. (F) Nearly pure hollandite is a common occurrence, with many samples featuring too little potassium to be datable using the $^{40}Ar/^{39}Ar$ technique. Sample 11-09-18D was collected at Capola Mountain Mine, VA.

Figure 4.8. (below). Backscatter electron images of dated samples showing locations of EDX analyses performed prior to irradiation and $^{40}Ar/^{39}Ar$ analysis. In most instances, cryptomelane is the lightest color/dominant mineralogy and quartz comprises most dark material. (A) Pb-bearing Gap Mountain sample 12-11-17A; (B) Pb-free Gap Mountain sample 12-11-17A; (C) Mica-bearing sample from Kendall-Flick Mine 12-18-17C; (D) Mica-free sample from Kendall-Flick Mine 12-18-17C; (E) Sample 02-12-18D from Mine Bank Mine; (F) Sample 02-16-18A from Fork Ridge Mine; (G) Sample 05-21-18B-1 from Big Levels Mine #1; (H) Sample 09-24-18B-1 from Adams Peak Mine; (I) Sample 09-25-18A-2 from Hogpen Hollow Mine; (J) Sample 09-25-18A-3 from Hogpen Hollow Mine; (K) Sample 09-25-18D-2 from Kelly Bank/Dixie Mine; (L) Sample 09-25-18D-3 from Kelly Bank/Dixie Mine; (M) Sample 11-08-18A-1 from Kelly Bank/Dixie Mine; (N) Sample 11-08-18A-S2 from Kelly Bank/Dixie Mine; (O) Sample 11-09-18D-S1-1 from Capola Mountain Mine; (P) Sample 11-09-18D-S2-3 from Capola Mountain Mine; (Q) Sample 11-09-18F-1 from Capola Mountain Mine; (R) Sample 11-09-18F-3 from Capola Mountain Mine; (S) Sample 11-09-18J-2 from Larry's Place; (T) Sample 11-09-18J-3 from Larry's Place.

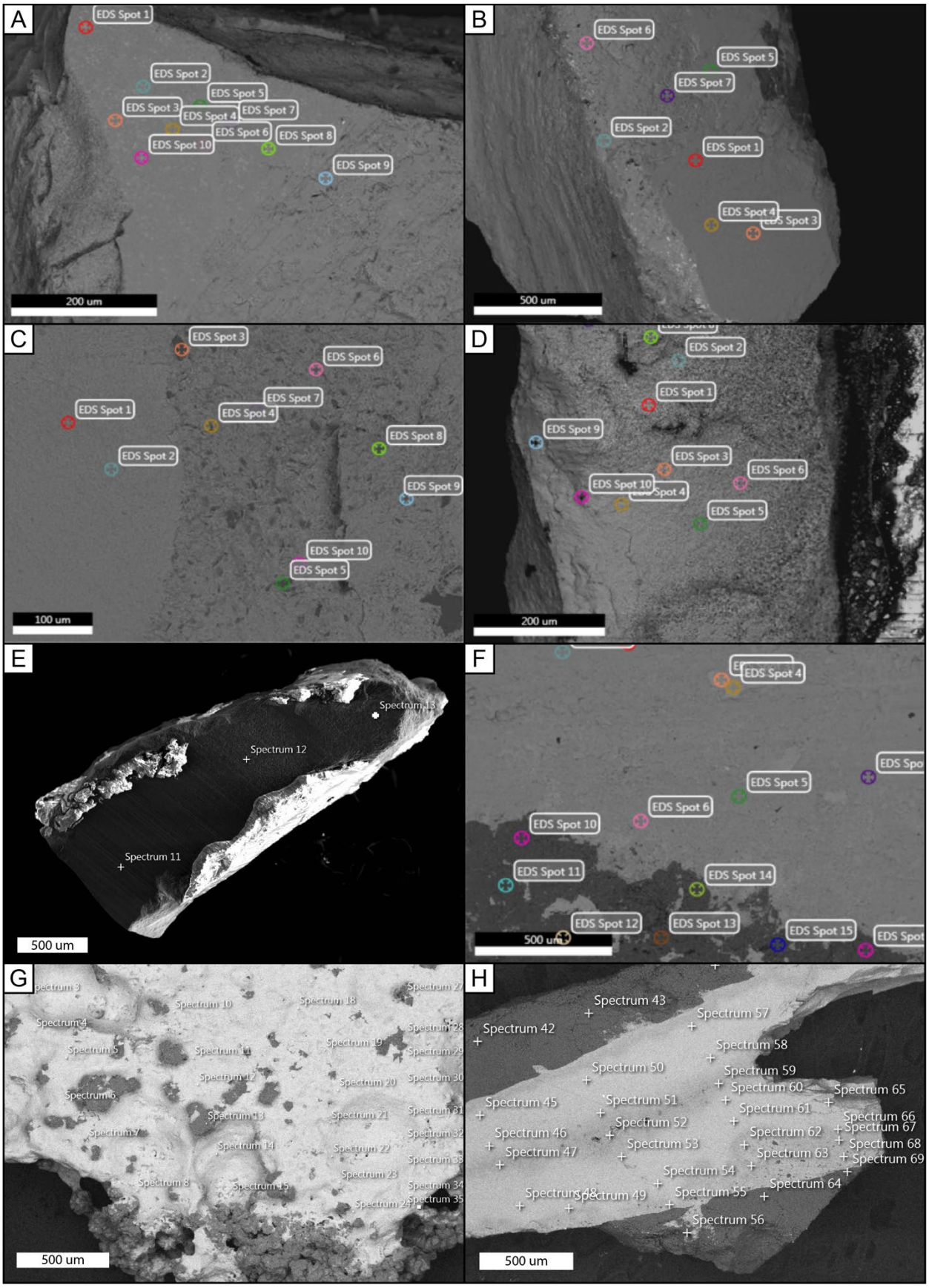
A
EDS Spot 1
EDS Spot 2
EDS Spot 5
EDS Spot 3
EDS Spot 4
EDS Spot 7
EDS Spot 6
EDS Spot 8
EDS Spot 10
EDS Spot 9
200 um
B
EDS Spot 6
EDS Spot 5
EDS Spot 7
EDS Spot 2
EDS Spot 1
EDS Spot 4
EDS Spot 3
500 um
C
EDS Spot 3
EDS Spot 6
EDS Spot 7
EDS Spot 1
EDS Spot 4
EDS Spot 8
EDS Spot 2
EDS Spot 9
EDS Spot 10
EDS Spot 5
100 um
D
EDS Spot 2
EDS Spot 1
EDS Spot 9
EDS Spot 3
EDS Spot 6
EDS Spot 10
EDS Spot 4
EDS Spot 5
200 um
E
Spectrum 13
Spectrum 12
Spectrum 11
500 um
F
EDS Spot 4
EDS Spot 5
EDS Spot 6
EDS Spot 10
EDS Spot 11
EDS Spot 14
EDS Spot 12
EDS Spot 13
EDS Spot 15
500 um
G
Spectrum 10
Spectrum 18
Spectrum 4
Spectrum 5
Spectrum 11
Spectrum 19
Spectrum 29
Spectrum 12
Spectrum 20
Spectrum 30
Spectrum 6
Spectrum 13
Spectrum 21
Spectrum 31
Spectrum 7
Spectrum 14
Spectrum 22
Spectrum 32
Spectrum 33
Spectrum 8
Spectrum 15
Spectrum 23
Spectrum 34
Spectrum 24
Spectrum 35
500 um
H
Spectrum 43
Spectrum 57
Spectrum 42
Spectrum 58
Spectrum 50
Spectrum 59
Spectrum 60
Spectrum 65
Spectrum 45
Spectrum 51
Spectrum 61
Spectrum 66
Spectrum 46
Spectrum 52
Spectrum 62
Spectrum 67
Spectrum 47
Spectrum 53
Spectrum 63
Spectrum 68
Spectrum 54
Spectrum 64
Spectrum 69
Spectrum 48
Spectrum 49
Spectrum 55
Spectrum 56
500 um

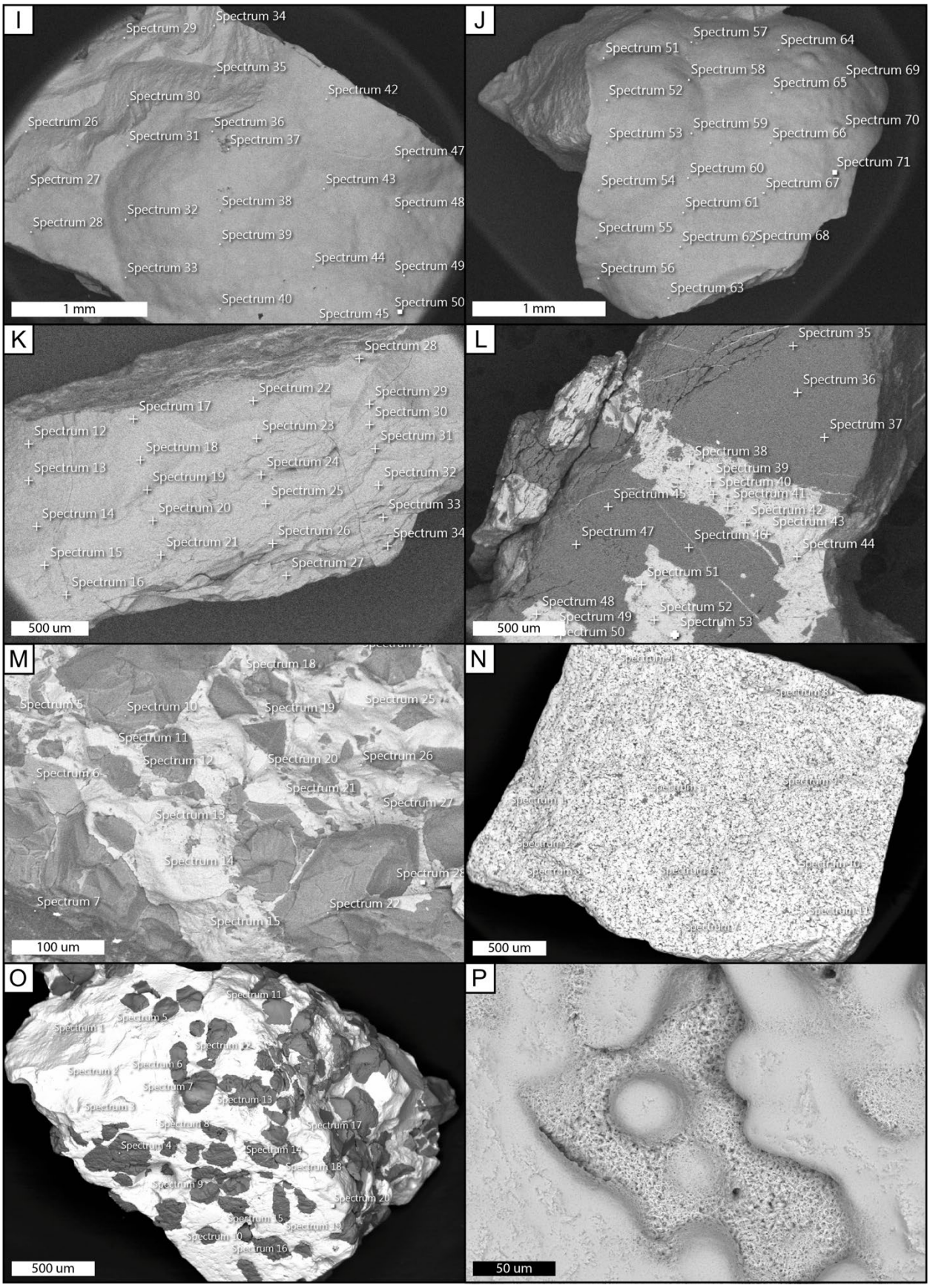
I
Spectrum 29
Spectrum 34
Spectrum 35
Spectrum 42
Spectrum 30
Spectrum 26
Spectrum 36
Spectrum 31
Spectrum 37
Spectrum 47
Spectrum 27
Spectrum 43
Spectrum 32
Spectrum 38
Spectrum 48
Spectrum 28
Spectrum 39
Spectrum 44
Spectrum 49
Spectrum 33
Spectrum 40
Spectrum 50
Spectrum 45
1 mm
J
Spectrum 57
Spectrum 64
Spectrum 51
Spectrum 58
Spectrum 69
Spectrum 65
Spectrum 52
Spectrum 70
Spectrum 59
Spectrum 53
Spectrum 66
Spectrum 71
Spectrum 60
Spectrum 54
Spectrum 67
Spectrum 61
Spectrum 55
Spectrum 62
Spectrum 68
Spectrum 56
Spectrum 63
1 mm
K
Spectrum 28
Spectrum 22
Spectrum 29
Spectrum 17
Spectrum 30
Spectrum 12
Spectrum 23
Spectrum 31
Spectrum 18
Spectrum 13
Spectrum 24
Spectrum 32
Spectrum 19
Spectrum 25
Spectrum 33
Spectrum 20
Spectrum 14
Spectrum 26
Spectrum 34
Spectrum 21
Spectrum 15
Spectrum 27
Spectrum 16
500 um
L
Spectrum 35
Spectrum 36
Spectrum 37
Spectrum 38
Spectrum 39
Spectrum 40
Spectrum 45
Spectrum 41
Spectrum 42
Spectrum 43
Spectrum 47
Spectrum 46
Spectrum 44
Spectrum 51
Spectrum 48
Spectrum 52
Spectrum 49
Spectrum 53
Spectrum 50
500 um
M
Spectrum 18
Spectrum 5
Spectrum 10
Spectrum 19
Spectrum 25
Spectrum 11
Spectrum 12
Spectrum 20
Spectrum 26
Spectrum 6
Spectrum 21
Spectrum 27
Spectrum 13
Spectrum 14
Spectrum 7
Spectrum 22
Spectrum 15
100 um
N
500 um
O
Spectrum 11
Spectrum 5
Spectrum 6
Spectrum 7
Spectrum 13
Spectrum 17
Spectrum 4
Spectrum 14
Spectrum 18
Spectrum 9
Spectrum 20
Spectrum 15
Spectrum 16
500 um
P
50 um

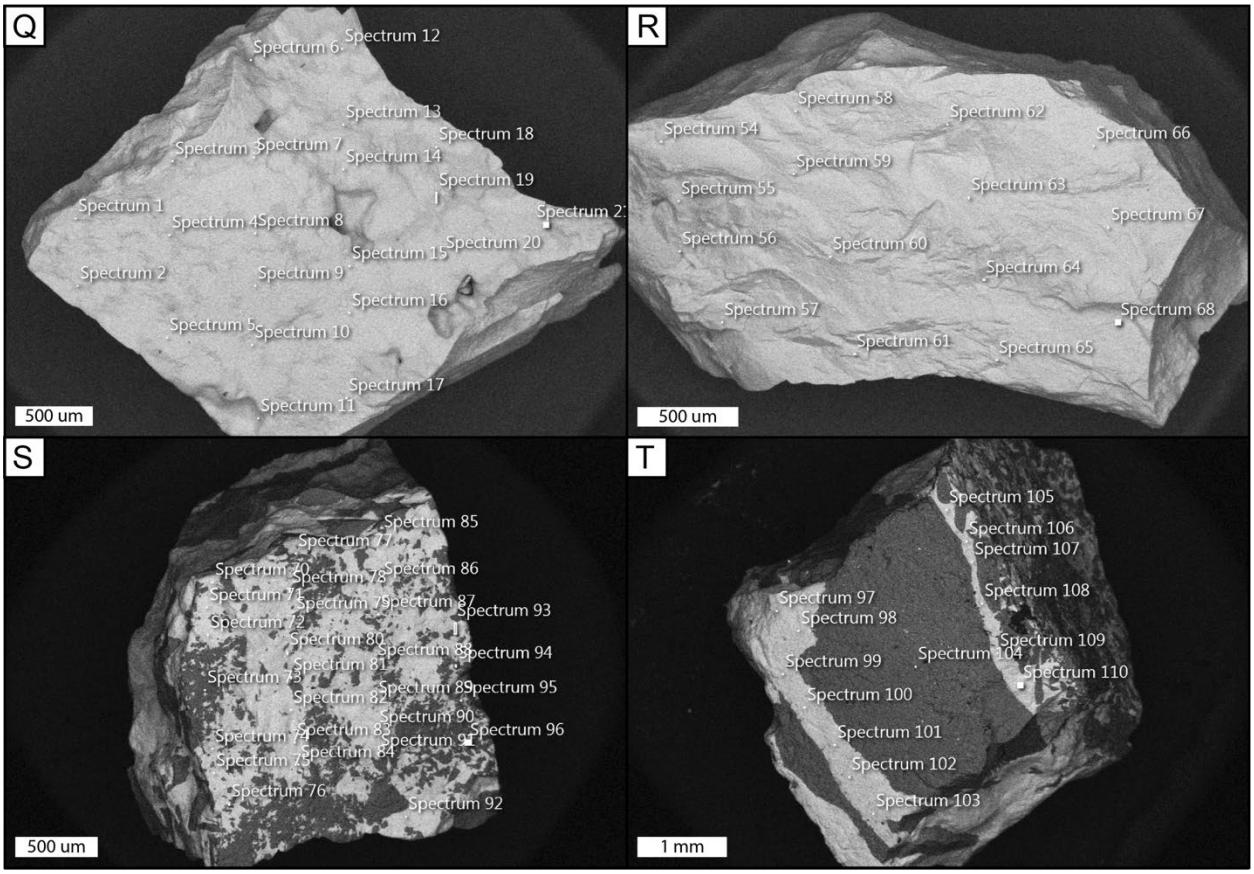
Q
Spectrum 12
Spectrum 6
Spectrum 13
Spectrum 18
Spectrum 3
Spectrum 7
Spectrum 14
Spectrum 19
Spectrum 1
Spectrum 4
Spectrum 8
Spectrum 15
Spectrum 20
Spectrum 2
Spectrum 9
Spectrum 16
Spectrum 5
Spectrum 10
Spectrum 17
Spectrum 11
500 um
R
Spectrum 58
Spectrum 62
Spectrum 54
Spectrum 66
Spectrum 59
Spectrum 55
Spectrum 63
Spectrum 67
Spectrum 56
Spectrum 60
Spectrum 64
Spectrum 57
Spectrum 68
Spectrum 61
Spectrum 65
500 um
S
Spectrum 85
Spectrum 77
Spectrum 70
Spectrum 86
Spectrum 78
Spectrum 71
Spectrum 79
Spectrum 87
Spectrum 93
Spectrum 72
Spectrum 80
Spectrum 88
Spectrum 94
Spectrum 81
Spectrum 73
Spectrum 89
Spectrum 95
Spectrum 82
Spectrum 90
Spectrum 96
Spectrum 74
Spectrum 83
Spectrum 91
Spectrum 84
Spectrum 75
Spectrum 76
Spectrum 92
500 um
T
Spectrum 105
Spectrum 106
Spectrum 107
Spectrum 108
Spectrum 97
Spectrum 98
Spectrum 109
Spectrum 104
Spectrum 99
Spectrum 110
Spectrum 100
Spectrum 101
Spectrum 102
Spectrum 103
1 mm

Figure 4.9. (below). Complete $^{40}Ar/^{39}Ar$ stepwise heating spectra, $^{36}Ar/^{40}Ar$-$^{39}Ar/^{40}Ar$ isochrons, and ideogram ages for dated samples. Stepwise elemental ratios for Ca, Cl, and K are also provided along with radiogenic yield. For detailed discussion of the construction and meanings of stepwise spectra, isochrons, and age ideograms, see Vasconcelos (1999) and Reiners et al. (2018).

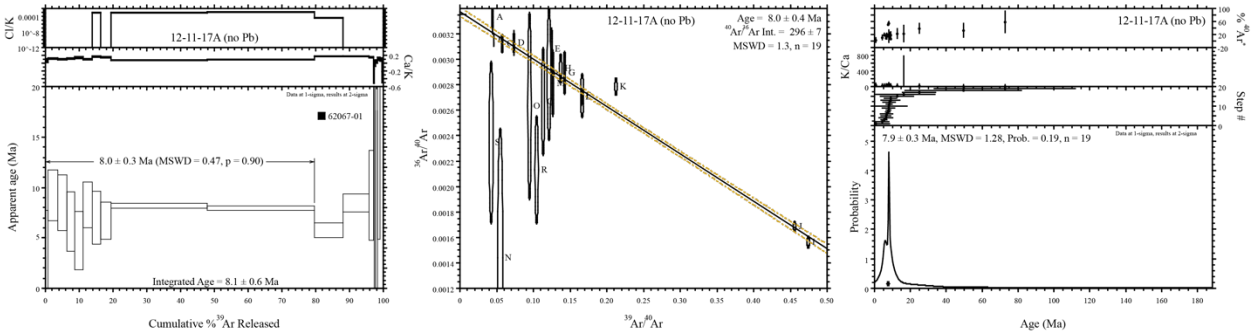
12-11-17A (no Pb)
62067-01
8.0 ± 0.3 Ma (MSWD = 0.47, p = 0.90)
Integrated Age = 8.1 ± 0.6 Ma
Cumulative %39Ar Released
Apparent age (Ma)
Cl/K
Ca/K
Age = 8.0 ± 0.4 Ma
40Ar/36Ar Int. = 296 ± 7
MSWD = 1.3, n = 19
36Ar/40Ar
39Ar/40Ar
7.9 ± 0.3 Ma, MSWD = 1.28, Prob. = 0.19, n = 19
K/Ca
% 40Ar*
Step #
Probability
Age (Ma)

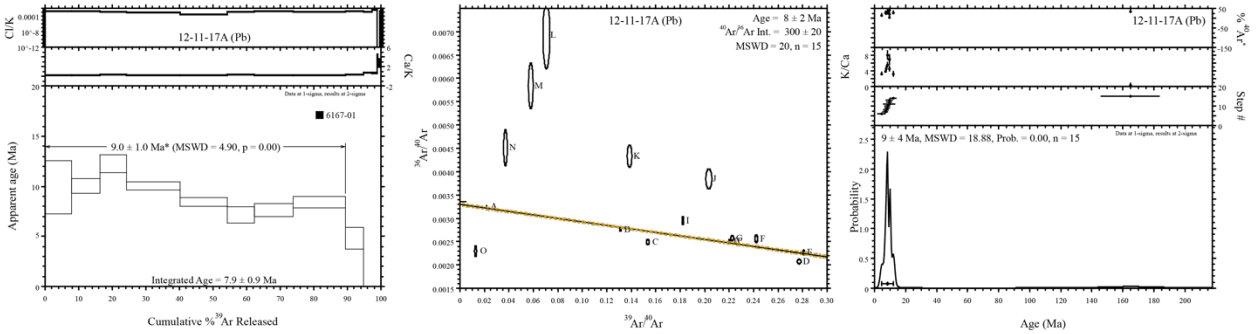
12-11-17A (Pb)
6167-01
9.0 ± 1.0 Ma* (MSWD = 4.90, p = 0.00)
Integrated Age = 7.9 ± 0.9 Ma
Cumulative %39Ar Released
Apparent age (Ma)
Cl/K
Ca/K
Age = 8 ± 2 Ma
40Ar/36Ar Int. = 300 ± 20
MSWD = 20, n = 15
36Ar/40Ar
39Ar/40Ar
9 ± 4 Ma, MSWD = 18.88, Prob. = 0.00, n = 15
K/Ca
% 40Ar*
Step #
Probability
Age (Ma)

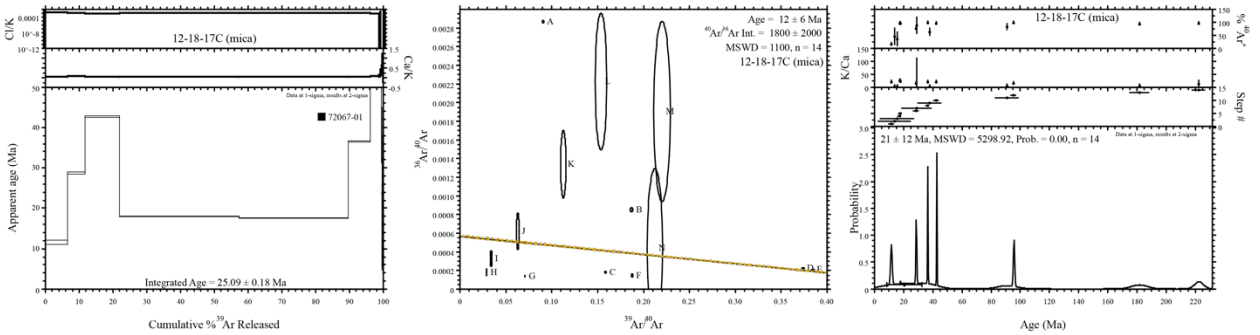
12-18-17C (mica)
72067-01
Integrated Age = 25.09 ± 0.18 Ma
Cumulative %39Ar Released
Apparent age (Ma)
Cl/K
Ca/K
Age = 12 ± 6 Ma
40Ar/36Ar Int. = 1800 ± 2000
MSWD = 1100, n = 14
12-18-17C (mica)
36Ar/40Ar
39Ar/40Ar
21 ± 12 Ma, MSWD = 5298.92, Prob. = 0.00, n = 14
K/Ca
% 40Ar*
Step #
Probability
Age (Ma)

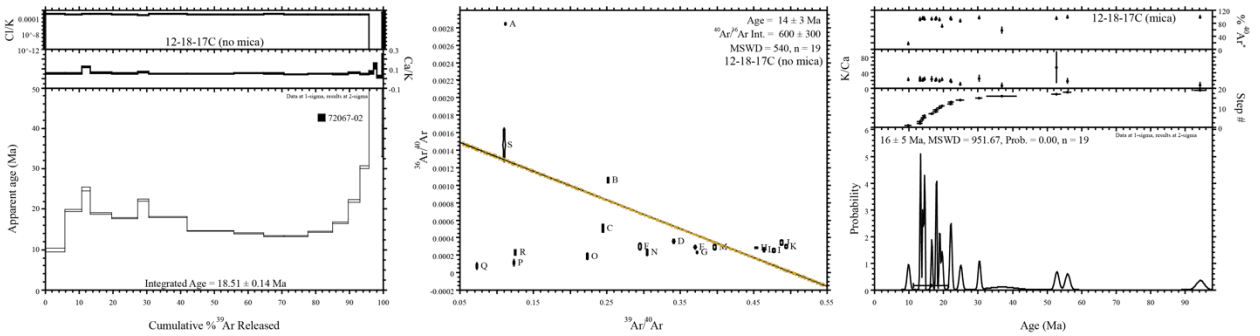
12-18-17C (no mica)
72067-02
Integrated Age = 18.51 ± 0.14 Ma
Cumulative %39Ar Released
Apparent age (Ma)
Cl/K
Ca/K
Age = 14 ± 3 Ma
40Ar/36Ar Int. = 600 ± 300
MSWD = 540, n = 19
12-18-17C (no mica)
36Ar/40Ar
39Ar/40Ar
16 ± 5 Ma, MSWD = 951.67, Prob. = 0.00, n = 19
K/Ca
% 40Ar*
Step #
Probability
Age (Ma)

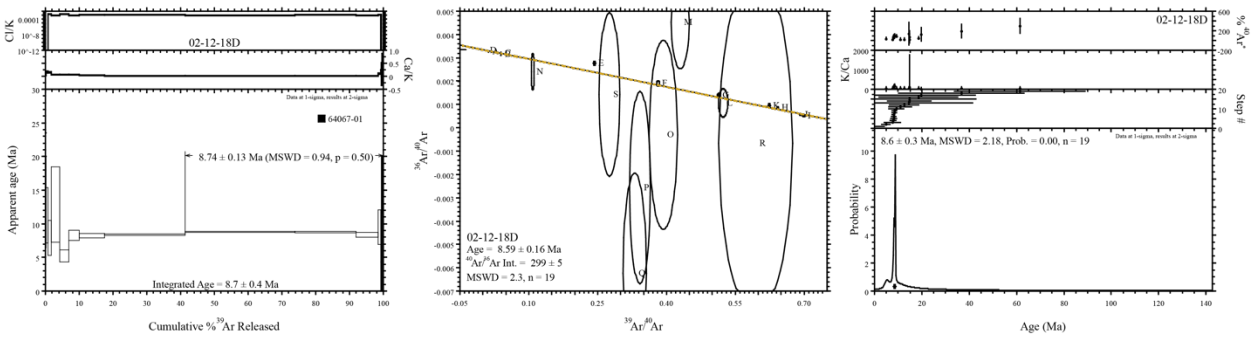
02-12-18D
64067-01
8.74 ± 0.13 Ma (MSWD = 0.94, p = 0.50)
Integrated Age = 8.7 ± 0.4 Ma
Cumulative %39Ar Released
Apparent age (Ma)
Cl/K
Ca/K
02-12-18D
Age = 8.59 ± 0.16 Ma
40Ar/36Ar Int. = 299 ± 5
MSWD = 2.3, n = 19
36Ar/40Ar
39Ar/40Ar
8.6 ± 0.3 Ma, MSWD = 2.18, Prob. = 0.00, n = 19
K/Ca
% 40Ar*
Step #
Probability
Age (Ma)

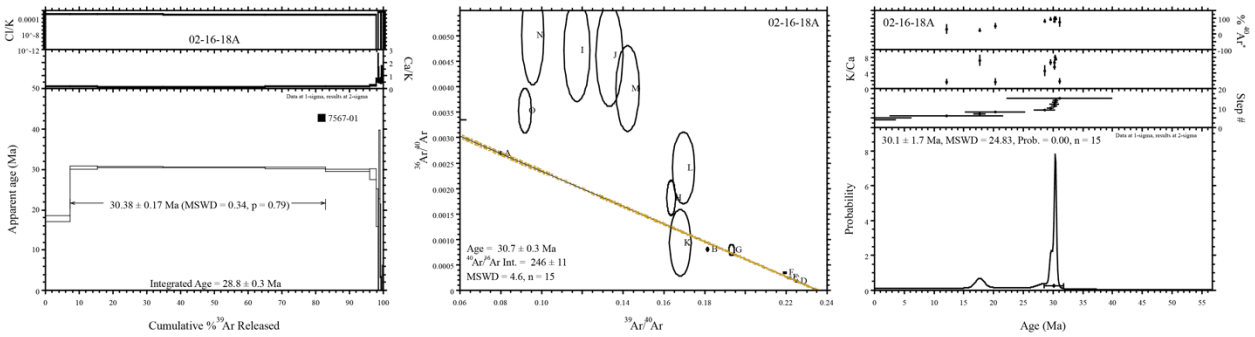
02-16-18A
7567-01
30.38 ± 0.17 Ma (MSWD = 0.34, p = 0.79)
Integrated Age = 28.8 ± 0.3 Ma
Cumulative % 39Ar Released
Apparent age (Ma)
Age = 30.7 ± 0.3 Ma
40Ar/36Ar Int. = 246 ± 11
MSWD = 4.6, n = 15
39Ar/40Ar
36Ar/40Ar
30.1 ± 1.7 Ma, MSWD = 24.83, Prob. = 0.00, n = 15
Age (Ma)
Probability
K/Ca
Step #
% 40Ar*

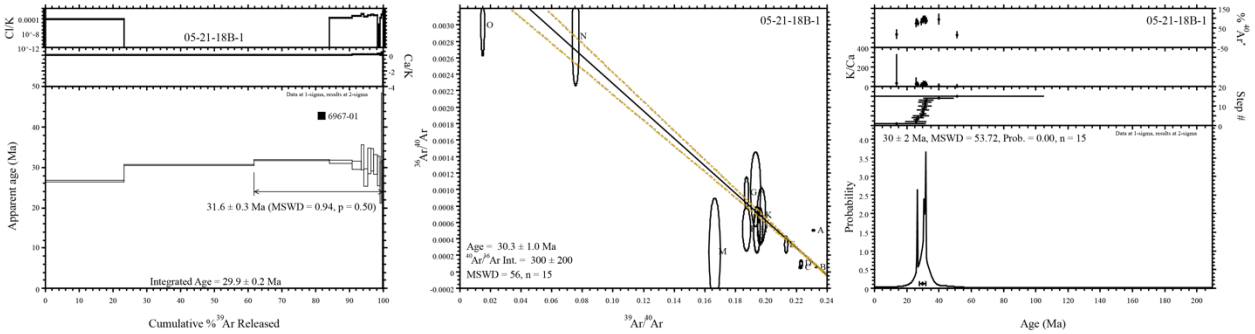
05-21-18B-1
6967-01
31.6 ± 0.3 Ma (MSWD = 0.94, p = 0.50)
Integrated Age = 29.9 ± 0.2 Ma
Cumulative % 39Ar Released
Apparent age (Ma)
Age = 30.3 ± 1.0 Ma
40Ar/36Ar Int. = 300 ± 200
MSWD = 56, n = 15
39Ar/40Ar
36Ar/40Ar
30 ± 2 Ma, MSWD = 53.72, Prob. = 0.00, n = 15
Age (Ma)
Probability
K/Ca
Step #
% 40Ar*

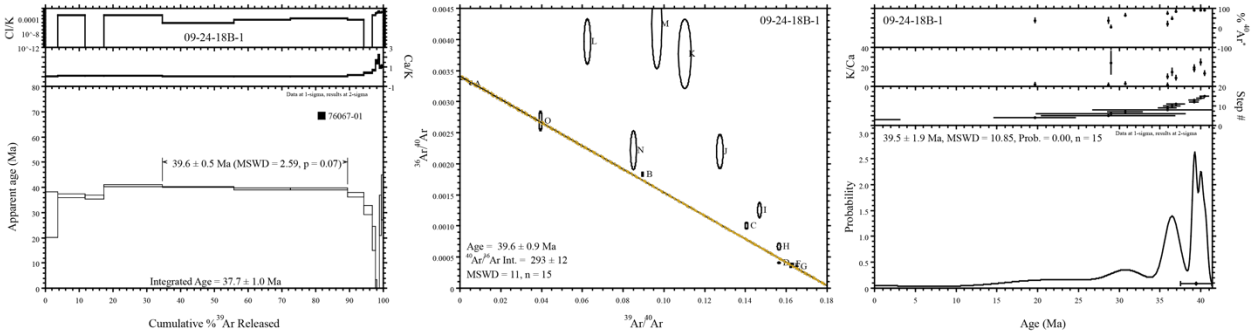
09-24-18B-1
76067-01
39.6 ± 0.5 Ma (MSWD = 2.59, p = 0.07)
Integrated Age = 37.7 ± 1.0 Ma
Cumulative % 39Ar Released
Apparent age (Ma)
Age = 39.6 ± 0.9 Ma
40Ar/36Ar Int. = 293 ± 12
MSWD = 11, n = 15
39Ar/40Ar
36Ar/40Ar
39.5 ± 1.9 Ma, MSWD = 10.85, Prob. = 0.00, n = 15
Age (Ma)
Probability
K/Ca
Step #
% 40Ar*

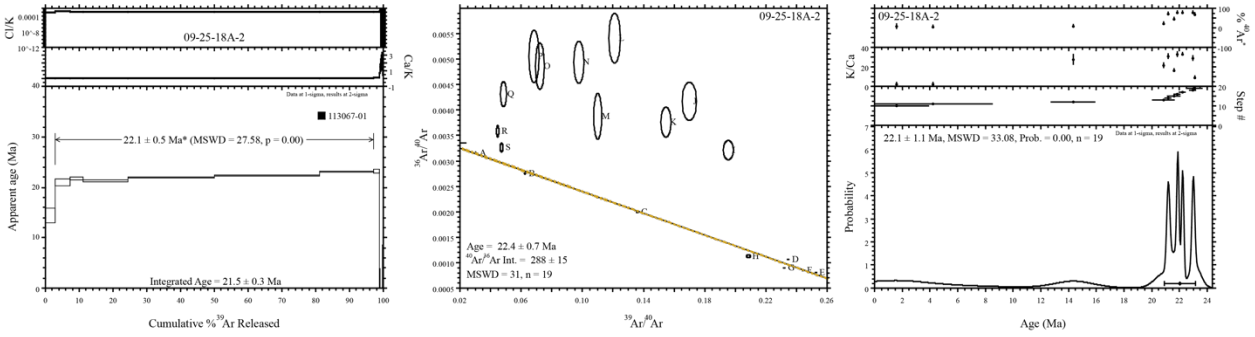
09-25-18A-2
113067-01
22.1 ± 0.5 Ma* (MSWD = 27.58, p = 0.00)
Integrated Age = 21.5 ± 0.3 Ma
Cumulative % 39Ar Released
Apparent age (Ma)
Age = 22.4 ± 0.7 Ma
40Ar/36Ar Int. = 288 ± 15
MSWD = 31, n = 19
39Ar/40Ar
36Ar/40Ar
22.1 ± 1.1 Ma, MSWD = 33.08, Prob. = 0.00, n = 19
Age (Ma)
Probability
K/Ca
Step #
% 40Ar*

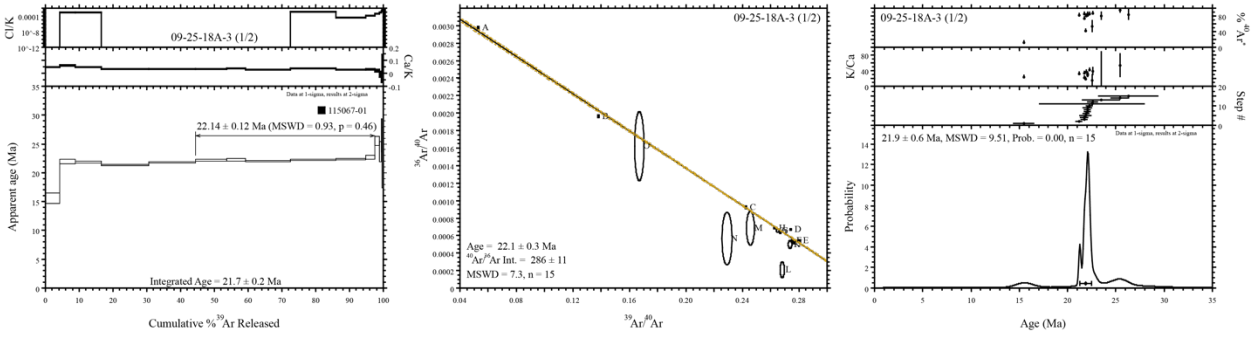
09-25-18A-3 (1/2)
115067-01
22.14 ± 0.12 Ma (MSWD = 0.93, p = 0.46)
Integrated Age = 21.7 ± 0.2 Ma
Cumulative % 39Ar Released
Apparent age (Ma)
Age = 22.1 ± 0.3 Ma
40Ar/36Ar Int. = 286 ± 11
MSWD = 7.3, n = 15
39Ar/40Ar
36Ar/40Ar
21.9 ± 0.6 Ma, MSWD = 9.51, Prob. = 0.00, n = 15
Age (Ma)
Probability
K/Ca
Step #
% 40Ar*

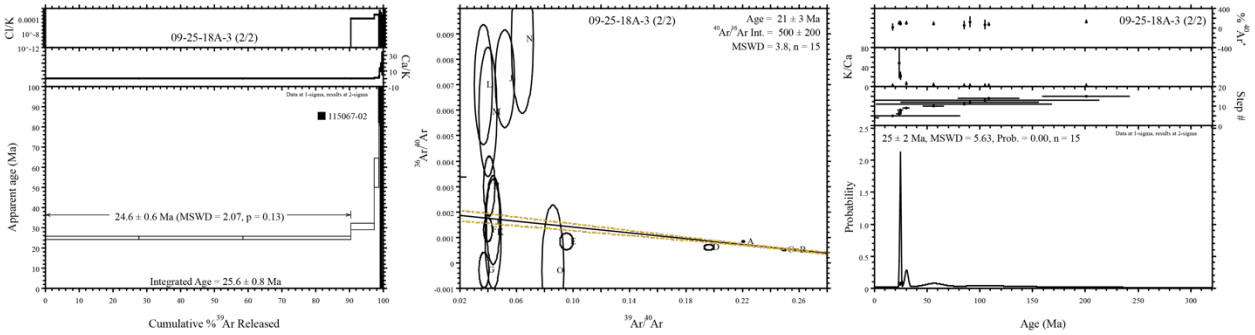
09-25-18A-3 (2/2)
Cl/K
Ca/K
Apparent age (Ma)
115067-02
24.6 ± 0.6 Ma (MSWD = 2.07, p = 0.13)
Integrated Age = 25.6 ± 0.8 Ma
Cumulative % 39Ar Released
09-25-18A-3 (2/2)
Age = 21 ± 3 Ma
40Ar/36Ar Int. = 500 ± 200
MSWD = 3.8, n = 15
36Ar/40Ar
39Ar/40Ar
09-25-18A-3 (2/2)
K/Ca
% 40Ar*
Step #
25 ± 2 Ma, MSWD = 5.63, Prob. = 0.00, n = 15
Probability
Age (Ma)

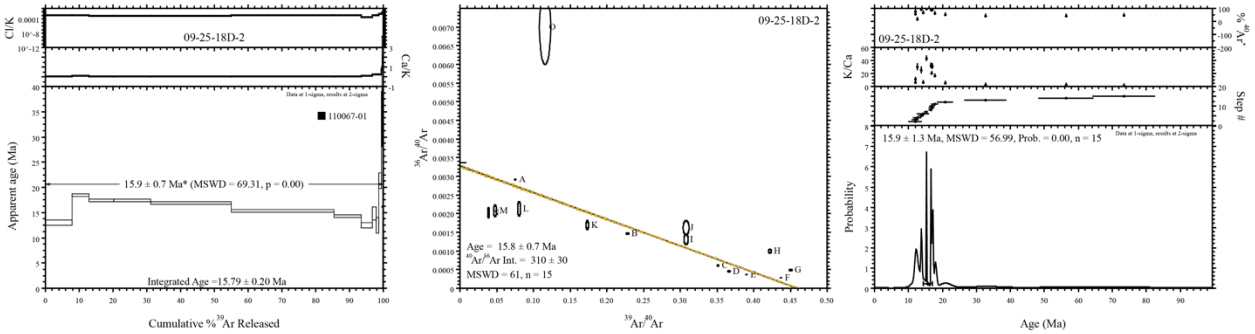
09-25-18D-2
Cl/K
Ca/K
Apparent age (Ma)
110067-01
15.9 ± 0.7 Ma* (MSWD = 69.31, p = 0.00)
Integrated Age =15.79 ± 0.20 Ma
Cumulative % 39Ar Released
09-25-18D-2
Age = 15.8 ± 0.7 Ma
40Ar/36Ar Int. = 310 ± 30
MSWD = 61, n = 15
36Ar/40Ar
39Ar/40Ar
09-25-18D-2
K/Ca
% 40Ar*
Step #
15.9 ± 1.3 Ma, MSWD = 56.99, Prob. = 0.00, n = 15
Probability
Age (Ma)

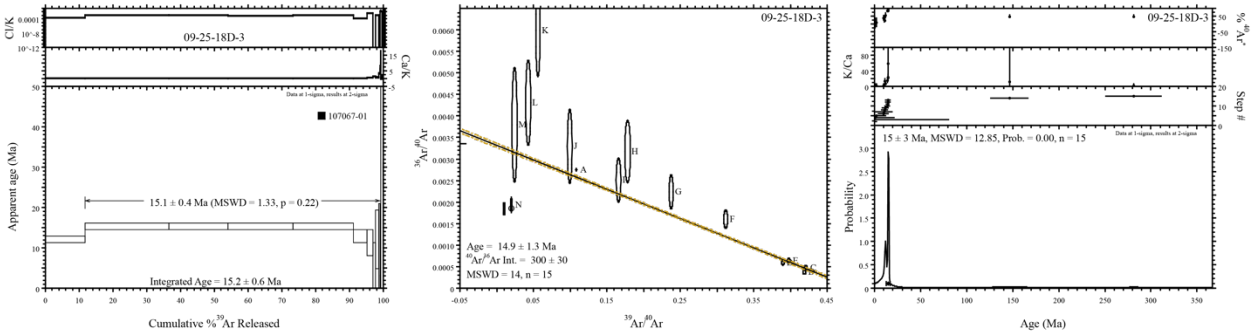
09-25-18D-3
Cl/K
Ca/K
Apparent age (Ma)
107067-01
15.1 ± 0.4 Ma (MSWD = 1.33, p = 0.22)
Integrated Age = 15.2 ± 0.6 Ma
Cumulative % 39Ar Released
09-25-18D-3
Age = 14.9 ± 1.3 Ma
40Ar/36Ar Int. = 300 ± 30
MSWD = 14, n = 15
36Ar/40Ar
39Ar/40Ar
09-25-18D-3
K/Ca
% 40Ar*
Step #
15 ± 3 Ma, MSWD = 12.85, Prob. = 0.00, n = 15
Probability
Age (Ma)

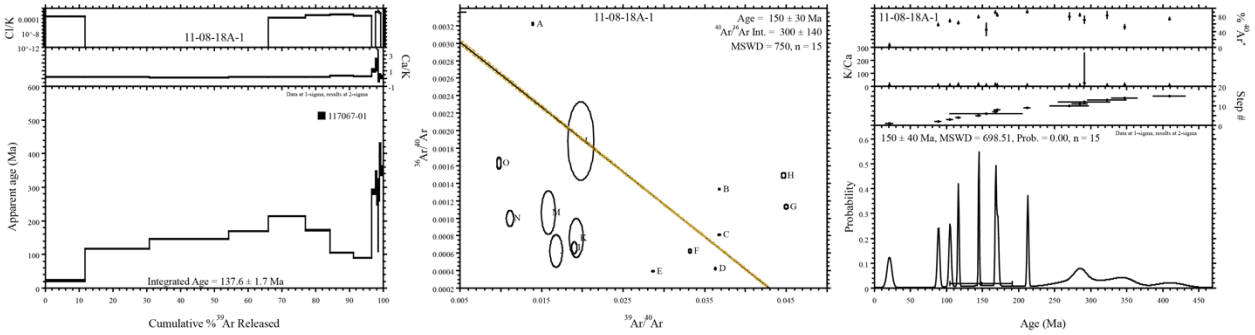
11-08-18A-1
Cl/K
Ca/K
Apparent age (Ma)
117067-01
Integrated Age = 137.6 ± 1.7 Ma
Cumulative % 39Ar Released
11-08-18A-1
Age = 150 ± 30 Ma
40Ar/36Ar Int. = 300 ± 140
MSWD = 750, n = 15
36Ar/40Ar
39Ar/40Ar
11-08-18A-1
K/Ca
% 40Ar*
Step #
150 ± 40 Ma, MSWD = 698.51, Prob. = 0.00, n = 15
Probability
Age (Ma)

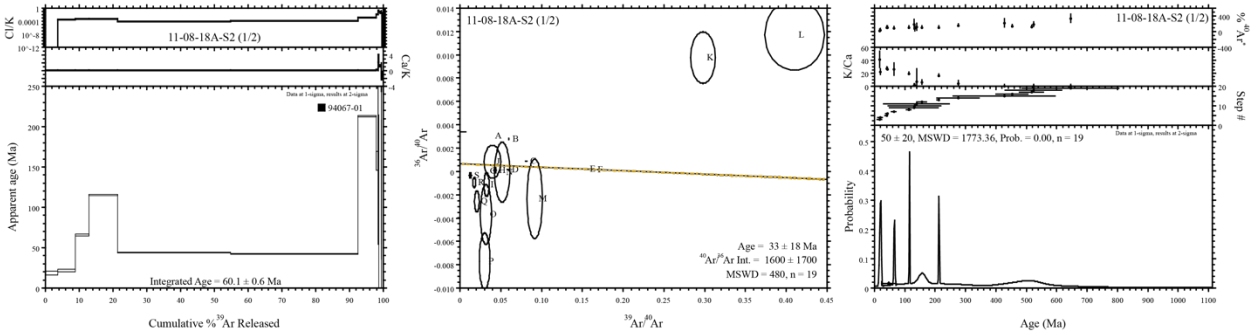
11-08-18A-S2 (1/2)
Cl/K
Ca/K
Apparent age (Ma)
94067-01
Integrated Age = 60.1 ± 0.6 Ma
Cumulative % 39Ar Released
11-08-18A-S2 (1/2)
Age = 33 ± 18 Ma
40Ar/36Ar Int. = 1600 ± 1700
MSWD = 480, n = 19
36Ar/40Ar
39Ar/40Ar
11-08-18A-S2 (1/2)
K/Ca
% 40Ar*
Step #
50 ± 20, MSWD = 1773.36, Prob. = 0.00, n = 19
Probability
Age (Ma)

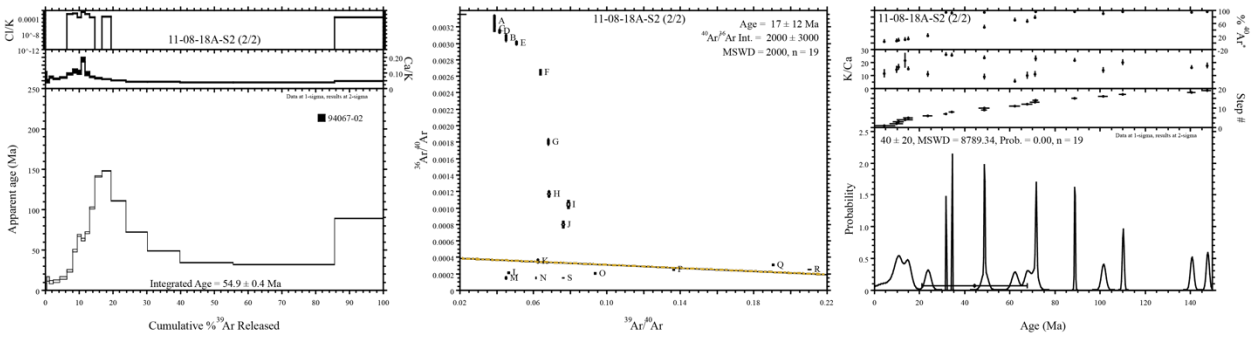
11-08-18A-S2 (2/2)
94067-02
Integrated Age = 54.9 ± 0.4 Ma
Cumulative %39Ar Released
Apparent age (Ma)
Cl/K
Ca/K
11-08-18A-S2 (2/2)
Age = 17 ± 12 Ma
40Ar/36Ar Int. = 2000 ± 3000
MSWD = 2000, n = 19
36Ar/40Ar
39Ar/40Ar
11-08-18A-S2 (2/2)
40 ± 20, MSWD = 8789.34, Prob. = 0.00, n = 19
K/Ca
% 40Ar*
Step #
Probability
Age (Ma)

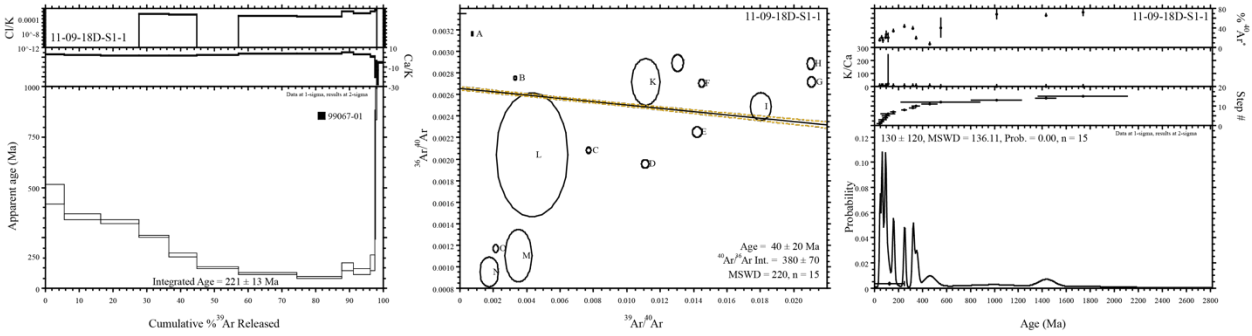
11-09-18D-S1-1
99067-01
Integrated Age = 221 ± 13 Ma
Cumulative %39Ar Released
Apparent age (Ma)
Cl/K
Ca/K
11-09-18D-S1-1
Age = 40 ± 20 Ma
40Ar/36Ar Int. = 380 ± 70
MSWD = 220, n = 15
36Ar/40Ar
39Ar/40Ar
11-09-18D-S1-1
130 ± 120, MSWD = 136.11, Prob. = 0.00, n = 15
K/Ca
% 40Ar*
Step #
Probability
Age (Ma)

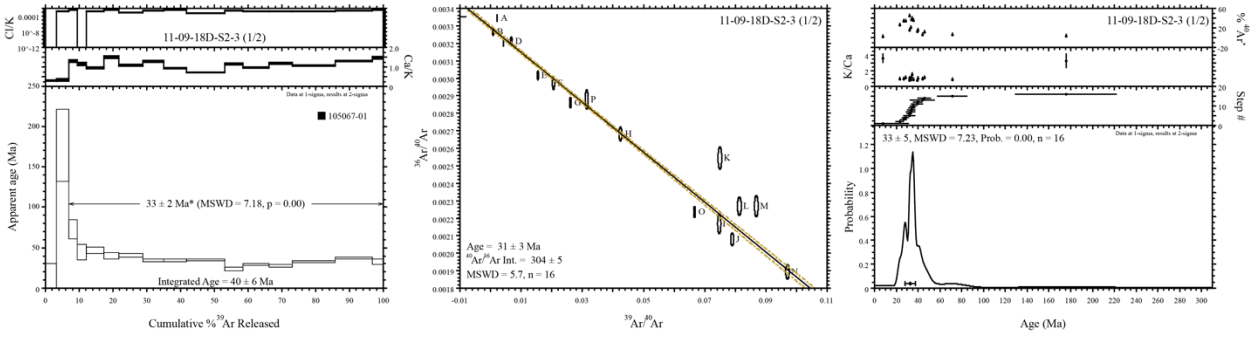
11-09-18D-S2-3 (1/2)
105067-01
33 ± 2 Ma* (MSWD = 7.18, p = 0.00)
Integrated Age = 40 ± 6 Ma
Cumulative %39Ar Released
Apparent age (Ma)
Cl/K
Ca/K
11-09-18D-S2-3 (1/2)
Age = 31 ± 3 Ma
40Ar/36Ar Int. = 304 ± 5
MSWD = 5.7, n = 16
36Ar/40Ar
39Ar/40Ar
11-09-18D-S2-3 (1/2)
33 ± 5, MSWD = 7.23, Prob. = 0.00, n = 16
K/Ca
% 40Ar*
Step #
Probability
Age (Ma)

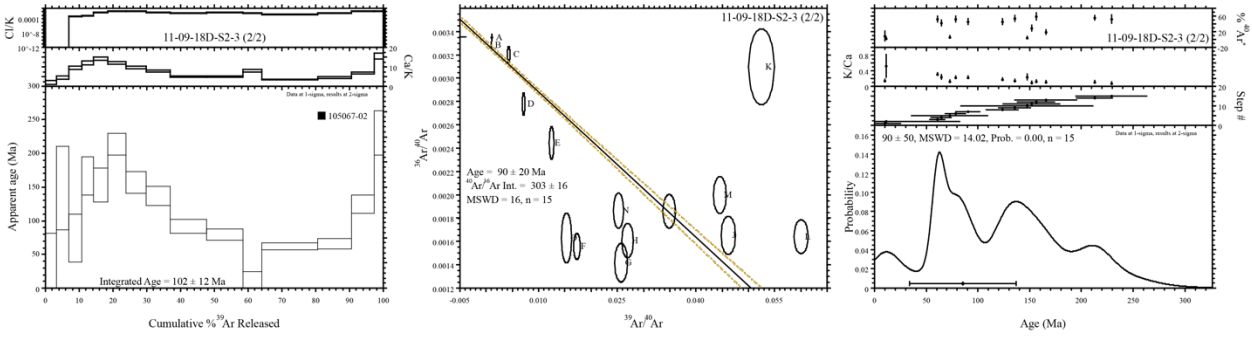
11-09-18D-S2-3 (2/2)
105067-02
Integrated Age = 102 ± 12 Ma
Cumulative %39Ar Released
Apparent age (Ma)
Cl/K
Ca/K
11-09-18D-S2-3 (2/2)
Age = 90 ± 20 Ma
40Ar/36Ar Int. = 303 ± 16
MSWD = 16, n = 15
36Ar/40Ar
39Ar/40Ar
11-09-18D-S2-3 (2/2)
90 ± 50, MSWD = 14.02, Prob. = 0.00, n = 15
K/Ca
% 40Ar*
Step #
Probability
Age (Ma)

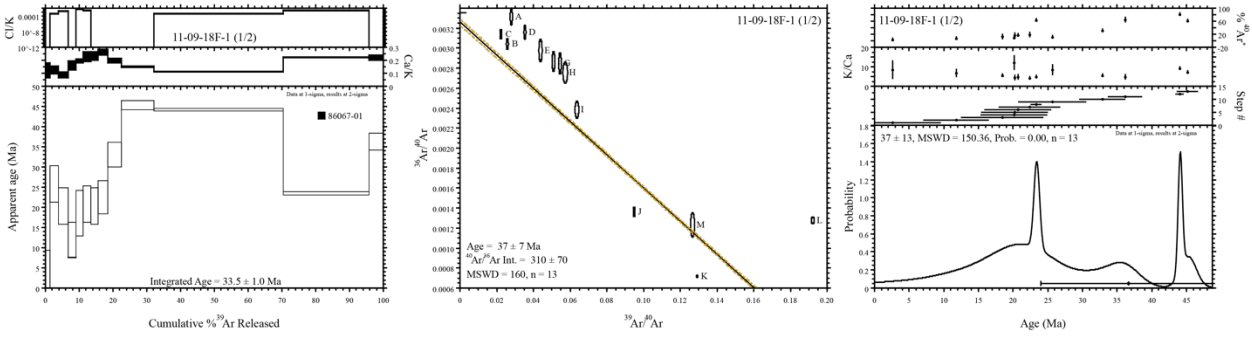
11-09-18F-1 (1/2)
86067-01
Integrated Age = 33.5 ± 1.0 Ma
Cumulative %39Ar Released
Apparent age (Ma)
Cl/K
Ca/K
11-09-18F-1 (1/2)
Age = 37 ± 7 Ma
40Ar/36Ar Int. = 310 ± 70
MSWD = 160, n = 13
36Ar/40Ar
39Ar/40Ar
11-09-18F-1 (1/2)
37 ± 13, MSWD = 150.36, Prob. = 0.00, n = 13
K/Ca
% 40Ar*
Step #
Probability
Age (Ma)

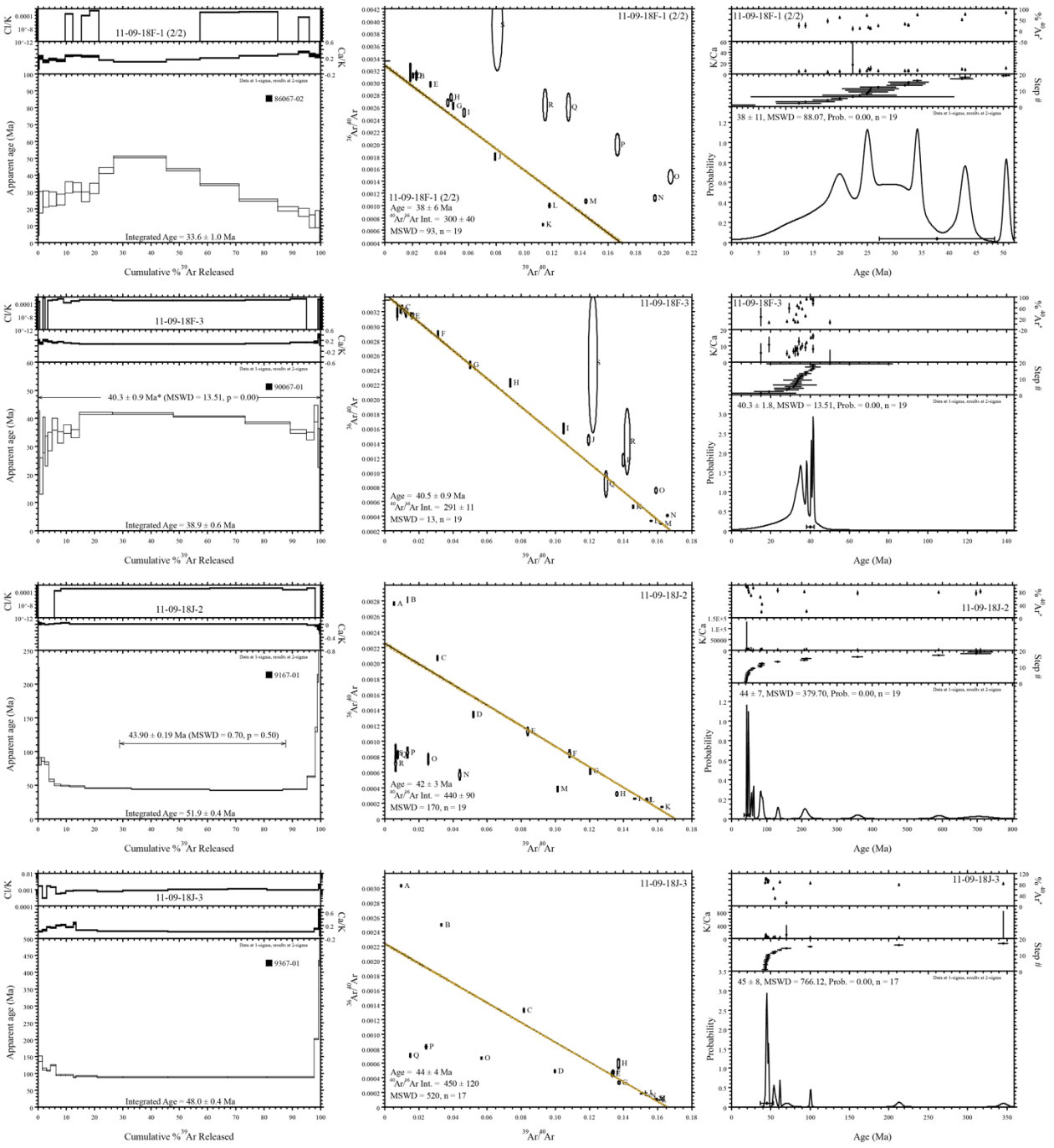
11-09-18F-1 (2/2)
Integrated Age = 33.6 ± 1.0 Ma
Cumulative % 39Ar Released
Apparent age (Ma)
11-09-18F-1 (2/2)
Age = 38 ± 6 Ma
40Ar/36Ar Int. = 300 ± 40
MSWD = 93, n = 19
39Ar/40Ar
11-09-18F-1 (2/2)
38 ± 11, MSWD = 88.07, Prob. = 0.00, n = 19
Age (Ma)
Probability
11-09-18F-3
40.3 ± 0.9 Ma* (MSWD = 13.51, p = 0.00)
Integrated Age = 38.9 ± 0.6 Ma
11-09-18F-3
Age = 40.5 ± 0.9 Ma
40Ar/36Ar Int. = 291 ± 11
MSWD = 13, n = 19
11-09-18F-3
40.3 ± 1.8, MSWD = 13.51, Prob. = 0.00, n = 19
11-09-18J-2
43.90 ± 0.19 Ma (MSWD = 0.70, p = 0.50)
Integrated Age = 51.9 ± 0.4 Ma
11-09-18J-2
Age = 42 ± 3 Ma
40Ar/36Ar Int. = 440 ± 90
MSWD = 170, n = 19
11-09-18J-2
44 ± 7, MSWD = 379.70, Prob. = 0.00, n = 19
11-09-18J-3
Integrated Age = 48.0 ± 0.4 Ma
11-09-18J-3
Age = 44 ± 4 Ma
40Ar/36Ar Int. = 450 ± 120
MSWD = 520, n = 17
11-09-18J-3
45 ± 8, MSWD = 766.12, Prob. = 0.00, n = 17

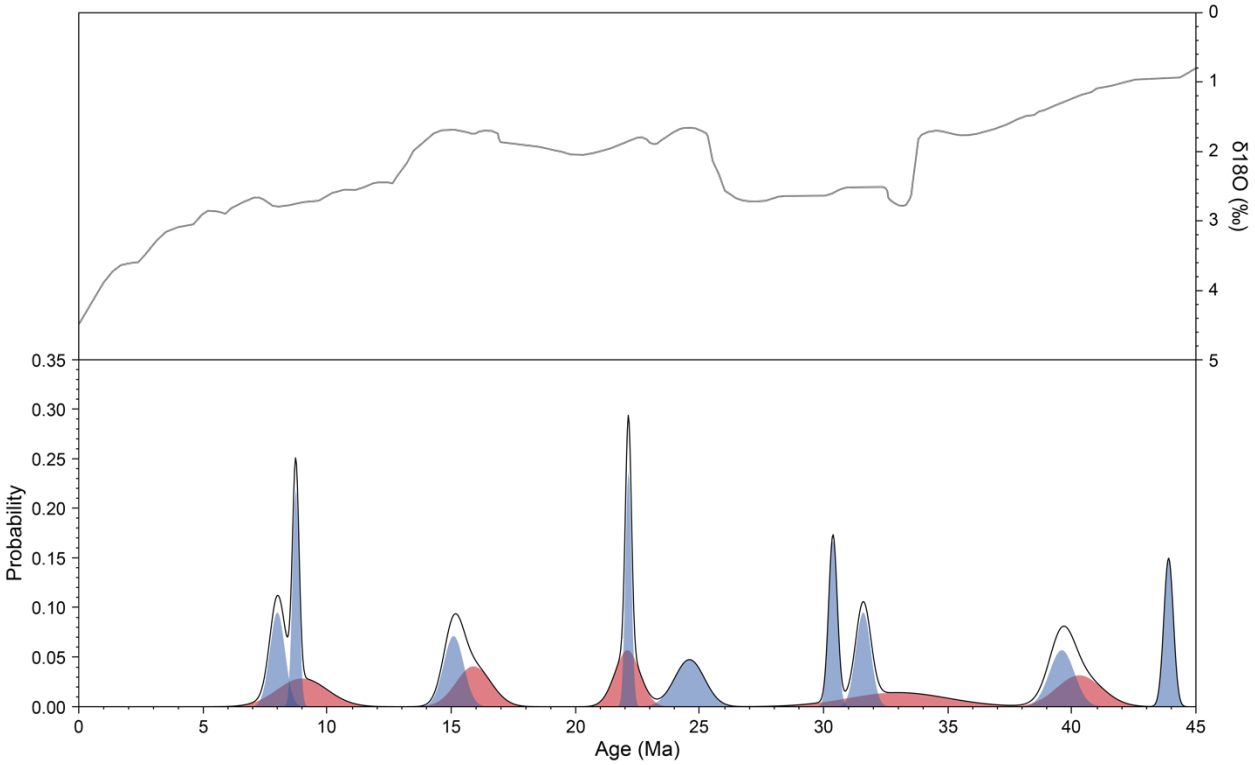

Figure 4.10. Top: $\delta^{18}O$ curve for the last 45 Ma (Zachos et al., 2001). Bottom: Probability distribution plot for all plateau ages; samples that did not yield plateaus are not shown. Well-defined plateau ages with low MSWD are shown in blue; forced plateaus are shown in red. Note that manganese oxide formation ages occur across a range of climatic regimes.

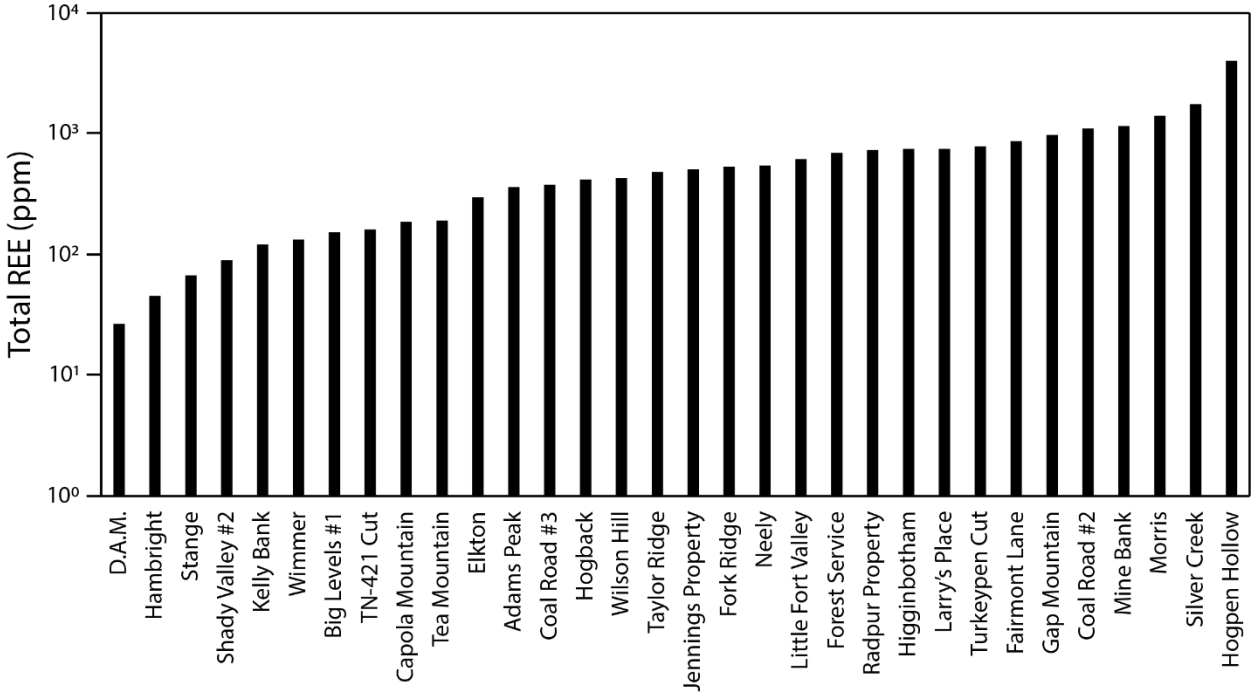

Figure 4.11. Total concentrations of REE in manganese oxides at all analyzed locations. Note that the y-axis is logarithmic, demonstrating the vast contrast in REE contents between sites and/or morphologies.

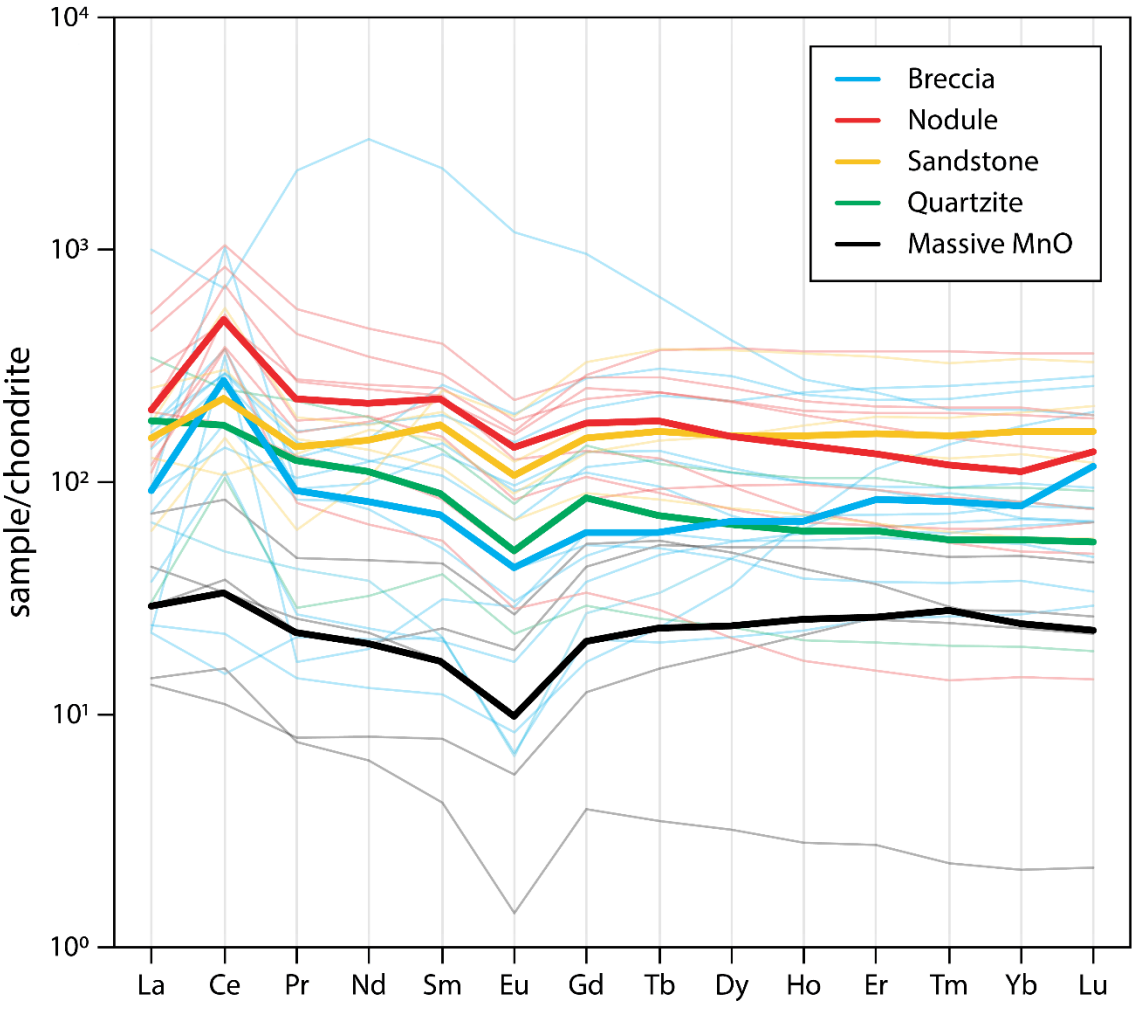

Figure 4.12. Chondrite normalized REE plots for all samples. Individual samples are shown as transparencies; median values for each morphology are indicated by opaque lines.

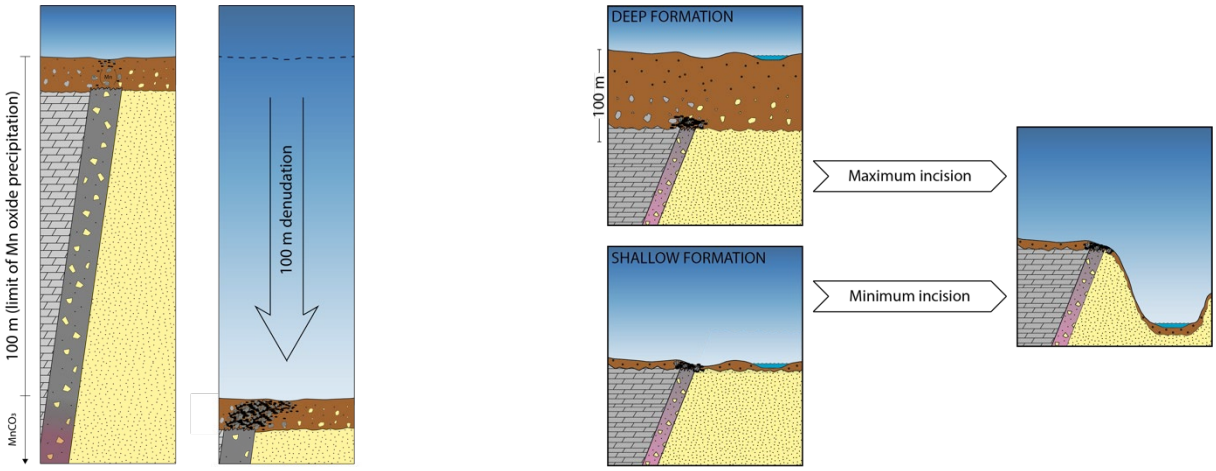

Figure 4.13. Left: Schematic image demonstrating the use of $^{40}Ar/^{39}Ar$-dated manganese oxide as a proxy for maximum denudation rates. Manganese oxides are often found along faults between carbonate (gray) and quartz-rich (yellow) units, typically having been sourced from the dissolution of manganese carbonate at depth (Varentsov, 1996). The deposits can form as breccias along the fault, or as nodules within the soil. As the landscape lowers, breccias are redissolved and reprecipitated as nodules that become more prevalent as downwasting continues. Right: Schematic images showing scenarios of maximum and minimum incision, accounting for the variable depths at which manganese oxides may form.

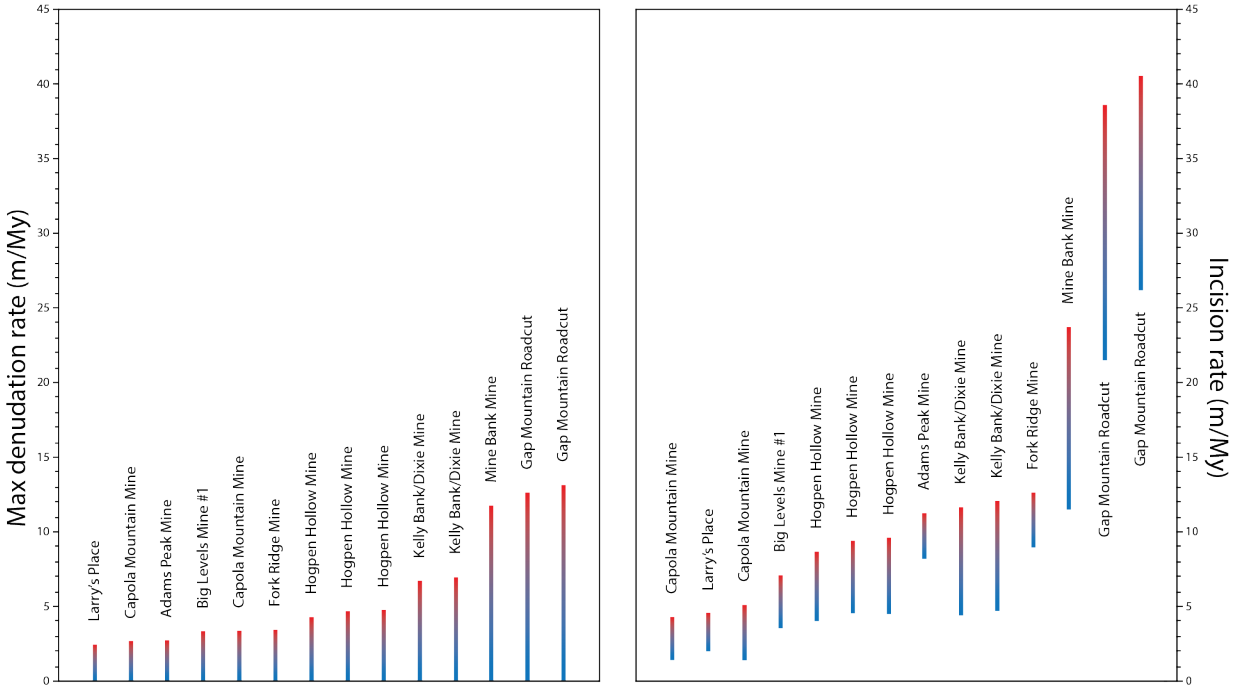

Figure 4.14. Left: Maximum local denudation rates inferred from ages of manganese oxides and assuming a formation depth of 100 m. Right: Minimum and maximum incision rates inferred from manganese oxide ages, assuming formation depths of 100 and 0 m, respectively. Both plots include 1σ age uncertainty.

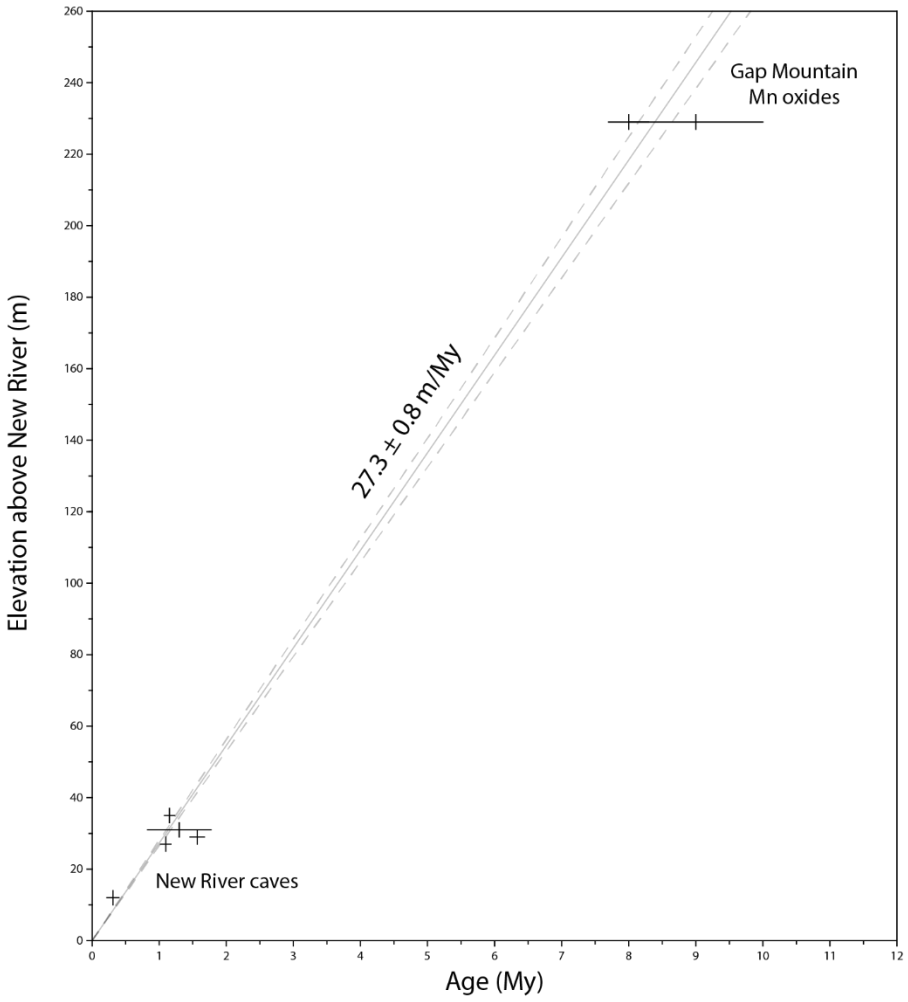

Figure 4.15. Elevation vs. age relationships for the cave sediments dated by Granger et al. (1997) and manganese oxides dated at Gap Mountain (this study). The $^{26}Al/^{10}Be$ ages have been recalculated to account for revisions in the mean-life of ^{10}Be. Incision appears to have remained constant since at least the late Miocene. Dashed lines reflect 1σ uncertainty in the incision rate, calculated following York et al. (2004).

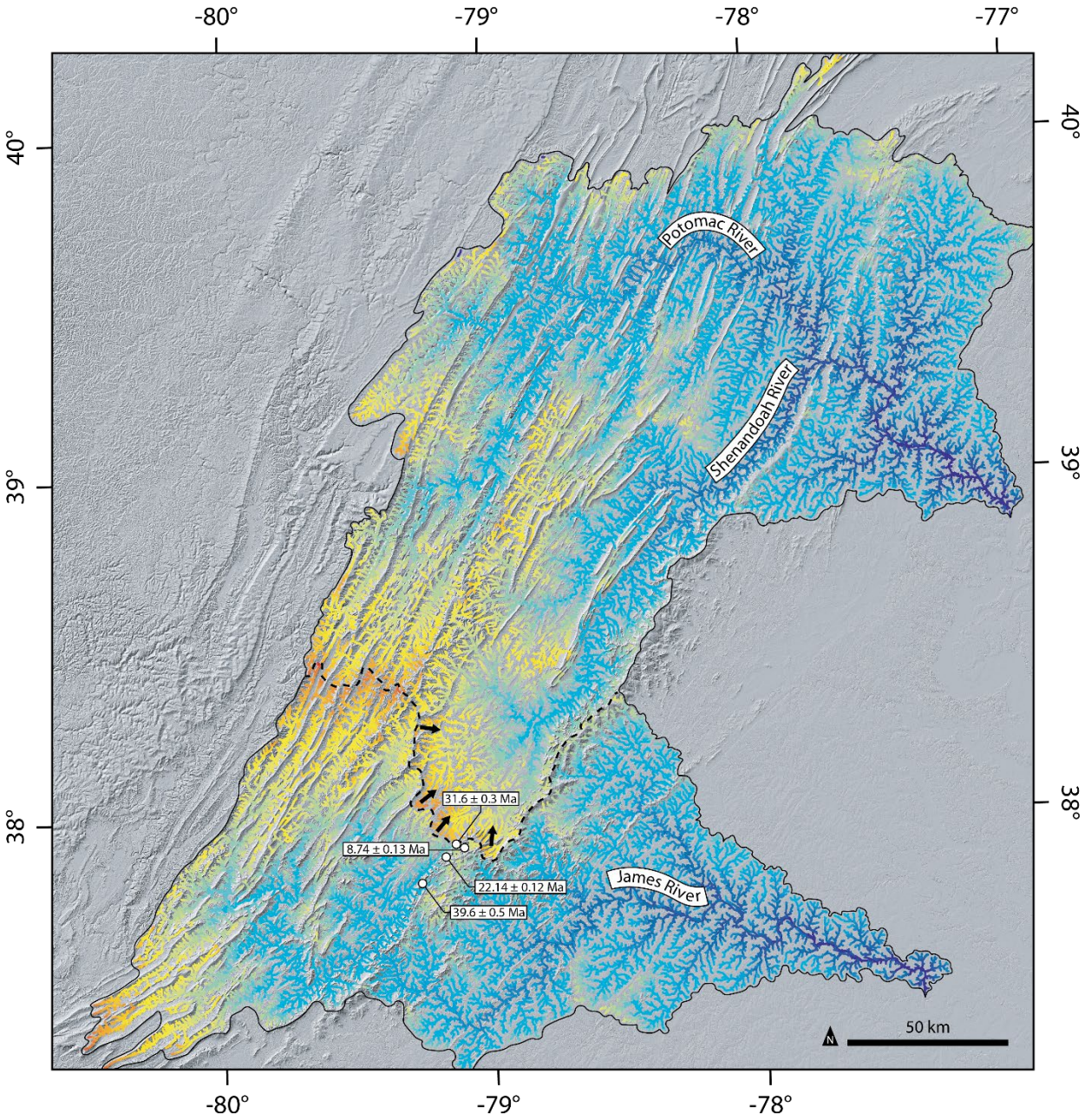

Figure 4.16. Map of χ values for the James and Potomac River watersheds. The low χ values along the upper watershed of the south fork of the Shenandoah River are consistent with its ongoing capture by the James River watershed. Inferred direction of capture indicated by arrows; plateau ages of nearby manganese oxides are also shown. Constructed from 1-arcsecond data from the National Map using TopoToolbox (Schwanghart and Scherler, 2014).

Table 4.1. Sampled locations for $^{40}Ar/^{39}Ar$ and geochemical analysis. Dated sites are highlighted in bold. Latitude and longitude are in degrees, assuming WGS84 datum. Regional differences in lithological nomenclature have been ignored here, generally opting for the Tennessee unit names. The equivalent names are as follows: Shady Dolomite - Tomstown Dolomite; Erwin Quartzite - Antietam Quartzite; Ridgeley Sandstone - Oriskany Sandstone.

Site	Latitude, longitude	Elevation (m)	Setting	Bedrock lithology
Adams Peak Mine	**37.8206, -79.2733**	**732**	**Fault (reverse)**	**Erwin Formation**
Big Levels Mine #1	**37.9371, -79.1387**	**642**	**Alluvial fan**	**Erwin Formation**
Capola Mountain Mine	**38.9705, -78.5575**	**480**	**Syncline (core)**	**Ridgeley Sandstone**
Coal Road Mine #2	37.9860, -79.0586	536	Alluvial fan	Shady Dolomite
Coal Road Mine #3	37.9870, -79.0658	543	**Alluvial fan**	Shady Dolomite
D.A.M. Mine	35.0239, -84.9086	268	Thrust sheet	Holston Formation
Fairmont Lane Prospect	39.0258, -78.5019	425	Alluvial fan	Ridgeley Sandstone
Forest Service Mines	36.4342, -82.0280	793	Syncline (limb)	Erwin Formation
Fork Ridge Mine	**37.4015, -80.6343**	**925**	**Syncline (core)**	**Keefer Sandstone**
Gap Mountain Cut	**37.2850, -80.4765**	**730**	**Wind gap**	**Keefer Sandstone**
Hambright Mine	35.0510, -84.8965	293	Thrust sheet	Lenoir Limestone
Higginbotham Mine	37.2926, -80.5122	715	Fault (reverse)	Reedsville-Eggleston
…	…	…	…	-Moccasin Formations
Hogback Mine	36.5724, -81.8320	908	Syncline (limb)	Shady Dolomite
Hogpen Hollow	**37.8988, -79.1800**	**600**	**Fault (reverse)**	**Erwin Formation**
Jennings Property Mine	35.1427, -85.0107	341	Thrust sheet	Fort Payne Formation
Kelly Bank/Dixie Mine	**37.9113, -79.1720**	**530**	**Alluvial fan**	**Shady Dolomite**
Kendall-Flick Mine	**38.3909, -78.6181**	**343**	**Alluvial fan**	**Waynesboro Formation**
Larry's Place	**39.0179, -78.0244**	**205**	**Fault (reverse)**	**Erwin Formation**
Little Fort Valley Pit	38.9161, -78.3894	444	Syncline (core)	Ridgeley Sandstone
Mine Bank Mine	**37.9237, -79.1081**	**717**	**Syncline (core)**	**Shady Dolomite**
Morris Prospect	37.2321, -80.9443	711	Alluvial fan	Keefer Sandstone
Neely Mine	36.5910, -81.8110	796	Syncline (limb)	Erwin Formation
Radpur Property Mine	35.1594, -85.1815	282	Thrust sheet	Knox Group
Shady Valley Mine #2	36.5850, -81.8180	813	Syncline (limb)	Shady Dolomite
Silver Creek Mine	37.2339, -80.9298	782	Syncline (limb)	Keefer Sandstone
Stange Mine	37.2053, -80.9312	938	Anticline (hinge)	Becraft Sandstone
Taylor Ridge Mine	36.4334, -82.0822	897	Syncline (limb)	Erwin Formation
Tea Mountain Mine	38.9675, -78.5635	496	Fault (reverse)	Ridgeley Sandstone
TN-421 Cut	36.4397, -81.7957	711	Fault (reverse)	Rome Formation
Turkeypen Cut Mine	37.9428, -79.0048	621	Alluvial fan	Erwin Formation
Wilson Hill Mine	36.3756, -81.8677	804	Fault (reverse)	Shady Dolomite
Wimmer Mine	37.5475, -80.3335	744	Thrust sheet	Keefer Sandstone

Table 4.2. Results of $^{40}Ar/^{39}Ar$ geochronology. Forced plateau ages are indicated with asterisks.

Site (type)	Sample	Integ. age (Ma)	Plateau age (Ma)	MSWD	$^{40}Ar/^{36}Ar_{int}$
Gap Mountain (breccia)	12-11-17A (Pb)	7.9 ± 0.9	9.0 ± 1.0*	4.90	300 ± 20
Gap Mountain (breccia)	12-11-17A (no Pb)	8.1 ± 0.6	8.0 ± 0.3	0.47	296 ± 7
Kendall-Flick Mine (nodule)	12-18-17C (mica)	25.09 ± 0.18	-	-	1800 ± 2000
Kendall-Flick Mine (nodule)	12-18-17C (no mica)	18.51 ± 0.14	-	-	600 ± 300
Mine Bank Mine (breccia)	02-12-18D	8.7 ± 0.4	8.74 ± 0.13	0.94	299 ± 5
Fork Ridge Mine (breccia)	02-16-18A	28.8 ± 0.3	30.38 ± 0.17	0.34	246 ± 11
Big Levels Mine #1 (sandstone)	05-21-18B-1	29.9 ± 0.2	31.6 ± 0.3	0.94	300 ± 200
Adams Peak Mine (breccia)	09-24-18B-1	37.7 ± 1.0	39.6 ± 0.5	2.59	293 ± 12
Hogpen Hollow Mine (breccia)	09-25-18A-2	21.5 ± 0.3	22.1 ± 0.5*	27.58	288 ± 15
Hogpen Hollow Mine (breccia)	09-25-18A-3 (1/2)	21.7 ± 0.2	22.14 ± 0.12	0.93	286 ± 11
Hogpen Hollow Mine (breccia)	09-25-18A-3 (2/2)	25.6 ± 0.8	24.6 ± 0.6	2.07	500 ± 200
Kelly Bank/Dixie Mine (breccia)	09-25-18D-2	15.79 ± 0.20	15.9 ± 0.7*	69.31	310 ± 30
Kelly Bank/Dixie Mine (breccia)	09-25-18D-3	15.2 ± 0.6	15.1 ± 0.4	1.33	300 ± 30
Kelly Bank/Dixie Mine (breccia)	11-08-18A-1	137.6 ± 1.7	-	-	300 ± 140
Kelly Bank/Dixie Mine (sandstone)	11-08-18A-S2 (1/2)	60.1 ± 0.6	-	-	1600 ± 1700
Kelly Bank/Dixie Mine (sandstone)	11-08-18A-S2 (2/2)	54.9 ± 0.4	-	-	2000 ± 3000
Capola Mountain Mine (breccia)	11-09-18D-S1-1	221 ± 13	-	-	380 ± 70
Capola Mountain Mine (breccia)	11-09-18D-S2-3 (1/2)	40 ± 6	33 ± 2*	7.18	304 ± 5
Capola Mountain Mine (breccia)	11-09-18D-S2-3 (2/2)	102 ± 12	-	-	303 ± 16
Capola Mountain Mine (breccia)	11-09-18F-1 (1/2)	33.5 ± 1.0	-	-	310 ± 70
Capola Mountain Mine (breccia)	11-09-18F-1 (2/2)	33.6 ± 1.0	-	-	300 ± 40
Capola Mountain Mine (breccia)	11-09-18F-3	38.9 ± 0.6	40.3 ± 0.9*	13.51	291 ± 11
Larry's Place (breccia)	11-09-18J-2	51.9 ± 0.4	43.90 ± 0.19	0.70	440 ± 90
Larry's Place (breccia)	11-09-18J-3	48.0 ± 0.4	-	-	450 ± 120

Table 4.3. Rare-earth element (REE) measurements. All values in parts per million (ppm). These measurements have been adjusted for quartz content but not normalized to typical chondrite concentrations.

Site name (sample)	**La**	**Ce**	**Pr**	**Nd**	**Sm**	**Eu**	**Gd**	**Tb**	**Dy**	**Ho**	**Er**	**Tm**	**Yb**	**Lu**	**Σ REE**
Adams Peak Mine (09-24-18B)	28	114	13	73	29	7	28	4	23	4	13	2	14	2	354
Coal Road Mine #2 (07-06-19B-3)	29	822	11	59	25	7	35	6	37	7	20	3	21	3	1085
Coal Road Mine #3 (05-21-18A)	7	281	2	11	6	2	16	3	18	4	12	2	11	2	377
Kendall-Flick Mine (Misc)	23	146	10	49	14	3	14	2	15	3	8	1	8	1	296
Fork Ridge Mine (02-16-18A)	55	234	18	74	21	5	30	6	35	7	19	3	15	2	523
Higginbotham Mine (07-25-19A-1)	43	219	15	91	51	14	72	15	91	17	47	7	51	8	743
Hogpen Hollow Mine (09-25-18A)	310	549	268	1784	437	87	247	30	130	20	51	7	43	6	3967
Jennings Property Mine (10-7-19C-1)	54	299	11	45	10	2	12	3	22	5	15	2	16	2	501
Larry's Place (11-09-18I)	50	238	20	107	38	11	54	11	71	17	53	8	57	9	744
Stange Mine (07-24-19G-2)	7	12	3	13	4	0	5	1	7	2	5	1	6	1	66
Tea Mountain Mine (06-26-19C-1)	11	89	3	14	4	1	10	2	18	4	13	2	14	2	189
TN-421 Cut (08-22-18F)	21	40	5	22	4	0	7	2	15	5	18	3	17	2	162
Wimmer Mine (09-26-18B)	7	18	2	8	2	1	4	1	11	5	24	5	36	6	130
Capola Mountain Mine (11-09-18A)	23	68	6	28	9	2	14	3	16	3	8	1	5	1	184
D.A.M. Mine (10-06-19C-2)	4	13	1	4	1	0	1	0	1	0	1	0	0	0	26
Hambright Mine (10-06-19B-3)	4	9	1	5	2	0	3	1	6	2	5	1	6	1	45
Kelly Bank/Dixie Mine (11-08-18A)	9	30	3	12	5	1	11	3	17	4	11	2	10	1	118
Shady Valley Mine #2 (08-22-18B)	13	27	3	13	3	1	5	1	8	2	5	1	5	1	89
Gap Mountain Cut (Misc)	64	566	33	150	46	9	35	6	31	5	14	2	10	2	972

Table 4.3 continued

Hogback Mine (08-22-18D)	62	144	16	66	16	4	22	4	31	7	19	3	17	2	414
Mine Bank Mine (Misc)	92	393	34	156	49	12	74	17	121	26	77	12	74	11	1150
Morris Prospect (07-24-19E-2)	139	681	53	207	57	13	59	12	71	14	41	6	40	6	1400
Radpur Property Mine (10-5-19A-5)	34	425	22	114	30	6	27	4	24	5	14	2	13	2	723
Silver Creek Mine (07-24-19C-5)	164	843	67	274	77	17	73	13	81	16	44	7	43	6	1727
Turkeypen Cut Mine (Misc)	44	308	20	109	44	12	66	11	71	14	36	5	29	4	773
Wilson Hill Mine (08-23-18C)	37	302	10	39	11	2	9	1	7	1	3	0	3	0	425
Big Levels Mine #1 (05-21-18B)	9	84	3	19	8	2	8	1	8	1	4	1	4	1	153
Little Fort Valley Pit (06-26-19D)	106	201	27	113	27	6	37	6	35	7	22	3	20	3	612
Fairmont Lane Prospect (06-26-19B-3)	56	450	23	106	39	9	45	8	50	10	28	4	27	4	860
Forest Service Mines (08-23-18I)	19	125	8	62	48	14	85	18	119	26	72	11	71	11	687
Neely Mine (08-22-18A)	78	246	19	82	22	5	23	4	25	5	14	2	12	2	539
Taylor Ridge Mine (08-23-18H)	39	86	16	100	30	6	34	7	51	13	40	6	42	7	477

Table 4.4. Correlations for select elements. Note strong correlation between aluminum and other elements in nodular samples, supporting a detrital origin.

Elements	R^2 (breccias)	R^2 (nodules)	R^2 (massive)
Mn, K	0.06	0.36	0.46
Mn, Rb	-	0.31	0.51
Mn, Sr	0.07	-	0.11
Mn, Co	-	0.22	0.03
Al, Ti	0.01	0.93	0.82
Al, Fe	0.19	0.01	0.20
Al, Nb	0.10	0.83	0.91
Al, Sn	-	0.64	0.93
Al, Ta	0.06	0.69	-
Al, Hf	0.06	0.77	-
Al, Th	0.08	0.87	0.68
Mg, La	0.01	0.23	0.91
Mg, Tm	-	0.54	0.01
Mg, Lu	0.01	0.60	0.05
Mn, Ba	0.61	0.01	0.20
Mn, As	0.33	0.37	0.43
Mn, Pb	0.02	0.04	0.02

Table 4.5. ^{10}Be measurements and derived erosion rates for quartz extracted from breccias. Concentrations are blank-corrected. Production rates are time-averaged over the past 10^5 years based on Lifton et al., (2014) and include shielding factors calculated at 10° elevation/azimuth increments according to Li (2013).

Site	**Mass (g)**	**Be carrier (µg)**	**N_{10} (10^6 at/g)**	**Shielding factor**	**P_{10} (at/g/yr)**	**E (m/My)**
Capola Mountain Mine	30.079	305.2	0.3169 ± 0.0088	0.98	6.4 ± 0.5	$11.9^{+0.4}/_{-0.4}$
Fork Ridge Mine	18.033	307.6	0.1237 ± 0.0087	0.97	9.1 ± 0.9	$43.4^{+2.3}/_{-2.2}$
Gap Mountain Roadcut	20.320	307.9	0.0883 ± 0.0046	0.95	7.7 ±0.7	$50.2^{+2.5}/_{-2.3}$
Hogpen Hollow Mine	20.886	306.3	0.0492 ± 0.0032	0.77	6.9 ±0.6	$66.5^{+3.2}/_{-3.1}$
Larry's Place	25.403	305.7	0.0697 ± 0.0037	0.96	5.0 ± 0.4	$41.9^{+1.7}/_{-1.8}$

Table 4.6. Estimates of maximum denudation rates (D_{max}), minimum river incision rates (I_{min}), and maximum incision rates (I_{max}). Asterisks denote forced plateaus. Denudation and incision uncertainties reflect 1σ age uncertainty.

Site/Mine	**Sample**	**Plateau age (Ma)**	**m arl**	**D_{max} (m/My)**	**I_{min} to I_{max} (m/My)**
Gap Mountain	12-11-17A (Pb)	9.0 ± 1.0*	229	11.1 ± 1.2	25.4 ± 2.8 – 36.6 ± 4.1
Gap Mountain	12-11-17A (no Pb)	8.0 ± 0.3	229	12.5 ± 0.5	28.6 ± 1.1 – 41.1 ± 1.5
Mine Bank	02-12-18D	8.74 ± 0.13	103	11.4 ± 0.2	11.8 ± 0.2 – 23.2 ± 0.3
Fork Ridge	02-16-18A	30.38 ± 0.17	277	3.3 ± 0.1	9.1 ± 0.1 – 12.4 ± 0.1
Big Levels #1	05-21-18B-1	31.6 ± 0.3	117	3.2 ± 0.1	3.7 ± 0.1 – 6.9 ± 0.1
Adams Peak	09-24-18B-1	39.6 ± 0.5	333	2.5 ± 0.1	8.4 ± 0.1 – 10.9 ± 0.1
Hogpen Hollow	09-25-18A-2	22.1 ± 0.5*	104	4.5 ± 0.1	4.7 ± 0.1 – 9.2 ± 0.2
Hogpen Hollow	09-25-18A-3 (1/2)	22.14 ± 0.12	104	4.5 ± 0.1	4.7 ± 0.1 – 9.2 ± 0.1
Hogpen Hollow	09-25-18A-3 (2/2)	24.6 ± 0.6	104	4.1 ± 0.1	4.2 ± 0.1 – 8.3 ± 0.2
Kelly Bank/Dixie	09-25-18D-2	15.9 ± 0.7*	75	6.3 ± 0.3	4.7 ± 0.2 – 11.0 ± 0.5
Kelly Bank/Dixie	09-25-18D-3	15.1 ± 0.4	75	6.6 ± 0.2	5.0 ± 0.1 – 11.6 ± 0.3
Capola Mountain	11-09-18D-S2-3 (1/2)	33 ± 2*	53	3.0 ± 0.2	1.6 ± 0.1 – 4.6 ± 0.3
Capola Mountain	11-09-18F-3	40.3 ± 0.9*	63	2.5 ± 0.1	1.6 ± 0.1 – 4.0 ± 0.1
Larry's Place	11-09-18J-2	43.90 ± 0.19	93	2.3 ± 0.1	2.1 ± 0.1 – 4.4 ± 0.1

4.7 References

Anthony, D. M., & Granger, D. E. (2006). Five million years of Appalachian landscape evolution preserved in cave sediments. Special papers – Geological Society of America, 404, 39.

Ashley, G. H. (1930). Age of the Appalachian peneplains. Bulletin of the Geological Society of America, 41(4), 695-700.

Bank, G., Harbor, D., & Whit Morriss, D. (1999). Quaternary erosional history of the St. Marys River, western Virginia. Banisteria, No. 13, 161-169.

Bartholomew, M. J., & Mills, H. H. (1991). Old courses of the New River: Its late Cenozoic migration and bedrock control inferred from high-level stream gravels, southwestern Virginia. Geological Society of America Bulletin, 103(1), 73-81.

Beauvais, A., Ruffet, G., Hénocque, O., & Colin, F. (2008). Chemical and physical erosion rhythms of the West African Cenozoic morphogenesis: the ^{39}Ar-^{40}Ar dating of supergene K-Mn oxides. Journal of Geophysical Research: Earth Surface, 113(F4).

Bentley Sr, S. J., Blum, M. D., Maloney, J., Pond, L., & Paulsell, R. (2016). The Mississippi River source-to-sink system: Perspectives on tectonic, climatic, and anthropogenic influences, Miocene to Anthropocene. Earth-Science Reviews, 153, 139-174.

Biryol, C. B., Wagner, L. S., Fischer, K. M., & Hawman, R. B., (2016). Relationship between observed upper mantle structures and recent tectonic activity across the Southeastern United States. Journal of Geophysical Research: Solid Earth.

Bonnet, N. J., Beauvais, A., Arnaud, N., Chardon, D., & Jayananda, M. (2014). First ^{40}Ar/^{39}Ar dating of intense Late Palaeogene lateritic weathering in Peninsular India. Earth and Planetary Science Letters, 386, 126-137.

Bridge, J., (1950). Bauxite deposits of the southeastern United States. Snyder, FG.

Bonnet, N. J., Beauvais, A., Arnaud, N., Chardon, D., & Jayananda, M. (2016). Cenozoic lateritic weathering and erosion history of Peninsular India from ^{40}Ar/^{39}Ar dating of supergene K–Mn oxides. Chemical Geology, 446, 33-53.

Boynton, W. V. (1984). Cosmochemistry of the rare earth elements: meteorite studies. In Developments in geochemistry (Vol. 2, pp. 63-114). Elsevier.

Carmichael, S. K., Doctor, D. H., Wilson, C. G., Feierstein, J., & McAleer, R. J. (2017). New insight into the origin of manganese oxide ore deposits in the Appalachian Valley and Ridge of northeastern Tennessee and northern Virginia, USA. GSA Bulletin, 129(9-10), 1158-1180.

Chan, M. A., Parry, W. T., Petersen, E. U., & Hall, C. M. (2001). $^{40}Ar/^{39}Ar$ age and chemistry of manganese mineralization in the Moab and Lisbon fault systems, southeastern Utah. Geology, 29(4), 331-334.

Davis WM. 1899. The geographical cycle. Geographical Journal 14: 481–504.

Davis, W. M. (1902). Baselevel, grade and peneplain. The Journal of Geology, 10(1), 77-111.

Doctor, D. H., McAleer, R. J., Carmichael, S. K., & Kunk, M. J. (2018). $^{40}Ar/^{39}Ar$ ages of manganese oxide ores in surficial and bedrock deposits of the central Appalachian Mountains. GSA Abstracts with Programs, Vol 50, No. 3.

Feng, J. L. (2010). Behaviour of rare earth elements and yttrium in ferromanganese concretions, gibbsite spots, and the surrounding terra rossa over dolomite during chemical weathering. Chemical Geology, 271(3-4), 112-132.

Force, E. R., & Cox, L. J. (1991). Manganese contents of some sedimentary rocks of Paleozoic age in Virginia. US Government Printing Office.

Franceschelli, M., Puxeddu, M., Carcangiu, G., Gattiglio, M., & Pannuti, F. (1996). Breccia-hosted manganese-rich minerals of Alpi Apuane, Italy: a marine, redox-generated deposit. Lithos, 37(4), 309-333.

Gallen, S. F., Wegmann, K. W., & Bohnenstiehl, D. R. (2013). Miocene rejuvenation of topographic relief in the southern Appalachians. GSA Today, 23(2), 4-10.

Gallen, S. F. (2018). Lithologic controls on landscape dynamics and aquatic species evolution in post-orogenic mountains. Earth and Planetary Science Letters, 493, 150-160.

Gallen, S. F., & Thigpen, J. R. (2018). Lithologic controls on focused erosion and intraplate earthquakes in the eastern Tennessee seismic zone. Geophysical Research Letters, 45(18), 9569-9578.

Galloway, W. E., Whiteaker, T. L., & Ganey-Curry, P. (2011). History of Cenozoic North American drainage basin evolution, sediment yield, and accumulation in the Gulf of Mexico basin. Geosphere, 7(4), 938-973.

Granger, D. E., Kirchner, J. W., & Finkel, R. C. (1997). Quaternary downcutting rate of the New River, Virginia, measured from differential decay of cosmogenic ^{26}Al and ^{10}Be in cave-deposited alluvium. Geology, 25(2), 107-110.

Granger, D. E., Fabel, D., & Palmer, A. N. (2001). Pliocene− Pleistocene incision of the Green River, Kentucky, determined from radioactive decay of cosmogenic ^{26}Al and ^{10}Be in Mammoth Cave sediments. Geological Society of America Bulletin, 113(7), 825-836.

Hack, J. T. (1960). Interpretation of erosional topography in humid temperate climate. Am. Jour. Sci., v. 258-A, 80.97.

Hack, J. T. (1965). Geomorphology of the Shenandoah Valley, Virginia, and West Virginia, and origin of the residual ore deposits (p. 84). US Govt. Print. Off.

Hack, J. T., (1982). Physiographic divisions and differential uplift in the Piedmont and Blue Ridge (No. 1265). US Govt. Print. Off.

Hack, J. T. (1989). Geomorphology of the Appalachian highlands. The Appalachian-Ouachita Orogen in the United States, The Geology of North America, 2, 459-470.

Harder, E. C. (1910). Manganese deposits of the United States, with sections on foreign deposits, chemistry and uses. US Geol. Surv., Bulletin 427.

Hewett, D. F. (1916). Some manganese mines in Virginia and Maryland. US Govt. Print. Off.

Hewett, D. F., & Fleischer, M. (1960). Deposits of the manganese oxides. Economic Geology, 55(1), 1-55.

Houser, B. (1981). Erosional history of the New River, Southern Appalachians, Virginia. U.S. Geol. Surv., Open-File Report 81-771.

Jordan, D. B., & Burgess, R. (2007). A Miocene Fault in South-East Ireland Revealed by ^{40}Ar-^{39}Ar Dating of Hydrothermal Cryptomelane. Irish Journal of Earth Sciences, 55-61.

King, P. B. (1949). The floor of the Shenandoah Valley. American Journal of Science, 73-93.

King, P. B. (1950). Geology of the Elkton area, Virginia. US Geol. Surv. Prof. Paper 230.

King, P. B., Ferguson, H. W., & Hamilton, W. (1960). Geology of northeasternmost Tennessee, with a section on the description of the basement rocks (No. 311).

Kiracofe, Z. A., Henika, W. S., & Schreiber, M.E. (2017). Assessing the geological sources of manganese in the Roanoke River watershed, Virginia. Environmental and Engineering Geoscience, 23(1), 43-64.

Ladd, H. S., Stead, F. W. (1944). Manganese deposits of the Flat Top and Round Mountain districts, Bland and Giles Counties, Virginia. U.S. Geological Survey, Bulletin 940-H.

Lee, J. Y., Marti, K., Severinghaus, J. P., Kawamura, K., Yoo, H. S., Lee, J. B., & Kim, J. S. (2006). A redetermination of the isotopic abundances of atmospheric Ar. Geochimica et Cosmochimica Acta, 70(17), 4507-4512.

Li, Y. K. (2013). Determining topographic shielding from digital elevation models for cosmogenic nuclide analysis: a GIS approach and field validation. Journal of Mountain Science, 10(3), 355-362.

Lifton, N., Sato, T., & Dunai, T. J. (2014). Scaling in situ cosmogenic nuclide production rates using analytical approximations to atmospheric cosmic-ray fluxes. Earth and Planetary Science Letters, 386, 149-160.

Liu, L. (2014). Rejuvenation of Appalachian topography caused by subsidence-induced differential erosion. Nature Geoscience, 7(7), 518-523.

Marshall, J. A., Roering, J. J., Bartlein, P. J., Gavin, D. G., Granger, D. E., Rempel, A. W., Praskievicz, S. J., and Hales, T. C. (2015). Frost for the trees: Did climate increase erosion in unglaciated landscapes during the late Pleistocene?. Science advances, 1(10), e1500715.

Matmon, A., Bierman, P. R., Larsen, J., Southworth, S., Pavich, M., Finkel, R., & Caffee, M. (2003). Erosion of an ancient mountain range, the Great Smoky Mountains, North Carolina and Tennessee. American Journal of Science, 303(9), 817-855.

Maynard, J. B. (2003). Manganiferous sediments, rocks, and ores (Vol. 7, p. 407).

Miller, S. R., Sak, P. B., Kirby, E., & Bierman, P. R. (2013). Neogene rejuvenation of central Appalachian topography: Evidence for differential rock uplift from stream profiles and erosion rates. Earth and Planetary Science Letters, 369, 1-12.

Miser, H. D. (1950). Manganese deposits of the southeastern states. In Snyder, FG, Symposium on mineral resources of the southeastern United States (pp. 152-169).

Nicholson, K. (1992). Contrasting mineralogical-geochemical signatures of manganese oxides; guides to metallogenesis. Economic Geology, 87(5), 1253-1264.

Nishiizumi, K., Imamura, M., Caffee, M. W., Southon, J. R., Finkel, R. C., & McAninch, J. (2007). Absolute calibration of ^{10}Be AMS standards. Nuclear Instruments and Methods in Physics Research Section B: Beam Interactions with Materials and Atoms, 258(2), 403-413.s

Odom, W. E., Hofmann, F., Van Arsdale, R. B., Granger, D. E. (2020). New $^{26}Al/^{10}Be$ and (U-Th)/He constraints on the age of the Upland Complex, central Mississippi River Valley. Geomorphology, https://doi.org/10.1016/j.geomorph.2020.107448.

Parc, S., Nahon, D., Tardy, Y., & Vieillard, P. (1989). Estimated solubility products and fields of stability for cryptomelane, nsutite, birnessite, and lithiophorite based on natural lateritic weathering sequences. American Mineralogist, 74(3-4), 466-475.

Pazzaglia, F. J., & Brandon, M. T. (1996). Macrogeomorphic evolution of the post-Triassic Appalachian Mountains determined by deconvolution of the offshore basin sedimentary record. Basin Research, 8(3), 255-278.

Poag, C. W., & Sevon, W. D. (1989). A record of Appalachian denudation in postrift Mesozoic and Cenozoic sedimentary deposits of the US middle Atlantic continental margin. Geomorphology, 2(1-3), 119-157.

Prince, P. S., Bartholomew, M. J., Schultz, A. P. (2019). Geologic map of the Newport quadrangle, Virginia. Virginia Department of Mines, Minerals, and Energy, Open-File Report 2019-10.

Rader, E. K., Biggs, T. H., & Coiner, L. V. (2013). Interstate 81 digital geologic compilation: Toms Brook quadrangle, Virginia. Virginia Division of Geology and Mineral Resources, Open-File Report 2013-06.

Reich, M., & Vasconcelos, P. M. (2015). Geological and economic significance of supergene metal deposits. Elements, 11(5), 305-310.

Reiners, P. W., Carlson, R. W., Renne, P. R., Cooper, K. M., Granger, D. E., McLean, N. M., & Schoene, B. (2018). Geochronology and thermochronology. John Wiley & Sons.

Ren, Z., & Vasconcelos, P. M. (2019). Argon diffusion in hypogene and supergene alunites: Implications to geochronology and thermochronometry on Earth and Mars. Geochimica et Cosmochimica Acta, 262, 166-187.

Rodgers, J. (1945). Manganese content of the Shady dolomite in Bumpass Cove, Tennessee. Economic Geology, 40(2), 129-135.

Rodgers, J. (1953). Geologic map of east Tennessee with explanatory text. Tennessee Division of Geology, Bulletin no. 58 [pt. 2, 167 p.].

Rovere, A., Raymo, M. E., Mitrovica, J. X., Hearty, P. J., O'Leary, M. J., & Inglis, J. D. (2014). The Mid-Pliocene sea-level conundrum: Glacial isostasy, eustasy and dynamic topography. Earth and Planetary Science Letters, 387, 27-33.

Rowley, D. B., Forte, A. M., Moucha, R., Mitrovica, J. X., Simmons, N. A., & Grand, S. P. (2013). Dynamic topography change of the eastern United States since 3 million years ago. Science, 340(6140), 1560-1563.

Ruffet, G., Innocent, C., Michard, A., Féraud, G., Beauvais, A., Nahon, D., & Hamelin, B. (1996). A geochronological $^{40}Ar/^{39}Ar$ and $^{87}Rb/^{81}Sr$ study of K-Mn oxides from the weathering sequence of Azul, Brazil. Geochimica et cosmochimica Acta, 60(12), 2219-2232.

Schultz, A., Bartholomew, M.J., Lewis, S.E. (1991). Map showing surficial and generalized bedrock geology and accompanying side-looking airborne radar image of the Radford 30' x 60' quadrangle, Virginia and West Virginia. U.S. Geological Survey, Miscellaneous Investigations Series Map I-2170-A.

Schwanghart, W., & Scherler, D. (2014). TopoToolbox 2-MATLAB-based software for topographic analysis and modeling in Earth surface sciences. Earth Surface Dynamics, 2(1), 1.

Stose, G. W. (1927). Possible post-Cretaceous faulting in the Appalachians. Bulletin of the Geological Society of America, 38(3), 493-504.

Stose, G. W., & Schrader, F. C. (1923). Manganese deposits of east Tennessee (No. 737). US Government Printing Office.

Swingle, G.D., Finlayson, C.P., Luther, E.T. (1964). Geologic map and mineral resources summary of the Daisy quadrangle. Tennessee Division of Geology, Geologic Quadrangle Map 112 NW.

Varentsov, I.M. (1996). Manganese Ores of the Supergene Zone: Geochemistry of Formation: Dordrecht, Netherlands, Kluwer Academic Publishers, 342 p., doi:10 .1007/97894017-21745.

Vasconcelos, P.M. (1996). Geochronological evidence for the preservation of Cretaceous weathering profiles in northwestern Queens- land. In Mesozoic Geology of the Eastern Australia Plate Conference, Geol. Soc. Aust. Extended Abstr. 43:543–544 (Abstr.)

Vasconcelos, P.M. (1998). Geochronology of weathering in the Mount Isa and Charters Towers regions, northern Queensland. Restricted Rep. 68R/E&M Rep. 452R, Perth, Australia: CRC LEME

Vasconcelos, P. M. (1999). K-Ar and $^{40}Ar/^{39}Ar$ geochronology of weathering processes. Annual Review of Earth and Planetary Sciences, 27(1), 183-229.

Vasconcelos, P. M., & Carmo, I. D. O. (2018). Calibrating denudation chronology through $^{40}Ar/^{39}Ar$ weathering geochronology. Earth-Science Reviews, 179, 411-435.

Vasconcelos, P. M., Becker, T. A., Renne, P. R., & Brimhall, G. H. (1992). Age and duration of weathering by ^{40}K-^{40}Ar and $^{40}Ar/^{39}Ar$ analysis of potassium-manganese oxides. Science, 258(5081), 451-455.

Vasconcelos, P.M., Becker, T.A., Renne, P.R., Brimhall G.H. (1994). Direct dating of weathering phenomena by K-Ar and $^{40}Ar/^{39}Ar$ analysis of supergene K-Mn oxides. Geochim. Cosmochim. Acta 58:1635–65

Vasconcelos, P. M., Reich, M., & Shuster, D. L. (2015). The paleoclimatic signatures of supergene metal deposits. Elements, 11(5), 317-322.

Wagner, L. S., Stewart, K., & Metcalf, K., (2012). Crustal-scale shortening structures beneath the Blue Ridge Mountains, North Carolina, USA. Lithosphere, 4(3), 242-256.

Werner, H. J. (1965). Geology of the Vesuvius quadrangle, Virginia. Virginia Division of Mineral Resources, Report of Investigations 7.

Willett, S. D., McCoy, S. W., Perron, J. T., Goren, L., & Chen, C. Y. (2014). Dynamic reorganization of river basins. Science, 343(6175).

Wilson, R.L. (1983). Geologic map and mineral resources summary of the Snow Hill quadrangle. Tennessee Division of Geology, Geologic Quadrangle Map 112 NE.

York, D., Evensen, N. M., Martinez, M. L., & De Basabe Delgado, J. (2004). Unified equations for the slope, intercept, and standard errors of the best straight line. American Journal of Physics, 72(3), 367-375.

Young, R. S., Rader, E. K., Coiner, L. V., & Heller, M. J. (2014). Interstate 81 corridor digital geologic compilation: Woodstock quadrangle, Virginia. Virginia Division of Geology and Mineral Resources, Open-File Report 2014-07.

Zachos, J., Pagani, M., Sloan, L., Thomas, E., & Billups, K. (2001). Trends, rhythms, and aberrations in global climate 65 Ma to present. Science, 292(5517), 686-693.

CHAPTER 5. A PROBABLE HEMPHILLIAN MINIMUM BURIAL AGE FOR THE GRAY FOSSIL SITE, TN FROM A COSMOGENIC $^{26}AL/^{10}BE$ DEPTH PROFILE

5.1 Introduction

The Gray Fossil Site (GFS) is a sinkhole complex located in Washington County near Gray, TN (36.3859°N, 82.4987°W) that was discovered in 2000 during a Tennessee Department of Transportation (TDOT) construction project. It was subsequently preserved because it represents one of the most diverse late Cenozoic fossil assemblages in eastern North America (Parmalee et al, 2002; Wallace, 2004; Wallace and Wang, 2004; Samuels et al, 2018). GFS hosts numerous Late Neogene flora and fauna whose presence provides important evidence for interpreting climate and species distribution patterns during this time (e.g Wallace, 2004; Wallace and Wang, 2004; DeSantis and Wallace, 2008; Ochoa et al, 2012; Liu and Quan, 2019). Because GFS is contained within a karst sinkhole, it also yields information about elevation of the water table at the time, providing important evidence for constraining regional river incision rates after the sinkhole filled. Using cosmogenic nuclide geochronology, we provide an independent burial age for GFS sediments and examine the erosional conditions that prevailed during and after the deposit's formation.

5.2 Background

5.2.1 Sinkhole formation and filling

The GFS sinkhole complex lies within the Ordovician Knox dolomite that comprises part of the larger karst landscape that dominates the Tennessee Valley and Ridge (Figures 5.1, 5.2) (Rodgers, 1953). Gravimetric surveying by Whitelaw et al. (2008) revealed that the site consists of numerous sinkholes with depths up to ~35 m. The semi-linear trend of the sinkholes likely reflects fault-related dissolution (Whitelaw et al., 2008). Though the formation age of the sinkhole complex itself is difficult to constrain, its filling with sediments and fossils during the Late Cenozoic has been intensely studied. Shunk et al. (2006, 2009) examined the stratigraphy of a core (GFS-1) through the sinkhole complex and interpreted it as a filled sinkhole lake on the basis of excellent depositional fabric preservation, a lack of bioturbation, and presence of framboidal

pyrite. The frequency of articulated skeletons over much of the site also suggests a predominantly low energy lacustrine environment (Hulbert et al, 2009). Shunk et al. (2006, 2009) also noted centimeter-scale graded beds in the lower sinkhole overlain by rhythmites, which the authors interpreted as reflecting a transition to a wetter period.

Sediments filling the sinkhole complex appear to be from multiple sources (Shunk et al., 2006, 2009). Grain size distributions of quartz within the GFS-1 core and estimates from flow velocity diagrams suggest that the core was located near the paleo-lake's inlet, and that relatively low-energy fluvial transport was responsible for delivering sediments to the site (Shunk et al., 2009). This conclusion is supported by a general westward coarsening of sediments, indicating that most sediment flux was from the sinkhole complex's western side. Shunk et al. (2006) also noted that some quartz grains had features consistent with Blue Ridge provenance (namely beta outlines, embayments, and resorption rims) that point to local and regional sources for the sediments filling the GFS basin. All sediments were magnetically reversed (Shunk et al., 2006; references therein), so it was not possible to identify a specific paleomagnetic sequence for additional age constraint.

5.2.2 Biostratigraphy

While the lacustrine depositional setting and Blue Ridge sediment provenance of the GFS has been generally accepted, the timing of its filling has been continually revised on the basis of emerging biostratigraphy. Based on varve-like stratigraphy, Shunk et al. (2009) estimated that the sinkhole filled relatively quickly over a period of 4.5-11 kyr. During this period, a large variety of fauna died and were preserved in the upper layers of the sinkhole complex. Ongoing discoveries of vertebrates with independently constrained emergence/extinction timelines have permitted increasingly precise age estimates for the site. Wallace and Wang (2004) provided one of the first age estimates for the site, estimating a broad age of 4.5-7 Ma based on the presence of the rhino *Teleoceras* and short-faced bear *Plionarctos*. The limited number of fossils useful for biostratigraphy at that stage of excavation contributed to the uncertainty of the deposit age.

Later palynological analysis by Zobaa et al. (2011) focused on the GFS-1 core, which was again sampled for this investigation. The authors provided significantly older estimates, concluding based on fossil palynomorphs that most of the sinkhole complex was deposited in the Paleocene-Eocene and subsequently covered with Miocene and younger sediments. This

Paleocene-Eocene age was estimated from the Early Cenozoic pollens *Caryapollenites imparalis*, *Caryapollenites inelegans*, and *Caryapollenites prodromas*. Zobaa et al. (2011) also inferred that the lack of Neogene grass pollen *Poaceae* was additional evidence for a Paleocene-Eocene age, though it should be noted that some Late Cenozoic pollen (*Cupuliferoipollenites pusillus, Tricolporopollenites kruschii, Ulmipollenites undulosus, Caryapollenites simplex, Tubulifloridites antipodica, Pinuspollenites strobipites, Malvacearumpollis mannanensis, Fraxinus Columbiana, Chenopodipollis granulata,* and *Pseudoschizaea ozeanica*) were present.

Most recently, a Pliocene age of the sinkhole was proposed by Samuels et al. (2018) on the basis of rhino, leporid, and cricetid remnants. Leporid and cricetid fossils provide a maximum estimated age and date to the onset of the Blancan North American stage (4.9 Ma). Samuels et al. (2018) infer a minimum age of 4.5 Ma from the presence of the rhino *Teleoceras*, but note that Gustafson (2012) documented *Teleoceras* as young as 3.5 Ma in North America. One potential issue is that biostratigraphic reference sites have generally sparse radiometric and/or paleomagnetic age constraints (Carrasco et al., 2005; references therein). In most cases, the reference fauna have been dated via stratigraphic or biostratigraphic correlation rather than absolute techniques. Furthermore, considering that most of these sites are located in western North America, the distances from reference fossil sites to the GFS leave open the possibility that the fauna at Gray did not live contemporaneously with their western counterparts. As such, considerable uncertainty still surrounds the age of the deposit and motivates direct radiometric dating of the site itself.

5.2.3 Geomorphological significance

In addition to being a significant locale for studying the emergence and migration of mammals and extinct taxa, the GFS is important from a geomorphological perspective. The GFS is located in the Valley and Ridge province of Tennessee, whose late Cenozoic erosional history has reemerged as a topic of interest (Gallen, 2018; Gallen and Thigpen, 2018), but for which a robust geochronologic dataset is lacking due to a paucity of well-preserved deposits. Fortunately, karst dissolution features such as caves and sinkholes preserve excellent sedimentary sequences that can be used to reconstruct histories of adjacent river incision (e.g., Anthony and Granger, 2006). Because specific karst features, caves, and sediment infills can be often be recognized as forming above the water table (vadose) *versus* below the water table (phreatic), understanding the

age of karst landforms and their sediment can be used to reconstruct water table lowering over time. Due to high secondary porosity, the water table tends to be governed closely by the elevation of the nearest river and this history can be interpreted in terms of river incision.

Consequently, the sinkhole complex at Gray can be related to a base level controlled by the Watauga River. In other words, the GFS was a lacustrine environment, which could either reflect a local water table perched above an impermeable layer, or alternatively the regional water table at the level of the Watauga River. As such, the burial age of the sinkhole fill material may be used to estimate the maximum average incision rate of the Watauga River *after* the sinkhole was filled with sediments (Figure 5.1). Such a record provides valuable insight into whether the area was undergoing response to tectonic and/or climatic forcing, at or since the time of filling, providing crucial data for interpreting the late Cenozoic history of the upper Tennessee River watershed. The age of the sinkhole fill can be estimated using cosmogenic $^{26}Al/^{10}Be$ burial dating, given its quartz-rich Blue Ridge sediment and suspected rapid filling over 4.5-11 ky (Shunk et al., 2009).

5.3 Methods

5.3.1 Cosmogenic nuclide production

Cosmogenic ^{26}Al and ^{10}Be are rare isotopes produced by the interaction of cosmic radiation with the atmosphere and Earth's surface. The rarest variety of cosmogenic nuclides, *in situ* cosmogenic nuclides, are produced when secondary cosmic rays penetrate rocks at or near the Earth's surface. Most production of ^{26}Al and ^{10}Be in rock occurs via neutron spallation when high-energy neutrons fragment nuclei of Si and O, respectively (Lal, 1991). Neutron spallation dominates cosmogenic nuclide production within the uppermost several meters of Earth's surface but is eclipsed at greater depths by muogenic production. This occurs because muons interact less with matter than neutrons, which allows them to penetrate deeper into buried materials and produce cosmogenic nuclides at depths of tens to hundreds of meters (Granger and Smith, 2000). Together, these production mechanisms form a zone of production that extends downward from the surface, with ~99% of neutron production occurring in the upper ~3 m of rock.

As eroding rock transits the zone of highest production near the surface, it accumulates cosmogenic nuclides at a rate dependent on erosion rate (Granger et al., 1996). Rapidly eroding rock will transit through the production zone quickly and accumulate a small inventory of

cosmogenic nuclides, whereas slowly eroding rock will move through the production zone gradually and accumulate a higher concentration of cosmogenic nuclides. The ^{26}Al and ^{10}Be concentrations as a function of erosion rate and local production rates are generally modeled using the equation:

$$\left(\frac{N_{26}}{N_{10}}\right)_{inh} = \frac{P_{26}}{P_{10}} \frac{\frac{1}{\tau_{10}} + \frac{\rho E}{\Lambda}}{\frac{1}{\tau_{26}} + \frac{\rho E}{\Lambda}}$$

where N_{26} and N_{10} are the concentrations of ^{26}Al and ^{10}Be (at/g), P_{26} and P_{10} are the production rates of ^{26}Al and ^{10}Be (at/g·yr), τ_{26} and τ_{10} are the mean lives of ^{26}Al ($1.020 \cdot 10^6$ yr) and ^{10}Be ($2.005 \cdot 10^6$ yr), ρ is the density of eroding rock (g/cm^3), and Λ is the attenuation length (160 g/cm^2) (Granger et al., 1997; Nishiizumi, 2004; Chmeleff et al., 2010; Korschinek et al., 2010). Prior to burial, the initial ratio of ^{26}Al and ^{10}Be, represented by $(N_{26}/N_{10})_{inh}$, approaches the ^{26}Al/^{10}Be production rate ratio as erosion rate increases. A higher erosion rate will result in lower overall concentrations of ^{26}Al and ^{10}Be.

5.3.2 Simple burial dating

The most straightforward burial dating approach using ^{26}Al and ^{10}Be assumes that the entire inventory of cosmogenic nuclides in a rock is controlled by production during exhumation of bedrock and radioactive decay following burial (Granger et al., 1997). Decay of ^{26}Al and ^{10}Be following burial is represented by the equation:

$$\frac{N_{26}}{N_{10}} = \left(\frac{N_{26}}{N_{10}}\right)_{inh} e^{-t/\tau_{bur}}$$

where t is burial age (yr) and $\tau_{bur} = (\tau_{26}^{-1} - \tau_{10}^{-1})^{-1} = 2.076$ My. Solving equations 1 and 2 will yield a most likely paleo-erosion rate and burial age after <10 iterations. Such an approach assumes no post-burial production of ^{26}Al and ^{10}Be, and is valid for rapidly and deeply buried sediments, such as those in caves (e.g., Granger et al., 1997, Granger et al., 2001). In the case where significant post-burial production has occurred via deeply penetrating muons, the approach will underestimate the true burial age, and instead provide a minimum burial age (Granger, 2006). Given the burial depths of the GFS sediments, we expect that significant post-burial production of ^{26}Al and ^{10}Be will have occurred, rendering simple burial dating inaccurate. However, minimum burial ages provide a useful constraint on the age of the deposit, so we have included them for reference.

5.3.3 Depth profile dating

The cosmogenic $^{26}Al/^{10}Be$ depth profile technique requires measurements of ^{26}Al and ^{10}Be concentrations across a vertical range of depths within a deposit. Because the concentrations of ^{26}Al and ^{10}Be at any given depth are functions of burial age, deposit density, and pre- and post-burial erosion rates, it is possible to model the most likely burial scenario by varying those parameters to fit the measured ^{26}Al and ^{10}Be concentrations (e.g., Granger and Smith, 2000; Wolkowinsky and Granger, 2004; Hidy et al., 2010; Braucher et al., 2013). It is often difficult to obtain ^{26}Al and ^{10}Be measurements over the depth range required for depth profile dating, but the GFS-1 sediment core provides an excellent opportunity to apply this approach. Moreover, it is preferable over other cosmogenic dating techniques at the GFS because (1) the deposit is expected to be at least Pliocene in age and has likely experienced significant post-burial production of ^{26}Al and ^{10}Be, thus rendering simple burial dating ineffective and (2) the sediments filling the sinkhole complex are too fine-grained (clay-to-sand size) to calculate a horizontal ^{26}Al-^{10}Be isochron burial age using individual clasts (e.g., Erlanger et al., 2012).

Depth profile dating takes advantage of the depth dependence of ^{26}Al and ^{10}Be production pathways. Deeply buried sands feature the most inherited ^{26}Al and ^{10}Be with minimal postburial production by muons, and thus provide the most accurate constraint on the age of the deposit. Conversely, sands near the surface are subject to significantly higher post-burial production rates and their cosmogenic nuclide concentrations are more dependent upon post-burial erosion rate. To calculate an age from a depth profile, concentrations of ^{26}Al and ^{10}Be at the sampled depths are modeled using the following equation of Granger and Smith (2000):

$$N_i = \frac{N_{i,inh}}{e^{t/\tau_i}} + \sum_j \frac{A_{i,j} e^{-\rho z/L_j} \left[1 - e^{-t\left(\frac{1}{\tau_i} + \frac{\rho E_d}{L_j}\right)}\right]}{\frac{1}{\tau_i} + \frac{\rho E_d}{L_j}}$$

Where N_i is the concentration of the nuclide of interest (at/g), $N_{i,inh}$ is the inherited (pre-burial) nuclide concentration (at/g), t is burial age (yr), ρ is the density of the deposit (g/cm^3), z is sample depth (cm), $A_{i,j}$ represents the production rate constants, L_j represents neutron and muon attenuation lengths (g/cm^2), and E_d is the erosion rate of the deposit following deposition (cm/yr), assumed to be constant. This approach requires good constraints on the ^{26}Al and ^{10}Be yielded by interactions with muons (A_1, A_2, A_3) and muon attenuation lengths (L_1, L_2, L_3). It is possible to parameterize production with fewer or more constants and muon attenuation lengths (e.g., Braucher et al., 2013; Schaller et al., 2001) but a four-part exponential production equation proved

sufficient for this application. Due to the fact that muogenic production varies worldwide and numerous revisions have been made to models of muogenic production, reparameterization of muon production constants (A_1, A_2, A_3, L_1, L_2, L_3) and was critical for calculating an accurate burial age. We estimated ^{26}Al and ^{10}Be production rates from negative and fast muons following Balco (2017). Constants and muon attenuation lengths are available in Table 5.1.

5.3.4 Modeling post-burial production rates

Because local production rates are known to vary through time, primarily due to fluctuations in Earth's magnetic field, we examined the effects of using the time-dependent Lifton-Sato-Dunai (Lifton et al., 2014) and time-independent (Stone, 2000) production rate scaling schemes. Modeling local production using the time-dependent model yielded an 8.7% variation in neutron production rates through time, while muon flux was taken to be independent of magnetic fluctuations. This variation did not have an appreciable influence on calculated burial age, and thus was not included in our burial age uncertainty calculations.

Post-burial production of cosmogenic nuclides in the deposit by neutrons and muons is highly dependent upon density. Many profile burial dating applications assume that the deposit of interest is of a consistent density, as is the case for most terraces and fans. Because the GFS sediments are buried within a sinkhole, however, shielding from cosmic radiation is controlled by the density of both the sinkhole fill and the surrounding bedrock, as well as the geometry of the sinkhole. Incoming muons arriving at a steep angle pass only through the sediment fill, while those arriving at a shallow angle pass through bedrock and fill. At shallow depths, the majority of radiation passes through sinkhole fill, whereas at the base of the sinkhole the muon flux through bedrock is more significant (see Figure 5.3). It is thus inappropriate to utilize the sinkhole fill density of 2.0 g/cm^3 (measured by Whitelaw et al., 2008), as this would underestimate density and overestimate post-burial production. Conversely, using a typical dolomite density of 2.8 g/cm^3 would overestimate density and underestimate post-burial production. Because the effective density is different for every depth, starting at 2.0 g/cm^3 at the surface and increasing with depth, each sample must have its own effective density that accounts for the relative muon flux through fill and dolomite. Effective densities for samples in the sinkhole were calculated by estimating the percentage of cosmic radiation that passed through sinkhole fill vs. the surrounding dolomite.

Intensity of incoming cosmic radiation (F) at a given angle (ϕ) from the zenith can be modeled using the equation:

$$F(\phi) = F_0 cos^m \phi$$

Where F_0 is the vertical intensity and m is a constant. The value for m varies with altitude (Argento et al., 2015). For the case here, m is closely approximated by a value of 2, which conveniently allows an analytical solution to the shielding equation. The fraction F of cosmic rays passing through a conical depression may be modeled by integrating through the volume:

$$F = \frac{\int_0^{2\pi}\int_0^{\theta} F_0 cos^2\theta \, d\theta d\phi}{\int_0^{2\pi}\int_0^{\pi/2} F_0 cos^2\theta \, d\theta d\phi} = \frac{2\theta}{\pi} + \frac{sin\, 2\theta}{\pi} \qquad where \qquad \theta = tan^{-1}\left(\frac{R}{z}\right)$$

Where θ is the angle from zenith to the mouth of the cone at depth z, R is the cone's maximum radius, and z is a given depth (Figure 5.3A). Because θ changes with depth (reaching a minimum at maximum depth z), the flux of muons through sinkhole fill shrinks as a function of depth (Figure 5.3B). The proportion of cosmic radiation passing through bedrock at depth z is represented by 1-F (Figure 5.3C). These factors can then be used to calculate effective density (ρ_{eff}) throughout the cone, using the simplifying approximation that all cosmic ray muons passing through bedrock are attenuated primarily by the bedrock itself:

$$\rho_{eff} = F\rho_{fill} + (1 - F)\rho_{rock}$$

With the assumption that ρ_{fill} = 2.0 g/cm^3 and ρ_{rock} = 2.8 g/cm^3. We derived a maximum modern diameter D = 41.5 m from Whitelaw et al. (2008)'s gravimetric survey and aerial photography in Zobaa et al. (2011). The core extended to 34.75 m and our model was configured to calculate effective densities that account for recently excavated material, 5.8 m according to local LIDAR surveys (Figure 5.2). The values were input into the burial equation of Granger and Smith (2000) and the nuclide concentration equation was evaluated at each depth for different values of age, pre-burial erosion rate, and post-burial erosion rate until a solution of best fit was found. Uncertainties were estimated using the chi-squared plus one approach (Bevington and Robinson, 2003).

5.3.5 Sampling and processing

Sand fractions were collected at a variety of depths from the GFS-1 core provided by East Tennessee State University. Because the greatest change in production rate occurs in the upper few meters of sediment column as production transitions from neutron- to muon-dominated, we

sampled shallow zones at closer intervals. Due to the compaction of the core material, high clay content, and small sample sizes, special care was taken to preserve quartz while disaggregating the material. Samples were soaked overnight in concentrated nitric acid, rinsed, and mixed with sodium hexametaphosphate to break down clays. Particularly cohesive materials were placed in an ultrasonic bath to disaggregate blocks of clay and sand. Grains with diameters >0.5 mm were removed via sieve to eliminate most chert and carbonate fragments. Samples that contained abundant contaminants underwent pyrophosphoric acid treatment (Mifsud et al., 2013) to preferentially attack non-quartz minerals. All samples were selectively dissolved in heated 1% hydrofluoric/nitric acid for three days to isolate the quartz fraction and were assayed with inductively-coupled plasma optical emission spectrometry (ICP-OES) prior to chemistry. See methods section of Chapter 2 and Appendix B for details of chemistry. Total aluminum, beryllium carrier, and AMS measurements are available in Table 5.2.

5.4 Results

Concentrations of ^{26}Al ranged from $0.3630 \pm 0.0630 \cdot 10^5$ at/g (GF-49A) to $2.6070 \pm 0.1760 \cdot 10^5$ at/g (GF-2A), while ^{10}Be concentrations ranged from $0.4270 \pm 0.0500 \cdot 10^5$ at/g (GF-35A) to $0.7270 \pm 0.0500 \cdot 10^5$ at/g (GF-2A) (Table 5.3). Blank corrections were generally low, although not negligible, ranging from 0.3-3.5% for ^{26}Al measurements and 2.0-9.9% for ^{10}Be measurements (see Table 5.2). The deepest sample (GF-49A), which exerts the greatest control on the age calculation, had ^{26}Al and ^{10}Be blank corrections of 3.2% and 2.3%, respectively. The ^{10}Be and ^{26}Al concentrations showed robust exponential relationships with depth ($R^2 = 0.96$ and $R^2 = 0.97$, respectively). The ^{26}Al/^{10}Be relationships with depth are shown in Figure 5.4. Minimum age calculations for each depth are provided in Table 5.3. The oldest minimum age (4.36 ± 0.37 My) is calculated at the base of the core, as expected, where postburial production was lowest but still substantial.

We modeled concentrations of ^{26}Al and ^{10}Be at depth following the methodology of Granger and Smith (2000) (Figure 5.4A-5.4H). Burial age, deposit erosion rate, and paleo-erosion rates of individual samples were allowed to vary, while the modern depth of each sample was taken as its depth in the core plus 5.8 m to reflect recent excavation during road construction. The effective density of each sample was modeled as a function of depth (Figure 5.4I). A burial age of $6.78\ ^{+6.99}/_{-1.09}$ My yielded the best-fit age, with $\chi^2 = 6.33$ and MSWD = 1.06 (Figure 5.5). Given that

virtually no inherited ^{26}Al and ^{10}Be would exist past ~8 My, this age is effectively unbounded on the upper end. The surface erosion rate was 2.2 $^{+0.8}/_{-0.6}$ m/My, and paleo-erosion rates varied from 6.5-10.2 m/My (Tables 5.4, 5.5). The similarity of our estimated paleo-erosion rates to Early Pliocene paleo-erosion rates along the Tennessee River and Plio-Pleistocene paleo-erosion rates along the New, Cumberland, Green Rivers (Anthony and Granger, 2006; Granger et al., 1997; Granger et al., 2001; Chapter 2, this thesis) indicates that erosion rates likely did not vary significantly during the later Neogene.

Our model was reasonably successful in matching measured ^{26}Al and ^{10}Be concentrations, as shown by residuals in Figures 5.4D-5.4F. Residuals were consistently low in the three deepest samples, which have experienced less postburial production of ^{26}Al and ^{10}Be than the overlying sediments and exert the greatest influence on the age calculation. Postburial production remained a significant factor; in the shallowest sample, 98% of ^{26}Al and 73% of ^{10}Be were postburially-produced. The deepest sample, GF-49A, featured a greater inherited component, but still 90% of ^{26}Al and 66% of ^{10}Be were produced following burial. Estimated postburial/total inventories of ^{26}Al and ^{10}Be are shown for all samples in Figures 5.4G and 5.4H.

The relative depletion of the inherited component of cosmogenic nuclides through decay and postburial production exerts the main limitation on our burial age estimate, given that measurable inherited components are necessary to calculate burial ages. This limitation is expressed in the probability distribution function of ages for the site (Figure 5.5), which has a steep curve for younger potential ages while the probability remains nonzero to infinity due to postburial production. Figure 5.5 also demonstrates that by 8 My, nearly all ^{26}Al and a significant portion of ^{10}Be has been postburially produced. We therefore cannot assign a maximum age to the deposit, but can assign a minimum age. The probability distribution function of burial ages at GFS demonstrates that the sinkhole fill dates to at least 4 My, consistent with the minimum burial age of 4.36 ± 0.37 My from the deepest sample.

Paleomagnetic data provide additional constraints that can improve the quality of ^{26}Al/^{10}Be burial age estimates (e.g., Muzikar and Granger, 2006). While the GFS does not contain a sequence of paleomagnetic fluctuations due to its rapid infilling, the fact that all sediments are magnetically reversed (Shunk et al., 2006; references therein) can be used to delineate more likely age intervals for the sinkhole fill. We set the probability distribution values to zero over intervals that were magnetically normal. Our 1σ age estimate overlaps with numerous magnetic reversals,

given its significant, effectively unbounded, upper uncertainty. As such, our radiometric approach cannot alone determine the age of the sediments filling the GFS sinkhole complex.

5.5 Discussion

5.5.1 Refuting an Early Cenozoic age

Our data broadly indicate – but do not necessitate – a Neogene age for the GFS deposits, contrasting with the observations of Zobaa et al. (2011) that estimated a Paleocene-Eocene age for the lower portion of the sinkhole. Examination of the ^{10}Be concentration vs. depth curve reveals a strongly exponential relationship ($R^2 = 0.96$) consistent with rapid burial, in contrast with the two-stage model set forth by Zobaa et al. (2011). If the lower section were Paleocene-Eocene, and the upper section Late Neogene in age, the ^{10}Be concentration curve would likely feature a doubled exponential reflecting the exposure and subsequent burial of the Paleocene-Eocene sediments by the Late Neogene sediments (e.g., Ivy-Ochs et al., 2013). Our results instead support the findings of Shunk et al. (2009), who proposed a rapid filling of the sinkhole over 4.5-11 kyr.

A re-examination of the palynological data presented in Zobaa et al. (2011) reveals the presence of several pollen types that were present during the late Cenozoic (*Cupuliferoipollenites pusillus, Tricolporopollenites kruschii, Ulmipollenites undulosus, Caryapollenites simplex, Tubulifloridites antipodica, Pinuspollenites strobipites, Malvacearumpollis mannanensis, Fraxinus Columbiana, Chenopodipollis granulata, and Pseudoschizaea ozeanica*) that are consistent with our age finding (White, 2008 and references therein). Zobaa et al. (2011) hypothesized that younger fossil pollens had percolated through cracks and fractures into the cored section, but it appears more likely that older pollen were preserved in the gradually eroding Cenozoic landscape and subsequently deposited in the sinkhole during the Late Miocene or Early Pliocene.

5.5.2 Supporting a Hemphillian minimum age

While it is not possible to place a maximum boundary on the GFS sediment age using ^{26}Al/^{10}Be burial dating alone, careful consideration of biostratigraphic evidence can place limits on our age probability distribution function and reveal the most likely age of the deposit. Given that our data exclude a Paleocene-Eocene age and broadly support a Neogene age for the GFS, we

consider the Neogene biostratigraphy that has thus far provided the most consistent age estimates for the deposit.

The biostratigraphic age estimates for the Gray Fossil Site have generally corresponded to the late Miocene and early Pliocene. Using bear and rhino fossils, Wallace and Wang (2004) estimated that the deposit dated to 4.5-7 My, which includes both the Blancan and Hemphillian North American Land Mammal Ages (NALMA). The later work of Samuels et al. (2018) hypothesized a significantly younger age that only included the Blancan, but our most likely radiometric age of ~6.8 My is significantly older. There are several potential causes for the variations between our age estimate and that of Samuels et al. (2018), primarily related to the current constraints on fauna used for biostratigraphy as well as the sensitivity of this technique to the surrounding environment. It is possible that the fossil record employed by biostratigraphers at the GFS has underestimated the dates of first appearance for the *Alilepus vagus*, *Neotoma*, *Notolagus lepusculus*, and *Symmetrodontomys* fossils.

We opted to narrow our probability distribution function to the broader estimate of 4.5-7 My from Wallace and Wang (2004). With this constraint, it is possible to close the probability distribution and evaluate the likelihood of each magnetic reversal between 4.5-7 My reflecting the true burial age of the GFS sediments (Table 5.6). During this interval, five magnetic reversals occurred (Cande and Kent, 1995). One reversal in this interval occurred in the Blancan (4.5-4.9 My), while four reversals occurred during the Hemphillian (4.9-7 My). Combined with the $^{26}Al/^{10}Be$ probability distribution function between 4.5-7 My, these reversals show a 2.5% probability that the GFS is Blancan in age and a 97.5% probability that the GFS is Hemphillian in age. The most likely individual reversal is 5.23-5.89 My, which has a 48.9% probability of being the site's true age. Other notable intervals include 6.57-6.94 My (33.9%) and 6.14-6.27 My (11.9%). While it is not possible to select an individual reversal as the true age of the GFS with absolute confidence, our results strongly favor a Hemphillian minimum age for the GFS if our analysis is limited to 4.5-7 My.

5.5.3 Implications for local and regional geomorphology

Considering the fine-grained, lacustrine nature of the sinkhole deposit, it does not appear to be related to any significant aggradational event. From a geomorphological standpoint, however, our results provide critical data regarding the incision and erosion history of the Watauga River.

Given that the modern sinkhole mouth is 122 m above the modern Watauga River, a maximum incision rate of ~18 m/My may be inferred from our most likely radiometric age of ~6.78 My. This maximum incision rate is significantly higher than the deposit erosion rate inferred since the Pliocene ($2.2\ ^{+0.8}/_{-0.6}$ m/My) and somewhat higher than upstream erosion rates (6.5-10.2 m/My), but the true average incision rate may be lower.

5.5.4 Assumptions regarding sinkhole geometry and cosmic ray flux

Applying cosmogenic $^{26}Al/^{10}Be$ profile dating to a sinkhole deposit introduces new complexities that are not present in other forms of profile dating. Unlike other deposits that have been dated using depth profiles (e.g., Granger and Smith, 2000; Wolkowinsky and Granger, 2006; Hidy et al., 2010), our deposit does not feature a uniform material lying atop bedrock or other materials. Rather, the fact that samples are located at different depths surrounded by varying amounts of bedrock introduces variations in the effective density that have significant implications for cosmic ray flux at depth and consequently impact our models of ^{26}Al and ^{10}Be concentrations. We have worked to account for this variation in effective density with depth by assuming a conical geometry for the sinkhole, but the exact geometry of the sinkhole – and consequently, muon flux to the sinkhole sediments – is not known. It is probable that the sinkhole is not a perfect cone, instead featuring irregular dissolution features that cannot be resolved without excavation. These features could introduce nonuniform shielding to the deposit and complicate post-burial production calculations. They may be partially responsible for discrepancies between modeled and measured ^{26}Al and ^{10}Be concentrations (Figure 5.4). High-resolution surveys, excavation, or future cores could conceivably improve our age estimate, as could measurement of additional nuclides.

5.5.5 Improving burial age constraints

Given the existing biostratigraphy, the Hemphillian minimum age yielded by our calculations is reasonable. This result demonstrates that the $^{26}Al/^{10}Be$ profile method has some applicability in the Miocene, by which point more than seven ^{26}Al half-lives have elapsed and almost no inherited ^{26}Al remains in the samples. The greatest uncertainty in our age calculations stems from the poorly constrained production rates of these nuclides within the core, which may be resolvable using shorter-lived radionuclides. One potential solution to this issue is to measure

^{36}Cl concentrations at or near the intervals where ^{26}Al and ^{10}Be were measured. Because ^{36}Cl has a shorter half-life than ^{26}Al and ^{10}Be and the core is at least 4.36 ± 0.37 My old, ^{36}Cl concentrations have likely reached secular equilibrium values. As such, they could be used to infer a local muon flux which may then be used to estimate production rates of ^{26}Al and ^{10}Be at depth. This approach would remove the necessity of modeling effective density and allow the direct measurement of muon flux throughout the core, regardless of the sinkhole's structural configuration. In turn, it would be possible to model the true age of the site using existing ^{26}Al and ^{10}Be measurements.

5.6 Conclusions

Our study provides the first direct radiometric constraints on the age of the Gray Fossil Site deposit. The results of our ^{26}Al/^{10}Be measurements and models for the GFS-1 core strongly point to a minimum Early Pliocene age, but cannot place definite upper bounds on the age of the sinkhole. They do, however, provide compelling evidence that the sinkhole deposit was not deposited in a two-stage model that contained a Paleocene-Eocene section at the base. Instead, it appears likely that the sinkhole complex filled relatively rapidly during the late Neogene. Considering the extant biostratigraphy and magnetically reversed sinkhole fill, we have further demonstrated that the deposit almost certainly not Blancan in age, and is likely at least Hemphillian in age. This conclusion contrasts with estimated ages for some mammal fauna at Gray, pointing to it potentially representing a first appearance site. Gradual surficial erosion, paleo-erosion, and average incision rates of the Watauga River further suggest that the northeast reaches of the Tennessee River watershed have not experienced substantial uplift during the Neogene.

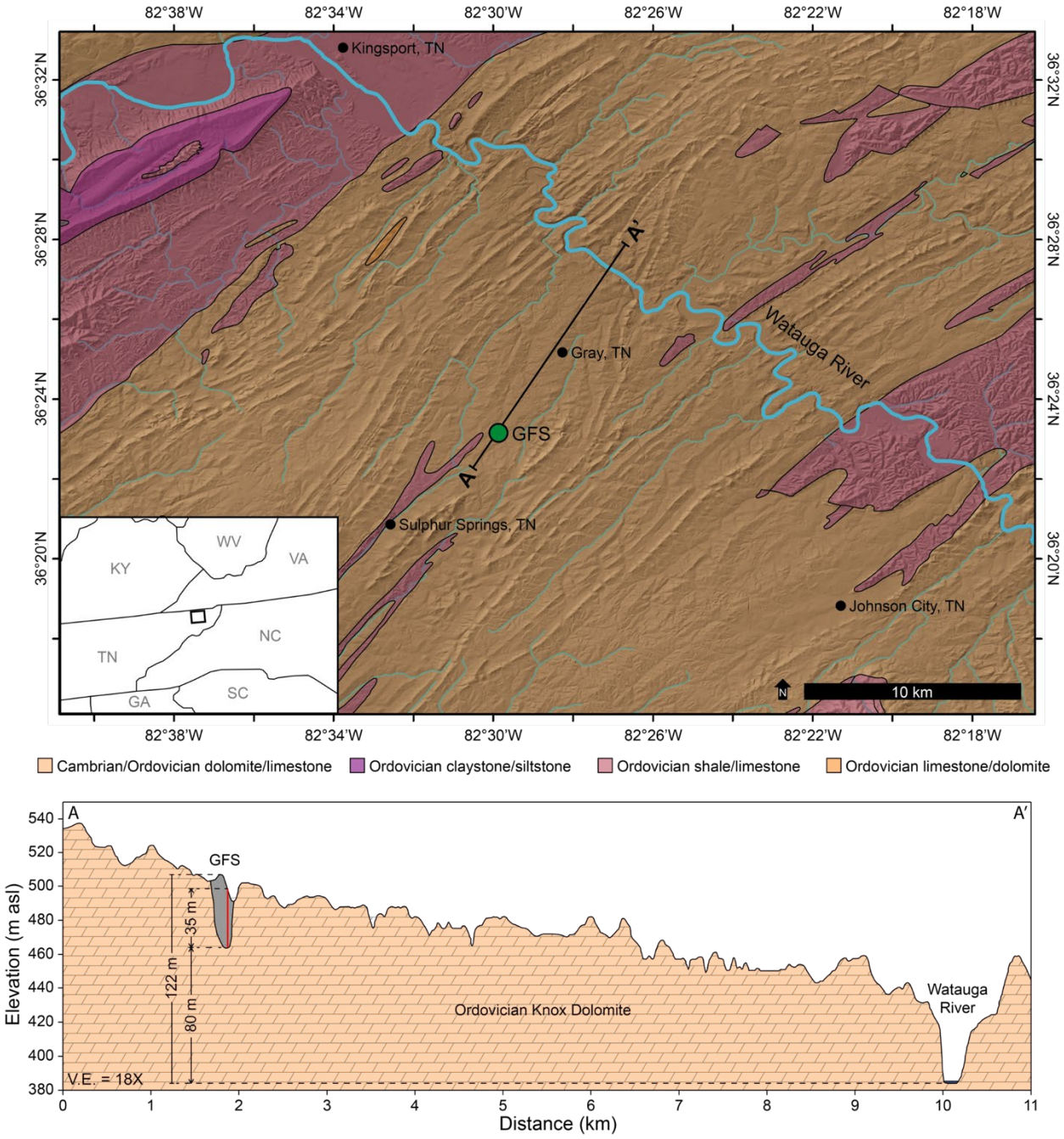

Figure 5.1. Top: Local geology of Gray, TN and the surrounding area. Most of the area is underlain by Cambrian and Ordovician carbonates, with some fine-grained detrital units. The Gray Fossil Site is located on the Ordovician Knox dolomite. Line A-A' indicates location of cross-section. Geology from Rodgers (1953). Bottom: Cross-section of landscape from Gray Fossil Site to nearest reaches of Watauga River, TN. Geometry of fossil site inferred from surficial exposures and core depth; red line denotes location of core. Vertical distances from the top and bottom of the Gray Fossil Site sinkhole deposit to the modern Watauga River are indicated. Note that the core was not taken from the highest exposure of the sinkhole; the modern maximum depth of the sinkhole is ~42 m.

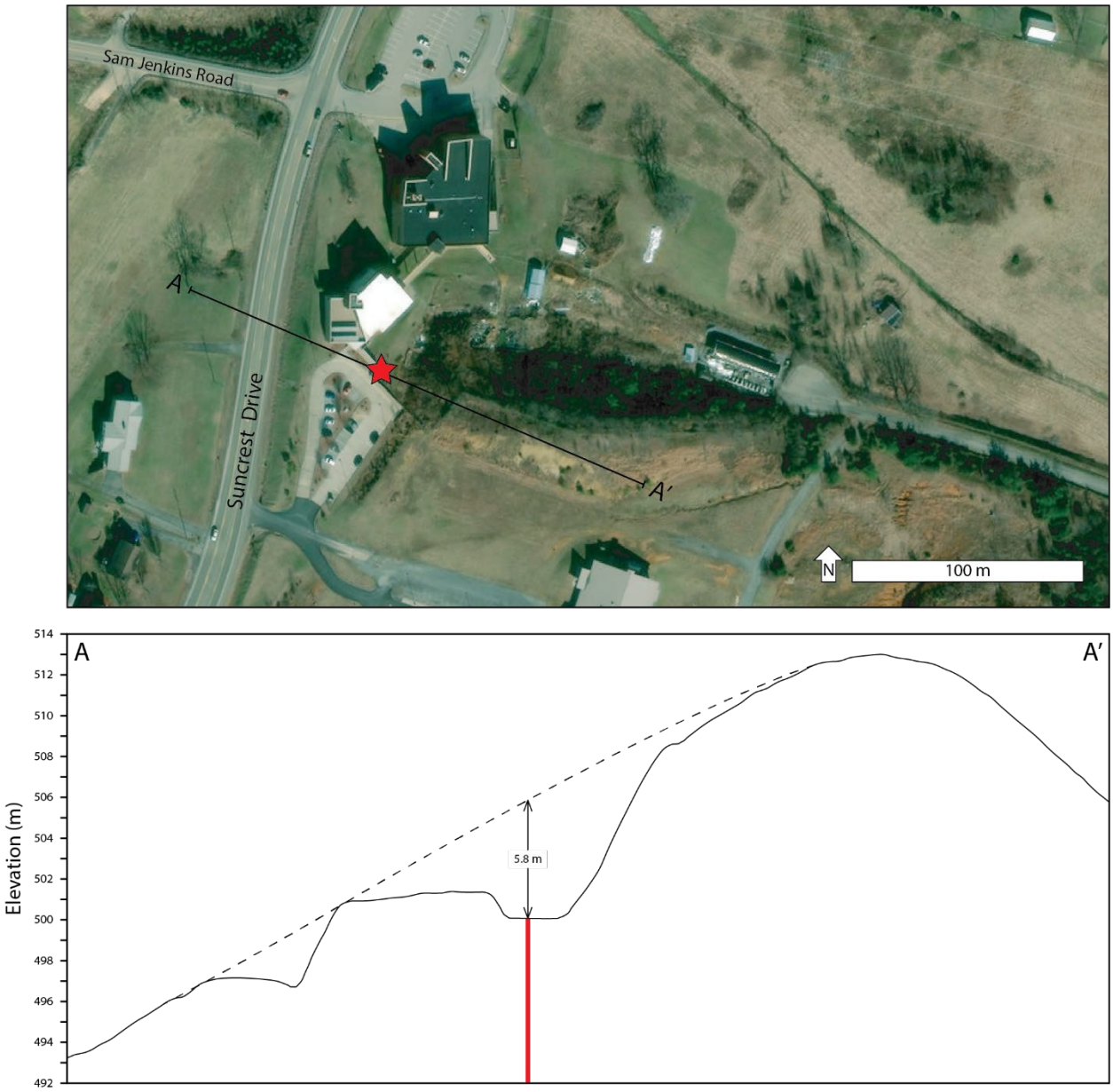

Figure 5.2. Top: Aerial image of the Gray Fossil Site. The location of the dated cored is indicated by the red star adjacent to the south museum building. Bottom: Topography of Gray Fossil Site showing 5.8 m of overburden excavated above GFS-1 core (indicated by red line). Imagery courtesy of Esri and LIDAR downloaded from The National Map.

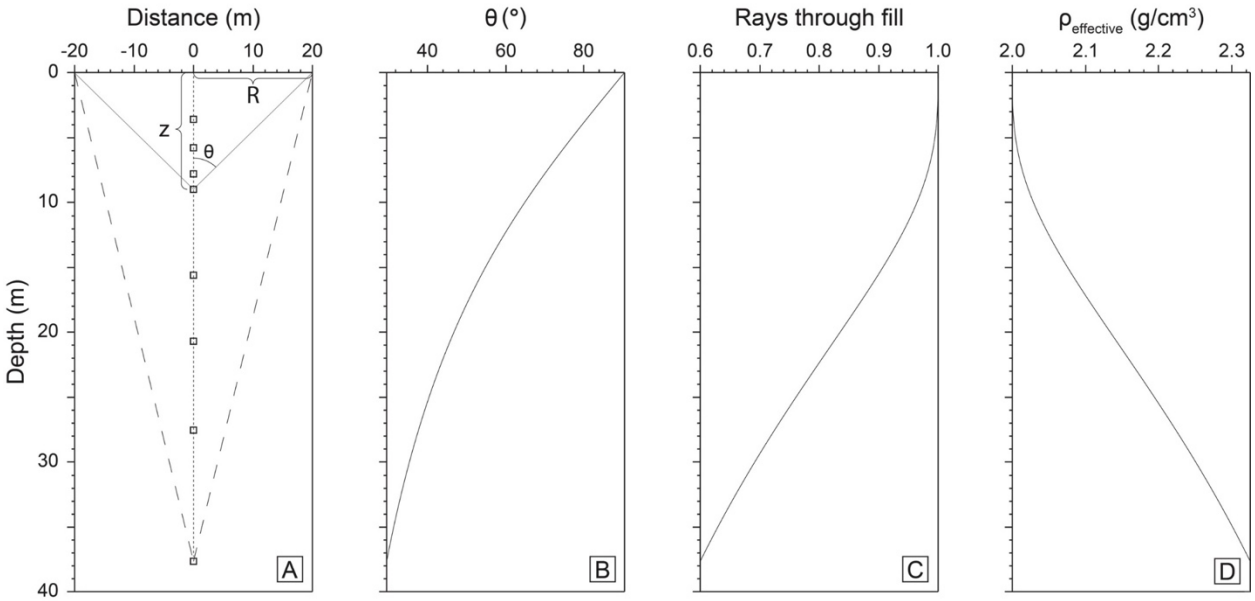

Figure 5.3. Effects of sinkhole geometry on cosmic radiation flux at given depths. (A) A conical sinkhole is assumed, with the sinkhole walls represented by dashed lines. The core is indicated by a dotted line and samples are represented by black squares. Examples of θ and z are provided for the fourth shallowest sample. The radius R remains constant between samples. Sample depths are shown for a scenario where 2.8 m of material were subsequently excavated. (B) As the base of the sinkhole is approached, the maximum angle from the zenith of cosmic rays passing through sinkhole fill approaches the angle of the sinkhole's walls from zenith. (C) As the window through the sinkhole fill shrinks with depth, the fraction of rays that pass through only the sinkhole fill is also reduced. (D) As depth increases and a greater fraction of radiation passes through dolomite, the effective density of the deposit increases.

Figure 5.4. (Below). Measured and best-fitting model concentrations of ^{26}Al (A) and ^{10}Be (B) are shown by dots and dashed lines, respectively, assuming 5.8 m of material was recently excavated. The measured and modeled $^{26}Al/^{10}Be$ ratios (C) are also shown by respective dots and dashed lines. All error bars represent 1σ analytical uncertainty. Residual data for ^{26}Al (D), ^{10}Be (E), and $^{26}Al/^{10}Be$ ratios (F) demonstrate the discrepancies between measured and modeled concentrations. The large discrepancies between measured and modeled ^{26}Al concentrations are likely due in part to the significant postburial component (G) at 6.78 My. Postburial production also affected ^{10}Be modeling to a large extent (H), albeit less so than for ^{26}Al. The effective densities for each sample based on modeled removal of material (I) are similar to the maximum possible values, shown in red.

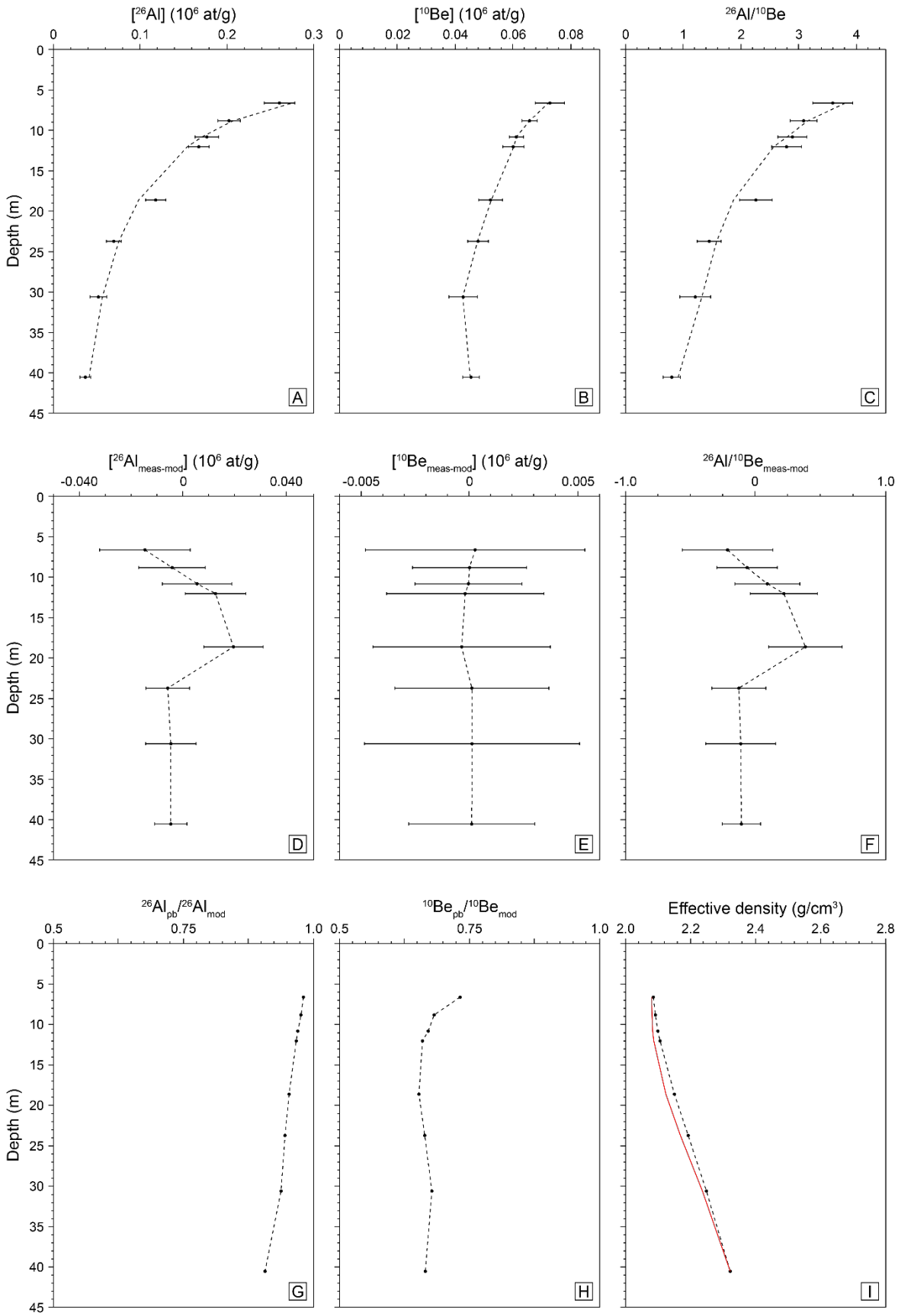
[26Al] (10^6 at/g)
[10Be] (10^6 at/g)
26Al/10Be
Depth (m)
A
B
C
[26Al meas-mod] (10^6 at/g)
[10Be meas-mod] (10^6 at/g)
26Al/10Be meas-mod
D
E
F
26Al pb/26Al mod
10Be pb/10Be mod
Effective density (g/cm3)
G
H
I

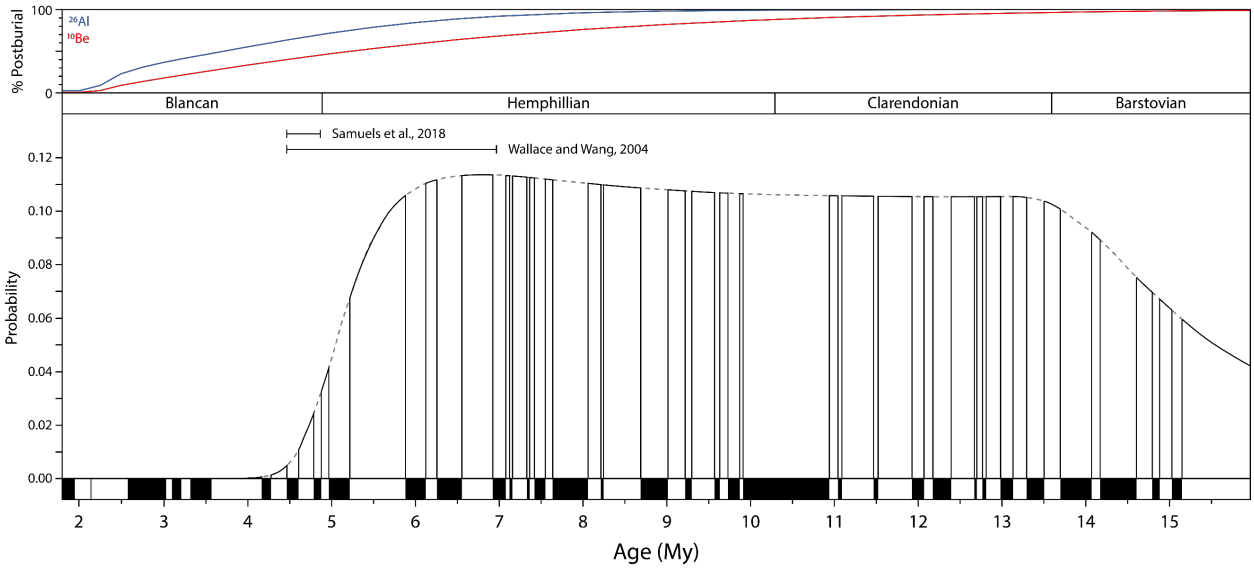

Figure 5.5. Burial age probability distribution for the Gray Fossil Site sediments during the Blancan through Barstovian. Probabilities were calculated for each age by allowing paleo-erosion rates and deposit erosion rates to vary, and solving for the minimum χ^2 value at each age step. That χ^2 value was then used to calculate a probability value for each age. Because the sediments filling the GFS sinkhole are magnetically reversed, ages corresponding to normal intervals can be discounted. Shaded areas reflect normal intervals. Note that the reversal from 5.23-5.89 My is the most likely burial age. The modeled postburial components of ^{26}Al (blue) and ^{10}Be (red) concentrations in the deepest sample are shown above the probability; virtually all ^{26}Al is postburially produced by the lower Hemphillian. As such, this approach cannot place a maximum burial age on the GFS. Paleomagnetic data from Cande and Kent (1995).

Table 5.1. Site- and nuclide-specific muon production constants calculated by parameterizing production-depth curve from Balco (2017).

Nuclide	A_1	A_2	A_3	L_1 (g/cm^2)	L_2 (g/cm^2)	L_3 (g/cm^2)
^{26}Al	0.584	0.042	0.206	990	16789	3199
^{10}Be	0.060	0.006	0.024	1007	16155	3260

Table 5.2. Masses, AMS-measured ratios, and percent blank corrections of aluminum (Al) and beryllium (Be). WO_BLANK11 corresponds only to GF-49A; WO_BLANK 14 corresponds to all other samples. ^{9}Be carrier masses correspond to ~0.25 g 1041±7 ppm Be carrier solution. Blank correction values reflect corrections on reported concentrations, not AMS ratios.

Sample ID	Total Al (mg)	$^{26}Al/^{27}Al$ (10^{-15})	% Al corr.	^{9}Be carrier (µg)	$^{10}Be/^{9}Be$ (10^{-15})	% Be corr.
GF-2A	1.731	79.03 ± 4.88	0.5	261.9	50.73 ± 2.79	4.7
GF-5A	3.942	54.32 ± 3.27	0.3	260.0	91.30 ± 2.98	2.6
GF-8A	8.028	33.45 ± 2.46	0.3	270.8	116.66 ± 4.05	2.0
GF-10A	3.706	47.33 ± 3.12	0.4	261.4	82.53 ± 4.26	2.9
GF-19A	1.879	36.68 ± 3.16	1.1	270.0	39.70 ± 2.37	5.8
GF-26A	2.013	20.50 ± 2.11	1.8	269.0	37.07 ± 2.02	6.3
GF-35A	1.589	13.42 ± 2.01	3.5	269.0	23.52 ± 1.90	9.9
GF-49A	2.237	17.76 ± 2.30	3.2	266.2	61.69 ± 3.21	2.3
WO_BLANK11	1.138	1.13 ± 1.30	-	266.3	1.43 ± 0.65	-
WO_BLANK14	1.048	0.71 ± 0.68	-	268.8	2.32 ± 0.56	-

Table 5.3. Results of AMS measurement and minimum ages calculated at each depth.

Sample	Depth (m)	Mass (g)	[^{26}Al] (10^6 at g^{-1})	[^{10}Be] (10^6 at g^{-1})	^{26}Al/^{10}Be	Minimum age (My)
GF-2A	0.8	11.646	0.2607 ± 0.0176	0.0727 ± 0.0051	3.59 ± 0.35	1.32 ± 0.22
GF-5A	3.0	23.523	0.2025 ± 0.0129	0.0657 ± 0.0026	3.08 ± 0.23	1.62 ± 0.16
GF-8A	5.0	33.839	0.1766 ± 0.0135	0.0611 ± 0.0025	2.89 ± 0.25	1.74 ± 0.15
GF-10A	6.2	23.304	0.1673 ± 0.0118	0.0601 ± 0.0036	2.78 ± 0.26	1.85 ± 0.21
GF-19A	12.8	12.934	0.1176 ± 0.0115	0.0522 ± 0.0041	2.26 ± 0.28	2.27 ± 0.27
GF-26A	17.9	13.056	0.0693 ± 0.0085	0.0478 ± 0.0036	1.45 ± 0.21	3.16 ± 0.25
GF-35A	24.8	08.921	0.0515 ± 0.0098	0.0427 ± 0.0050	1.21 ± 0.27	3.53 ± 0.42
GF-49A	34.8	23.611	0.0363 ± 0.0063	0.0454 ± 0.0029	0.80 ± 0.15	4.36 ± 0.37

NOTE: Depths are taken from top of core and do not reflect anthropogenic removal of material.

Table 5.4. Best-fit model results, given that 5.8 m of material were recently removed and allowing deposit age, surface erosion rate, and paleo-erosion rates of samples to vary. Uncertainties were derived from the $\chi^2_{min}+1$ approach.

Burial age (My)	Surface erosion rate (m/My)	χ^2_{min}	MSWD
$6.78\ ^{+6.99}/_{-1.09}$	$2.2\ ^{+0.8}/_{-0.6}$	6.33	1.06

Table 5.5. Effective densities and paleo-erosion rates for all samples at best fit age of 6.78 My.

Sample	Effective density (g/cm^3)	Paleo-erosion rate (m/My)
GF-2A	2.01	7.0
GF-5A	2.01	6.5
GF-8A	2.02	6.7
GF-10A	2.03	6.6
GF-19A	2.09	7.5
GF-26A	2.14	8.6
GF-35A	2.21	10.2
GF-49A	2.30	9.1

Table 5.6. Overall probabilities for each sampled reversed polarity interval, assuming sediments filling sinkhole fall within the 4.5-7 My age estimate by Wallace and Wang (2004).

Reversal (Ma)	Probability (%)
4.620 – 4.800	2.5
4.890 – 4.980	2.7
5.230 – 5.894	48.9
6.137 – 6.269	11.9
6.567 – 6.935	33.9

5.7 References

Anthony, D. M., & Granger, D. E. (2006). Five million years of Appalachian landscape evolution preserved in cave sediments. Special papers – Geological Society of America, 404, 39.

Argento, D. C., Stone, J. O., Reedy, R. C., & O'Brien, K. (2015). Physics-based modeling of cosmogenic nuclides part II–key aspects of in-situ cosmogenic nuclide production. Quaternary Geochronology, 26, 44-55.

Balco, G. (2017). Production rate calculations for cosmic-ray-muon-produced 10Be and 26Al benchmarked against geological calibration data. Quaternary Geochronology, 39, 150-173.

Braucher, R., Bourlès, D., Merchel, S., Romani, J. V., Fernadez-Mosquera, D., Marti, K., Leanni, L., Chauvet, F., Arnold, M., Aumaitre, G., & Keddadouche, K. (2013). Determination of muon attenuation lengths in depth profiles from in situ produced cosmogenic nuclides. Nuclear Instruments and Methods in Physics Research Section B: Beam Interactions with Materials and Atoms, 294, 484-490.

Cande, S. C., & Kent, D. V. (1995). Revised calibration of the geomagnetic polarity timescale for the Late Cretaceous and Cenozoic. Journal of Geophysical Research: Solid Earth, 100(B4), 6093-6095.

Carrasco, M. A., Kraatz, B. P., Davis, E. B., & Barnosky, A. D. (2005). Miocene mammal mapping project (MIOMAP). University of California Museum of Paleontology.

Chmeleff, J., von Blanckenburg, F., Kossert, K., Jakob, D. Determination of the ^{10}Be half-life by multicollector ICP-MS and liquid scintillation counting. Nuclear Instruments and Methods in Physics Research Section B: Beam Interactions with Materials and Atoms, 268 (2010), 92-199.

DeSantis, L. R., & Wallace, S. C. (2008). Neogene forests from the Appalachians of Tennessee, USA: geochemical evidence from fossil mammal teeth. Palaeogeography, Palaeoclimatology, Palaeoecology, 266(1-2), 59-68.

Erlanger, E. D., Granger, D. E., & Gibbon, R. J. (2012). Rock uplift rates in South Africa from isochron burial dating of fluvial and marine terraces. Geology, 40(11), 1019-1022.

Gallen, S. F. (2018). Lithologic controls on landscape dynamics and aquatic species evolution in post-orogenic mountains. Earth and Planetary Science Letters, 493, 150-160.

Gallen, S. F., & Thigpen, J. R. (2018). Lithologic controls on focused erosion and intraplate earthquakes in the eastern Tennessee seismic zone. Geophysical Research Letters, 45(18), 9569-9578.

Granger, D. E. (2006). A review of burial dating methods using ^{26}Al and ^{10}Be. Geological Society of America Special Papers 415, 1-16.

Granger, D. E., & Smith, A. L. (2000). Dating buried sediments using radioactive decay and muogenic production of ^{26}Al and ^{10}Be. Nuclear Instruments and Methods in Physics Research Section B: Beam Interactions with Materials and Atoms, 172(1-4), 822-826.

Granger, D. E., Kirchner, J. W., & Finkel, R. C. (1996). Spatially averaged long-term erosion rates measured from in situ-produced cosmogenic nuclides in alluvial sediment. The Journal of Geology, 104(3), 249-257.

Granger, D. E., Kirchner, J. W., & Finkel, R. C. (1997). Quaternary downcutting rate of the New River, Virginia, measured from differential decay of cosmogenic ^{26}Al and ^{10}Be in cave-deposited alluvium. Geology, 25(2), 107-110.

Granger, D. E., Fabel, D., & Palmer, A. N. (2001). Pliocene− Pleistocene incision of the Green River, Kentucky, determined from radioactive decay of cosmogenic 26Al and 10Be in Mammoth Cave sediments. Geological Society of America Bulletin, 113(7), 825-836.

Gustafson, E. P. (2012). New records of rhinoceroses from the Ringold Formation of central Washington and the Hemphillian-Blancan boundary. Journal of Vertebrate Paleontology, 32(3), 727-731.

Hidy, A. J., Gosse, J. C., Pederson, J. L., Mattern, J. P., & Finkel, R. C. (2010). A geologically constrained Monte Carlo approach to modeling exposure ages from profiles of cosmogenic nuclides: An example from Lees Ferry, Arizona. Geochemistry, Geophysics, Geosystems, 11(9).

Ivy-Ochs, S., Dühnforth, M., Densmore, A. L., & Alfimov, V. (2013). Dating fan deposits with cosmogenic nuclides. In Dating torrential processes on fans and cones (243-263). Springer, Dordrecht.

Korschinek, G., Bergmaier, A., Faestermann, T., Gerstmann, U. C., Knie, K., Rugel, G., Wallner, A., Dillmann, I., Dollinger, G., Von Gostomski, C. L., Kossert, K., 2010. A new value for the half-life of ^{10}Be by heavy-ion elastic recoil detection and liquid scintillation counting. Nuclear Instruments and Methods in Physics Research Section B: Beam Interactions with Materials and Atoms, 268, 187-191.

Lal, D. (1991). Cosmic ray labeling of erosion surfaces: in situ nuclide production rates and erosion models. Earth and Planetary Science Letters, 104(2-4), 424-439.

Lifton, N., Sato, T., & Dunai, T. J. (2014). Scaling in situ cosmogenic nuclide production rates using analytical approximations to atmospheric cosmic-ray fluxes. Earth and Planetary Science Letters, 386, 149-160.

Liu, Y. S., & Quan, C. (2019). Neogene oak diversity of southeast United States: pollen evidence from the Gray Fossil Site. Grana, 59(1), 19-24.

Mifsud, C., Fujioka, T., & Fink, D. (2013). Extraction and purification of quartz in rock using hot phosphoric acid for in situ cosmogenic exposure dating. Nuclear Instruments and Methods in Physics Research Section B: Beam Interactions with Materials and Atoms, 294, 203-207.

Muzikar, P., & Granger, D. (2006). Combining cosmogenic, stratigraphic, and paleomagnetic information using a Bayesian approach: General results and an application to Sterkfontein. Earth and Planetary Science Letters, 243(3-4), 400-408.

Nishiizumi, K. (2004). Preparation of ^{26}Al AMS standards. Nuclear Instruments and Methods in Physics Research Section B: Beam Interactions with Materials and Atoms, 223, 388–392.

Ochoa, D., Whitelaw, M., Liu, Y. S. C., & Zavada, M. (2012). Palynology of Neogene sediments at the Gray Fossil Site, Tennessee, USA: floristic implications. Review of Palaeobotany and Palynology, 184, 36-48.

Parmalee, P. W., Klippel, W. E., Meylan, P. A., & Holman, J. A. (2002). A late Miocene-early Pliocene population of Trachemys (Testudines: Emydidae) from east Tennessee. Annals of Carnegie Museum, 71(4), 233-239.

Rodgers, J. (1953). Geologic map of east Tennessee with explanatory text. Tennessee Division of Geology, Bulletin 58.

Samuels, J. X., Bredehoeft, K. E., & Wallace, S. C. (2018). A new species of Gulo from the Early Pliocene Gray Fossil Site (Eastern United States); rethinking the evolution of wolverines. PeerJ, 6, e4648.

Schaller, M., von Blanckenburg, F., Hovius, N., & Kubik, P. W. (2001). Large-scale erosion rates from in situ-produced cosmogenic nuclides in European river sediments. Earth and Planetary Science Letters, 188(3-4), 441-458.

Shunk, A. J., Driese, S. G., & Clark, G. M. (2006). Latest Miocene to earliest Pliocene sedimentation and climate record derived from paleosinkhole fill deposits, Gray Fossil Site, northeastern Tennessee, USA. Palaeogeography, Palaeoclimatology, Palaeoecology, 231(3-4), 265-278.

Shunk, A. J., Driese, S. G., & Dunbar, J. A. (2009). Late Tertiary paleoclimatic interpretation from lacustrine rhythmites in the Gray Fossil Site, northeastern Tennessee, USA. Journal of Paleolimnology, 42(1), 11-24.

Stone, J. O. (2000). Air pressure and cosmogenic isotope production. Journal of Geophysical Research: Solid Earth, 105(B10), 23753-23759.

Wallace, S. C. (2004). Reconstructing the past: Applications of surveying and GIS to fossil localities. In Proceedings of the Annual Meeting for the American Congress on Surveying and Mapping, Tennessee Association of Professional Surveyors, Nashville, TN (1-12).

Wallace, S. C., & Wang, X. (2004). Two new carnivores from an unusual late Tertiary forest biota in eastern North America. Nature, 431(7008), 556.

White, J. M. (2008). Palynodata datafile: 2006 version, with introduction by JM White. In Geological Survey of Canada Open File 5793, 1 CD-ROM.

Whitelaw, J. L., Mickus, K., Whitelaw, M. J., & Nave, J. (2008). High-resolution gravity study of the Gray Fossil Site. Geophysics, 73(2), B25-B32.

Wolkowinsky, A. J., & Granger, D. E. (2004). Early Pleistocene incision of the San Juan River, Utah, dated with ^{26}Al and ^{10}Be. Geology, 32(9), 749-752.

Zhao, Z., Granger, D., Zhang, M., Kong, X., Yang, S., Chen, Y., & Hu, E. (2016). A test of the isochron burial dating method on fluvial gravels within the Pulu volcanic sequence, West Kunlun Mountains, China. Quaternary Geochronology, 34, 75-80.

Zobaa, M. K., Zavada, M. S., Whitelaw, M. J., Shunk, A. J., & Oboh-Ikuenobe, F. E. (2011). Palynology and palynofacies analyses of the Gray Fossil Site, eastern Tennessee: their role in understanding the basin-fill history. Palaeogeography, Palaeoclimatology, Palaeoecology, 308(3-4), 433-444.

CHAPTER 6. NEW ^{26}AL/^{10}BE AND (U-TH)/HE CONSTRAINTS ON THE AGE OF THE UPLAND COMPLEX, CENTRAL MISSISSIPPI RIVER VALLEY

6.1 Introduction

The Upland Complex of the central Mississippi River Valley is a high-level terrace of the ancestral Mississippi River (Autin et al., 1991; Van Arsdale et al., 2007; Lumsden et al., 2016). This dominantly sand and gravel terrace deposit has been mapped from Illinois to Louisiana and has been assigned different names in different states. In Illinois and Missouri it is the Mounds gravel (Willman and Frye, 1970; Harrison, et al., 1999), in Kentucky the Lafayette gravel (Potter, 1955a; 1955b) and subsequently the Continental deposits (Olive, 1980), in Arkansas and Tennessee the Upland Complex (Autin et al., 1991; Saucier, 1994), and in Mississippi the pre-loess sand and gravel (Dockery, 1996). The Upland Complex is particularly important for several reasons beyond its significant economic value as the primary source of gravel over its extent (Van Arsdale et al., 2012; Behrman et al., 2019). It has been interpreted to be the southern remnant of a much larger Pliocene Mississippi River floodplain and drainage basin that extended well into Canada (Cox et al., 2014; Cupples and Van Arsdale, 2014; Lumsden et al., 2016). Van Arsdale and Cupples (2013) used the base of the Upland Complex as a structural datum to identify Quaternary fault displacement within the central Mississippi River Valley. Additionally, the base of the Upland Complex's elevation 70 m above the Holocene Mississippi River near Memphis, Tennessee has been attributed to Quaternary isostatic uplift initiated by Pleistocene sea level decline and commensurate ancestral Ohio and Mississippi river incision. This regional erosion and isostatic uplift may be contributing to Quaternary faulting and ongoing seismicity in the New Madrid seismic zone (Calais et al., 2010; Van Arsdale et al., 2019). Furthermore, Pleistocene erosion of the Upland Complex would have contributed a significant volume of sediment (>11,460 km^3) to the Pleistocene Mississippi River delta (Van Arsdale et al., 2019).

The Upland Complex is interpreted to be the remnant of a flood plain that once formed a continuous ~150 m thick blanket (Van Arsdale et al., 2019), extending at least 100 km east-west from western Tennessee to Crowley's Ridge in eastern Arkansas, and 700 km north-south along the Mississippi River (Saucier and Snead 1989; Autin et al. 1991; Van Arsdale et al. 2007; Cox et al. 2014; Cupples and Van Arsdale 2014; Lumsden et al., 2016). It consists of fluvial gravel and

fine-to-coarse-grained quartz sand with minor silt and clay (Autin et al., 1991). Grain diameters are generally less than 2 cm, but individual clasts up to 60 cm in diameter are present (Russell, 1987). Typically, >80% of the gravel consists of well-rounded chert coated with iron oxides, with the remainder consisting of well-rounded quartz and quartzite (Potter, 1955a; Guccione et al., 1990). The polished red-brown patina on the chert shows no percussion marks, indicating that it is post-depositional (Lumsden et al., 2016). The Upland Complex is capped by a ~ 2 m thick, iron-rich paleosol disconformably buried beneath Pleistocene loess that dates up to 250 ka (Markewich et al., 1992). At the base of the Upland Complex is a south-sloping, relatively flat disconformity that overlies Paleogene formations (Saucier, 1994; Van Arsdale et al., 2007).

Given the widespread nature of this deposit, its apparent deposition near the Pliocene-Pleistocene climatic transition, and its proposed triggering relationship with the New Madrid seismic zone (Van Arsdale et al., 2019), constraining the age of the Upland Complex has significant implications for the geomorphic and geodynamic history of central North America. Proposed depositional ages range from Miocene (May, 1981) to Pliocene (Potter, 1955b; Anthony and Granger, 2006; Van Arsdale et al., 2007; 2019), early Pleistocene (Fisk, 1944; Doering, 1958), and Pliocene-Pleistocene (Autin et al., 1991; Rovey and Spoering, 2020). In this paper we present new age determinations for several quarries in Arkansas, Kentucky, Mississippi, and Tennessee. We use $^{26}Al/^{10}Be$ burial dating to constrain minimum and maximum depositional times (supplementing previous work of Van Arsdale et al., 2014) and (U-Th)/He geochronology to provide a minimum age for the terrace from the crystallization of pedogenic goethite cement.

6.2 Methods

6.2.1 Cosmogenic $^{26}Al/^{10}Be$ burial dating

We directly dated terrace deposits of the Upland Complex using the cosmogenic nuclides ^{26}Al and ^{10}Be. Cosmogenic nuclides are rare isotopes that are produced by the interaction of high-energy cosmic particles with Earth's atmosphere and rocks. Most surficial production of in-situ cosmogenic ^{26}Al and ^{10}Be is driven by spallation due to cosmic-ray produced neutrons. In quartz, spallation of silicon forms ^{26}Al ($t_{1/2}$ = 0.705 My), while spallation of oxygen forms ^{10}Be ($t_{1/2}$ = 1.389 My) (Nishiizumi, 2004; Chmeleff et al., 2010; Korschinek et al., 2010). Below ~3 m of rock, production of cosmogenic nuclides via neutron spallation falls below approximately 1% its

surficial value and most production occurs via muon interactions. Muons are secondary cosmic rays produced in the upper atmosphere, and cosmogenic nuclides may be produced from high energy muon reactions or capture of low energy muons. Because muons can penetrate significantly deeper than neutrons – on the order of hundreds of meters – they are an important consideration for post-burial production of cosmogenic nuclides in buried deposits.

6.2.1.1 Minimum burial age dating

The simplest form of burial dating works under the assumption that buried sediments originated from a steadily eroding landscape. In this scenario, the concentrations of ^{26}Al and ^{10}Be are functions of the cosmogenic nuclide production rates and rock erosion rates. The preburial concentration of a given nuclide is modeled by the equation:

$$(1) \qquad N_{i,inh} = \frac{P_i}{\frac{1}{\tau_i}+\frac{\rho E}{\Lambda}}$$

where $N_{i,inh}$ is the inherited (pre-burial) concentration of the nuclide (at/g), P_i is the production rate of the nuclide (at/g/yr), τ_i is the radioactive mean-life of the nuclide, ρ is rock density (~2.6 g/cm^3), E is the pre-burial erosion rate (cm/yr), and Λ is the nucleon attenuation length (160 g/cm^2). As the pre-burial erosion rate increases, the pre-burial concentration of the nuclide will decrease. Equation (1) shows production by only nucleons for simplicity but can be extended to include muon reactions as well (e.g., Granger and Smith, 2000; Balco, 2017). Following burial, the nuclide's concentration will decrease with time:

$$(2) \qquad N_i = N_{i,inh} e^{-t/\tau_i}$$

where N_i is the measured concentration of the nuclide. Combining equations (1) and (2) yields a model of nuclide concentration N_i that is a function of pre-burial erosion rate and burial age:

$$(3) \qquad N_i = \frac{P_i}{\frac{1}{\tau_i}+\frac{\rho E}{\Lambda}} e^{-t/\tau_i}$$

Simultaneously solving equation (3) for measured concentrations of ^{26}Al and ^{10}Be yields both the burial age and pre-burial erosion rate, with the assumption that no post-burial production of ^{26}Al or ^{10}Be has occurred. It is appropriate for dating sediments that have been rapidly buried to depths where production via muons is negligible such as in caves (e.g., Granger et al., 1997), but this assumption is often violated in the case of terrace deposits, which can undergo significant post-burial production of cosmogenic nuclides due to deeply penetrating muons. Post-burial

production raises the measured $^{26}Al/^{10}Be$ ratio; as such, burial ages calculated using this approach are minimum deposit ages.

6.2.1.2 Maximum burial age dating

Post-burial production by muons causes equation (3) to underestimate the true age. We can place a maximum bound on the burial age by considering the maximum post-burial production by muons. If we assume that the sampled deposit was previously thicker and has been eroding over time, then the present depth of the sample is its minimum depth since the time of deposition. The production rate by muons at the present depth is therefore the maximum that the sample has experienced, and we can use its current depth to constrain the maximum depositional age. The maximum age may be modeled by adding a post-burial component to equation 3:

$$(4) \qquad N_i = \frac{P_i}{\frac{1}{\tau_i}+\frac{\rho E}{\Lambda}} e^{-t/\tau_i} + P_{i,z}\tau_i\left(1 - e^{-t/\tau_i}\right)$$

where $P_{i,z}$ is the production rate of a given nuclide at the modern burial depth (at/g/yr). The value of $P_{i,z}$ for a given location may be estimated using exponential approximations (e.g., Granger and Smith, 2000; Schaller et al., 2001; Braucher et al., 2013) or computerized models based on geological calibration sites (e.g., Marrero et al., 2016; Balco, 2017). As with the minimum burial age approach, equation (4) may also be solved simultaneously for measured concentrations of ^{26}Al and ^{10}Be. One complication brought on by high post-burial production, however, is that the maximum ages may be unconstrained, placing no upper bound on the true age. We have modified the traditional minimum-maximum burial dating approach to generate relative likelihood functions for the ages of dated deposits, as detailed in section 6.4.2. See Chapter 2 and Appendix B for details of sample processing.

6.2.2 (U-Th)/He dating

6.2.2.1 Overview

(U-Th)/He dating of goethite was used to determine the formation age of iron-oxide cement of the Upland Complex. The goethite cement in the interstitial space of this quartz-dominated sand displays a mostly botryoidal growth texture, which is developed on length scales of tens of micrometers. Poly-crystalline goethite aggregates typically retain >90% of radiogenic helium at

earth-surface conditions and on timescales of millions of years, as shown by previous diffusion experiments and $^{4}He/^{3}He$ studies (e.g. Shuster et al., 2005; Vasconcelos et al., 2013; Hofmann et al., 2017). SEM images reveal homogenous goethitic material without obvious grain boundaries or inclusions of tens to hundreds of micrometers in diameter. Therefore, the goethite cement of the Upland Complex is a valid target phase for (U-Th)/He dating. Previous studies on iron-oxides formed in weathering environments, most of all duricrusts (e.g. Vasconcelos et al., 2013; Riffel et al., 2016; Allard et al., 2018; Monteiro et al., 2018), have yielded geologically meaningful ages using similar material. Analytical procedures, including laser heating, helium measurement, sample dissolution, and elemental analysis, followed the ones outlined in Hofmann et al. (2020).

These ages provide information on the timescales of post-depositional weathering and soil formation. Iron-rich surficial systems frequently display dissolution of previous generations of iron-oxide and re-precipitation to form new material (e.g. Hofmann et al., 2017; Monteiro et al., 2018). This cycling of iron-oxides through dissolution-precipitation reactions leads to an age distribution skewed towards more recent ages. We therefore dated >100 aliquots to explore the temporal range of weathering and the earliest phase of post-depositional weathering, which can yield constraints on the depositional age of the Upland Complex.

6.2.2.2 Sample preparation

We sampled the Upland Complex for goethite (U-Th)/He dating in four different quarries: De Soto quarry, Drum quarry, Kuhn quarry, and Arlington quarry (Figure 6.1). Samples consisted of bulk soil material with iron-oxide cement and groundwater crusts. Groundwater crusts were crushed to ~200-500 μm grainsize. Bulk soil material and crushate was sieved to remove material <20 μm and >2 mm, and then density separated using a sodium polytungstate (SPT) solution of density ~3050 kg/m^3. The material was mixed with the SPT and centrifuged at 3200 rpm for 30 min. The supernatant was discarded, and the settled material was rinsed several times in distilled water. This process removed most of the quartz and other light minerals and left material highly enriched in iron-oxides. Samples of the Kuhn quarry were treated with 0.1 M hydroxylamine hydrochloride at room temperature for 4 hours to selectively dissolve Mn-oxide grains (procedure after Chao, 1972).

6.2.2.3 Analysis

Aliquots of iron-oxide cement free of visible inclusions and intergrowth with other phases were picked from this material and loaded into Pt tubes. Aliquots representing the center of interstitial goethite cement away from neighboring phases were picked, in order to reduce the effect of possible alpha ejection and implantation. Degassing, ^{4}He measurement, dissolution, and ICP-MS measurement of U, Th, Sm, Fe, Mn, Al, and Si followed the goethite protocol described in Hofmann et al. (2020). Procedural He blanks were around 1 pcc (~45 amol) and measured He amounts were at least a factor of 3 above blank level (>3 pcc). Blanks were interspersed among sets of 6-12 sample measurements. Reported He measurements were blank-corrected using these procedural blank measurements.

Aliquots were screened for being pure iron-oxide by measuring elemental contributions from substitution for Fe and from other phases. We rejected aliquots based on the following criteria: (1) the Fe-based mass was significantly lower than expected based on the physical dimensions of the aliquot, (2) aliquots with an Al, Si, and Mn content above reasonable limits for goethite stoichiometry, (3) Fe-based mass and trace element concentrations were comparable to other aliquots of the same sample but contained a much higher He concentration and subsequently produced ages that were geologically unreasonable. An elevated He concentration is most likely due to He implanted from and contained in insoluble mineral inclusions, such as zircon, and has been observed in previous studies (e.g. Hofmann et al., 2017; Hofmann, 2019).

The mineral phases of samples were identified using Attenuated Total Reflection Fourier-Transform Infrared (ATR-FTIR) spectroscopy by comparing them to known goethite, hematite, and quartz samples. Characteristic peaks for goethite are at 795 cm^{-1}, 899 cm^{-1}, 1662 cm^{-1}, and 1793 cm^{-1}, with an additional broad peak with a center around 3090-3110 cm^{-1}. Quartz peaks are at 1079 cm^{-1} and 453 cm^{-1}, with an additional doublet at 783 cm^{-1}.

6.3 Results

6.3.1 Initial ^{26}Al/^{10}Be geochronology

Van Arsdale et al. (2014) previously dated a remnant of the Upland Complex in Arlington, Tennessee, 15 km northeast of Memphis using cosmogenic ^{26}Al/^{10}Be in two samples from a Memphis Stone and Gravel Company quarry. These samples were collected at a depth of

approximately 10 m below the top of the Upland Complex and processed by G. Balco for AMS measurement. Gravel sample 12-GG-UC2 yielded a minimum burial age of 1.35 ± 0.15 Ma and a maximum burial age of 2.84 ± 0.52 Ma, while sand sample 12-GG-UC1S yielded a minimal burial age of 1.57 ± 0.15 Ma and a maximum burial age of 3.14 ± 0.49 Ma (all 1σ analytical uncertainties). These results indicate that this section of the Upland Complex is at least Early Pleistocene in age and may be Pliocene.

6.3.2 New $^{26}Al/^{10}Be$ burial ages

Measured ^{26}Al and ^{10}Be concentrations are provided in the supplementary data. The minimum ages were generally Pleistocene, with the exceptions of samples VA-DRUM (sand), MID-1 (quartz gravel), and VA-TRI-52 (chert). Sample MID-1, a single quartz clast, featured an unusually old age and low $^{26}Al/^{10}Be$ ratio relative to its counterparts at the Mid-South quarry, indicating that it experienced previous burial. As such, it was excluded from further calculations. Similarly, the chert clast VA-TRI-52 had an excess concentration of ^{10}Be that lowered its $^{26}Al/^{10}Be$ ratio and increased its apparent age. This was attributed to meteoric ^{10}Be contamination that commonly occurs with cherts and led to the sample's exclusion from the final age estimate. VA-DRUM, being a sand fraction, likely contained minimal reworked material and yielded a valid Pliocene minimum age of 2.68 ± 0.27 Ma (1σ analytical uncertainty).

Pre-burial erosion rates were generally low, but can be difficult to quantify when significant post-burial production has occurred. If post-burial production of $^{26}Al/^{10}Be$ is unaccounted for, the calculated pre-burial erosion rates will likely overestimate the true values. Conversely, accounting for maximum post-burial production will potentially yield underestimates of pre-burial erosion rates (see Figure 6.2). Nonetheless, the pre-burial erosion rates that ignore post-burial production are useful for placing bounds on maximum erosion rates prior to sediment burial (see supplementary table). Sand fractions yielded generally slow pre-burial erosion rates, ranging from 6.6-21.8 m/My. Gravel fractions and individual clasts yielded somewhat higher pre-burial erosion rates, ranging from 7.0-33.9 m/My when the ^{10}Be-contaminated chert clast was ignored.

While minimum burial ages for the remaining samples were generally Early Pleistocene and featured low uncertainties, the maximum burial ages were more widely distributed. In most cases, maximum ages were unconstrained toward infinity. These partial maximum burial ages aid in identifying more likely burial ages but leave open the possibility of infinite burial ages. Samples

12-GG-UC2 and 12-GG-UC-1S, both from the Arlington quarry, produced the only completely constrained maximum burial ages. Their respective burial ages permit either a Pleistocene or Pliocene burial age for the Upland Complex at the Arlington quarry. This wide span of possible ages motivates an additional constraint – (U-Th)/He geochronology – on the true age of the Upland Complex. The high precision of (U-Th)/He dating on goethite cements allows a further constraint on the minimum age of Upland Complex deposits.

6.3.3 (U-Th)/He Results

We acquired (U-Th)/He formation ages of a total of 102 individual aliquots, of which 18 were rejected based on the criteria outlined in the methods section. The ATR-FTIR spectra (Figure 6.3) of samples analyzed for (U-Th)/He dating show that they mainly consist of goethite. The spectra also show a minor contribution of quartz in the bulk samples used for ATR-FTIR analysis. The aliquots picked from this material for (U-Th)/He dating were single grains of pure goethite with diameters of several hundred micrometers and did not contain any quartz. Since they are much larger than the mean alpha ejection distance (~20 μm), no correction for alpha ejection or implantation was applied. A correlation between age and effective uranium concentration (eU), which would indicate detectable loss of U due to sample heating (see Hofmann et al., 2020), was not observed.

(U-Th)/He formation ages of goethite cements from the Upland Complex taken on depth profiles starting just below the "clay gravel" paleosol in the De Soto and Arlington quarries decline with depth (Figure 6.4). All (U-Th)/He dates are given with analytical uncertainties to the 1σ level. The oldest ages (2-3.5 Ma) occur close to the contact with the well-developed paleosol. About 0.5 m below the contact, ages range from 0.5 Ma to 2 Ma. Ages are <1 Ma at ~1 m below the contact. A sample of a groundwater crust just above the modern groundwater table (Arlington-D) yielded a near-zero age.

Groundwater crusts from the Drum quarry yielded ages between 0.4 Ma and 3 Ma. A goethite cemented boulder from a depth of approximately 15 m beneath the top of the Upland Complex from the Kuhn quarry yielded ages of 0.1-1.5 Ma, with most ages between 0.2 Ma and 0.4 Ma, and only two aliquots >0.6 Ma.

6.4 Discussion

6.4.1 Implications of $^{26}Al/^{10}Be$ and (U-Th)/He results

Taken together, the $^{26}Al/^{10}Be$ and (U-Th)/He geochronology reveal a Late Neogene history of floodplain and terrace formation followed by post-depositional weathering. Based on $^{26}Al/^{10}Be$ ages alone, it appears likely that the Upland Complex formed during the Pliocene or Pleistocene; however, it is not possible to determine whether all dated terraces are the same age. The best $^{26}Al/^{10}Be$ constraints on the age of the Upland Complex were sourced from the Arlington quarry, but even these results cannot resolve the Pliocene or Pleistocene age of the Upland Complex. Our estimates of pre-burial erosion rates from sands indicate generally slow erosion rates that support a pre-glacial origin, but do not conclusively demonstrate a Pliocene age.

The (U-Th)/He ages resulting from this study place basic constraints on the minimum ages of the dated sites, as in-place goethite formation must have postdated the formation of the Upland Complex. The similar distributions of (U-Th)/He ages from the Arlington and Kuhn quarries – mostly Late Pleistocene with rare Early Pleistocene to Pliocene ages – reflect the likelihood that older goethite deposits have likely been dissolved and reprecipitated, skewing the distributions toward younger ages (Figure 6.5). An additional indication for this process is that the youngest ages are found close to the modern groundwater table, whereas the oldest ages are found well above the groundwater table. Some young ages may also be the result of intergrowth between older and younger material at length scales below that of an individual aliquot or partial helium-loss in the case of very fine-grained material. This could potentially lead to an underestimation of the minimum age. Though less evident at the DeSoto and Drum quarries, skewed age distributions demonstrate a potential limitation of using goethite formation ages as minimum bounds on the true age of a deposit. Even so, incorporating each site's oldest (U-Th)/He age significantly improved age estimates for three of the four sites dated with (U-Th)/He that featured Pliocene (U-Th)/He ages: De Soto quarry (2.8 ± 0.1 Ma), Drum quarry (2.8 ± 0.1 Ma), and Arlington quarry (3.6 ± 0.1 Ma). Based on (U-Th)/He data alone, it appears that the Upland Complex is a pre-glacial unit as these ages significantly predate the first major Pleistocene glaciation at 2.42 ± 0.14 Ma (Balco and Rovey, 2010).

6.4.2 Generating relative likelihood functions for dated deposits

To calculate the permissible range of $^{26}Al/^{10}Be$ ages for each sample, we solved equations (3) and (4) for measured concentrations of ^{26}Al and ^{10}Be. Uncertainties were propagated numerically assuming normal distributions for the isotope measurements. We constructed a likelihood function for the total permissible age distribution of each sample by taking the minimum age from the left (younger) side of the minimum age likelihood function, and the maximum age from the right (older) side of the maximum age likelihood function. For cases with minor post-burial production, this approach yielded closed likelihood functions. In cases where the theoretical post-burial production calculated with equation (4) yielded greater concentrations than actually measured, the maximum age likelihood function was unconstrained on the high end.

To generate overall age estimates for individual quarry sites with multiple samples, we assumed that (1) all sands and gravels of a given terrace deposit were the same age and (2) all (U-Th)/He ages represented minimum ages for the deposit, since goethite formation post-dated terrace deposition. We generated a likelihood function for the oldest (U-Th)/He age at each location that featured constant likelihood for all ages exceeding the (U-Th)/He age. This likelihood function was then multiplied by all of the $^{26}Al/^{10}Be$ likelihood functions at that location to generate an overall likelihood function for the site. We opted to multiply, rather than add, likelihood functions in order to set likelihood to zero in age ranges forbidden by any sample. At locations where only $^{26}Al/^{10}Be$ measurements were available (i.e. Mid-South and Tri-County quarries), we multiplied all $^{26}Al/^{10}Be$ likelihood functions. This yielded one final likelihood function of permissible ages per quarry, six in total. These likelihood functions were then normalized for each site to generate relative likelihood functions (Figure 6.6).

6.4.3 Confirming a Pliocene age for the Upland Complex

By combining $^{26}Al/^{10}Be$ and (U-Th)/He geochronology, new age estimates emerge for several sites. Kuhn, Mid-South, and Tri-County quarries may still be Pleistocene in age, given their distributions of $^{26}Al/^{10}Be$ and (U-Th)/He ages. It is clear, however, that the deposits at the Arlington, DeSoto, and Drum quarries date to at least the Late Pliocene. Summing all of the likelihood functions yields a curve that sharply increases during the Late Pliocene and reaches a maximum value at 3.61 Ma. Given the high uncertainty of most maximum ages, the relative

likelihood function gradually tapers as age increases. If it is assumed that all deposits must be the same age, multiplying the relative likelihood functions for each site yields a well-constrained likelihood function for the age of the Upland Complex. This function is strongly controlled by the likelihood function for the Arlington quarry and also yields a most likely age of 3.61 Ma, with potential ages ranging from 3.40-4.29 Ma (Figure 6.6). Whether or not the deposits were coevally formed, these models indicate that the Upland Complex is likely a Pliocene deposit.

The strong dependence of our age estimate on the ages from Arlington quarry is an important consideration when estimating the overall age of the Upland Complex. If the $^{26}Al/^{10}Be$ and (U-Th)/He ages from Arlington are discarded when estimating the Upland Complex's age, a slightly different age distribution is revealed. Due to the Pliocene (U-Th)/He ages for goethite deposits at the DeSoto and Drum quarries, it remains likely that the Upland Complex is indeed at least Pliocene in age. The lack of Pliocene goethite at the Kuhn, Mid-South, and Tri-County quarries may reflect dissolution of older generations of cement at those sites and does not preclude a Pliocene minimum age for those locations. While the uncertainties of $^{26}Al/^{10}Be$ maximum ages at the remaining sites remain high, the maximum age distributions for the Drum, Kuhn, and Mid-South quarries all indicate a likely Messinian – but possibly Tortonian – maximum age (Figure 6.6). As such, it appears likely that the Upland Complex is at least Pliocene in age and no older than Late Miocene, even in the absence of the measurements at the Arlington quarry.

These age ranges overlap within uncertainty with cosmogenic $^{26}Al/^{10}Be$ burial ages for the Grover Gravel deposits in southern Missouri (Rovey et al., 2016) that have been argued to represent the transition from the late Pliocene to the early Pleistocene (Rovey and Spoering, 2020). Our age estimate could correspond to a period of normal or reverse magnetic polarity (Cande and Kent, 1995), so it is not possible to compare with the observation of Rovey and Spoering (2020) that the Grover Gravel was deposited during a period of normal polarity. Our evidence is compatible with the Grover Gravel and Upland Complex being equivalent but does not unequivocally demonstrate this hypothesis.

6.4.4 The Upland Complex floodplain and Pliocene sea level

Prior to the formation of the Upland Complex, a higher elevation Mississippi River deposited a floodplain mapped as the Citronelle Formation (Dockery and Thompson, 2016), preserved in southern Mississippi. Dockery and Thompson (2016) report that the Citronelle

Formation is the remnant of a vast fluvial deposit preserved on drainage divides and is probably Pliocene in age. Near Crystal Springs, Mississippi, the base of the Citronelle is 141 m above msl and slopes south at ~ 1m/km. The top of the Upland Complex at the latitude of Crystal Springs is ~ 115 m amsl, thus illustrating that these do not represent the same level of the ancestral Mississippi River. We hypothesize that incision through the Citronelle Formation and establishment of an Upland Complex floodplain may have been controlled by an Early Pliocene base level drop, perhaps coincident with a currently unidentified continental glaciation.

Our range of possible Pliocene burial ages for different deposits of the Upland Complex may reflect its gradual formation during a prolonged period of base level stability. At the De Soto, Drum, Kuhn, Mid-South, and Tri-County Quarries, we observed overlapping age distributions during the mid-to-late Pliocene that postdate the Arlington Quarry deposit's formation at ~3.6 Ma. We propose that, given its broad areal extent and thickness, the Upland Complex was gradually deposited during the Pliocene. This gradual mechanism of formation yields similar yet asynchronous age distributions for different dated sites of the Upland Complex, as represented by a broad plateau on the sum of likelihood distributions for all quarries (Figure 6.6).

The late Pliocene featured generally high sea levels (Miller et al., 2020) and included the mid Piacenzian Warm Period (mPWP), a well-documented period of elevated temperatures and high sea level (Robinson et al., 2018). Similar conditions were likely responsible for the formation of numerous erosional and aggradational features in North America. Along the east coast of North America, widespread wave-cut shorelines provide evidence of a sea level high stand from ~3.3-2.9 Ma (Rovere et al., 2015). In the Shenandoah Valley, Virginia, $^{26}Al/^{10}Be$ dating of alluvial fans and terraces has revealed widespread aggradation at ~3.3 Ma followed by gradual incision (Odom et al., 2019). It appears likely that the Upland Complex also formed as a result of Pliocene aggradation resulting from prolonged base level stability and a high sea level.

6.5 Conclusion

The age of the Upland Complex has been debated for decades. Previous efforts to date the Upland Complex with cosmogenic $^{26}Al/^{10}Be$ improved age constraints but were unable to discern a Pliocene or Pleistocene age. Our combination of $^{26}Al/^{10}Be$ burial dating with (U-Th)/He dating of goethite cements demonstrates that the Upland Complex predates the Pleistocene and is very

likely Pliocene in age. This supports the hypothesis that the Upland Complex was deposited prior to Pleistocene glaciation.

6.6 Acknowledgements

We thank Greg Balco for his work to date the Arlington quarry. We wish to thank a number of people who allowed us to sample in their quarries: Jeff Drum (Drum Sand and Gravel, Inc.), Ken McCarley (Kuhn quarry owned by Hammett Gravel Company, Inc.), David Gavin (Mid-South Construction and Old Hickory Clay Company), Dale Gulledge (Tri-County Sand and Gravel quarry). We are also grateful for Ken Miller for providing us with the sea level curve data. Thoughtful suggestions from Atsunori Nakamura, Lewis Owen, and an anonymous reviewer helped us improve the manuscript. This project was partially supported by the National Science Foundation (Grant #1700821) and a PRIME Lab seed grant.

6.7 Data availability

A complete dataset of (U-Th)/He ages, goethite compositions, and related data are available in the supplementary data for this article on *Geomorphology*. This includes $^{26}Al/^{10}Be$ data, burial ages, and non-blank-corrected AMS data for $^{26}Al/^{27}Al$ and $^{10}Be/^{9}Be$ measurements. MATLAB code for likelihood function calculations is included in supplementary documentation: https://data.mendeley.com/datasets/jfjbvnr6fw/draft?a=f5fd9c9d-aa26-45b8-882c-08856c46c931

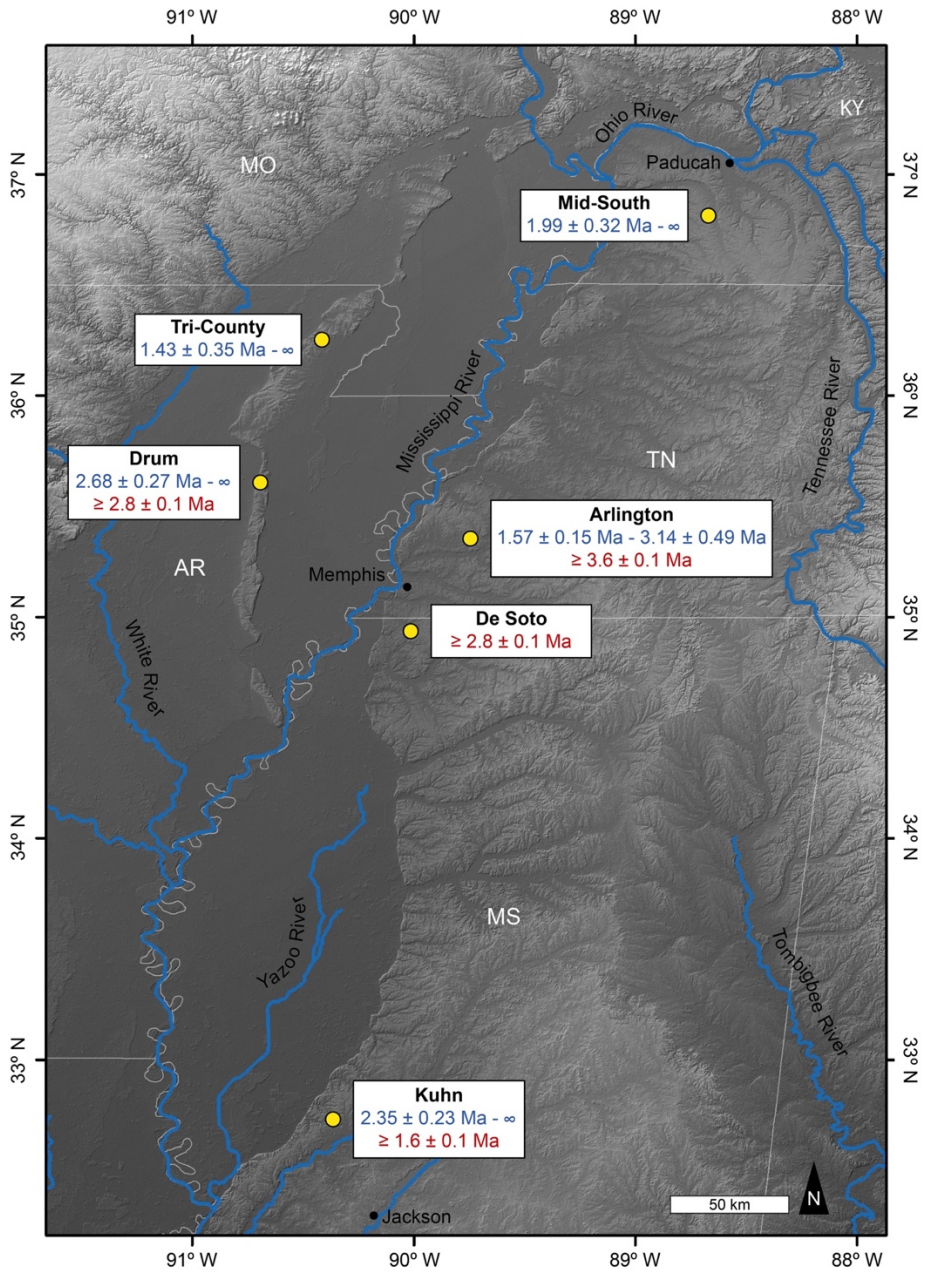

Figure 6.1. Locations of sites dated with cosmogenic $^{26}Al/^{10}Be$ and (U-Th)/He geochronology. Cosmogenic $^{26}Al/^{10}Be$ burial ages of terraces are shown above (U-Th)/He ages and represent the 1σ (analytical uncertainty) minimum and maximum ages where available; minimum age constraints derived from the oldest (U-Th)/He ages (with 1σ uncertainty) for each site are shown below burial ages. Note that the Mid-South and Tri-County quarries only have $^{26}Al/^{10}Be$ burial ages, while the De Soto quarry only has a (U-Th)/He age.

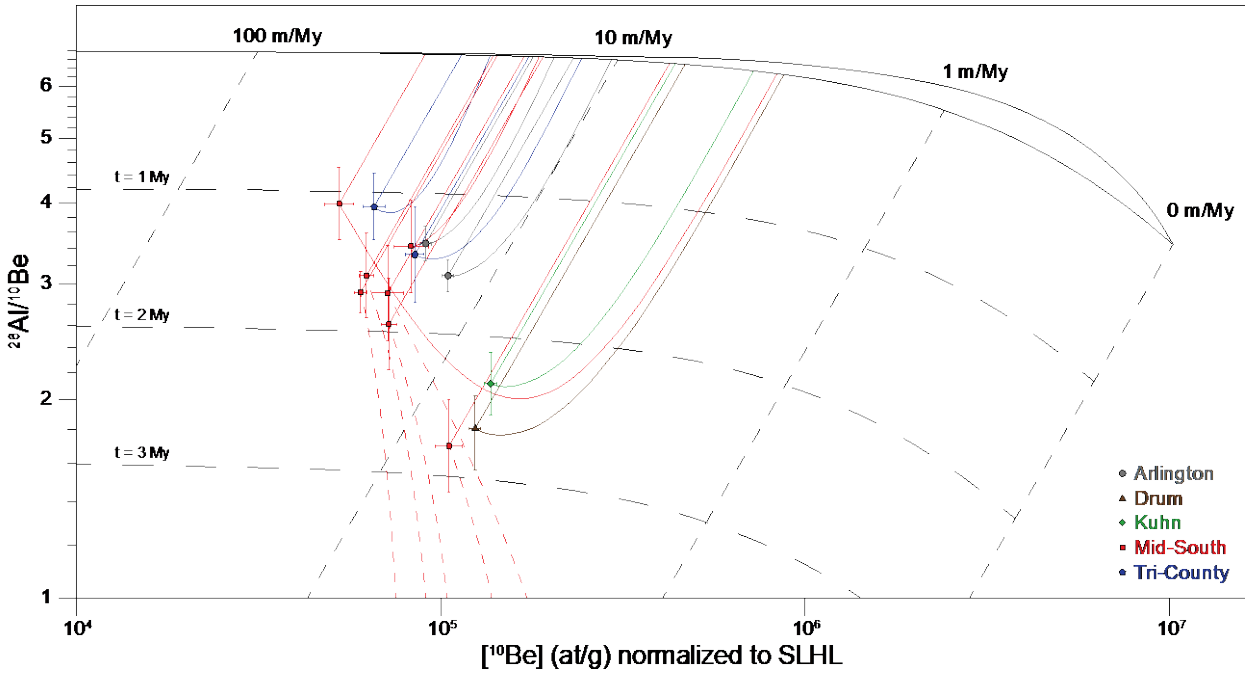

Figure 6.2. Measured samples and their projected pre-burial histories are shown on the exposure-burial diagram. Simple burial histories that do not account for post-burial production (minimum ages) are represented by straight lines; burial histories that do account for post-burial production (maximum ages) are represented by curves. Samples that yielded indefinite maximum ages have unconstrained burial histories represented by dashed lines. Note that pre-burial erosion rate estimates are lower when post-burial production is incorporated into sample histories.

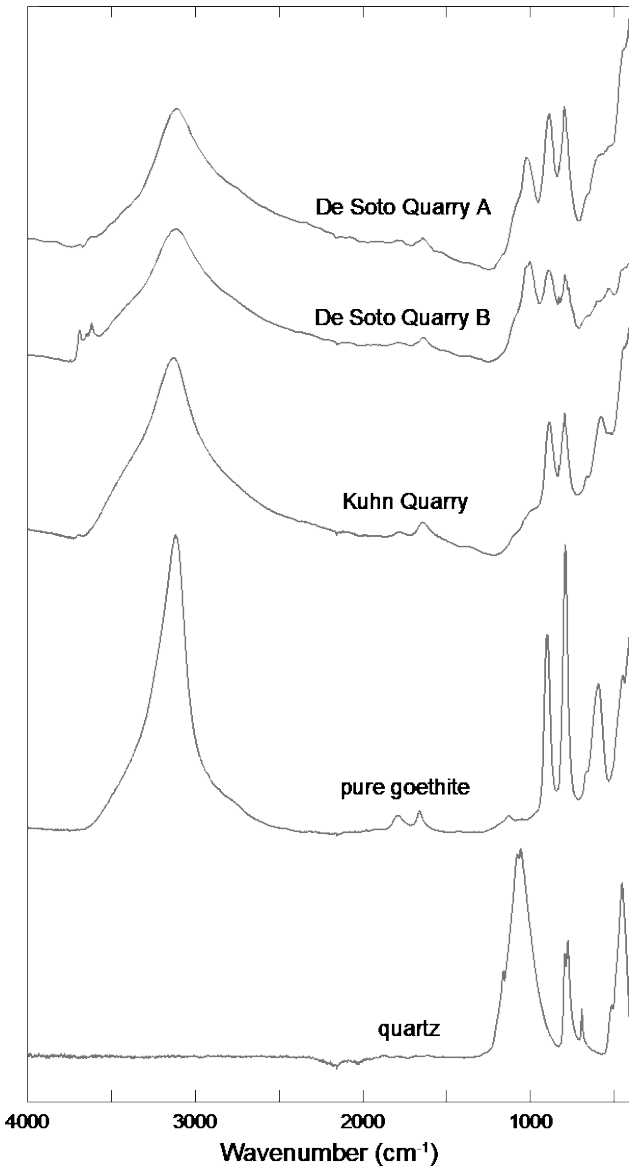

Figure 6.3. ATR-FTIR spectra of separates from the De Soto and Kuhn quarries compared against pure goethite and quartz. Separates are mostly composed of goethite, with a small amount of quartz present in the bulk material (only goethite was selected for (U-Th)/He dating). Samples from De Soto quarry also show a minor contribution from kaolinite (peaks at 3635, 3730 cm^{-1}).

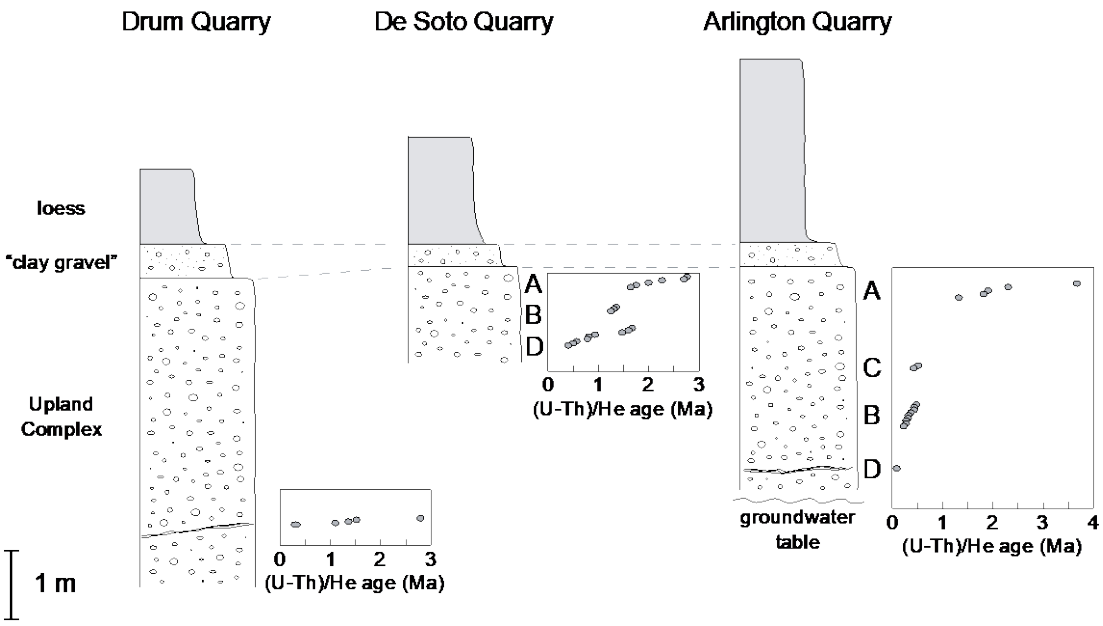

Figure 6.4. (U-Th)/He dates of goethite cements from the Upland Complex, which is capped by a paleosol ("clay gravel"), and Pleistocene loess. Ages are oldest close to the bottom of the paleosol and decline with depth. Groundwater crusts (indicated by black streaks in the stratigraphic sections) near the modern groundwater table (Arlington quarry) have a near-zero age.

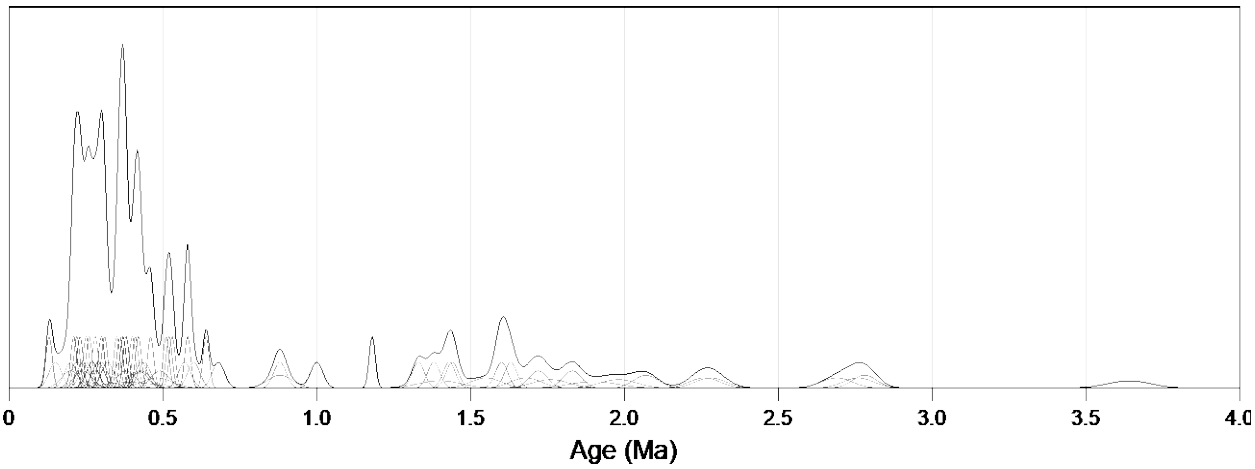

Figure 6.5. Normal kernel density estimates of (U-Th)/He ages of goethite cements. Individual ages are shown in gray; overall age distribution is shown in black. Note that the age distribution is skewed toward ages <0.5 Ma, reflecting the likely dissolution and reprecipitation of older iron oxide deposits. Plot created using camelplot.m MATLAB code by G. Balco, available at http://depts.washington.edu/cosmolab/pubs/gb_pubs/camelplot.m

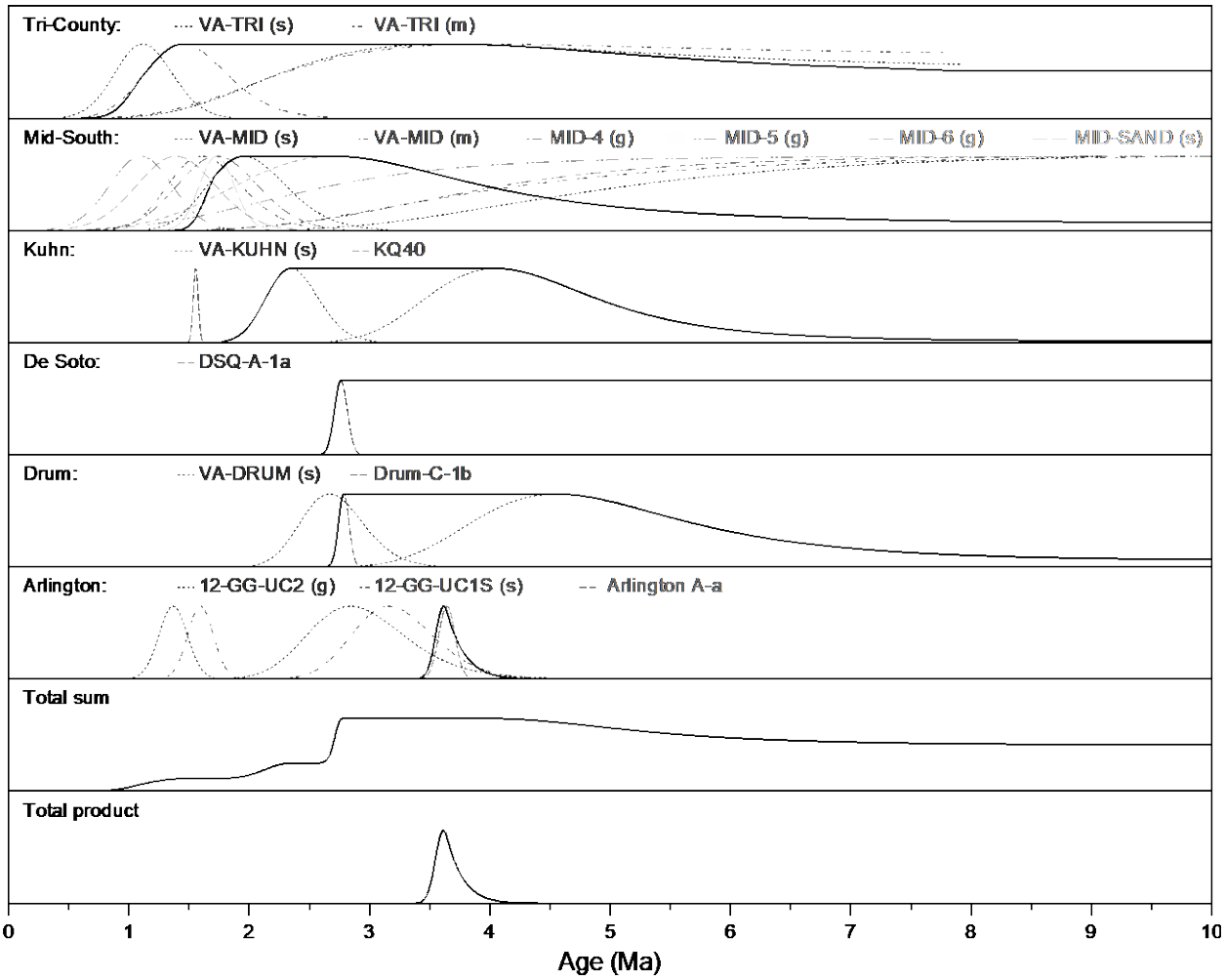

Figure 6.6. Relative likelihood functions for all sites and the Upland Complex as a whole. Each site's most likely age is represented by a solid line and was calculated by multiplying the normalized likelihood functions for the $^{26}Al/^{10}Be$ minimum/maximum ages and the oldest (U-Th)/He age at each site, where available. Dashed lines represent minimum and maximum ages from $^{26}Al/^{10}Be$ and (U-Th)/He dating; individual likelihood functions are available in the supplementary figure. The total sum represents the normalized sum of relative likelihood functions from all sites, while the total product assumes coeval deposition and was calculated from the normalized product of all relative likelihood functions.

6.8 References

Allard, T., Gautheron, C., Riffel, S. B., Balan, E., Soares, B. F., Pinna-Jamme, R., et al., 2018. Combined dating of goethites and kaolinites from ferruginous duricrusts. Deciphering the Late Neogene erosion history of Central Amazonia. Chemical Geology 479, 136-150.

Anthony, D.M., Granger, D.E., 2006. Five million years of Appalachian landscape evolution preserved in cave sediments. Spec. Pap. Geol. Soc. Am. 404, 39–50. https://doi.org/10.1130/2006.2404(05)

Autin, W. J., Burns, S. F., Miller, B. J., Saucier, R. T., Snead, J. I., 1991. Quaternary geology of the Lower Mississippi Valley, in Quat. Nonglac. Geol.: Conterminous US. Geol. Soc. Am., 547-582.

Balco, G., 2017. Production rate calculations for cosmic-ray-muon-produced ^{10}Be and ^{26}Al benchmarked against geological calibration data. Quat. Geochronol. 39, 150–173. https://doi.org/10.1016/j.quageo.2017.02.001

Balco, G., Rovey, C.W., 2010. Absolute chronology for major Pleistocene advances of the Laurentide Ice Sheet. Geology 38, 795–798. https://doi.org/10.1130/G30946.1

Behrman, C., Van Arsdale, R., Kwon, Y., Stockslager, K., Leverett, D., and Lumsden, D., 2019, Drone geologic mapping of an active sand and gravel quarry, DeSoto County, Mississippi. Drones, v. 3, n. 57, p. 1-14. https://doi.org/10.3390/drones3030057

Braucher, R., Bourlès, D., Merchel, S., Vidal Romani, J., Fernadez-Mosquera, D., Marti, K., Léanni, L., Chauvet, F., Arnold, M., Aumaître, G., Keddadouche, K., 2013. Determination of muon attenuation lengths in depth profiles from in situ produced cosmogenic nuclides. Nucl. Instruments Methods Phys. Res. Sect. B Beam Interact. with Mater. Atoms 294, 484–490. https://doi.org/10.1016/j.nimb.2012.05.023

Calais, E., Freed, A.M., Van Arsdale, R., and Stein, S., 2010, Triggering of New Madrid seismicity by late-Pleistocene erosion. Nat., v. 466, p. 608-611. https://doi.org/10.1038/nature09258

Cande, S.C., Kent, D. V., 1995. Revised calibration of the geomagnetic polarity timescale for the late Cretaceous and Cenozoic. J. Geophys. Res. 100, 6093–6095. https://doi.org/10.1029/94JB03098

Chao, T.T., 1972. Selective dissolution of manganese oxides from soils and sediments with acidified hydroxylamine hydrochloride. Soil Sci. Soc. Am. J. 36, 764–768. https://doi.org/10.2136/sssaj1972.03615995003600050024x

Chmeleff, J., von Blanckenburg, F., Kossert, K., Jakob, D., 2010. Determination of the ^{10}Be half-life by multicollector ICP-MS and liquid scintillation counting. Nucl. Instruments Methods Phys. Res. Sect. B Beam Interact. with Mater. Atoms 268, 192–199. https://doi.org/10.1016/j.nimb.2009.09.012

Cooper, F. J., Adams, B. A., Blundy, J. D., Farley, K. A., McKeon, R. E., Ruggiero, A., 2016. Aridity-induced Miocene canyon incision in the Central Andes. Geology 44(8), 675-678. https://doi.org/10.1130/G38254.1

Cox, R.T., Lumsden, D.N., Van Arsdale, R.B., 2014. Possible relict meanders of the Pliocene Mississippi River and their implications. J. Geol. 122, 609–622. https://doi.org/10.1086/676974

Cupples, W., Van Arsdale, R., 2014. The preglacial "Pliocene" Mississippi River. J. Geol. 122, 1–15. https://doi.org/10.1086/674073

Dockery, D.T., 1996. Toward a revision of the generalized stratigraphic column of Mississippi. Mississippi Geol. 17, 2–8.

Dockery, D.T., Thompson, D.E., 2016. The geology of Mississippi. University Press of Miss., Jackson, 751.

Doering, J. A., 1958. Citronelle Age Problem. Am. Assoc. Pet. Geol. Bull. 42, 764–786. https://doi.org/10.1306/0bda5ac2-16bd-11d7-8645000102c1865d

Fisk, H.N., 1944. Geological investigation of the alluvial valley of the lower Mississippi River: Vicksburg, Mississippi. U.S. Army Corps of Eng., Miss. River Comm., 78.

Granger, D.E., 2006. A review of burial dating methods using ^{26}Al and ^{10}Be. Spec. Pap. Geol. Soc. Am. 415, 1–16. https://doi.org/10.1130/2006.2415(01)

Granger, D.E., Kirchner, J.W., Finkel, R.C., 1997. Quaternary downcutting rate of the New River, Virginia, measured from differential decay of cosmogenic ^{26}Al and ^{10}Be in cave-deposited alluvium. Geology 25, 107–110. https://doi.org/10.1130/0091-7613(1997)025<0107:QDROTN>2.3.CO;2

Granger, D.E., Smith, A.L., 2000. Dating buried sediments using radioactive decay and muogenic production of ^{26}Al and ^{10}Be. Nucl. Instruments Methods Phys. Res. Sect. B Beam Interact. with Mater. Atoms 172, 822–826.

Guccione, M.J., Prior, W.L., Rutledge, E.M., 1990. The Tertiary and early Quaternary geology of Crowley's Ridge, in Guccione, M., and Rutledge, E., eds., Field Guide to the Mississippi Alluvial Valley Northeast Arkansas and Southeast Missouri: Fayetteville, Arkansas. Friends of the Pleistocene South Central Cell, 23–44.

Harrison, R.W., Hoffman, D., Vaughn, J.D., Palmer, J.R., Wiscombe, C.L., McGeehin, J.P., Stephenson, W.J., Odum, J.K., Williams, R.A., Forman, S.L., 1999. An example of neotectonism in a continental interior - Thebes Gap, Midcontinent, United States. Tectonophysics 305, 399–417. https://doi.org/10.1016/S0040-1951(99)00010-4

Hofmann, F., 2019. Iron-oxide geochronology to constrain the formation of soils and paleosols. Calif. Inst. of Technol., PhD thesis.

Hofmann, F., Reichenbacher, B., Farley, K.A., 2017. Evidence for >5 Ma paleo-exposure of an Eocene–Miocene paleosol of the Bohnerz Formation, Switzerland. Earth Planet. Sci. Lett. 465, 168–175. https://doi.org/10.1016/j.epsl.2017.02.042

Hofmann, F., Treffkorn, J., Farley, K.A., 2020. U-loss associated with laser-heating of hematite and goethite in vacuum during (U–Th)/He dating and prevention using high O_2 partial pressure. Chem. Geol. 532, 119350. https://doi.org/10.1016/j.chemgeo.2019.119350

Korschinek, G., Bergmaier, A., Faestermann, T., Gerstmann, U.C., Knie, K., Rugel, G., Wallner, A., Dillmann, I., Dollinger, G., von Gostomski, C.L., Kossert, K., Maiti, M., Poutivtsev, M., Remmert, A., 2010. A new value for the half-life of ^{10}Be by heavy-ion elastic recoil detection and liquid scintillation counting. Nucl. Instruments Methods Phys. Res. Sect. B Beam Interact. with Mater. Atoms 268, 187–191. https://doi.org/10.1016/j.nimb.2009.09.020

Lumsden, D.N., Cox, R.T., Van Arsdale, R.B., Cupples, W.B., 2016. Petrology of Pliocene Mississippi River alluvium: provenance implications 124, 501–517. https://doi.org/10.1086/686997

Markewich, H. W., Millard Jr, H. T., Pavich, M. J., Rodbell, D. T., Rich, F. J., Rutledge, E. M., Ward, L., Van Valkenberg, S., Wysocki, D., 1992. Chronostratigraphic and paleoclimatic data for Quaternary loessial and fluvial deposits in the Mississippi River Valley of Arkansas and Tennessee. Geol. Soc. Am., Abstr. with Progr., A50.

Marrero, S.M., Phillips, F.M., Borchers, B., Lifton, N., Aumer, R., Balco, G., 2016. Cosmogenic nuclide systematics and the CRONUScalc program. Quat. Geochronol. 31, 160–187. https://doi.org/10.1016/j.quageo.2015.09.005

May, J.H., 1981. The updip limit of Miocene sediments in Mississippi. Geol. Soc. Am. Abstr. with Progr. 13, 1, 29.

Miller, K.G., Browning, J. V, Schmelz, W.J., Kopp, R.E., Mountain, G.S., Wright, J.D., 2020. Cenozoic sea-level and cryospheric evolution from deep-sea geochemical and continental margin records. Science Advances 6(20), eaaz1346.

Monteiro, H.S., Vasconcelos, P.M.P., Farley, K.A., Lopes, C.A.M., 2018. Age and evolution of diachronous erosion surfaces in the Amazon: Combining (U-Th)/He and cosmogenic 3He records. Geochim. Cosmochim. Acta 229, 162–183. https://doi.org/10.1016/j.gca.2018.02.045

Odom, W. E., Granger, D. E., Doctor, D. H., 2019. Dating a mid-Pliocene aggradational episode and subsequent river incision in the Shenandoah Valley with cosmogenic ^{26}Al and ^{10}Be. Geol. Soc. Am., Abstr. with Prog. 51, 5.

Olive W. W., 1980. Geologic maps of the Jackson Purchase Region, Kentucky. U.S. Geol. Surv. Misc. Investigations Ser. Map I-1217, scale 1:250,000.

Nishiizumi, K., 2004. Preparation of ^{26}Al AMS standards. Nucl. Instruments Methods Phys. Res. Sect. B Beam Interact. with Mater. Atoms 223–224, 388–392. https://doi.org/10.1016/j.nimb.2004.04.075

Nishiizumi, K., Imamura, M., Caffee, M.W., Southon, J.R., Finkel, R.C., McAninch, J., 2007. Absolute calibration of ^{10}Be AMS standards. Nucl. Instruments Methods Phys. Res. Sect. B Beam Interact. with Mater. Atoms 258, 403–413. https://doi.org/10.1016/j.nimb.2007.01.297

Potter, P. E., 1955a. The petrology and origin of the Lafayette Gravel. Part 1. Mineralogy and petrology. J. of Geology 63, 1–38.

Potter, P.E., 1955b. The petrology and origin of the Lafayette Gravel. Part 2. Geomorphic history. J. of Geology 63, 115–132.

Riffel, S. B., Vasconcelos, P. M., Carmo, I. O., & Farley, K. A., 2016. Goethite (U–Th)/He geochronology and precipitation mechanisms during weathering of basalts. Chemical Geology 446, 18-32.

Robinson, M. M., Dowsett, H. J., Foley, K. M., Riesselman, C. R., 2018. PRISM marine sites—The history of PRISM sea surface temperature estimation. US Geol. Surv., No. 2018-1148.

Rovere, A., Hearty, P. J., Austermann, J., Mitrovica, J. X., Gale, J., Moucha, R., Forte, A., Raymo, M. E., 2015. Mid-Pliocene shorelines of the US Atlantic Coastal Plain — an improved elevation database with comparison to Earth model predictions. Earth-Sci. Rev., 145, 117-131.

Rovey, C. W., II, Siemens, M., Balco, G., 2016. Provenance, age, and depositional mechanisms of the Grover Gravel: evidence for multiple erosion cycles, volcanic eruptions, and early glaciations, in Lasemi, Z. and Elrick, S. D. (eds.): 1967–2016 – Celebrating 50 years of Geoscience in the Mid-Continent, 97–124. Guidebook for the 50th Annual Meeting of the Geological Society of America – North-Central Section, April 18–19, 2016. Ill. State Geol. Surv. Guidebook 43.

Rovey, C. W., Spoering, G., 2020. Age and provenance of upland gravels in Missouri, USA, and their relationship to Early Pleistocene glaciation. Boreas 49(2), 333-349.

Russell, E.E., 1987. Gravel aggregate in Mississippi—Its origin and distribution. Miss. Geology 7, 3, 7.

Saucier, R.T., 1994. Geomorphology and Quaternary geologic history of the lower Mississippi valley. Vicksburg, Miss., U.S. Army Eng. Waterw. Exp. Stn., 1, 364.

Saucier, R. T., Snead, J. I., 1989. Quaternary geology of the Lower Mississippi Valley. Baton Rouge La. Geol. Surv., scale 1:1,000,000, 1 sheet.

Schaller, M., von Blanckenburg, F., Hovius, N., Kubik, P. W., 2001. Large-scale erosion rates from in situ-produced cosmogenic nuclides in European river sediments. Earth Planet. Sci. Lett. 188(3-4), 441-458.

Shuster, D.L., Vasconcelos, P.M., Heim, J.A., Farley, K.A., 2005. Weathering geochronology by (U-Th)/He dating of goethite. Geochim. Cosmochim. Acta 69, 659–673. https://doi.org/10.1016/j.gca.2004.07.028

Van Arsdale, R.B., Arellano, D., Stevens, K.C., Hill, A.A., Lester, J.D., Parks, A.G., Csontos, R.M., Rapino, M.A., Deen, T.S., Woolery, E.W., Harris, J.B., 2012. Geology, Geotechnical Engineering, and Natural Hazards of Memphis, Tennessee, USA. *Environ. & Eng. Geosci.*, v. 18, p. 113-158. https://doi.org/10.2113/gseegeosci.18.2.113

Van Arsdale, R. B., Balco, G., Bierman, P. R., Rood, D. H., Rovey, C., Cox, R. T., Lumsden, D. N., Parks, A., 2014. The Pliocene Mississippi River. Geol. Soc. Am., Abstr. with Prog. 46, 228.

Van Arsdale, R.B., Bresnahan, R., McCallister, N., Waldren, B., 2007. Upland complex of the central Mississippi River valley: Its origin, denudation, and possible role in reactivation of the New Madrid seismic zone. Spec. Pap. Geol. Soc. Am. 425, 177–192. https://doi.org/10.1130/2007.2425(13)

Van Arsdale, R., Cupples, W., 2013. Late Pliocene and Quaternary deformation of the Reelfoot rift. Geosphere 9, 1819–1831. https://doi.org/10.1130/GES00906.1

Van Arsdale, R.B., Cox, R.T., Lumsden, D.N., 2019. Quaternary uplift in the lower Mississippi River valley. J. Geol. 127, 1–13. https://doi.org/10.1086/700405

Vasconcelos, P. M., Heim, J. A., Farley, K. A., Monteiro, H., & Waltenberg, K., 2013. $^{40}Ar/^{39}Ar$ and (U–Th)/He–$^{4}He/^{3}He$ geochronology of landscape evolution and channel iron deposit genesis at Lynn Peak, Western Australia. Geochimica et Cosmochimica Acta 117, 283-312.

Willman, H.B., Frye, J.C., 1970. Pleistocene stratigraphy of Illinois. Ill. State Geol. Surv. Bull. 94, 204.

CHAPTER 7. CONCLUSION

This thesis examined the Cenozoic history of the southern and central Appalachians using cosmogenic $^{26}Al/^{10}Be$ and $^{40}Ar/^{39}Ar$ geochronology, focusing on the Shenandoah and Tennessee River watersheds. Our work was driven by four main hypotheses that: (1) the central and southern Appalachian Mountains experienced no significant uplift during the Cenozoic; (2) modern river incision reflects drainage reorganization and Pleistocene climate change, as observed along other Appalachian rivers; (3) deep weathering products, particularly manganese oxides, are remnants of previous climate regimes and are not in dynamic equilibrium as proposed in the Hackian model; and (4) fragments of Paleogene landscapes are preserved where the Valley Floor surface was mapped.

Chapter 2 examined hypotheses (1) that no major Cenozoic uplift occurred in the southern Appalachians and (2) that modern river incision resulted from Pleistocene climate fluctuations and/or drainage reorganization using $^{26}Al/^{10}Be$ burial dating along the lower Tennessee River. This locale was chosen due to its hosting the only major exposures of the Tennessee River's terraces, as well-preserved terrace deposits are sparse upstream of the Muscle Shoals knickpoint. We dated three terraces near Pickwick, TN to 4.36 ± 0.41 My, 2.78 ± 0.08 My, and 2.63 ± 0.11 My. The ages of these terraces provide radiometric constraints on the course of the modern Tennessee River and demonstrate that it has flowed along its current course for at least four million years, possibly since the Late Miocene. These results concur with existing detrital zircon and species vicariance studies in the Tennessee River basin and neighboring basins (i.e., the Mobile River basin). Moreover, our ages for the Tennessee River terraces demonstrate that, like the previously dated fellow tributaries of the preglacial Ohio River, the Tennessee River experienced minor incision during the Pliocene followed by rapid incision and subsequent aggradation during the Pleistocene.

As with chapter 2, chapter 3 tested the hypotheses that (1) the Appalachians were not significantly uplifted during the Cenozoic and (2) that modern river incision is a consequence of drainage reorganization and Pleistocene climate change, albeit in the Shenandoah River valley, outside of the Mississippi River drainage network. We dated four alluvial fans and two fluvial terraces using $^{26}Al/^{10}Be$ minimum/maximum and isochron burial dating. The Pliocene and Pleistocene ages for these deposits demonstrate that, while elements of Hackian dynamic

equilibrium (e.g., the differences in erodibility of underlying lithologies) indeed affect the geomorphology of the Shenandoah Valley, climate-driven base level fluctuations likely exert highly discontinuous effects on the erosional behavior of the Shenandoah River basin. The highest upstream dated deposits in the Shenandoah Valley, the Briery Branch alluvial fan and the Timberville terrace, both feature ages of ~3.3 My and accelerated paleo-erosion rates (>15 m/My) that indicate that the warm climate of the mid-Piacenzian Warm Period likely drove rapid erosion in the Shenandoah Valley. Pleistocene (~1.5 My, ~0.9 My) burial ages for deposits downstream illustrate rapid incision of the Shenandoah River's lower reaches in response to base level fluctuations during the Pleistocene, loosely mirroring the behavior of the Tennessee River. It is possible that incision may also be driven in part by dynamic topography in the area, though its magnitude west of the Blue Ridge is not as well constrained as along the east coast of North America. Overall, our results show the Late Neogene Shenandoah Valley to be a sensitive landscape with widespread aggradation and incision in response to Pliocene and Pleistocene base level fluctuations.

Chapter 4 examined the hypotheses that the Appalachians experienced no significant uplift during the Cenozoic, that deep weathering products (specifically manganese oxides) are remnants of former climate regimes and are not in dynamic equilibrium with the modern landscape as proposed in the Hackian model, and that the previously mapped Valley Floor peneplain is preserved at scattered locations throughout the region. We characterized numerous manganese oxide deposits within the Shenandoah Valley, Tennessee River watershed, and intervening watersheds using scanning electron microscopy, energy dispersive X-Ray spectroscopy, rare-earth and trace element analyses, in-situ ^{10}Be, and ^{40}Ar/^{39}Ar geochronology. Our results broadly demonstrate that Appalachian manganese oxides form over extended intervals (≥2 My) and have been doing so throughout the Cenozoic. The relative REE enrichment of nodules relative to massive manganese oxides and breccias likely reflects the multiple generations of manganese oxides that form during extended dissolution and reprecipitation. Our Eocene, Oligocene, and Miocene ^{40}Ar/^{39}Ar formation ages provide compelling evidence that the Appalachian landscape has been gradually eroding since at least the mid-Cenozoic and precludes the possibility of massive base level perturbations – climatic, tectonic, or geodynamic – in the southern and central Appalachians during the late Cenozoic.

Chapter 5 aimed to test the Neogene uplift hypothesis while also providing an independent radiometric constraint on the age of the Gray Fossil Site, a fossil-bearing sinkhole of contested Miocene/Pliocene age located in northeastern Tennessee. We dated the Gray Fossil Site using an 8-point $^{26}Al/^{10}Be$ depth profile obtained from a 35-meter-deep sediment core through the deposit. Our models indicate a most likely burial age of 5.2-5.9 My for the sinkhole fill, based on simplifications regarding the sinkhole's geometry and prior knowledge that all sediments are magnetically reversed. This latest Miocene/earliest Pliocene age for the Gray Fossil Site is slightly older than the most recent biostratigraphy had indicated, potentially highlighting the Gray Fossil Site as a first appearance location for several index fauna. Our results also demonstrate that the area has been gradually eroding since the sinkhole filled with sediment. This gradually eroding landscape since the latest Miocene/earliest Pliocene is not consistent with substantial late Neogene uplift, as discussed in previous chapters.

Chapter 6 sought to constrain the age of the Upland Complex, a broadly distributed terrace of the Mississippi River. Its age has been debated for decades, but recent $^{26}Al/^{10}Be$ burial dating efforts narrowed its age to either the Pliocene or Pleistocene. This collaborative study between Purdue University, CalTech, and the University of Memphis dated the burial of terrace gravels with in-situ $^{26}Al/^{10}Be$ and the post-depositional formation of goethite cements with (U-Th)/He geochronology. Our results indicate that the Upland Complex is a Pliocene deposit that likely formed throughout the mid-to-late Pliocene during a prolonged period of base level stability. This provides new insight into the longstanding debate regarding the preglacial nature of the Upland Complex and is consistent with widespread Pliocene base level stability observed on multiple tributaries of the Mississippi River.

The studies that comprised this thesis largely answered our driving hypotheses. Cosmogenic nuclide dating in the Shenandoah and Tennessee River basins provides strong evidence that the southern and central Appalachian Mountains were not uplifted in the late Neogene, and $^{40}Ar/^{39}Ar$ ages of manganese oxides demonstrate gradual landscape lowering since at least the Eocene. Modern incision along both rivers appears to be the consequence of Pleistocene climate fluctuation, though it is likely that dynamic topography plays some role in long-term evolution of these landscapes, as it does along the east coast of North America. The extended preservation of manganese oxides illustrates that manganese oxides throughout the entire region are clearly not in dynamic equilibrium with the landscape and may represent multiple relict

surfaces. Overall, these results indicate that the southern and central Appalachian Mountains are a largely quiescent landscape that has been recently perturbed by Pleistocene base level fluctuations.

APPENDIX A. SUPPLEMENTARY AMS DATA

Table A.1. Sample masses, stable Al/Be data, and AMS results for Tennessee River terraces.

Sample ID	Mass (g)	Be carrier (µg)	$^{10}Be/^{9}Be$ (10^{-15})	Total Al (µg)	$^{26}Al/^{27}Al$ (10^{-15})
PW4-1	16.954	266.9	81.95 ± 3.67	986	194.47 ± 10.74
PW4-2	41.443	268.1	422.86 ± 9.07	1009	802.13 ± 31.93
PW4-3	33.432	268.5	188.89 ± 7.21	874	488.19 ± 24.80
PW4-4	32.207	270.0	254.37 ± 9.94	875	441.76 ± 18.22
PW4-5	22.526	268.4	169.02 ± 7.74	1083	289.72 ± 14.54
WO_BLANK0	-	269.3	8.10 ± 1.77	1010	0.84 ± 0.81
PW1-1	10.83	268.6	129.71 ± 5.60	1211	178.01 ± 13.66
PW1-2	8.202	253.5	87.60 ± 3.28	1077	155.14 ± 11.47
PW1-3	4.511	267.8	22.90 ± 1.78	1254	57.19 ± 6.68
PW1-4	2.962	265.7	46.23 ± 3.07	1106	64.52 ± 5.97
PW4-18	16.135	267.6	255.19 ± 5.86	1270	280.14 ± 18.81
PW1-S	29.716	267.0	248.64 ± 6.23	2743	188.18 ± 8.00
PW4-S	11.906	269.8	138.92 ± 4.69	1307	234.87 ± 12.85
WO_BLANK3	-	270.1	1.72 ± 0.41	1045	2.92 ± 1.84
QFL4-1	18.232	268.0	115.94 ± 6.13	1222	209.11 ± 12.63
QFL4-3	14.893	267.1	219.01 ± 8.24	1319	297.07 ± 14.76
QFL4-4	9.277	267.6	61.83 ± 3.95	1236	129.46 ± 9.91
WO_BLANK10	-	267.0	0.76 ± 0.60	1067	0.00± 0.51
PW1-10	5.519	266.3	66.50 ± 4.41	1026	91.51 ± 6.11
PW4-13	13.241	263.2	280.34 ± 8.59	1082	371.12 ± 25.53
QFL4-6	9.861	269.3	136.72 ± 9.37	1344	164.94 ± 10.12
QFL4-7	19.76	262.4	699.33 ± 13.16	1815	150.80 ± 6.77
QFL4-SAND	35.012	268.2	332.18 ± 7.24	3437	200.69 ± 9.21
WO_BLANK11	-	266.3	1.43 ± 0.65	1138	1.13 ± 1.30

Table A.2. Sample masses, stable Al/Be data, and AMS results for Shenandoah Valley, VA.

Sample ID	Mass (g)	Be spike (µg)	$^{10}Be/^{9}Be$ (10^{-15})	Total Al (µg)	$^{26}Al/^{27}Al$ (10^{-15})
S12-3	31.365	266.4	124.94 ± 4.46	1667	268.43 ± 10.96
S12-4	20.61	267.6	90.94 ± 7.12	2272	123.63 ± 7.00
S12-6	15.28	266.0	56.63 ± 2.47	1609	137.94 ± 7.36
S12-8	19.02	266.7	89.83 ± 7.43	2699	98.05 ± 5.26
S12-9	23.983	267.1	130.46 ± 4.21	1959	171.75 ± 8.10
WO_BLANK2	-	266.4	1.91 ± 1.09	510	0.43 ± 0.62
MC-1	15.558	266.0	206.76 ± 7.02	3285	229.78 ± 15.37
MC-2	17.551	266.1	296.30 ± 9.38	2558	251.67 ± 19.66
MC-4	27.099	266.7	304.66 ± 10.24	1575	661.24 ± 36.54
MC-SAND	18.782	266.2	453.94 ± 12.12	3293	399.69 ± 21.25
WO_BLANK6	-	266.9	2.69 ± 0.81	2159	7.77 ± 3.09
BB-7	16.923	267.1	63.36 ± 2.64	4264	40.14 ± 3.42
BB-8	25.193	268.1	125.31 ± 3.84	8659	44.55 ± 6.32
BB-SAND	22.263	268.3	130.49 ± 4.87	5383	60.32 ± 4.27
TV-1	29.946	269.3	120.07 ± 3.53	4884	92.23 ± 5.60
TV-2	4.575	268.1	18.92 ± 1.65	4255	14.26 ± 2.15
TV-SAND	5.389	267.6	39.01 ± 2.52	2129	46.39 ± 3.90
WO_BLANK7	-	266.9	4.97 ± 1.08	1100	0.49 ± 0.71
TV-5	14.192	268.0	90.25 ± 3.56	1377	177.42 ± 11.04
WO_BLANK8	-	268.5	1.67 ± 0.56	1022	0.00 ± 0.64
BB-6	15.571	267.0	49.19 ± 3.79	3515	54.81 ± 4.76
MC-5	21.095	266.9	249.71 ± 7.74	3613	195.35 ± 9.14
TV-3	21.227	267.1	111.71 ± 7.05	3892	82.36± 5.73
WO_BLANK10	-	267.0	0.76 ± 0.60	1067	0.00± 0.51
BB-10	30.863	263.5	86.85 ± 4.19	2072	170.68 ± 8.45
WO_BLANK11	-	266.3	1.43 ± 0.65	1138	1.13 ± 1.30
MC-10	27.56	266.5	181.90 ± 5.65	2915	253.14 ± 9.90
MC-11	44.123	266.1	863.57 ± 20.59	3813	564.77 ± 19.14
TILT-2	50.545	266.2	484.25 ± 14.97	4469	256.33 ± 8.87
TILT-4	28.938	264.9	1087.90 ± 27.51	2123	2061.99 ± 50.68

TILT-SAND	29.814	263.0	1054.35 ± 18.60	4080	823.48 ± 21.35
WO_BLANK12	-	268.8	1.36 ± 0.61	1548	1.20 ± 0.60
LYNN-SAND	46.707	268.7	242.72 ± 5.67	5130	112.76 ± 5.27
TILT-8	55.314	268.3	443.18 ± 8.77	4631	292.27 ± 9.26
WO_BLANK13	-	268.4	1.46 ± 0.45	978	4.13 ± 1.48

Table A.3. Sample masses, stable Al/Be data, and AMS results for Gray Fossil Site.

Sample ID	Mass (g)	Al (µg)	$^{26}Al/^{27}Al$ (10^{-15})	^{9}Be carrier (µg)	$^{10}Be/^{9}Be$ (10^{-15})
GF-2A	11.646	1731	79.03 ± 4.88	261.9	50.73 ± 2.79
GF-5A	23.523	3942	54.32 ± 3.27	260.0	91.30 ± 2.98
GF-8A	33.839	8028	33.45 ± 2.46	270.8	116.66 ± 4.05
GF-10A	23.304	3706	47.33 ± 3.12	261.4	82.53 ± 4.26
GF-19A	12.934	1879	36.68 ± 3.16	270.0	39.70 ± 2.37
GF-26A	13.056	2013	20.50 ± 2.11	269.0	37.07 ± 2.02
GF-35A	8.921	1589	13.42 ± 2.01	269.0	23.52 ± 1.90
GF-49A	23.611	2237	17.76 ± 2.30	266.2	61.69 ± 3.21
WO_BLANK11	-	1138	1.13 ± 1.30	266.3	1.43 ± 0.65
WO_BLANK14	-	1048	0.71 ± 0.68	268.8	2.32 ± 0.56

Table A.4. Sample masses, stable Al/Be data, and AMS results for Upland Complex sites.

Sample	Mass (g)	Al (µg)	$^{26}Al/^{27}Al$ (10^{-15})	^{9}Be carrier (µg)	$^{10}Be/^{9}Be$ (10^{-15})
VA-DRUM (s)	18.666	1870	97.69 ± 10.1	265.7	125.28 ± 4.44
VA-KUHN (s)	20.294	1952	123.51 ±10.5	267.7	140.55 ± 5.19
VA-MID (s)	12.689	1378	79.92 ±9.19	267.1	51.68 ± 2.24
VA-MID (m)	19.402	564	303.43 ± 36.04	263.8	69.09 ± 2.60
VA-TRI (s)	11.086	1254	114.3 ± 14.48	265.9	53.3 ± 2.77
WO_BLANK5	0	1584	2.27 ± 2.17	266.6	0.55 ± 0.27
VA-TRI (m)	17.634	1398	144.94 ± 13.11	268.1	65.87 ± 3.85
WO_BLANK8	0	1022	0.00 ± 0.64	268.5	1.67 ± 0.56
VA-TRI-52 (g)	20.374	4881	44.51 ± 4.05	274.0	596.92 ± 12.56
WO_BLANK12	0	1548	1.20 ± 0.60	268.8	1.36 ± 0.61
MID-1 (g)	4.689	1064	39.83 ± 3.58	266.7	29.16 ± 1.85
MID-4 (g)	4.938	1073	47.59 ± 4.30	267.2	21.17 ± 1.54
MID-5 (g)	8.26	1124	74.15 ± 4.98	270.1	25.58 ± 1.74
MID-6 (g)	4.595	1092	58.42 ± 5.14	268.4	22.69 ± 1.87
MID-SAND (s)	62.406	6199	80.54 ± 4.40	269.5	210.4 ± 8.14
WO_BLANK13	0	978	4.13 ±1.48	268.4	1.46 ± 0.45

APPENDIX B. COSMOGENIC NUCLIDE PROCESSING – MINERAL SEPARATION AND CHEMISTRY

Mineral separation

All samples were photographed and massed following collection. For isochrons, care was taken to select samples that exhibited a range of morphologies. Large samples were crushed using a jaw crusher and grain size was subsequently reduced using a disk mill. For isochron gravels and sand fractions, a grain size range of 250-500 microns was selected via sieving. In the case of small gravels (<20 g), samples were crushed manually to ~1 mm to avoid the sample loss associated with milling.

Following grain size reduction, all samples were rinsed in deionized water to remove very fine grains. Materials collected in carbonate-rich environments were soaked in pure HNO_3 overnight to dissolve carbonates. All samples were leached in dilute (1-5%) HF/HNO_3 in bottles to remove meteoric nuclides and reduce contamination from other minerals. Bottles were placed on hot dog rollers for at least three days to warm and agitate sample material, with the acid solution being replaced daily. Following acid treatment, all samples were run through a magnetic separator to remove small metallic grains. Samples that contained significant amounts of non-quartz materials were cleaned using a froth flotation technique. The frothing solution was a mixture of dodecylamine, acetic acid, and eucalyptus oil delivered using a carbonating pump. Following frothing, samples were again leached in dilute HF/HNO_3. Samples that still contained heavy minerals were subjected to heavy liquid density separation, wherein quartz was isolated from other minerals in lithium heteropolytungstate (LST). Following heavy liquid separation, samples were leached in dilute HF/HNO_3 for two days. In the case of small samples with significant contamination (e.g., the samples collected from the Gray Fossil Site, TN), feldspars and other minerals were removed using pyrophosphoric acid treatment (Mifsud et al., 2013). As with other treatments, samples were leached in dilute HF/HNO_3 following the pyrophosphoric acid procedure.

Prior to chemical processing, samples were assayed using inductively coupled plasma-optical emission spectrometry (ICP-OES). ICP-OES analysis measures concentrations of numerous elements in an aliquot and is primarily used to identify the presence of Al-bearing contaminant minerals. In most cases, analyzed samples contained 100-200 ppm of aluminum.

Quartzite clasts were the exception, frequently containing significantly lower concentrations of Al (<50 ppm).

Cosmogenic nuclide chemistry

Samples that contained sufficiently low aluminum concentrations were placed in PFA jars and massed. Each sample received ~0.25 g of beryllium carrier, and samples that contained less than one milligram of aluminum were spiked with ACROS atomic absorption spectrometry aluminum standard.

All samples were dissolved in a 5:1 mixture of HF:HNO_3, with one milliliter of HNO_3 for each gram of quartz. Jars were placed on a griddle at 120°C and left to dissolve, which was generally accomplished in 1-2 days. Following dissolution, samples were removed from heat and massed. Small (2 ml) aluminum aliquots were taken from each sample and dried down three times in aqua regia prior to dissolution and measurement via ICP-OES. Concentrated H_2SO_4 (1 ml) was then added to each jar, and jars were placed on griddles at 160°C to evaporate the HF/HNO_3 solution. Drydown generally lasted 1-2 days, depending on sample size.

Following drydown, the samples dissolved in H_2SO_4 were rinsed with deionized H_2O and pipetted to a 15% NaOH solution. This step precipitated iron and titanium oxides while leaving Al and Be dissolved. Samples were centrifuged, the supernatant decanted, and rinsed again. Al and Be were subsequently precipitated from the supernatant at pH 7.5, rinsed with ammoniated H_2O, and dissolved in oxalic acid.

Anion and cation chromatography were performed to isolate Al and Be from the dissolved solution. Columns were rinsed with concentrated HCl, and samples were run through columns with HCl and oxalic acid solutions. Beryllium and later aluminum were eluted into separate 15 ml centrifuge tubes.

Beryllium was precipitated at pH 9 following the addition of EDTA, a chelating agent. The precipitate was centrifuged and rinsed with ammoniated H2O, then dissolved in 8N HNO_3 and added to a small quartz vial. Aluminum was precipitated at pH 7, then centrifuged and rinsed with pH 7 deionized water. It was then dissolved in 6N HCl and added to a separate quartz vial. All vials were placed in an aluminum block and allowed to dry down on low heat (<100°C) overnight.

Following drydown, each quartz vial was capped. The aluminum block was then heated to 160°C, as verified by an infrared thermometer. This temperature was maintained for at least 30

minutes, after which the block was allowed to cool. Each sample was then heated with a propane torch for 90 seconds to decompose the samples to oxides, then placed in a secure container for transportation to the loading room in PRIME Lab.

Beryllium and aluminum samples were mixed with three scoops of niobium from the size #0 curette. The mixture was dissolved in acetone, stirred, and allowed to dry for at least 30 minutes. Samples were subsequently loaded into stainless steel cathodes and submitted to the operators of the accelerator mass spectrometer for measurement.

APPENDIX C. MATLAB CODE FOR MINIMUM BURIAL AGE CALCULATIONS

This thesis utilized a number of cosmogenic nuclide techniques with a particular emphasis on burial dating. While these concepts are rigorously explained in the literature and numerous calculators are available online (e.g. Vermeesch, 2007; Hidy et al., 2010), recent revisions to nuclide half-lives and production rate mechanisms motivate straightforward, easily modified codes for age calculations. The code below can be easily customized, and parameters manipulated according to the user's needs.

This code calculates simple burial ages and paleo-erosion rates for any number of samples under the assumption that buried materials were sourced from a steadily eroding landscape. Measured concentrations of ^{26}Al and ^{10}Be are treated as Gaussian distributions and randomly sampled 100 times by default (this may be changed using the "samplecount" parameter). Each concentration is iterated through the simple burial equations n times. Convergence is usually reached quickly, but by default n=50. The output array "datasheet" contains burial ages, paleo-erosion rates, and their respective uncertainties. As an example, the ^{26}Al/^{10}Be data for the Timberville, VA terrace are included. This deposit underwent significant postburial production, so the resultant ages underestimate the true burial age.

```
clear all
% Input data as [Al        Al unc   Be       Be unc] in 10^6 at/g
data=[
0.2512   0.0150   0.0776   0.0057
0.4352   0.0178   0.1792   0.0047
0.2841   0.0150   0.0970   0.0048
0.5699   0.0351   0.2078   0.0077]*1000000;

allT=[];
alleT=[];
allE=[];
alleE=[];
for k=1:size(data,1)
        n26=data(k,1);
        e26=data(k,2);
        n10=data(k,3);
        e10=data(k,4);
        % Number of randomly sampled concentrations
        samplecount=100;
        % Number of iterations per randomly sampled concentration
        n=50;
```

```
        %Guessed erosion rate (m/My)
        erosion=5;
        % Be-10 production rate estimate
        p10=5;
        % CONSTANTS
        tau10=2005000;
        tau26=1020000;
        taubur=1/(1/tau26-1/tau10);
        prodratio=6.8;
        Lambda=160;
        rho=2.6;
        all_t=[];
        all_E=[];
        for j=1:samplecount
                N26=normrnd(n26,e26);
                N10=normrnd(n10,e10);
                Rmeas=N26/N10;
                E=erosion/10000;
                run_t=[];
                run_E=[];
                for i=1:n
                        Rinh=prodratio*((1/tau10+(rho*E)/Lambda)/(1/tau26+(rho*E)/Lambda));
                        t=taubur*log(Rinh/Rmeas);
                        E=(p10/exp(t/tau10)-N10/tau10)*(Lambda/(N10*rho));
                        run_t(end+1)=t;
                        run_E(end+1)=E*10000;
                end
                all_t=[all_t;run_t];
                all_E=[all_E;run_E];
        end
        mean_E=mean(all_E(:,size(all_E,2)));
        std_E=std(all_E(:,size(all_E,2)));
        mean_t=mean(all_t(:,size(all_t,2)));
        std_t=std(all_t(:,size(all_t,2)));
        allE(end+1)=mean_E;
        alleE(end+1)=std_E;
        allT(end+1)=mean_t;
        alleT(end+1)=std_t;
end

% Outputs an array that can be easily exported to Excel (age/age unc/erosion/erosion unc)
datasheet=[];
datasheet=[datasheet allT'/1000000];
datasheet=[datasheet alleT'/1000000];
datasheet=[datasheet allE'];
datasheet=[datasheet alleE'];
```

APPENDIX D. MANGANESE OXIDE SAMPLE PREPARATION FOR $^{40}AR/^{39}AR$ GEOCHRONOLOGY

Obtaining reliable $^{40}Ar/^{39}Ar$ data for manganese oxide samples requires a solid solution of cryptomelane/hollandite that is devoid of other potassium-bearing minerals (e.g., muscovite, biotite, potassium feldspar) that could influence the measured $^{40}Ar/^{39}Ar$ ratio and produce inaccurate age data. Unlike quartz, cryptomelane-hollandite is very susceptible to damage by acid treatment (Vasconcelos, 1999) and thus mechanical purification is required. Over the course of this study, methods for isolating pure cryptomelane-hollandite evolved and became more streamlined. Below are the initial and refined procedures for isolating and identifying dateable material, the latter of which largely mirrors the methods used by P. Vasconcelos. Sample processing took place at Purdue University and the United States Geological Survey headquarters in Reston, VA.

2016-2018 methodology

Hand samples that appeared to contain manganese oxides were cut with a water-cooled rotary saw or band saw to reveal mineral composition and structure. Where potentially dateable manganese oxides were seen (e.g., in veins or breccia fill), the sample was cut into a ~8 mm-thick slab. *NOTE: when cut with water-cooled saws, manganese oxides release dust particles that mix with the mist from the saw's water jets. A respirator mask is highly recommended when cutting or grinding samples.* The slab was subsequently polished on one side using a rotating polishing machine. A sequence of 60 micron, 15 micron, and 6 micron polishing surfaces were used to obtain a smooth reflective surface on one face of the samples.

Following polishing, the reflective surface was mounted to a glass slide. This was accomplished by heating the glass slide on a hot plate, placing Crystalbond adhesive material on the slide, and allowing the adhesive to melt. The sample was then placed in the molten Crystalbond and removed from heat. The sample was left to cool for at least 30 minutes before grinding, to allow the Crystalbond to dry completely. Slides bearing the manganese oxide samples were then mounted in a water-cooled grinder for creating sections. Each sample was gently ground to ~1 mm thickness, taking special care to not shatter the sample. In cases where samples contained thin veins or other structures, they were ground thinner until structures were visible on both sides of

the slide. When samples contained localized pure cryptomelane/hollandite, subsampling was occasionally performed. This was accomplished by one of two methods: cracking or drilling. Where pure cryptomelane/hollandite was concentrated in large zones, the target mineral was manually broken from the unwanted sample material. In instances where cryptomelane and/or hollandite were concentrated in veins, however, special care was required. Veins were sampled using a Dremel drill with a diamond bit with the aid of a hand sample microscope. This process, while time-consuming, allowed precise subsampling of heterogeneous samples. Following subsampling, each sample slide was placed in a 50 ml centrifuge tube. The centrifuge tube was then filled with acetone (to dissolve the Crystalbond adhesive) and placed in an ultrasonic bath for one hour. The sample was removed, rinsed, and filled with deionized water before being placed back into the ultrasonic bath for another hour. The sample was then removed and dried in a laboratory oven overnight prior to SEM analysis.

2018-2020 methodology (recommended)

The methods described above, while moderately effective, are time consuming and yielded low amounts of dateable cryptomelane. The procedures are nonetheless included, as they were used to prepare several samples in this study for $^{40}Ar/^{39}Ar$ dating. A revised methodology, developed from conversations with P. Vasconcelos, allows archiving of samples and precise subsampling while reducing sample destruction and processing time. Following collection, a 1-2 cm thick slab was cut from each sample using a water-cooled saw. The slab was then polished using a rotating polishing machine and cryptomelane-rich zones were verified visually. Using a water-cooled 2.75 mm (inner) diameter diamond corer installed on a drill press, cryptomelane-bearing zones were precisely sampled. The core was then crushed manually with a mortar and pestle to <2 mm diameter fragments. The fragments were placed in bottles with deionized water and submerged in an ultrasonic bath for up to one week. Most non-cryptomelane minerals were destroyed by the ultrasonic action, leaving behind cryptomelane and other resistant minerals. Each sample was then sonicated in acetone, then ethanol for one hour each. Samples were then rinsed, dried, and examined for purity with a reflected light microscope. Those which appeared dateable were subsequently examined via SEM.

SEM analysis

Morphological and chemical analyses of sample materials are necessary to confirm that dateable minerals have been successfully liberated from collected materials. Analyses were performed at Purdue University using a FEI Quanta 3D field emission gun scanning electron microscope and at USGS Reston using a Hitachi SU-5000 field emission gun scanning electron microscope. Both SEMs were equipped with backscatter electron (BSE) detectors that aided in visually determining chemical homogeneity and energy-dispersive X-ray (EDX) detectors that permitted detailed chemical analysis of samples. Samples did not require any coating and were simply mounted on aluminum pins with carbon tape. In most instances, a beam current of 20 kV was employed while spot size was varied based on desired resolution. BSE imaging was first performed to identify zones of chemical homogeneity. EDX analyses were subsequently performed on suspect minerals and at random throughout samples to identify constituent elements and characterize the bulk composition of the sample. Included below are samples of BSE and EDX imagery that demonstrate both pure cryptomelane-hollandite solid solutions and samples that contain contaminants such as micas.

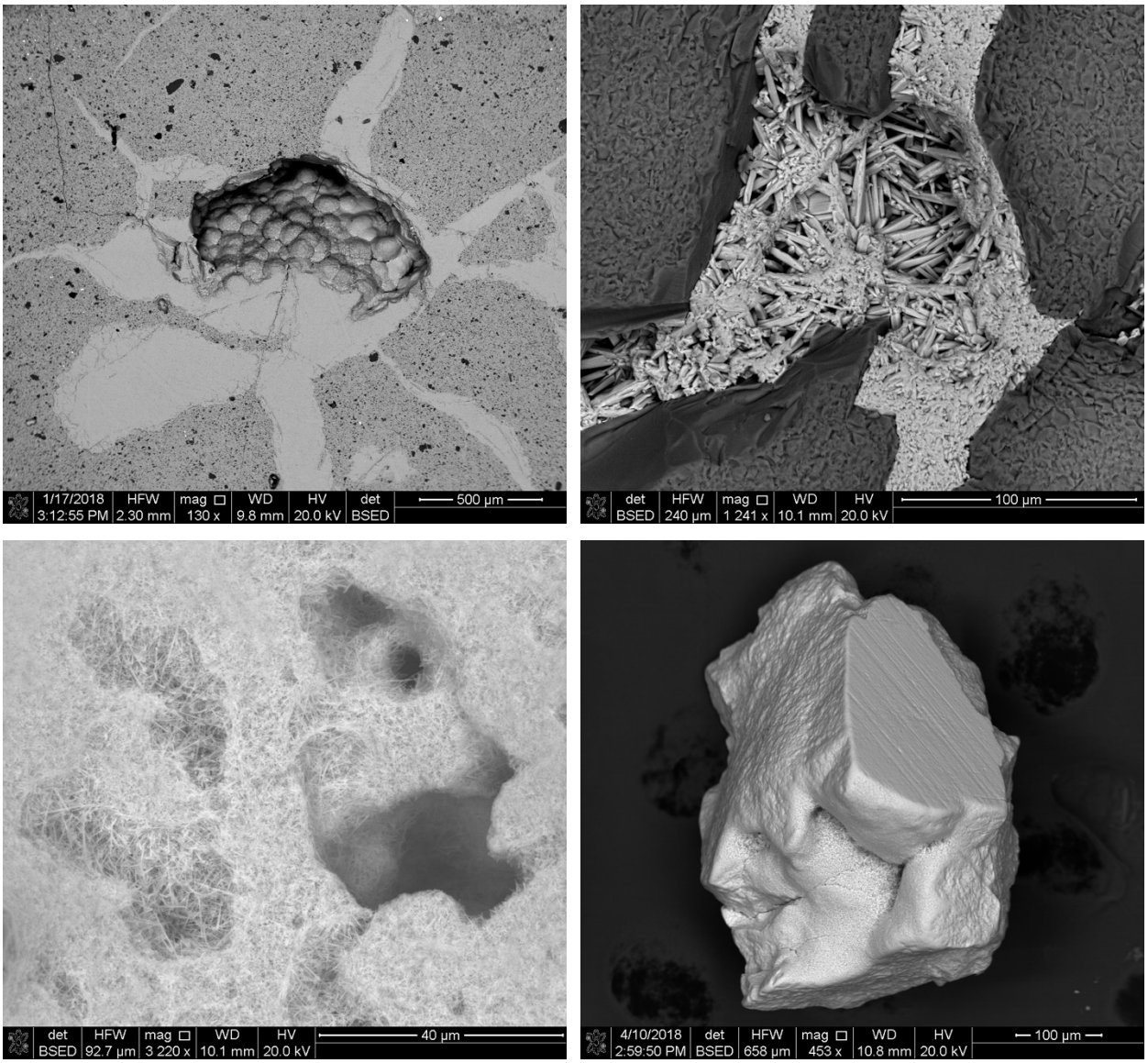

Top left: Pure cryptomelane/hollandite veins with botryoidal growth in center. Veins are surrounded by muscovite and other lithics, as indicated by dark specks in groundmass. **Top right:** Pure cryptomelane/hollandite (light gray) cementing together quartz grains (dark gray). The characteristic acicular habit of cryptomelane/hollandite is visible. **Bottom left:** Fine acicular cryptomelane/hollandite at high magnification. **Bottom right:** Sample of cryptomelane/hollandite with no contaminants. Acicular grains are visible.

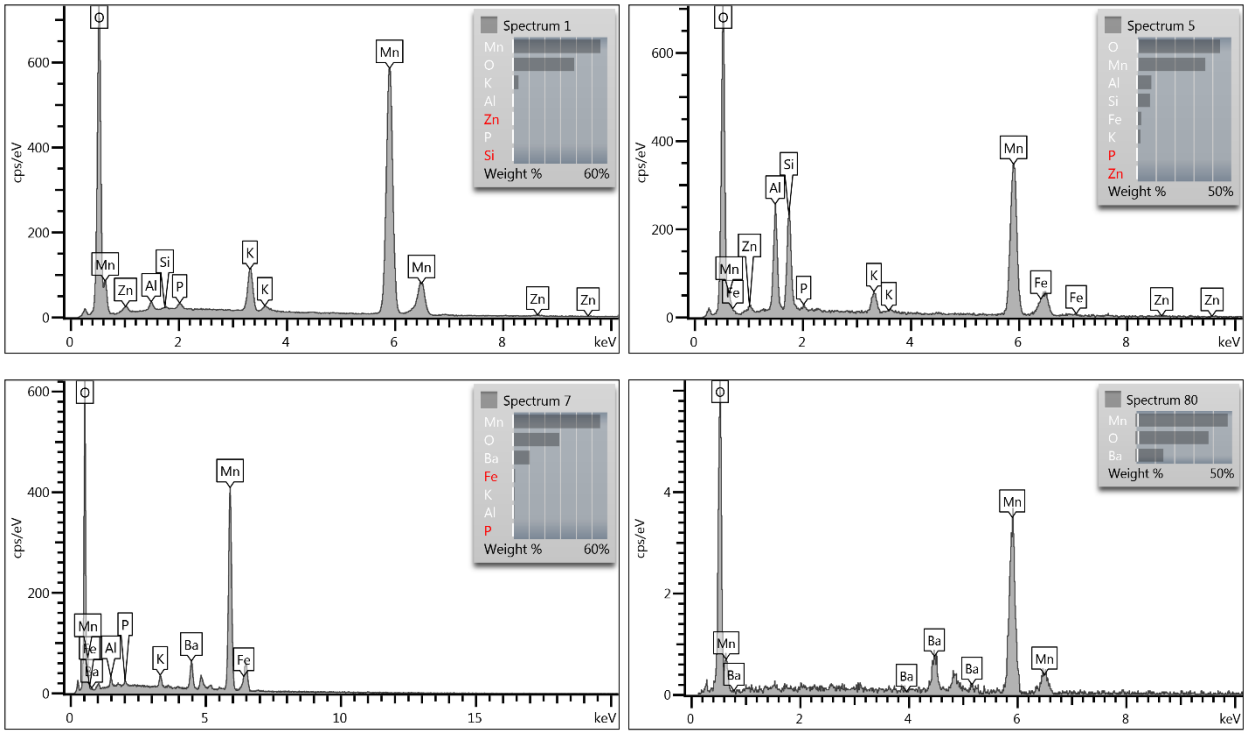

Top left: This spectrum shows nearly pure cryptomelane with minor aluminum, suitable for $^{40}Ar/^{39}Ar$ dating. **Top right:** The abundant aluminum and silicon in this spectrum likely reflect the presence of micas or feldspars, which are commonly found within botryoidal samples. **Bottom left:** Sample with a solid solution of cryptomelane/hollandite, suitable for $^{40}Ar/^{39}Ar$ dating. **Bottom right:** Sample with predominantly hollandite and undetectable quantities of cryptomelane, unsuitable for $^{40}Ar/^{39}Ar$ dating.

APPENDIX E. COSMOGENIC SITE DESCRIPTIONS

Nt$_4$ gravel pit

The Nt$_4$ pit is located 9 kilometers northeast of Savannah, TN. A former landfill has been converted into a long-distance shooting range, which may be accessed with the owner's permission. I sampled an exposure at 35.2641°N, 88.1639°W. The upper portion of the exposure (sample 1) features centimeter-sized gravels within an iron-cemented sandstone. The 2 meters below the gravels (samples 2, 3) are predominantly clay and overlie a thick deposit of unconsolidated sand. The sand (samples 4-6) is less oxidized than the clay and features well-preserved crossbedding features.

The high quartzite content of the iron-cemented gravels relative to lower terraces is consistent with Self's (2003) description of the Nt$_4$ terrace, as is its elevation at 72 m above modern river level and 89 m above the bedrock channel. The underlying clays and cross bedded sands appear to be part of the Cretaceous Eutaw Formation mapped in this area. Samples were collected along a vertical transect through the outcrop, but none were processed for dating.

Relevant map

Parks, W. & Russell, E. (1975). Geologic map showing upper Cretaceous, Paleocene, and Lower and Middle Eocene units and distribution of younger fluvial deposits in western Tennessee. U.S. Geological Survey, Miscellaneous Investigations Series Map I-916. https://ngmdb.usgs.gov/Prodesc/proddesc_9806.htm

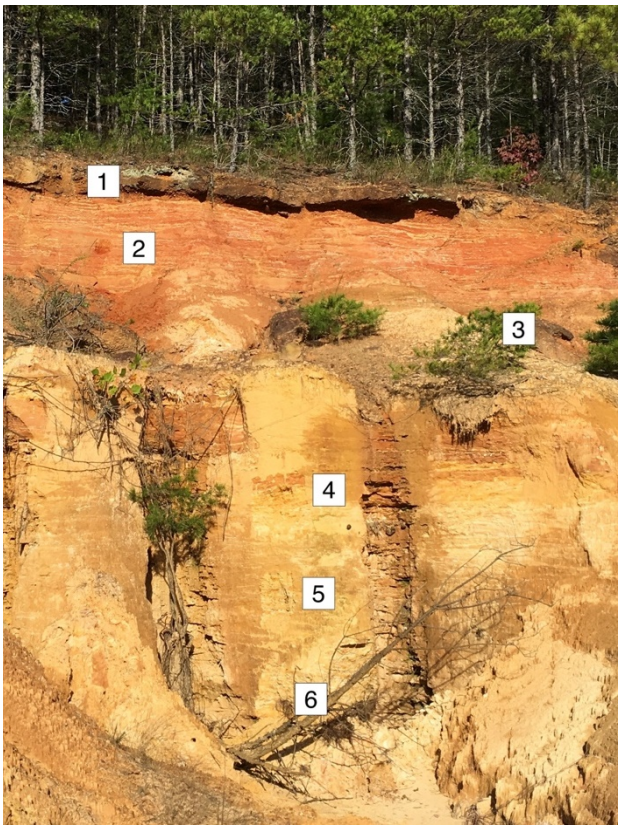

Left image: Sediments were collected from the Nt_4 pit at ~1 m depth intervals at each numbered site. Samples from location 1 were examined for quartzite content and the quality of iron cement investigated for possible U-Th-He dating of goethite. **Right image:** Crossbedded sands in the underlying unit (location 5) are consistent with Parks and Russell's (1975) description of the Eutaw Formation.

Nt_3 gravel pit

The Nt_3 pit is located six kilometers south of the Pickwick Landing Dam. It is an active gravel pit that may be sampled with the permission of the site employees. The site is notable for its high tripoli content, as well as the excellent crossbedding of the terrace sediments (see below). It consists of predominantly subrounded to rounded chert with some quartz and quartzites. There is local cementation by iron oxides (Russell et al., 1972) but none noted at the present excavation site. Quartzite content is low (~12%), consistent with Self's (2003) description of this terrace level at 57 above modern river level (74 m above bedrock channel). We interpreted this site as the Nt_3 terrace level that overlies Cretaceous Eutaw clays and sands.

We sampled the terrace at 35.0146°N, 88.2445°W, collecting quartzite clasts and sand. The samples were crushed to 0.25-0.50 mm, etched with dilute hydrofluoric and nitric acids, and their $^{26}Al/^{10}Be$ contents measured by accelerator mass spectrometry at PRIME Lab.

Relevant map

Russell, E., Wilson, C., & Jewell, J. (1972). Geologic map and mineral resources summary of the Pickwick quadrangle, Tennessee Division of Geology, Geologic Quadrangle Map 24 SW. https://ngmdb.usgs.gov/Prodesc/proddesc_67925.htm

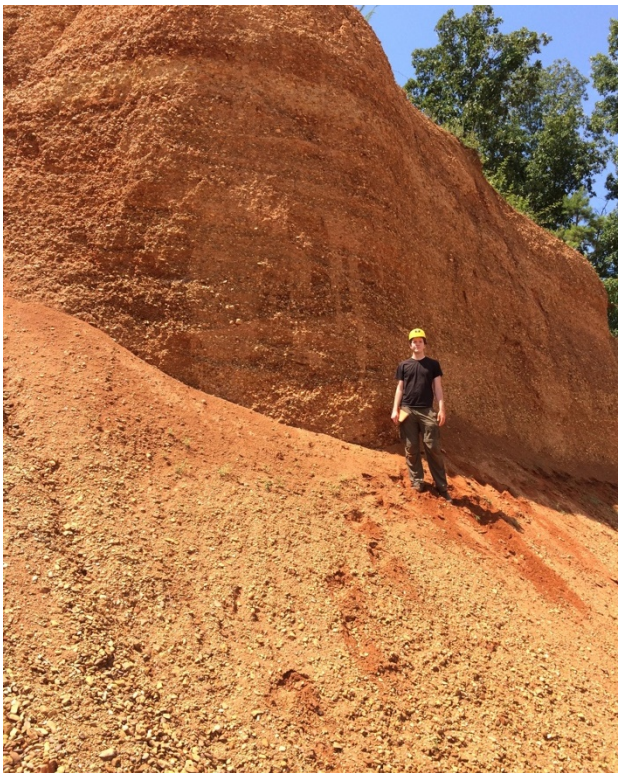


Left image: Location where quartzites and sand were collected at the Nt_3 pit for burial dating. **Right image:** Crossbedded sands and gravels in the terrace deposit.

Nt_2 gravel pit

The Nt_2 terrace pit is located approximately 7 kilometers west-southwest of Counce, TN on Dr. Williams Drive. Gravels at this site overlie the Cretaceous Coffee Formation, which primarily consists of quartz sand and bedded clays. This gravel pit was described by Self (2003) and appears to be abandoned at present. The exposure was relatively uniform in bedding and featured occasional iron-oxide cements. Most gravels were <5 centimeters in diameter and cherty. Quartzites were rare but present, in agreement with Self's estimation of a ~10:1 chert to quartz ratio; however, the sand was very quartz rich. The site is located 44 m above the modern river level, 61 m above bedrock channel.

I sampled an exposure at 35.0199°N, 88.3459°W for quartzites and sand. The samples were crushed to 0.25-0.50 mm, etched with dilute hydrofluoric and nitric acids, and their $^{26}Al/^{10}Be$ contents measured by accelerator mass spectrometry at PRIME Lab.

Relevant map

Russell, E. (1968). Geologic map and mineral resources summary of the Counce quadrangle (including the Tennessee portion of the Doskie quadrangle, Mississippi-Tennessee). Tennessee Division of Geology, Geologic Quadrangle Map 13 SE. https://ngmdb.usgs.gov/Prodesc/proddesc_67925.htm

Left image: Overview of Nt_2 gravel pit on Dr. Williams Drive. **Right image:** Close-up image of outcrop. Hammer indicates location where samples were collected for isochron burial dating.

Nt_1 gravel pit

The Nt_1 terrace pit is located approximately 5.6 kilometers north-northeast of Counce, TN near the intersection of TN-128 and Wharf Road. Gravels at this site overlie the Cretaceous Eutaw Formation which, like the Coffee Formation, primarily consists of quartz sand and bedded clays. This gravel pit was described by Self (2003) and is actively being quarried. Access to the site was permitted by the owner-operator of the gravel business. The exposure featured abundant iron-oxide cements and replacements. Most gravels were <5 centimeters in diameter and cherty. As with the QFl^4 deposits, Self (2003) estimated a ~10:1 chert to quartz ratio. The site is located 27 m above the modern river level, 44 m above bedrock channel.

I sampled an exposure at 35.0908°N, 88.2593°W for quartzite clasts and sand. The samples were crushed to 0.25-0.50 mm, etched with dilute hydrofluoric and nitric acids, and their $^{26}Al/^{10}Be$ contents measured by accelerator mass spectrometry at PRIME Lab. This site featured multiple reworked samples, as evidenced by the isochron.

Relevant map

Russell, E. (1968). Geologic map and mineral resources summary of the Counce quadrangle (including the Tennessee portion of the Doskie quadrangle, Mississippi-Tennessee). Tennessee Division of Geology, Geologic Quadrangle Map 13 SE. https://ngmdb.usgs.gov/Prodesc/proddesc_67925.htm

Left image: Overview of Nt_1 gravel pit with D. Granger for scale. Note the large (2 m) cross-beds in the deposit. **Right image:** close-up view of an iron-cemented sandstone. The owner-operator reported finding many such deposits, locally known as "sand pipes."

Shenandoah alluvial fan cut – Page County, VA

The area near Shenandoah, VA features broad alluvial fans sourced from the nearby Blue Ridge Mountains. The fans terminate at the South Fork of the Shenandoah River; locally to the west of the river, steeper fans have formed on the slopes of Massanutten Mountain. Alluvium in the eastern fans is highly oxidized and features coarse cobbles with high quartz contents; thickness to bedrock is not known. A similarly configured fan deposit approximately 65 kilometers southeast of Shenandoah, VA was dated to 6.9-7.9 My using cosmogenic $^{26}Al/^{10}Be$ burial dating by Heller et al. (2014), though such ages are close to the limit of these geochronometers.

This site is located along State Road 340 at 38.4958°N, 78.6206°W, only 800 m from the modern Shenandoah River and perched at 30 m arl. It exposes six meters of alluvial sands and cobbles, generally <20 cm in diameter. Unlike the Briery Branch fan deposit, no kaolinite is apparent and the clasts themselves are *not* deeply weathered. Imbrication of the clasts suggests a roughly northern flow direction. The preservation of cobbles despite the extreme age of this deposit suggests that fan thickness may have previously been thicker at this location than at Briery Branch. For this study, quartzites, sandstones, and sands were collected and analyzed.

Relevant map

King, P. (1950). Geology of the Elkton area, Virginia. U.S. Geological Survey Professional Paper 230. https://ngmdb.usgs.gov/Prodesc/proddesc_4221.htm


Left image: Excavated portion of S12 fan with W. Odom for scale. The fan was sampled for burial dating near Odom's feet. **Right image:** D. Granger and W. Odom examining clasts within the fan deposit.

McCarty Pit #1 – Warren County, VA

Nine kilometers northeast of Front Royal, VA, a large gravel pit is visible near the intersection of Howellsville Rd and Morgans Ridge Rd. A 10 m-thick layer of fan gravels is perched 30 m above the nearby Shenandoah River. Excavations at this pit have removed the layer gravels and continued into the underlying Cambrian Harpers Formation, which in this location has weathered to saprolite (Lukert and Nuckols, 1976). While no exposed fan deposits remain in the pit itself, a small stream immediately southeast of the pit has deeply incised into the fan and exposed the gravel-saprolite contact. The gravels are subrounded to rounded, generally smaller than 15 cm in diameter, and lie within a sandy matrix. Near the contact, gravels were cemented by a crumbly iron oxide crust. The crust was analyzed with energy-dispersive X-Ray spectroscopy, but revealed no manganese oxides.

This site was selected due to its proximity to the Shenandoah River. We sampled the fan-saprolite contact at 38.9542°N, 78.1079° W. Gravel types included sandstones, cherts, and quartzites. Three gravel clasts and the sand fraction were processed for a preliminary isochron at PRIME Lab. The gravels were crushed via disk mill. Both sand and gravels were subsequently sieved to 250-500 μm and prepared for AMS measurement.

Relevant map

Lukert, M. & Nuckols, E. (1976). Geology of the Linden and Flint Hill quadrangles, VA. Virginia Division of Mineral Resources, Report of Investigations 44. https://ngmdb.usgs.gov/Prodesc/proddesc_38898.htm


Left image: The contact between the MC terrace and underlying Harpers Formation is visible directly at the end of the hammer's handle. Note the dark cement between clasts. **Right image:** W. Odom sampling for burial dating. The area immediately behind the hill has been quarried for gravels.

Briery Branch roadcut – Rockingham County, VA

Briery Branch is a tributary of the North River that has incised through several levels of fan deposits 19 km west of Harrisonburg, VA. The deposits primarily consist of gravels sourced from the Catoctin greenstone, Chilhowee quartzites, Tuscarora and Massanutten sandstones, and the Pocono sandstone (Hack, 1965). Fan deposits in the Shenandoah Valley were initially described by King (1949), who proposed that the gravels were produced during discrete periods of deposition during the Pleistocene as a function of colder climate and enhanced scree formation. Hack (1965) asserted that the variation in erodibility between the bedrock upstream (sandstones, quartzites, and shales) and the bedrock downstream (carbonates and shales) led to the development of transitional deposits at the boundaries between the two lithologies. Consequently, Hack (1965) argued for continuous deposition of the piedmont aprons.

The roadcut is located adjacent to a bridge on Jason Lane, off Nazarene Church Road. It exposes a mid-level fan along Briery Branch and is perched approximately 10 m above the modern channel. Clasts range in diameter from <10 cm to ~50 cm, with larger clasts being more angular than the smaller clasts. Kaolinite is present throughout the deposit, and many clasts themselves have weathered to saprolites. More resistant clasts, such as sandstones and quartzites, have remained lithified. The matrix is predominantly sand. This site is of interest due to its unknown age since King's (1949) discussion and its pivotal role in Hack's model of dynamic equilibrium. In addition to providing a test of episodic versus continuous weathering, it also revealed an average incision rate for a tributary of the Shenandoah River. We sampled the base of the exposure at 38.4230°N, 79.0828°W for gravels and sands. In collecting the sand fraction, special care was taken to ensure that only sand from the matrix – and none from crumbling rocks – was collected. Gravel clasts and the sand fraction were processed for an isochron at PRIME Lab.

Relevant map

Rader, E., & Wilkes, G. (2001). Geologic map of the Virginia portion of the Staunton 30x60 minute quadrangle. Virginia Division of Mineral Resources, Publication 163. https://ngmdb.usgs.gov/Prodesc/proddesc_78181.htm

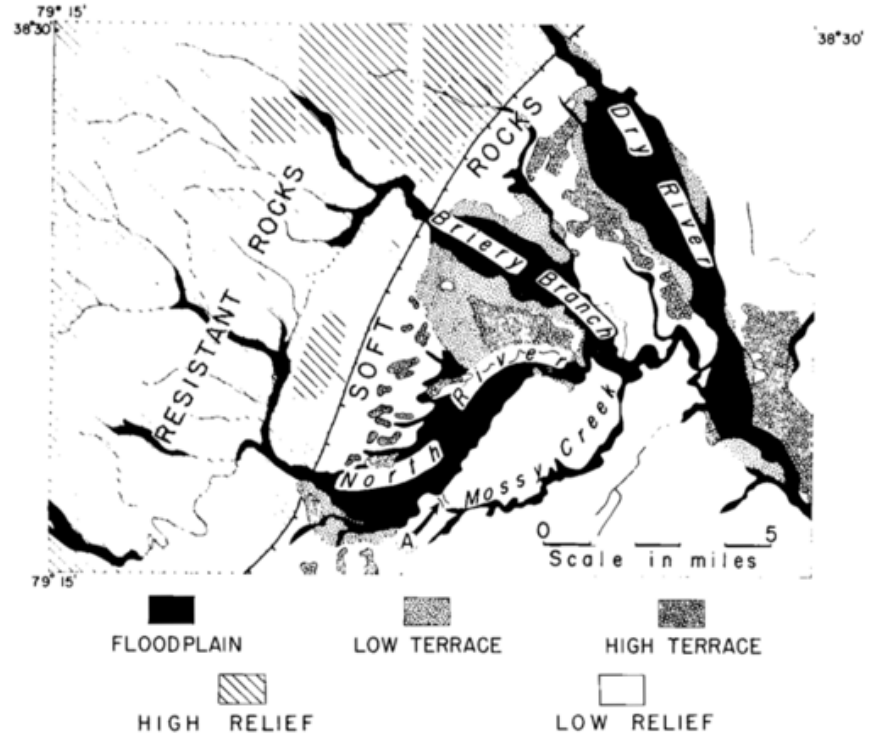

Upper image: Diagram from Hack (1960) illustrating multilevel fans at the boundary between resistant highland lithologies and the easily weathered carbonates and shales of the Shenandoah Valley. The dated site falls under the "low terrace" classification. **Lower image:** Sampled exposure at Briery Branch. Note the whitish hue of most clasts, reflecting high clay content.

Tilthammer Mill Road terrace – Clarke County, VA

The Tilthammer Mill Road site is a roadcut located at the junction of Tilthammer Mill Road and Millwood Road, 1.6 kilometers northwest of Berrys, VA. It was located by D. Doctor during a nearby geologic mapping project. It is a ~10 m thick terrace exposure, with its base perched approximately 22 m above the modern Shenandoah River. Sandstone clasts and sand fractions were collected by W. Odom from the site for cosmogenic isochron burial dating at 39.0488°N, 78.0092°W. This site is of particular interest because it is located at a similar elevation above modern river level to the fan deposit at McCarty pit. The date gleaned from this deposit sheds light on the incision history of the main trunk of the Shenandoah River. Gravel clasts and the sand fraction were processed for an isochron at PRIME Lab.

Left image: sampling location along Tilthammer Mill Road. **Right image:** closeup of terrace gravels; note well-roundedness. This photograph was taken near the sampling site.

Relevant map

Edmundson, R. and Nunan, W. (1973). Geology of the Berryville, Stephenson, and Boyce quadrangles, Virginia. Virginia Division of Mineral Resources, Report of Investigations 34. https://ngmdb.usgs.gov/Prodesc/proddesc_38888.htm

Timberville gravel pit – Rockingham County, VA

The Timberville gravel pit is located 2.6 km ENE of Timberville, VA, approximately 10 m above the modern level of the north fork of the Shenandoah River. It is interpreted as a fluvial deposit – rather than alluvial fan material – that overlies the Ordovician Conococheague Formation. The sample site at 38.6343°N, 78.7443°W features a seven-meter-thick exposed section of fluvial gravels, primarily sandstones, and sands. Sandstone clasts and sand fractions were collected from the site for cosmogenic isochron burial dating.

Relevant map

Campbell, E., Hibbitts, H, Williams, S., Duncan, I., Reis, J., Floyd, J., Wilkes, G. (2006). Interstate 81 corridor digital geologic compilation. Virginia Division of Mineral Resources, Open File Report 06-01. https://ngmdb.usgs.gov/Prodesc/proddesc_78189.htm

Left image: Terrace exposure near Timberville, VA. D. Doctor is visible to the left of center; the sampling location is near center. **Right image:** D. Doctor excavates fresh gravels for isochron.

Gray Fossil Site sinkhole complex – Washington County, TN

The Gray Fossil Site is a complex of fossil- and flora-bearing sinkholes located at 36.3860°N, 82.4982°W in eastern Tennessee. It was located during routine construction in 2000, when workers with the Tennessee Dept. of Transportation recognized bones while remaking a local road 15 km northwest of Johnson City, TN. Access to a core through this deposit was provided in 2018 by Professor Stephen Wallace, Director of Field Operations at the Gray Fossil Site. We sampled the core at 12 intervals (shown below), focusing on the shallower zone where the transition from neutron- to muon-dominated cosmogenic nuclide production should be observed. Samples were also collected at the modern excavation zone at the shoulders of a proboscidean.

Core Name	**Top of segment (m)**	**Bottom of segment (m)**	**Depth of sample (m)**	**Sample description**
2A	0.4	1.1	0.75	Gray sandy clay w/ brown layers
4A	1.9	2.6	2	Oxidized orange w/ gray clays and lithics
5A	2.6	3.2	3	Orange, granular, blocky clay
7A	3.9	4.6	4.25	Light brown, granular
8A (1)	4.6	5.4	4.7	Light brown, granular
8A (2)	4.6	5.4	5.2	Light brown, granular
10A	6.1	6.9	6.2	Light brown granular clay
11A	6.9	7.6	7.25	Medium to dark brown granular clay
13A	8.4	9.1	8.5	Light to medium brown, blocky
15A	9.8	10.4	9.9	Tan granular clay
19A	12.6	13.4	12.7	Tan granular clay
26A	17.8	18.5	18.6	Dark brown to black clay
29A	20.0	20.8	20.1	Dark brown clay
~~35A~~	~~24.4~~	~~25.2~~	~~24.8~~	~~Light brown, competent clay~~
39A	23.7	24.4	23.8	Dark brown clay
44A	31.1	31.8	31.1	Dark brown clay
49A	34.8	35.1	35	Dark brown sandy clay

APPENDIX F. MANGANESE OXIDE SITE DESCRIPTIONS

Location	$^{40}Ar/^{39}Ar$ dating	REE/trace elements	$^{40}Ar/^{39}Ar$ sample type	REE sample type
Adams Peak Mine	Y	Y	Breccia	Breccia
Big Levels #1	Y	Y	Breccia	Mn-rich quartzite
Capola Mtn Mine	Y	Y	Breccia, veins	Massive MnO w/ round qtz
Coal Road #2	Y	Y	Breccia	Breccia (Mn+Fe)
Coal Road #3	N	Y	N/A	Breccia (Mn+Fe)
D.A.M. Mine	N	Y	N/A	Massive, angular Mn
Fairmont Lane Prospect	N	Y	N/A	Sandstone (coarse Mn-cemented)
Forest Service Mines	N	Y	N/A	Sandstone (Mn-cemented)
Fork Ridge Mine	Y	Y	Breccia	Breccia
Gap Mountain	Y	Y	Breccia	Nodule
Hambright Mine	Y	Y	Massive, angular Mn	Massive, angular Mn
Higginbotham Mine	Y	Y	Breccia	Breccia
Hogback Mine	Y	Y	Nodule	Nodule
Hogpen Hollow Mine	Y	Y	Breccia	Breccia
Jennings Property	N	Y	N/A	Breccia
Kelly Bank/Dixie Mine	Y	Y	Breccia	Massive, angular Mn
Kendall and Flick Mine	Y	Y	Nodule vein	Breccia
Larry's Place	Y	Y	Breccia	Breccia
Little Fort Valley Pit	Y	Y	Quartzite covered in Mn	Quartzite covered in Mn
Mine Bank Mine	Y	Y	Breccia	Nodule
Mineral Ridge Mine	Y	N	Nodule	N/A
Morris Prospect	N	Y	N/A	Nodule
Neely Mine	Y	Y	Sandstone (coarse Mn-cemented)	Sandstone (coarse Mn-cemented)
Radpur Property	Y	Y	Nodule	Nodule
Shady Valley #2	N	Y	N/A	Massive, angular Mn
Silver Creek Mine	N	Y	N/A	Nodule
Stange Mine	N	Y	N/A	Breccia
Taylor Ridge Mine	Y	Y	Breccia	Sandstone (coarse Mn-cemented)
Tea Mountain Mine	Y	Y	Breccia	Breccia
Turkeypen Cut Mine	N	Y	N/A	Nodule
US-421 Roadcut	Y	Y	Breccia	Breccia
Wilson Hill Mine	Y	Y	Massive Mn with quartz inclusions	Nodule
Wimmer Mine	N	Y	N/A	Breccia/nodule

Adams Peak Mine – Rockbridge County, VA

The Adams Peak Mine is located five kilometers SSW of Marlbrook, VA on South Mountain. It is one of several mines located on South Mountain; others are found along the mountain's flanks. Most of the mountain is comprised of the resistant Erwin quartzite, which has been thrusted and eroded such that it is now topographically above the Shady dolomite. Along the mountain's ridge, numerous pits for iron and manganese mining have been dug.

Along with collaborators Mark Carter and Dan Doctor, I sampled a loose rock fragment at 37.8206°N, 79.2733°W. The sample was primarily composed of cryptomelane, hollandite, and lithiophorite between clasts of quartz. Following mineral identification at the Purdue Electron Microscopy facility, the sample (09-24-18B-4) was delivered to collaborators at the USGS in Reston, VA for irradiation and $^{40}Ar/^{39}Ar$ analysis. An aliquot was also processed for REE/trace element analysis.

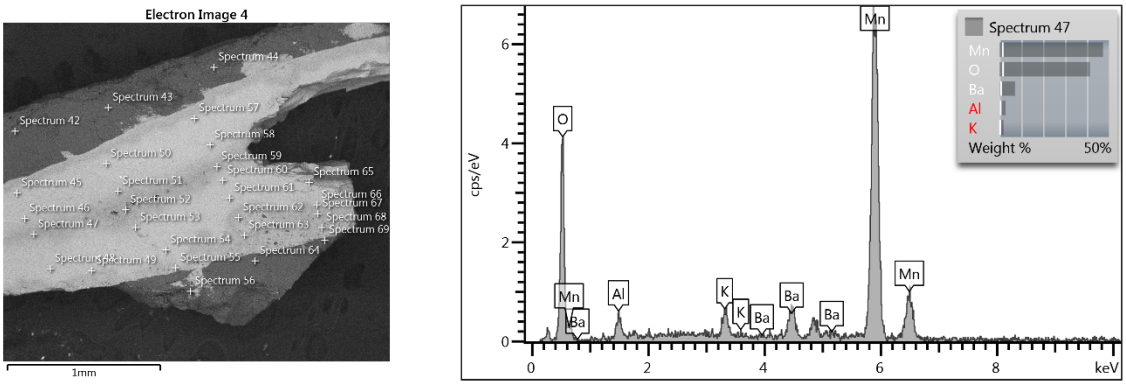

Backscatter electron image and energy-dispersive X-ray spectrum of sample 09-24-18B-4 collected by W. Odom. This spectrum demonstrates the solid solution of manganese oxides in the sample, as well as a lack of other K-contributing minerals.

Relevant map

Bick, K.F., (1960). Geology of the Lexington quadrangle, Virginia. Virginia Division of Mineral Resources, Report of Investigations 1. https://ngmdb.usgs.gov/Prodesc/proddesc_38900.htm

Big Levels Mine – Augusta County, VA

The Big Levels Mine (MRV156B_613) is a pit-type manganese oxide mine located off Coal Road six kilometers ENE of Steeles Tavern, VA. It is located in alluvium overlying the Cambrian Antietam Formation near its contact with the overlying Cambrian Shady Formation. In this particular location, the two formations dip steeply as the westward limb of the Buena Vista anticline (Werner, 1965).

I sampled a waste pile off of Coal Road (37.937°N, 79.139°W). The site is located on National Forest Service land and may be reached via a short hike from the road. One collected sample contained appreciable cryptomelane in conjunction with pure quartz (05-21-18B-1). Following mineral verification by scanning electron microscopy at Purdue University, the sample was analyzed for $^{40}Ar/^{39}Ar$ geochronology and REE/trace elements.

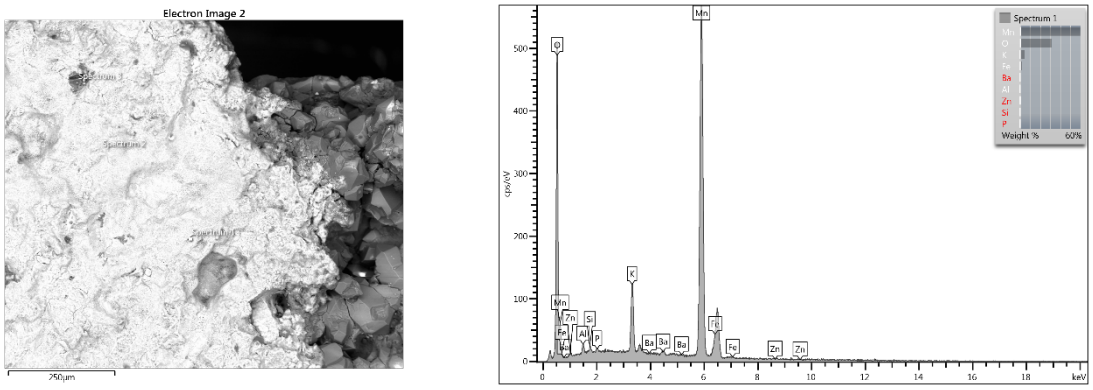

Backscatter electron image and energy-dispersive X-ray spectrum of sample 05-21-18B-1 collected by W. Odom. The left image shows the brecciated morphology of the sample. This sample shows characteristic peaks for cryptomelane and hollandite, as well as trace aluminum and iron oxides.

Relevant map

Werner, H. (1965). Geology of the Vesuvius quadrangle, Virginia. Virginia Division of Mineral Resources, Report of Investigations 7. https://ngmdb.usgs.gov/Prodesc/proddesc_38863.htm

Capola Mountain Mine – Shenandoah County, VA

The Capola Mountain Mine (MRV210A_204) is a large manganese oxide mine located 6.5 kilometers southwest of Zepp, VA. It is situated within the core of a syncline involving the Devonian Ridgeley Sandstone, Devonian Marcellus Shale/Tioga Ash/Needmore Formation (undivided), and Devonian/Silurian Rocks (undivided). Much of the exposed outcrop consists of sandstone with significant manganese oxide development and fossils (see photo).

I visited the site twice, once alone and once with D. Doctor, D. Granger, R. McAleer, and P. Vasconcelos. We collected samples at and around 38.9702°N, 78.5575°W. Samples included breccias, veins, and a vertical transect through the exposed area. Dateable samples were primarily composed of cryptomelane and hollandite (see EDX spectrum). The following samples were processed for $^{40}Ar/^{39}Ar$ geochronology: 11-09-18A-5, 11-09-18F-1, 11-09-18F-2, 11-09-18F-3, 09-23-18B, 11-09-18D-S1-1, 11-09-18D-S2-2, and 11-09-18D-S2-3. Sample 11-09-18A was also processed for REE/trace element analysis.

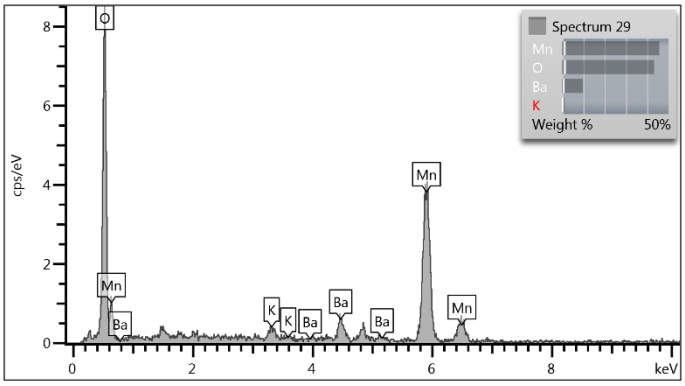

Relevant Map

Rader, E. K., Gathright, T. M. (2001). Geologic map of the Front Royal 30 x 60 minute quadrangle: portions of Clark, Page, Rockingham, Shenandoah, and Warren Counties, Virginia. Virginia Division of Mineral Resources, Publication 162.

Coal Road #2 – Augusta County, VA

The Coal Road #2 site is a small excavated area located 5.4 kilometers SSW of Stuarts Draft, VA. It is situated on the broad alluvial fan complex that overlies the contact between the Cambrian Shady Dolomite and Antietam (Erwin) Formation. The site has not been mapped or described and was located using a high-resolution digital elevation model. Manganese oxides at the site were generally massive, though highly weathered lenticular sandstone clasts appeared in some samples.

I sampled the site at 37.9860°N, 79.0586°W. The samples contained weathered sandstones (see below) with solid solution cryptomelane-hollandite cements. Some samples also contained appreciable lithiophorite and were not prepared for $^{40}Ar/^{39}Ar$ dating. Samples 07-06-19B-1 and 07-06-19B-2 were processed for $^{40}Ar/^{39}Ar$ geochronology and sample 07-06-19B-3 for REE/trace element analysis, following SEM characterization at the USGS Reston office.

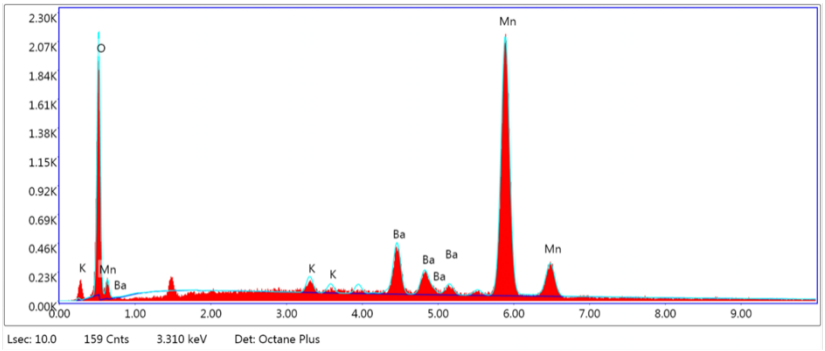

Relevant map

Werner, H.J. (1965). Geology of the Vesuvius quadrangle, Virginia. Virginia Division of Mineral Resources, Report of Investigations 7. https://ngmdb.usgs.gov/Prodesc/proddesc_38863.htm

Coal Road #3 – Augusta County, VA

The Coad Road #3 site (MRV156A_203) is located 5.6 kilometers southwest of Stuarts Draft, VA in the Big Levels area. It is a defunct underground manganese oxide mine located on a broad alluvial fan complex that overlies the contact between the Cambrian Shady Dolomite and Antietam (Erwin) Formation. Scattered oxides around the site generally featured iron and manganese.

I collected samples at 37.9870°N, 79.0658°W. None featured appreciably pure manganese oxides, and were not imaged via SEM. Sample 05-21-18A (pictured below) was prepared for REE/trace element analysis. No $^{40}Ar/^{39}Ar$ measurements were performed for this location.

Relevant map

Werner, H.J. (1965). Geology of the Vesuvius quadrangle, Virginia. Virginia Division of Mineral Resources, Report of Investigations 7. https://ngmdb.usgs.gov/Prodesc/proddesc_38863.htm

D.A.M. Mine – Bradley County, TN

The D.A.M. Mine is a large iron and manganese mine located approximately 15 kilometers SSW of Cleveland, TN. It is situated along the contact between the Ordovician Tellico Sandstone and Ordovician Holston Marble (Stose and Schrader, 1923). This NNE-SSW-striking contact forms a linear series of hills south of Cleveland, TN, many of which have been prospected and/or mined for iron and manganese oxides. The D.A.M. Mine site is notable for the bedded sandstones with iron cements that have been locally exposed by mining (see photo).

I sampled massive manganese oxides at 35.0239°N, 84.9086°W. SEM analysis revealed barite and cryptomelane-hollandite, though the latter was insufficiently pure for $^{40}Ar/^{39}Ar$ geochronology. Sample 10-06-19C-2 was prepared for REE/trace element analysis.

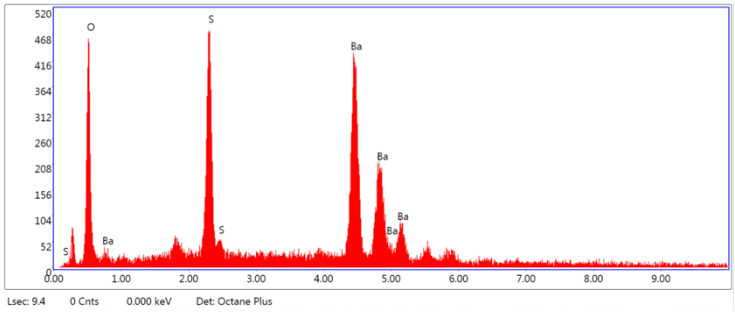

Relevant map

Rodgers, J. (1953). Geologic map of east Tennessee with explanatory text. Tennessee Division of Geology, Bulletin no. 58 [pt. 2, 167 p.]. https://ngmdb.usgs.gov/Prodesc/proddesc_91763.htm

See also:

Stose, G. W., Schrader, F. C. (1923). Manganese deposits of east Tennessee. US Government Printing Office, No. 737.

Fairmont Lane Prospect – Shenandoah County, VA

The Fairmont Lane Prospect (MRV219D_901) is located 2.2 kilometers north of Zepp, VA. It is situated on the Devonian Oriskany Sandstone (also known as the Ridgeley Sandstone) near its contact with the Devonian Needmore Shale. Locally, the formations have undergone significant folding. This site is accessible via forest service road.

I collected samples from the Fairmont Lane prospect at 39.0258°N, 78.5019°W. The manganese oxides at the site were substantially weathered and friable breccias that yielded no dateable cryptomelane grains. However, I processed sample 06-26-19B-3 for REE/trace element analysis.

Relevant map

McDowell, R. C. (1995). Preliminary geologic map of the Mountain Falls quadrangle, Frederick and Shenandoah counties, Virginia, and Hampshire County, West Virginia. U.S. Geological Survey, Open-File Report 95-620. https://pubs.er.usgs.gov/publication/ofr95620

Forest Service Mines – Carter County, TN

The Forest Service Mines are a set of pits and cuts located 19 kilometers northeast of Elizabethton, TN. They are situated on the western flank of Iron Mountain, immediately downslope of the contact of the Cambrian Erwin Quartzite and Cambrian Shady Dolomite. Iron Mountain forms the western flank of a syncline whose axis trends alongside nearby Stony Creek. No formal names were found for the mines, which were located via high resolution digital elevation model.

I sampled the site at 36.4342°N, 82.0280°W. The collected material primarily consisted of coarse sandstone cemented by manganese and iron oxides. Cryptomelane was not present in sufficient quantities for $^{40}Ar/^{39}Ar$ geochronology. Nonetheless, sample 08-23-18I was processed for REE/trace element analysis.

Relevant Map

King, P.B., Ferguson, H.W., Hamilton, W. (1960). Geology of northeasternmost Tennessee, with a section on the description of the basement rocks. U.S. Geological Survey, Professional Paper 311. https://ngmdb.usgs.gov/Prodesc/proddesc_4294.htm

Fork Ridge – Giles County, VA

The Fork Ridge outcrop is located near Butt Mountain 3.8 km northeast of Goldbond, VA. One manganese prospect (MRV112A_703) is located on the same ridge at 37.4138, -80.6023 but was not visited as part of this study. This ridge is comprised of the Rocky Gap sandstone, which in this location forms the brecciated core of a syncline. The syncline is cored by the Silurian Tonoloway Limestone/Keefer Sandstone.

I sampled a small bedrock outcrop on Fork Ridge (37.401°N, 80.634°W). The area is on National Forest Service land and may be accessed via hiking trails. One breccia sample (02-16-18A) yielded sufficient pure cryptomelane to warrant $^{40}Ar/^{39}Ar$ analysis. As with the Gap Mountain samples, this sample contained appreciable hollandite. Following mineral verification by scanning electron microscopy at the United States Geological Survey headquarters in Reston, VA, the sample was analyzed for $^{40}Ar/^{39}Ar$ geochronology. Fractions of the sample were also analyzed for REE/trace element concentrations, and the sandstone was extracted for in-situ ^{10}Be measurement.

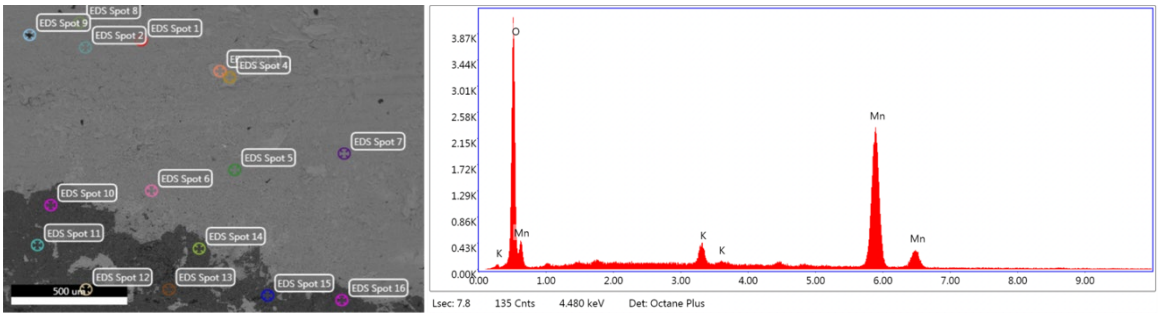

Backscatter electron image and energy-dispersive X-ray spectrum of sample 02-16-18A collected by W. Odom and imaged by R. McAleer. This sample shows characteristic peaks for cryptomelane; quartz and hollandite were imaged in additional spectra.

Relevant map

Schultz, A., Stanley, C., Gathright, T., Rader, E., Bartholomew, M., Lewis, S., & Evans, N. (1986). Geology of Giles County, Virginia. Virginia Division of Mineral Resources, Publication 69. https://ngmdb.usgs.gov/Prodesc/proddesc_39822.htm

Gap Mountain – Montgomery County, VA

The Gap Mountain outcrop is located along US-460 approximately two kilometers ESE of Newport, VA. It is situated along a wind gap, on a ridge supported by the Silurian Tuscarora Formation. The site is approximately 230 meters above the modern New River. Quartzite gravels have been described nearby (Bartholomew, personal communication) but fieldwork did not reveal any notable deposits.

I sampled the road cut at 37.286°N, 80.473°W and revisited the site with D. Doctor. Sample morphologies were variable, but mostly consisted of quartzite breccias cemented by manganese oxides (see photo). Botryoidal growths occurred both independently and as accessories to breccias. Sample 12-11-17A, a cryptomelane breccia (see EDX spectrum), was dated using $^{40}Ar/^{39}Ar$ geochronology. A nodular sample was prepared for REE/trace element analysis.

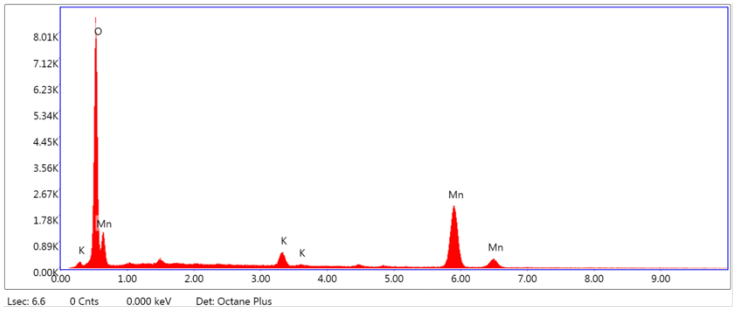

Relevant maps

Schultz, A., Stanley, C., Gathright, T., Rader, E., Bartholomew, M., Lewis, S., & Evans, N. (1986). Geology of Giles County, Virginia. Virginia Division of Mineral Resources, Publication 69. https://ngmdb.usgs.gov/Prodesc/proddesc_39822.htm

Schultz, A., Bartholomew, M., & Lewis, S. (1991). Map showing surficial and generalized bedrock geology and accompanying side-looking airborne radar image of the Radford 30' X 60' quadrangle, Virginia and West Virginia. U.S. Geological Survey, Miscellaneous Investigations Series Map I-2170-A. https://ngmdb.usgs.gov/Prodesc/proddesc_10165.htm

Hambright Mine – Bradley County, TN

The Hambright Mine, like the D.A.M. mine, is a large manganese mine located along the contact between the Ordovician Tellico Sandstone and Ordovician Holston Marble (Stose and Schrader, 1923). The Hambright Mine was originally dug into a rounded hilltop and had a maximum areal extent of 61 m by 152 m, but has since been filled in.

I collected manganese oxide float at 35.0510°N, 84.8965°W. The collection site did not feature any trenches or in-situ samples, but recent excavation by the landowner (removal of a hilltop for hunting purposes) revealed several clasts of massive manganese oxide. SEM analysis revealed generally pure cryptomelane, with localized inclusions of pyrolusite. Sample 10-06-19B-2 was prepared for $^{40}Ar/^{39}Ar$ dating, 10-06-19B-3 for REE/trace element analysis.

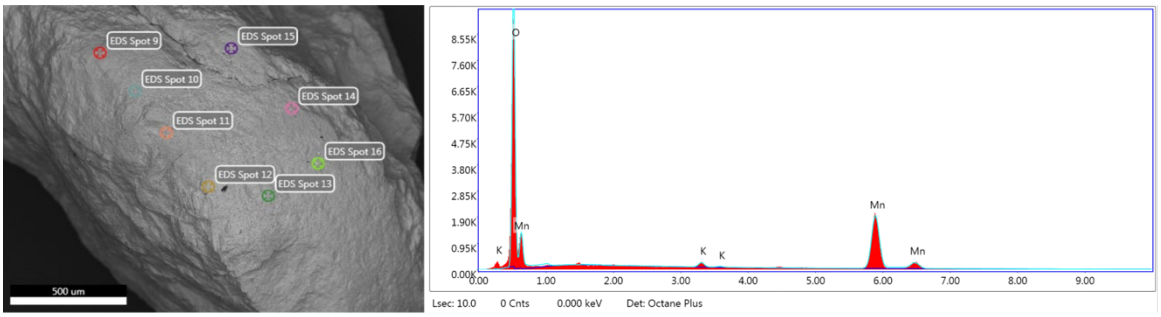

Relevant map

Rodgers, J. (1953). Geologic map of east Tennessee with explanatory text. Tennessee Division of Geology, Bulletin no. 58 [pt. 2, 167 p.]. https://ngmdb.usgs.gov/Prodesc/proddesc_91763.htm

See also:

Stose, G. W., Schrader, F. C. (1923). Manganese deposits of east Tennessee. US Government Printing Office, No. 737.

Higginbotham Mine – Giles County, VA

The Higginbotham Mine (MRV112D_603), so named for its proximity to Higginbotham Cave, is an underground manganese oxide mine located 1.5 kilometers west of Newport, VA. It is situated along a thrust fault between the Ordovician Reedsville, Eggleston, and Moccasin Formations (undivided) and Lower Ordovician/Upper Cambrian dolomites. Evidence of mining activity includes pits, large tailings piles, and remnants of shaker/sorter machinery.

Along with D. Doctor, I sampled a tailings pile at 37.2926°N, 80.5122°W. The majority of collected samples were generally massive manganese oxides, with no well-developed breccias or nodules present. One sample, 07-25-19A-2, yielded a pure cryptomelane-hollandite solid solution suitable for geochronology. Following SEM analysis at the USGS Reston office, aliquots were prepared for geochronology. Another sample, 07-25-19A-1, was processed for REE/trace element analysis.

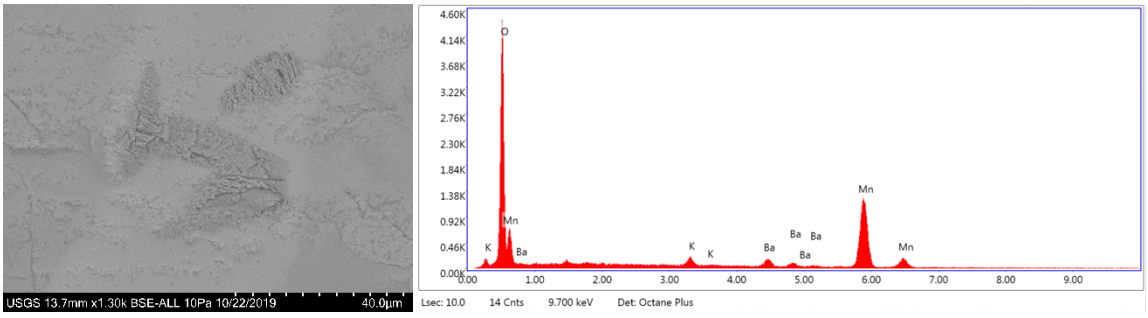

Relevant map

Schultz, A., Stanley, C., Gathright, T., Rader, E., Bartholomew, M., Lewis, S., & Evans, N. (1986). Geology of Giles County, Virginia. Virginia Division of Mineral Resources, Publication 69. https://ngmdb.usgs.gov/Prodesc/proddesc_39822.htm

Hogback Mine – Johnson County, TN

The Hogback Mine is a manganese mine located 750 m southwest of TN-133 in Shady Valley, TN. It is located on an exposed section of Cambrian Shady dolomite overlying the Cambrian Erwin formation and its constituent Helenmode shale/sandstone and Hesse quartzite members. The formations dip gently westward, with no major faults mapped nearby. It is one of a series of mines in this area that have been connected via a network of defunct roads. The Hogback Mine is ~180 m above the modern level of Beaverdam Creek, the primary drainage of Shady Valley and a tributary of the Holston River.

I sampled the pit and associated waste piles at 36.5740°N, 81.8320°W. A breccia sample (08-22-18C) yielded quartz clasts and mica fragments suspended in a hollandite-cryptomelane solid solution. I sampled an adjacent pit at 36.5724°N, 81.8320°W. A non-brecciated sample (08-22-18D-5, 08-22-18D-10) contained veins of pure cryptomelane amongst mica-laden manganese oxides. Several milligrams of clean cryptomelane or cryptomelane-hollandite solid solution were obtained from each sample via crushing and manual separation. Following mineral verification by scanning electron microscopy at Purdue University, the sample was analyzed for $^{40}Ar/^{39}Ar$ geochronology. A fraction of 08-22-18D was also processed for REE/trace element analysis.

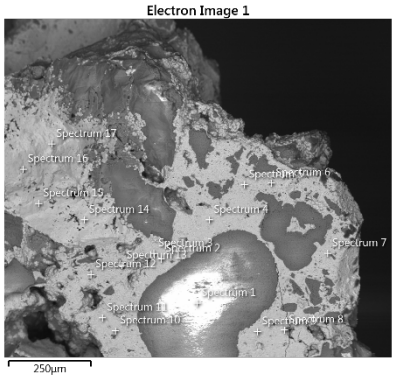

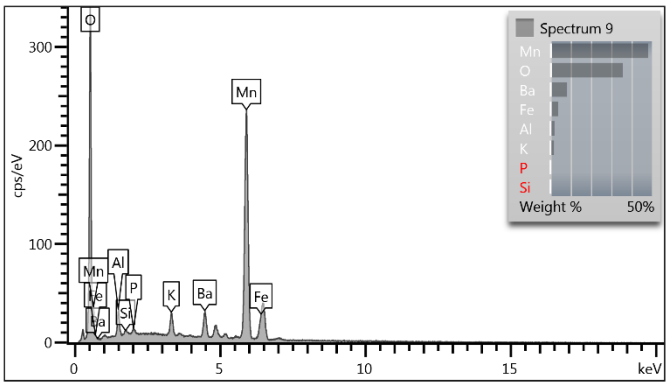

Backscatter electron image and energy-dispersive X-ray spectrum of sample 08-22-18C collected by W. Odom. This sample shows characteristic peaks for cryptomelane and hollandite, as well as trace iron and aluminum oxides.

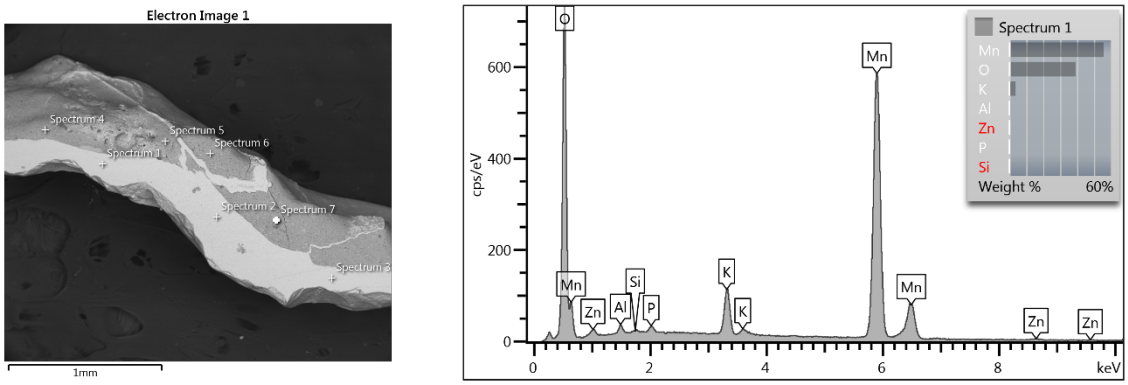

Backscatter electron image and energy-dispersive X-ray spectrum of sample 08-22-18D collected by W. Odom. This sample shows characteristic peaks for cryptomelane but not hollandite. Trace aluminum oxides are present.

Relevant map

King, P., Ferguson, H., & Hamilton, W. (1960). Geology of northeasternmost Tennessee, with a section on the description of the basement rocks. U.S. Geological Survey Professional Paper 311. https://ngmdb.usgs.gov/Prodesc/proddesc_4294.htm

Hogpen Hollow Mine – Rockbridge County, VA

The Hogpen Hollow Mine is a manganese oxide mine located 1.7 kilometers southeast of Vesuvius, VA. It is situated along a thrust fault developed in the Cambrian Hampton Formation, and is close to a contact with the Cambrian Antietam (Erwin) Formation. It is likely that the area was previously overlain by folded Cambrian Shady Dolomite that has since eroded. At present, the site maintains high relief and abundant scree deposits, some of which feature slickensides from the thrust fault.

I visited the site with D. Doctor and collected samples at 37.8988°N, 79.1800°W. Most samples were well-developed manganese oxide breccias with quartzite clasts suspended in a manganese oxide matrix. Most breccias featured small botryoidal growths on their exterior surfaces (see SEM image). EDX analyses revealed the presence of cryptomelane and lithiophorite. The following samples were processed for $^{40}Ar/^{39}Ar$ dating: 09-25-18A-2, 09-25-18A-3, 09-25-18A-4, 09-25-18A-S2-2, 09-25-18A-S2-3, and DR092518B-2. Sample 09-25-18A was also processed for REE/trace element analysis.

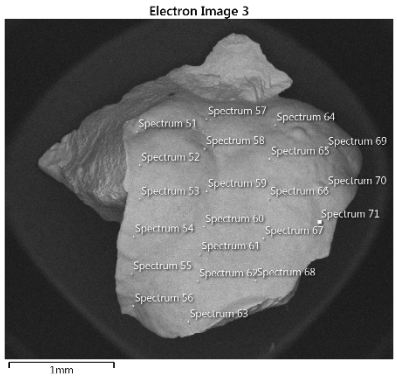

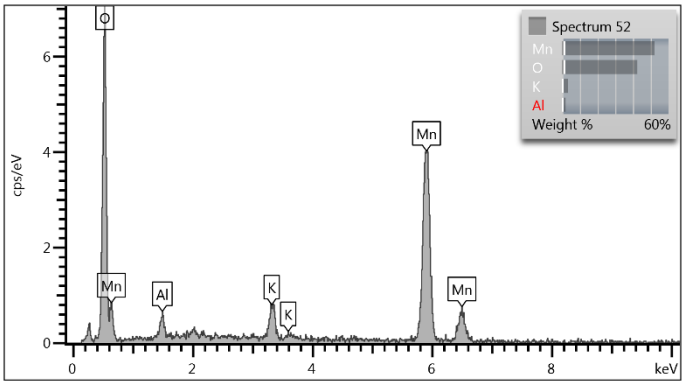

Relevant map

Werner, H. (1965). Geology of the Vesuvius quadrangle, Virginia. Virginia Division of Mineral Resources, Report of Investigations 7. https://ngmdb.usgs.gov/Prodesc/proddesc_38863.htm

Jennings Property – Bradley County, TN

The Jennings Property site is located along Whiteoak Mountain, TN approximately 12 kilometers WSW of Cleveland, TN. It features multiple roadcuts and scattered deposits, primarily consisting of manganese and iron oxides. The site has not been previously described on maps and was located using high-resolution digital elevation models. Disused mining roads allowed easy access to the site, with permission of property owners. Underlying geology primarily consists of the Mississippian Fort Payne Formation, Mississippian Chattanooga Shale, and Silurian Rockwood Formation, all which have been thrusted to form Whiteoak Mountain.

I sampled an exposure along a mining road at 35.1427°N, 85.0107°W. Samples primarily consisted of lithiophorite, easily identified by its platy morphology (see SEM image) and high Al content. Some cryptomelane was present, but not in sufficient quantities for $^{40}Ar/^{39}Ar$ geochronology. Sample 10-07-19C-1 was processed for REE/trace element analysis.

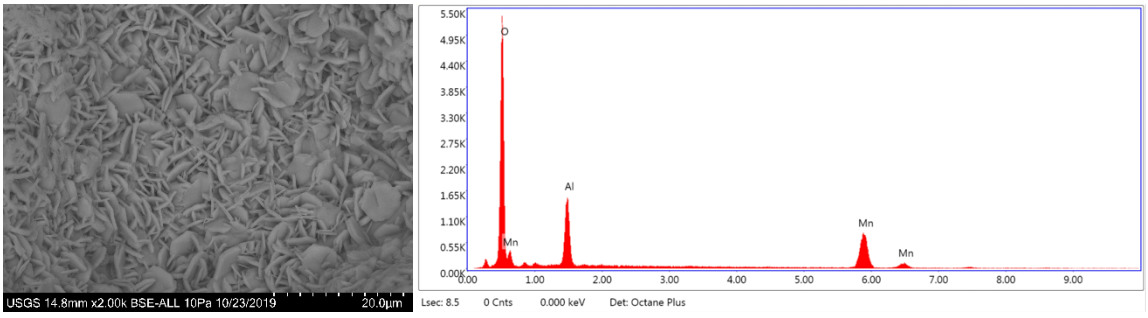

Relevant map

Wilson, R.L. (1983). Geologic map and mineral resources summary of the Snow Hill quadrangle. Tennessee Division of Geology, Geologic Quadrangle Map 112 NE. https://ngmdb.usgs.gov/Prodesc/proddesc_68156.htm

Kelly Bank/Dixie Mine – Augusta County, VA

The Kelly Bank/Dixie Mine (MRV156B_812-7) is a cluster of several mines and prospects located 2.3 kilometers ENE of Vesuvius, VA. The property is owned by a descendent of one of the former mine workers. It is situated in quaternary alluvium that is immediately downslope of the contact between the Cambrian Shady Dolomite and Cambrian Antietam Formation, and directly underlain by a thrust fault that has displaced the Shady/Antietam units over the Cambrian Rome Formation and Cambrian Shady Dolomite. As such, the site features abundant breccias cemented by manganese oxides.

I visited the site on two occasions with D. Doctor, D. Granger, R. McAleer, and P. Vasconcelos. We sampled at 37.9113°N, 79.1720°W and the nearby area. SEM analyses yielded numerous pure cryptomelane samples, which were processed for $^{40}Ar/^{39}Ar$ geochronology. Those samples include 09-25-18D-2, 09-25-18D-3, 11-08-18A-1 (SEM results shown below), 11-08-18A-2-1, 11-08-18A-2-2, 11-08-18A-2-3, and DR092518F-1. An additional sample, 11-08-18A, was processed for REE/trace element analysis.

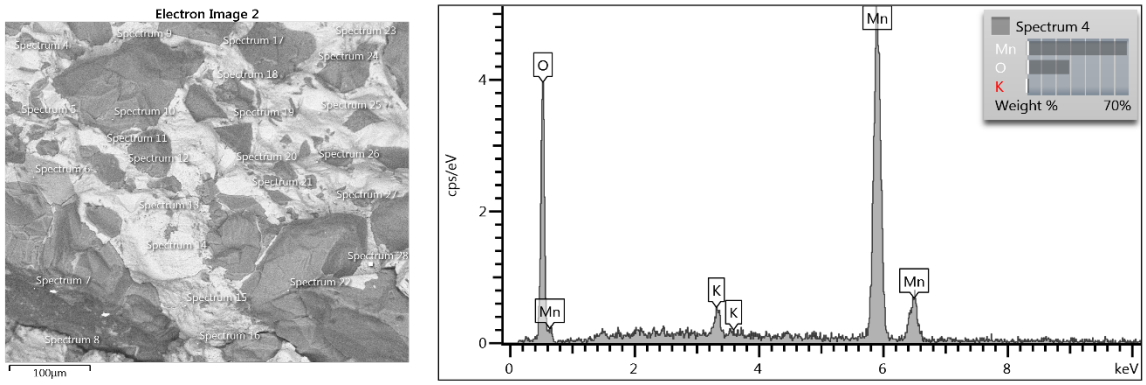

Relevant map

Werner, H.J. (1965). Geology of the Vesuvius quadrangle, Virginia. Virginia Division of Mineral Resources, Report of Investigations 7. https://ngmdb.usgs.gov/Prodesc/proddesc_38863.htm

Kendall and Flick Mine – Rockingham County, VA

The Kendall and Flick Mine (MRV187A_702), also known as the Elkton Mine, is a defunct underground iron and manganese oxide mine located off Hanse Mountain Lane, 2.5 km directly south of Elkton, VA. It features multiple documented waste piles as well as culverts that host manganese oxides. The site is developed on alluvial material that covers the Cambrian Shady Formation. In this location, the Shady lies upon the northern limb of the Hanse Mountain anticline. No major faults are known in the immediate vicinity of the mine, though the broad alluvial cover may obscure such features.

This site is of particular interest due to its proximity to the Shenandoah River and the nature of its manganese oxides. Given that the site is merely 700 m from the modern course of the Shenandoah River, it is reasonable to assume that it is strongly influenced by the Shenandoah itself, rather than tributaries. Moreover, the botryoidal manganese oxides in this location feature abundant cracks filled with cryptomelane; filled cracks were larger than average and more easily sampled for dating. Given that samples were collected from multiple waste piles, one must account for the inherent uncertainty regarding the actual source elevation of the samples.

Multiple samples were collected around the property with permission from the landowner. The samples were analyzed using scanning electron microscopy at the United States Geological Survey headquarters in Reston, VA. One sample (12-18-17C) collected at 38.391°N, 78.618°W, featured mica-free cryptomelane and was analyzed for $^{40}Ar/^{39}Ar$ geochronology. A miscellaneous sample from the site was also processed for REE/trace element analysis.

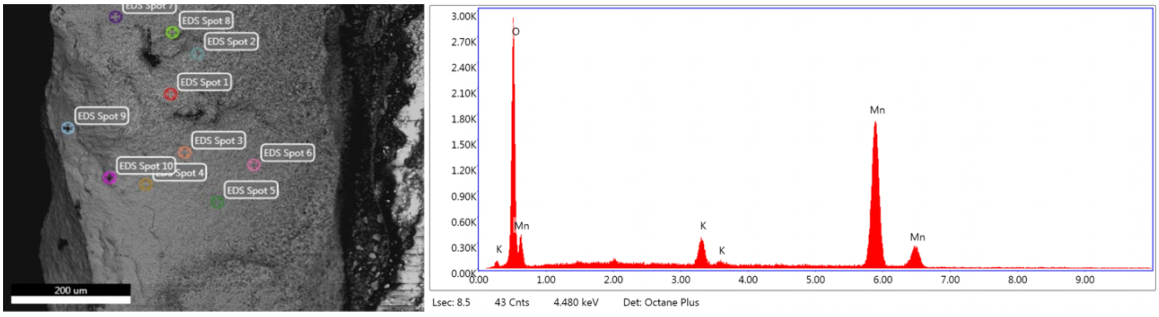

Backscatter electron image and energy-dispersive X-ray spectrum of sample 12-18-17C collected by W. Odom and imaged by R. McAleer. This sample hosts needlelike crystals and shows characteristic peaks for cryptomelane.

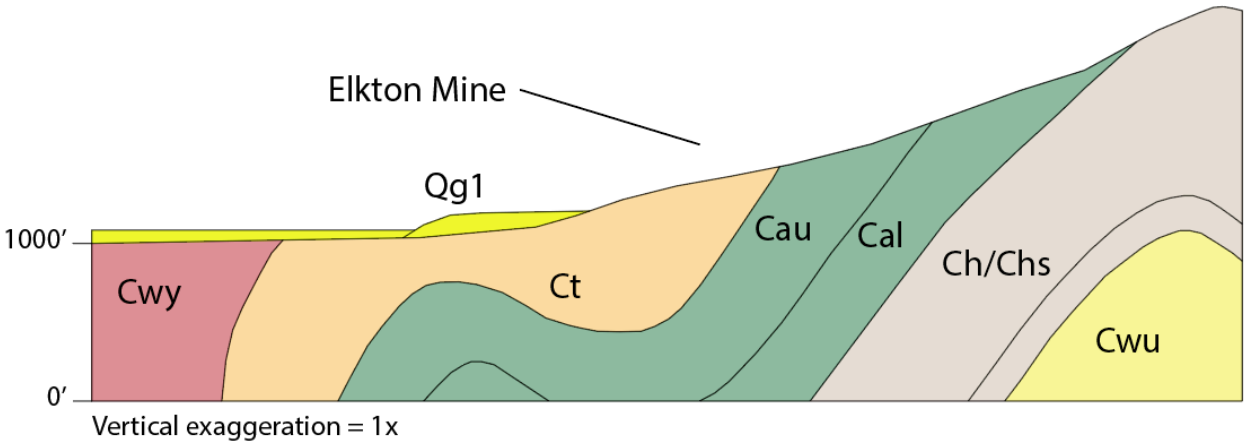

Cross-section showing the location of Kendall and Flick Mine and its position near the contact of the Cambrian Antietam and Tomstown (Shady) Formations. Image modified from King (1950).

Relevant map

King, P. (1950). Geology of the Elkton area, Virginia. U.S. Geological Survey Professional Paper 230. https://ngmdb.usgs.gov/Prodesc/proddesc_4221.htm

Larry's Place, VA – Clarke County, VA

Larry's Place is an exposure of extensively brecciated Cambrian Antietam Quartzite that hosts abundant cryptomelane but has not been mined. It is located along Howellsville Road (SR 638) approximately 3.25 kilometers southwest of Berrys, VA. In this location, the Antietam Quartzite has been thrusted over the Cambrian Shady Dolomite (see cross-section below). No mines are located in this area; this site was located by D. H. Doctor during fieldwork. Doctor and McAleer dated a manganese oxide sample collected approximately halfway up the length of the outcrop. This outcrop extends to ~100 m above the modern Shenandoah River.

We sampled manganese oxides at the base, middle, and top of the outcrop at 39.0179°N, 78.0244°W. The samples were cored and examined with scanning electron microscopy. Samples collected at the base and middle of the outcrop – 11-9-18I-1 and 11-9-18J-2,3, respectively – featured pure cryptomelane intergrown with hollandite. Low concentrations of aluminum were occasionally noted, but BSE investigation revealed no micas or feldspars. The uppermost sample – 11-9-18K – incorporated substantial amounts of micas that rendered it unacceptable for dating. Following mineral verification by scanning electron microscopy at Purdue University, the sample was analyzed for $^{40}Ar/^{39}Ar$ geochronology. An aliquot of 11-09-18I was also processed for REE/trace element analysis.

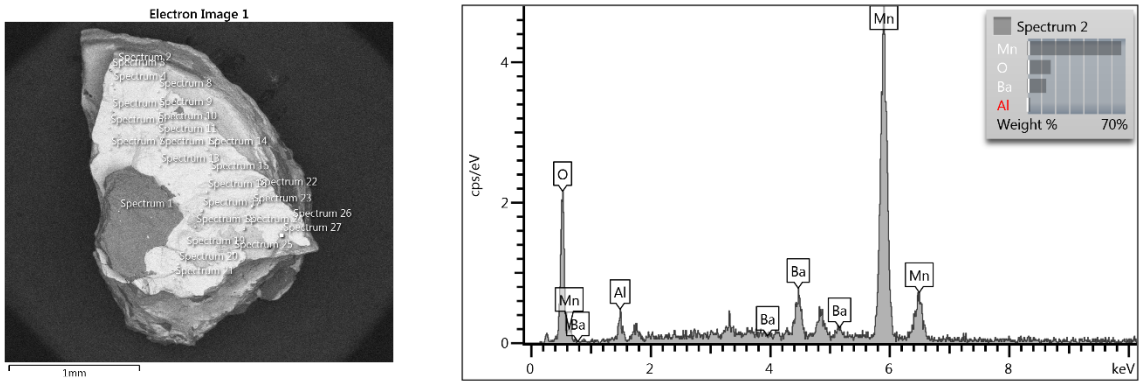

Backscatter electron image and energy-dispersive X-ray spectrum of sample 11-9-18I collected by W. Odom and D. Doctor. The left image shows a quartzite grain encased by manganese oxides. This sample shows characteristic peaks for cryptomelane and hollandite, as well as trace aluminum.

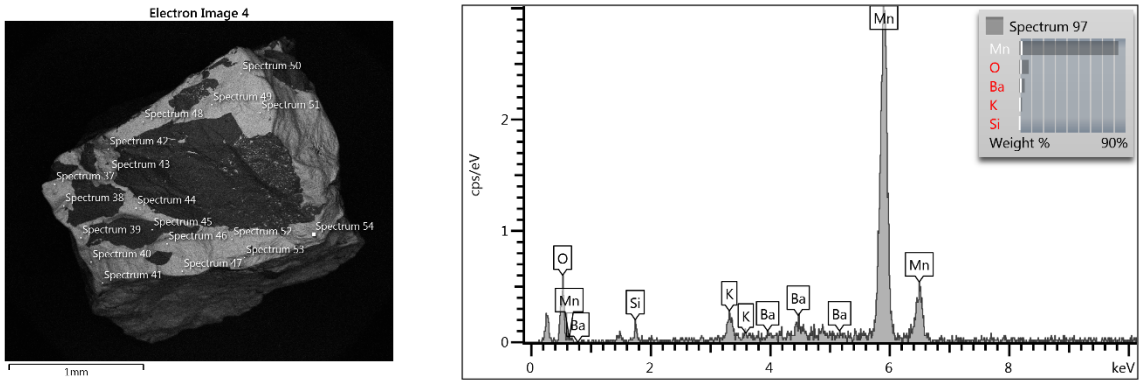

Backscatter electron image and energy-dispersive X-ray spectrum of sample 11-9-18J collected by W. Odom and D. Doctor. The left image shows the brecciated morphology of the sample. This sample shows characteristic peaks for cryptomelane and hollandite.

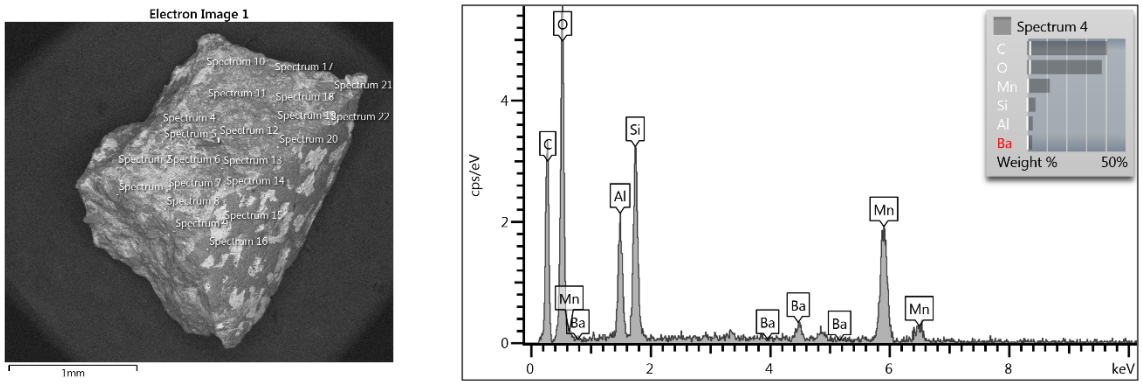

Backscatter electron image and energy-dispersive X-ray spectrum of sample 11-9-18K collected by W. Odom and D. Doctor. This sample shows characteristic peaks for hollandite and micas; note the apparent lack of cryptomelane.

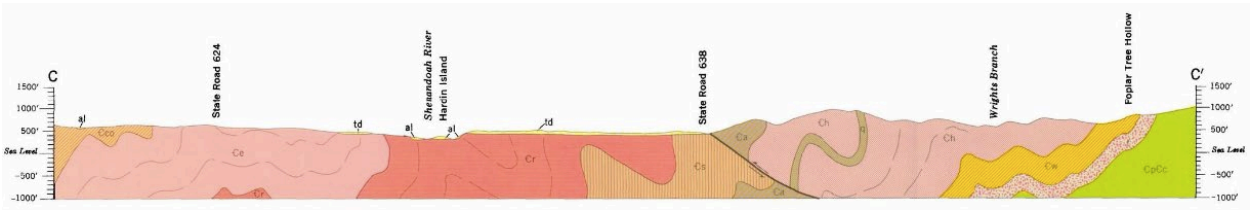

Cross-section through the area. Larry's Place is located immediately uphill of State Road 638 in this figure. Image modified from Edmundson and Nunan (1973).

Relevant map

Edmundson, R. S., Nunan, W. E. Geology of the Berryville, Stephenson, and Boyce quadrangles, Virginia. Virginia Division of Mineral Resources, Report of Investigations 34. https://ngmdb.usgs.gov/Prodesc/proddesc_38888.htm

Little Fort Valley Pit – Shenandoah County, VA

The Little Fort Valley Pit (MRV209B_905) is a disused iron and manganese pit-style mine located off of Boyer Road 6.1 km east-northeast of Seven Fountains, VA. It is developed on the Devonian Ridgeley sandstone, which forms part of a northeast-trending syncline cored by the Devonian Needmore formation. The fold axis of the syncline forms the nearby Little Fort Valley, while the mine site is located on the adjacent Three Top Mountain.

This manganese oxide mine is of interest because it is located in a distinctly different environment (bedrock syncline) than most of the mines in the Shenandoah Valley, which typically are found in alluvium. Moreover, it will provide a proxy for an additional tributary of the Shenandoah River, Passage Creek.

I sampled the pit and surrounding waste piles at 38.916°N, 78.390°W. One breccia sample (05-21-18C-1) appeared yield sufficient pure cryptomelane to warrant $^{40}Ar/^{39}Ar$ analysis. Following mineral verification by scanning electron microscopy at Purdue University, the sample was recharacterized by R. McAleer (USGS) and found to contain excessive hollandite. Further sampling yielded a more K-rich sample, 06-26-19D-3, that was submitted for dating. An aliquot was also processed for REE/trace element analysis.

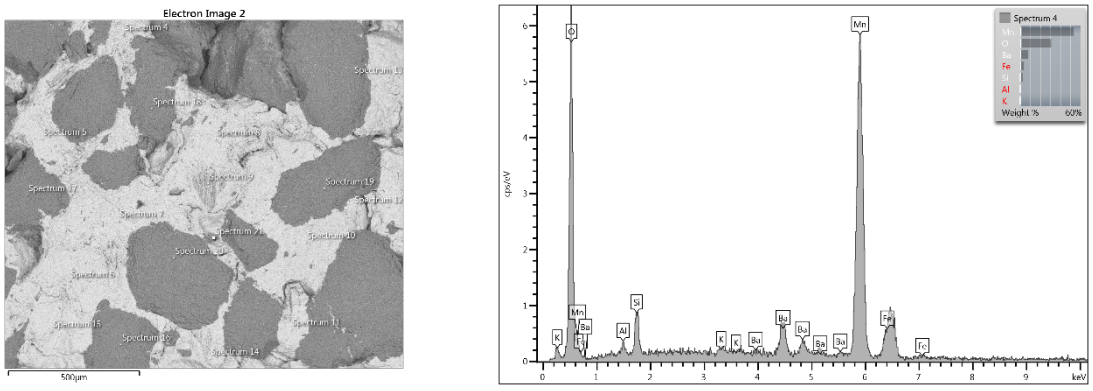

Backscatter electron image and energy-dispersive X-ray spectrum of sample 05-21-18C-1 collected by W. Odom. This sample is comprised of a hollandite-cryptomelane solid solution, dominated by the former as revealed by a high barium concentration relative to the potassium concentration. Trace iron oxides are also present.

Relevant map

Rader, E., & Biggs, T. (1976). Geology of the Strasburg and Toms Brook quadrangles, Virginia. Virginia Division of Mineral Resources, Report of Investigations 45. https://ngmdb.usgs.gov/Prodesc/proddesc_38899.htm

Mine Bank Mine – Augusta County, VA

The Mine Bank Mine (MRV156A_401) is a large pit-type manganese oxide mine located 8.3 kilometers east of Steeles Tavern, VA along the St. Marys River. It is situated in a syncline cored by the Cambrian Shady Dolomite and underlain by the Cambrian Antietam (Erwin) Formation (see cross-section below from Werner, 1965). The mined area appears to have been covered by an alluvial apron of coarse gravels/cobbles prior to excavation, which may have shielded the site from erosion despite locally high relief.

M. Carter, D. Doctor, D. Granger, and I sampled this site at multiple locations. This area is located in a National Forest and may be easily accessed by trails along the Saint Mary's River. A breccia collected by D. Doctor (02-12-18D) at 37.924°N, 79.108°W yielded mica-free cryptomelane sufficient for dating (see EDX spectrum). Following mineral verification by scanning electron microscopy at Purdue University, the sample was analyzed for $^{40}Ar/^{39}Ar$ geochronology. A nodule was also processed for REE/trace element analysis.

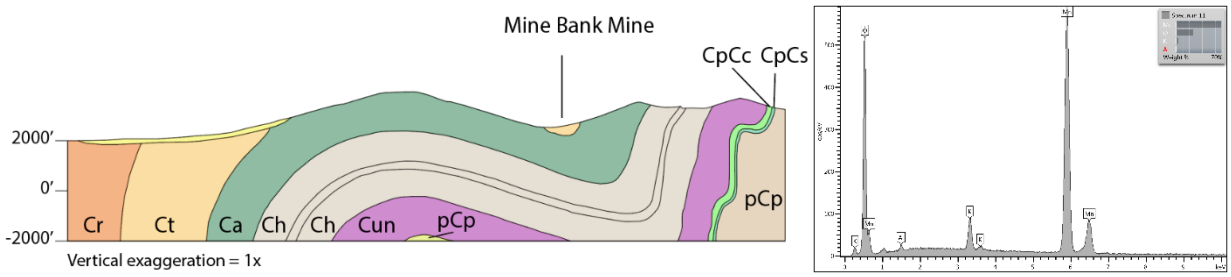

Relevant map

Werner, H. (1965). Geology of the Vesuvius quadrangle, Virginia. Virginia Division of Mineral Resources, Report of Investigations 7. https://ngmdb.usgs.gov/Prodesc/proddesc_38863.htm

Mineral Ridge Mine – Frederick County, VA

The Mineral Ridge Mine (MRV218C_406, 701-704) is located four kilometers NNE of Zepp, VA. It is situated in alluvial cover that overlies the Devonian Helderberg Group, which includes limestones, sandstones, and cherts. Several other mines are situated along the exposed Helderberg Group in this thrust sheet, including the Fairmont Lane Prospect. This site includes several cuts and a defunct mining road that extends across a cleared powerline route.

I sampled loose boulders in the cleared powerline route at 39.0405°N, 78.4864°W. The samples were primarily brecciated with some botryoidal exterior growths. Internally, the breccias exhibited well-developed acicular cryptomelane/hollandite (see SEM image and EDX spectrum). Sample 06-26-19A-3 was processed for $^{40}Ar/^{39}Ar$ geochronology. Given the proximity of this site to the Fairmont Lane Prospect, Capola Mountain Mine, and Tea Mountain Mine, no REE/trace element analyses were done for samples from this site.

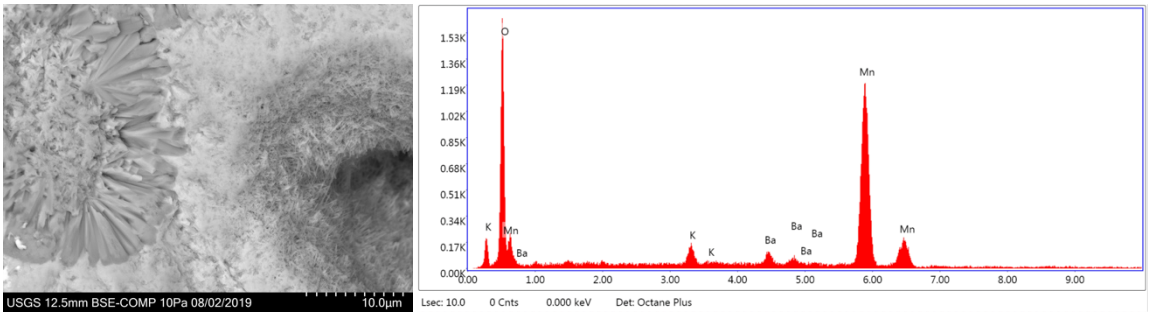

Relevant Map

McDowell, R. C. (1995). Preliminary geologic map of the Mountain Falls quadrangle, Frederick and Shenandoah counties, Virginia, and Hampshire County, West Virginia. U.S. Geological Survey, Open-File Report 95-620. https://pubs.er.usgs.gov/publication/ofr95620

Morris Prospect – Giles County, VA

The Morris Prospect is a pit prospect located off No Business Road, 1.4 kilometers west of the Silver Creek Mine. It is situated in alluvial fan deposits that overlie the Devonian Huntersville/Rocky Gap Sandstone Formations. The site is on the southern limb of a syncline cored by the Devonian Brallier and Millboro Formations.

I visited the site with D. Doctor and collected samples from the prospect at 37.2321°N, 80.9443°W. The samples appear to be very fine sandstones with manganese oxide cements. Compositionally, the cements varied from cryptomelane to hollandite and lithiophorite. Given the high concentration of SiO_2 and relatively rare pure cryptomelane, the samples could not be processed for $^{40}Ar/^{39}Ar$ geochronology. Sample 07-24-19E-2, however, was prepared for REE/trace element analysis.

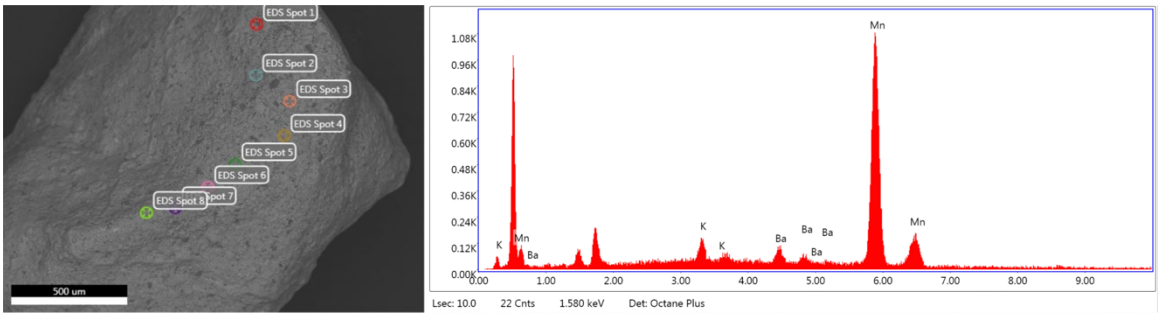

Relevant map

Schultz, A., Stanley, C., Gathright, T., Rader, E., Bartholomew, M., Lewis, S., & Evans, N. (1986). Geology of Giles County, Virginia. Virginia Division of Mineral Resources, Publication 69. https://ngmdb.usgs.gov/Prodesc/proddesc_39822.htm

Neely Mine – Johnson County, TN

The Neely Mine is a manganese oxide mine located 5.3 kilometers SSE of Damascus, VA near the northern end of Shady Valley, TN. As with the other mines in this area, it is situated near the contact between the Cambrian Shady Dolomite and underlying Cambrian Erwin Formation (quartzite), which are part of the southeastern limb of the Shady Valley syncline. It is accessible via defunct mining roads that link the local mines.

I collected samples at 36.5910°N, 81.8110°W. Most samples were breccias with (Erwin) quartzite clasts and manganese oxide cements (see SEM image). The cements were generally composed of cryptomelane and lithiophorite and were adequate for geochronology (see EDX spectrum). Samples 08-22-18A-1 and 08-22-18A-2 were processed for $^{40}Ar/^{39}Ar$ dating, and 08-22-18A was subsampled for REE/trace element analysis.

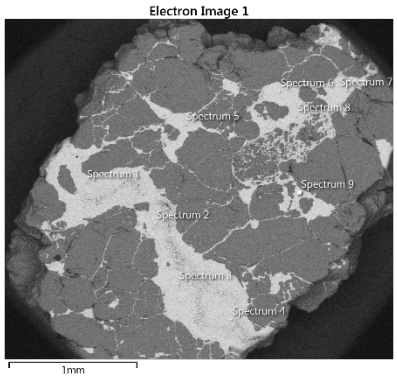

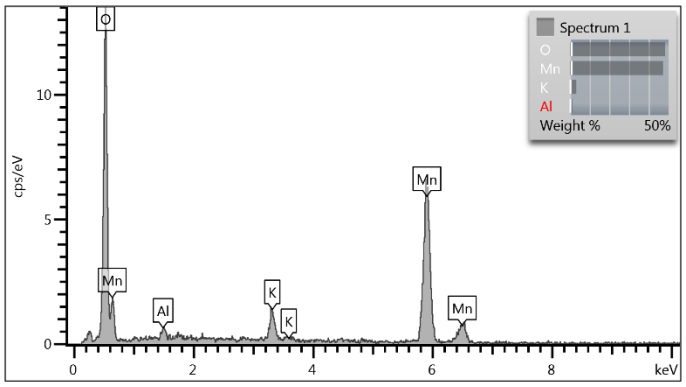

Relevant Map

King, P.B., Ferguson, H.W., Hamilton, W. (1960). Geology of northeasternmost Tennessee, with a section on the description of the basement rocks. U.S. Geological Survey, Professional Paper 311. https://ngmdb.usgs.gov/Prodesc/proddesc_4294.htm

Radpur Property – Hamilton County, TN

The Radpur Property Mine is an open quarry located 18 kilometers northeast of Chattanooga, TN. It is perched approximately 65 m above the modern Tennessee River, and is underlain by a thrust fault that has displaced the Ordovician Knox Group over the Ordovician Chickamauga Limestone. The quarry walls expose limestone cliffs alongside a lake (see photograph), though no in-place manganese oxides were found. Manganese oxides were generally found on the surfaces of scattered chert blocks and within breccias in a nearby field.

I sampled manganese oxides at and around 35.1594°N, 85.1815°W. Sample 10-05-19A-5 featured pure cryptomelane (see EDX image below) and was processed for $^{40}Ar/^{39}Ar$ geochronology. A subsample was also extracted for REE/trace element analysis.

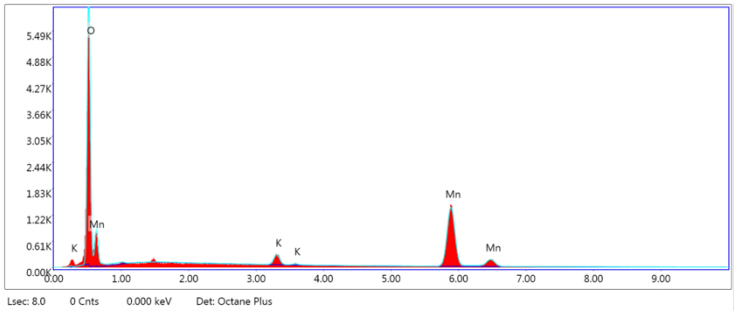

Relevant map

Swingle, G.D., Finlayson, C.P., Luther, E.T. (1964). Geologic map and mineral resources summary of the Daisy quadrangle. Tennessee Division of Geology, Geologic Quadrangle Map 112 NW. https://ngmdb.usgs.gov/Prodesc/proddesc_67930.htm

Shady Valley #2 – Johnson County, TN

The Shady Valley #2 site is located in Shady Valley, TN approximately six kilometers SSW of Damascus, VA. It is one of a series of mines perched above the nearby Beaverdam Creek that has locally incised the area. These mines are linked by defunct mining roads that are visible on high-resolution digital elevation models. Many of the mines are located near the contact between the Cambrian Shady Dolomite and underlying Cambrian Erwin Formation (quartzite), which form part of the southeastern limb of the Shady Valley syncline in this location.

I sampled manganese/iron oxides at 36.5850°N, 81.8180°W. The collected materials at this site did not contain appreciably pure cryptomelane for dating, as evidenced by their high iron content. While no subsamples were processed for $^{40}Ar/^{39}Ar$ geochronology, sample 08-22-18B (pictured below) was prepared for REE/trace element analysis.

Relevant Map

King, P.B., Ferguson, H.W., Hamilton, W. (1960). Geology of northeasternmost Tennessee, with a section on the description of the basement rocks. U.S. Geological Survey, Professional Paper 311. https://ngmdb.usgs.gov/Prodesc/proddesc_4294.htm

Silver Creek Mine – Giles County, VA

The Silver Creek Mine is located off No Business Road, 20 kilometers southwest of Pearisburg, VA. Geologically, it is similar to the Morris Prospect in that it is located in fan material that overlies the Devonian Huntersville/Rocky Gap Sandstone Formations, however it is closer to the contact with the Silurian Keefer Sandstone/Tonoloway Limestone than the Morris Prospect. This may influence the fact that the Silver Creek Mine yielded significantly more samples of manganese oxides than the Morris Prospect.

I visited the site with D. Doctor and collected samples at and around 37.2339°N, 80.9298°W. Sample morphologies were primarily botryoidal (see photo) with well-developed bands. Internal mineralogy was highly heterogeneous – as is often the case with botryoidal deposits (see SEM image) – and was unsuitable for $^{40}Ar/^{39}Ar$ dating. Nonetheless, we processed sample 07-24-19C-5 for REE/trace element analysis.

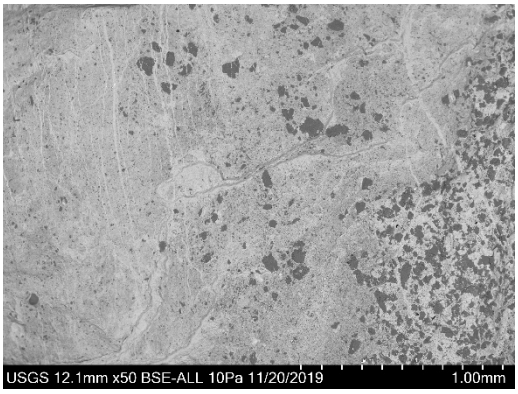

Relevant map

Schultz, A., Stanley, C., Gathright, T., Rader, E., Bartholomew, M., Lewis, S., & Evans, N. (1986). Geology of Giles County, Virginia. Virginia Division of Mineral Resources, Publication 69. https://ngmdb.usgs.gov/Prodesc/proddesc_39822.htm

Stange Mine – Bland County, VA

The Stange Mine is located 20 kilometers WSW of Staffordsville, VA. It features several pits and trenches near the crest of Flat Top Mountain that are connected by mining roads. The manganese oxides are primary found in a cross-bedded sandstone and occur both as breccias and well-developed veins (see photo). The sandstone was described by Ladd and Stead (1944) as the Devonian Becraft Sandstone, underlain by the residual clay of the Tonoloway Limestone (see figure).

I visited the site with D. Doctor and collected samples at 37.2053°N, 80.9312°W. SEM and EDX analysis revealed the samples contain mostly hollandite with minimal cryptomelane; potassium concentrations were not sufficiently high to attempt $^{40}Ar/^{39}Ar$ dating. Sample 07-24-19G-2 was processed for REE/trace element analysis.

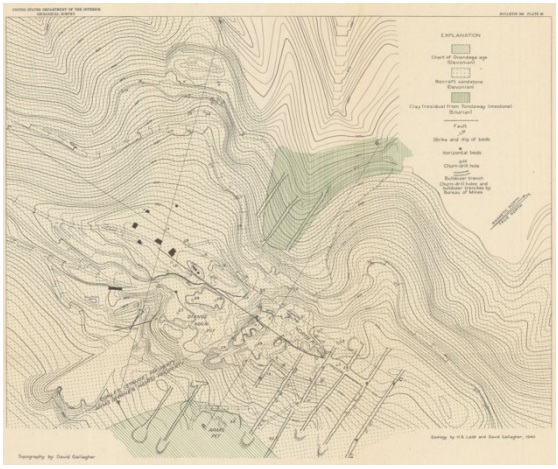

Relevant map

Schultz, A., Bartholomew, M.J., Lewis, S.E. (1991). Map showing surficial and generalized bedrock geology and accompanying side-looking airborne radar image of the Radford 30' x 60' quadrangle, Virginia and West Virginia. U.S. Geological Survey, Miscellaneous Investigations Series Map I-2170-A. https://ngmdb.usgs.gov/Prodesc/proddesc_10165.htm

See also:

Ladd, H. S., Stead, F. W. (1944). Manganese deposits of the Flat Top and Round Mountain districts, Bland and Giles Counties, Virginia. U.S. Geological Survey, Bulletin 940-H.

Taylor Ridge Mine – Carter County, TN

The national forest land northeast of Elizabethton, TN hosts numerous manganese oxide prospects and mines. This site is located 15 kilometers from Elizabethton and can be accessed via parking on Lewis Cole Loop at the closed entrance to the national forest land. The hike to this site takes approximately 45 minutes. It was described by King et al. (1960) as an iron and manganese mine and is found near the contacts of the Cambrian Shady Dolomite, Cambrian Helenmode Shale, and Cambrian Hesse Quartzite Formations. At this location, these formations are located within the northwestern limb of a northeast-trending syncline (see King et al. (1960), cross-section 23). This site is located approximately 320 meters above Stony Creek, which drains the valley into the Watauga River.

I sampled the mine at several locations and found a viable breccia (sample 08-23-18H) at 36.4334°N, 82.0822°W. The sample was cored, crushed, and analyzed via scanning electron microscopy at Purdue University. Analysis revealed quartz grains suspended in a cryptomelane-lithiophorite (?) matrix. The sample was analyzed for $^{40}Ar/^{39}Ar$ geochronology, and a fraction (08-23-18H-1) was processed for REE/trace element analysis.

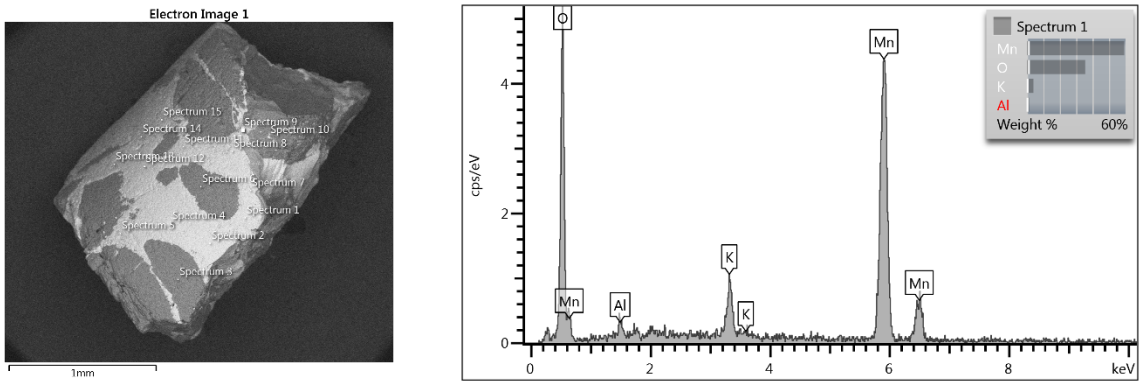

Backscatter electron image and energy-dispersive X-ray spectrum of sample 08-23-18H collected by W. Odom. This sample shows the characteristic peaks of cryptomelane and possibly lithiophorite.

Relevant map

King, P., Ferguson, H., & Hamilton, W. (1960). Geology of northeasternmost Tennessee, with a section on the description of the basement rocks. U.S. Geological Survey Professional Paper 311. https://ngmdb.usgs.gov/Prodesc/proddesc_4294.htm

Tea Mountain Mine – Shenandoah County, VA

The Tea Mountain Mine (MRV210A_210) is an iron and manganese mine located seven kilometers southwest of Zepp, VA. It is a small site relative to the nearby Capola Mountain Mine, with only scattered blocks of manganese and iron oxides remaining at the surface. The Ridgeley Sandstone and undivided Marcellus Shale, Tioga Ash, and Needmore Formation (all Devonian) underlie the area, with a thrust fault located below. The area surrounding this site features numerous prospects.

I sampled a loose manganese oxide at 38.9675°N, 78.5635°W. The sample (06-26-19C-1) was a sandstone-dominated breccia with a matrix composed of lithiophorite and cryptomelane. Following SEM analysis at the USGS Reston office, subsamples were processed for REE/trace element analysis and $^{40}Ar/^{39}Ar$ geochronology.

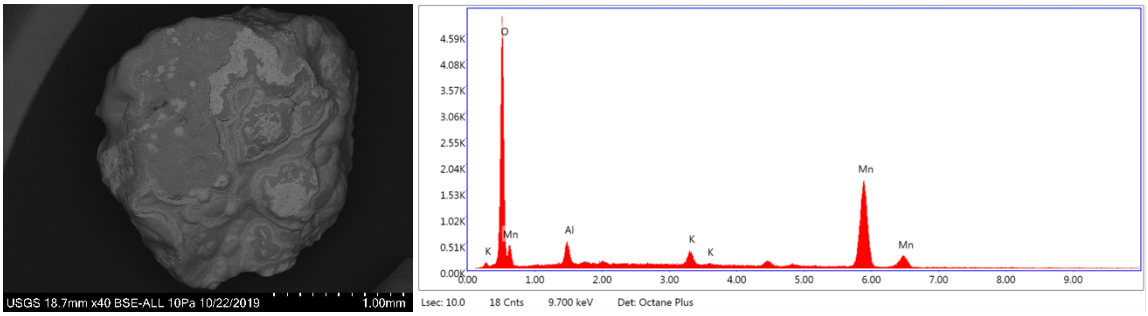

Relevant map

Rader, E.K., Gathright, T.M. (2001). Geologic map of the Front Royal 30 x 60 minute quadrangle: portions of Clarke, Page, Rockingham, Shenandoah, and Warren Counties, Virginia. Virginia Division of Mineral Resources, Publication 162. https://ngmdb.usgs.gov/Prodesc/proddesc_78182.htm

Turkeypen Cut Mine – Augusta County, VA

The Turkeypen Cut Mine (MRV156A_602) is a defunct underground manganese oxide mine 6.2 kilometers southwest of Sherando, VA. It is situated in the Cambrian Antietam (Erwin) Formation, which was previously overlain by the Cambrian Shady Dolomite. The Shady Dolomite is now only present in select synclines in the Big Levels area – namely, the Mine Bank syncline – and has elsewhere eroded away. Immediately downslope of the Turkeypen Cut Mine are the broad alluvial fans of the Big Levels area.

I visited the site with D. Doctor, D. Granger, and M. Carter. We collected manganese and iron oxides at 37.9428°N, 79.0048°W, which primarily occurred in botryoidal form and occasionally were large (> 20 cm in diameter). Massive manganese oxides were also present. None of the samples were suitable for $^{40}Ar/^{39}Ar$ geochronology, but a manganese oxide sample (see photo) was processed for REE/trace element analysis.

Relevant map

Werner, H.J. (1965). Geology of the Vesuvius quadrangle, Virginia. Virginia Division of Mineral Resources, Report of Investigations 7. https://ngmdb.usgs.gov/Prodesc/proddesc_38863.htm

US-421 Roadcut – Johnson County, TN

The US-421 roadcut is located four kilometers south of Mountain City, TN on the edge of Gentry Mountain (see photo). It exposes the Cambrian Rome formation, which hosts abundant manganese oxides in the form of breccia fills and nodules. In this location, the Rome formation completely obscures the Shady dolomite. No faults are present in the immediate vicinity of the exposure. Nearby sites of interest include the Haskell Mine and Shouns Prospect, both of which produced manganese oxides.

This site is of interest because it is one of the few visited locations to host in-place manganese oxides that have not been mined from bedrock. As such, the elevation of the samples during formation is well-constrained. The conditions during formation have been investigated in detail by Carmichael et al. (2017), who interpreted a formation temperature <120°C based on the absence of fluid inclusions in the samples.

I collected a breccia cemented by manganese oxides (08-22-18F-1, 08-22-18F-2) at 36.4397°N, 81.7957°W. Several milligrams of cryptomelane-hollandite solid solution were obtained from each sample via crushing and manual separation. Following mineral verification by scanning electron microscopy at Purdue University, the sample was analyzed for $^{40}Ar/^{39}Ar$ geochronology. An aliquot was also processed for REE/trace element analysis.

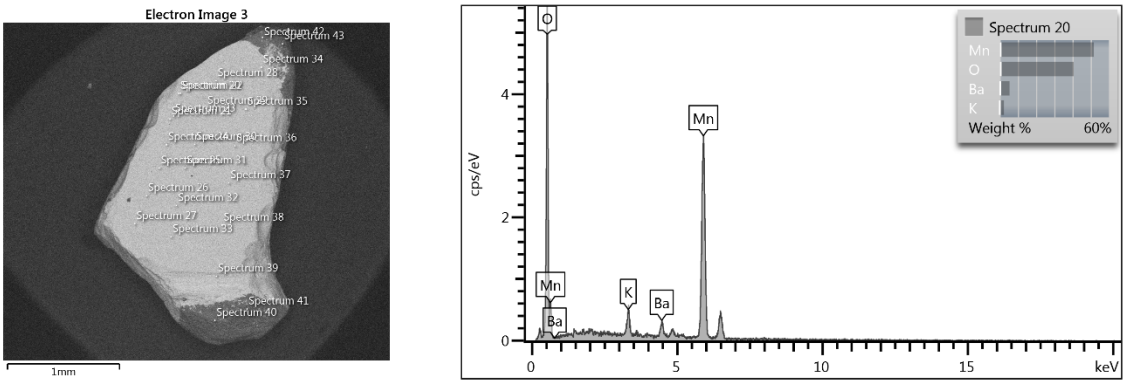

Backscatter electron image and energy-dispersive X-ray spectrum of sample 08-22-18F collected by W. Odom. This sample shows characteristic peaks for cryptomelane and hollandite. Additional analyses including X-ray diffraction and REE data are available in Carmichael et al., 2017.

Relevant map

King, P., Ferguson, H., & Hamilton, W. (1960). Geology of northeasternmost Tennessee, with a section on the description of the basement rocks. U.S. Geological Survey Professional Paper 311. https://ngmdb.usgs.gov/Prodesc/proddesc_4294.htm

Wilson Hill Mine – Johnson County, TN

The Wilson Hill Mine is an inactive manganese oxide mine located on Wilson Hill, accessible by Big Dry Run Road near Neva, TN. It hosts multiple trenches and pits along the top of Wilson Hill that were dug into the Cambrian Rome formation. This site is located on the hanging wall of a thrust fault that places the Rome formation above the Cambrian Shady dolomite. Disused mining roads render this an easily accessible site.

Multiple pits at the Wilson Hill Mine were sampled for manganese oxide float, as was a cut face at 36.3746°N, 81.8711°W. Three samples (08-23-18A-1,3, 08-23-18C-1,3, and 08-23-18D-1) collected at 36.3756°N, 81.8677°W yielded clean cryptomelane-trace hollandite mixed with quartz fragments. Following mineral verification by scanning electron microscopy at Purdue University, the sample was analyzed for $^{40}Ar/^{39}Ar$ geochronology. An aliquot of 08-23-18C was also processed for REE/trace element analysis.

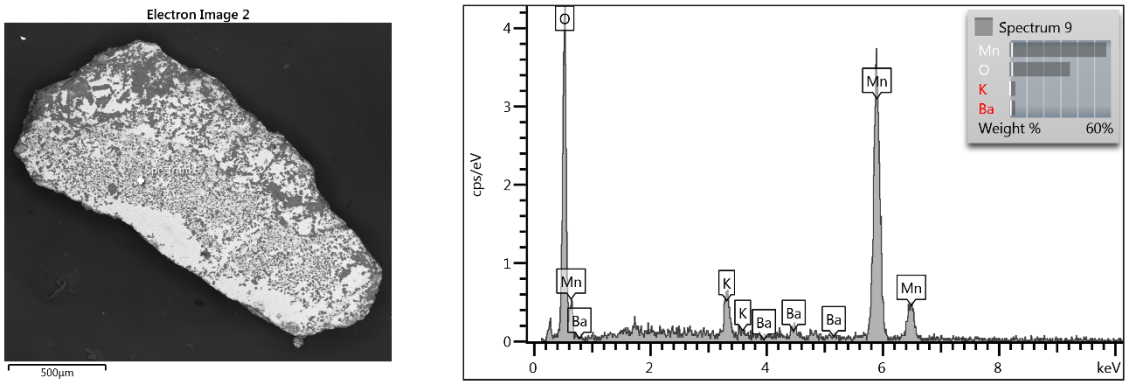

Backscatter electron image and energy-dispersive X-ray spectrum of sample 08-23-18A collected by W. Odom. This sample shows the characteristic peaks of cryptomelane and hollandite.

Relevant map

King, P., Ferguson, H., & Hamilton, W. (1960). Geology of northeasternmost Tennessee, with a section on the description of the basement rocks. U.S. Geological Survey Professional Paper 311. https://ngmdb.usgs.gov/Prodesc/proddesc_4294.htm

Wimmer Mine – Monroe County, WV

The Wimmer Mine is located 6.7 kilometers WSW of Paint Bank, VA, and is one of several manganese mines in the area. Local topography is governed by folds and thrusts that underlie the area, and the mine itself is situated on the Devonian Oriskany sandstone. The site is 12 kilometers southwest of Sweet Springs, WV, known for its natural hot spring.

I visited the site with D. Doctor and collected samples at 37.5475°N, 80.3335°W. Most samples were heavily brecciated with pure matrices and some botryoidal exterior growths (see photo). SEM analysis revealed the matrices to be predominantly hollandite with trace cryptomelane. As such, the breccias were not suitable for $^{40}Ar/^{39}Ar$ dating. Sample 09-26-18B was processed for REE/trace element analysis.

Relevant Map

Reger, D.B., Price, P.H. (1926). Mercer, Monroe, and Summers Counties. West Virginia Geological Survey, County Geologic Report CHR-15. https://ngmdb.usgs.gov/Prodesc/proddesc_10511.htm

VITA

WILLIAM E. ODOM, III

Department of Earth, Atmospheric, and Planetary Sciences

550 Stadium Mall Drive

Purdue University

West Lafayette, IN 47907

EDUCATION

2015-2020	Ph.D., Geology	Purdue University
2010-2014	B.S., Geology	University of North Carolina at Chapel Hill

PROFESSIONAL EXPERIENCE

2020-present	Career Intern, United States Geological Survey
2019	Graduate Intern, United States Geological Survey
2017-2020	Research Assistant, Purdue University
2015-2016	Teaching Assistant, Purdue University
2013-2014	Lab chemist, UNC Chapel Hill Geochronology and Isotope Geochemistry Lab
2014	Tutor, UNC Chapel Hill Department of Geological Sciences
2011-2012	Seismic analyst, UNC Chapel Hill Wave Propagation Laboratory

PUBLICATIONS

Odom, W. E., Hofmann, F., Van Arsdale, R. B., Granger, D. E. (2020). New $^{26}Al/^{10}Be$ and (U-Th)/He constraints on the age of the Upland Complex, central Mississippi River Valley. Geomorphology, https://doi.org/10.1016/j.geomorph.2020.107448.

AWARDS AND HONORS

2019	AGU Earth & Planetary Surface Processes Young Researcher Spotlight Nominee
2019	Chevron Graduate Student Research Support Award
2019	Mobil Oil Geology Award
2019	Outstanding Oral Presentation, EAPS Student Research Expo

2019 Paleontological Society Graduate Student Poster Award, First Place
2018 Cedric J. Newby Award
2018 Chevron Graduate Student Research Support Award
2017 American Federation of Mineralogical & Geological Societies Scholarship
2017 Cedric J. Newby Award
2017 Chevron Graduate Student Research Support Award
2017 Michael C. Gardner Award
2016 Michael C. Gardner Award
2016 Purdue University TA Honor Roll
2015 Purdue University TA Honor Roll

GRANTS

2019 Characterizing and dating manganese oxide deposits in the central and southern Appalachian Mountains - National Science Foundation/United States Geological Survey
2017 Dating the Cenozoic incision history of the Tennessee and Shenandoah Rivers with cosmogenic nuclides and $^{40}Ar/^{39}Ar$ in manganese oxides - National Science Foundation
2017 Dating a Pliocene advance of the Cordilleran Ice Sheet with isochron burial dating in the Tintina Trench, Yukon - Geological Society of America
2017 Travel Grant - Geological Society of America
2016 Travel Grant - Geological Society of America

CONFERENCE ABSTRACTS

Odom, W.E., Granger, D.E., Doctor, D.H., McAleer, R.J., (2020). Long-term denudation rates in the Virginia Valley and Ridge estimated from $^{40}Ar/^{39}Ar$ dating of supergene manganese oxide ores. GSA Abstracts with Programs, Vol. 52, No. 2.

Odom, W.E., Granger, D.E., Wallace, S.C., (2019). An independent constraint on the age of the Gray Fossil Site, TN using cosmogenic nuclide burial dating on a 35-m-deep core. GSA Abstracts with Programs, Vol. 51, No. 5.

Odom, W.E., Granger, D.E., Doctor, D.H., (2019). Dating a Mid-Pliocene aggradational episode and subsequent river incision in the Shenandoah Valley with cosmogenic ^{26}Al and ^{10}Be. GSA Abstracts with Programs, Vol. 51, No. 5.

Santiago-Perez, Y., Odom, W.E., Hughes, K.S., (2019). Relict Caribbean topography and tectonically triggered erosion rates in the Cordillera Central of Puerto Rico. GSA Abstracts with Programs, Vol. 51, No. 5.

Odom, W.E., Granger, D.E., (2018). Isochron burial dating of Plio-Pleistocene terrace deposits along the lower Tennessee River. GSA Abstracts with Programs, Vol. 50, No. 6.

Granger, D.E., Odom, W.E., Fabel, D., (2018). A re-evaluation of the timing of Mammoth Cave development and formation of the Ohio River. GSA Abstracts with Programs, Vol. 50, No. 6.

Odom, W.E., Granger, D.E., (2017). Dating terrace deposits along the Tennessee River using cosmogenic ^{26}Al and ^{10}Be. GSA Abstracts with Programs, Vol. 49, No. 6.

Odom, W.E., Granger, D.E., (2017). Photovoltaic silicon panels as artificial targets for ^{26}Al production. 14th International Conference on Accelerator Mass Spectrometry.

Caffee, M. W., Granger, D.E., Moore, A., Odom, W.E., Ruleman, C., (2017). Precise measurement of the ^{26}Al/^{10}Be production rate ratio from glacial moraine boulders at mid-latitudes, USA. 14th International Conference on Accelerator Mass Spectrometry.

Odom, W.E., Granger, D.E., (2016). Deep weathering products as Appalachian landscape markers: did Neogene uplift occur? GSA Abstracts with Programs, Vol. 48, No. 7.

Odom W.E., Granger D.E., (2015). Calibrating ^{26}Al production using solar panels. GSA Abstracts with Programs, Vol. 47, No. 7.

Granger, D.E., Caffee, M.W., Zhao, Z., Odom, W.E., (2015). High-precision isochron burial dating using a gas-filled magnet. GSA Abstracts with Programs, Vol. 47, No. 7.

Odom W.E., Stewart K.G., (2014). Analyzing symmetry of stream valleys to characterize possible Neogene uplift in the Blue Ridge Mountains of North Carolina. GSA Abstracts with Programs, Vol. 46, No. 3.

SEMINARS

Odom, W.E., (2020). The Appalachians in the Plio-Pleistocene. EAPS Department, Purdue University.

Odom, W.E., (2019). The effects of Plio-Pleistocene climate fluctuations on Appalachian weathering and erosion: aggradation and incision in the Shenandoah and Tennessee River basins revealed by cosmogenic nuclide geochronology. Bascom Geoscience Center Seminar, USGS.

Odom, W.E., (2018). Quantifying Cenozoic erosion and deposition in the southern Appalachians with cosmogenic nuclide geochronology. EAPS Department, Purdue University.

Odom, W.E., (2016). Tectonics or climate? Investigating the driving forces behind Appalachian landscape evolution during the Cenozoic. EAPS Department, Purdue University.

AFFILIATIONS

American Association for the Advancement of Science

American Association of Petroleum Geologists

American Geophysical Union

American Institute of Professional Geologists

Association of Environmental and Engineering Geologists

Geological Society of America

Indiana Academy of Science

Paleontological Society

Purdue University Dean's Leadership Council

Graduate Representative (2017)

Purdue University Graduate Student Association

President (2017-2018)

Chair of Colloquia Selection Committee (2017-2018)

Chair of Professional Development (2016-2017)

Sigma Gamma Epsilon National Honor Society for the Earth Sciences

PROFESSIONAL COURSES ATTENDED

2019 Sequence Stratigraphy: Concepts and Applications

2018 Sequence Stratigraphy for Graduate Students

2018 ExxonMobil Global Geoscience Recruiting Bighorn Basin Field Course

2017 Structural and Stratigraphic Concepts Applied to Basin Exploration

2017	Gravity and Magnetics for the Earth Sciences
2017	Deepwater Exploration Strategies in the Gulf of Mexico
2015	Thermochronology Methods and Applications

OUTREACH

2018	Participated in litter pick-ups at local parks through EAPS Graduate Student Association
2017-2018	Volunteered as an instructor with sedimentology/stratigraphy field trips
2017	Independently authored a graduate-level instructional manual for ArcMap GIS software
2017	Worked with the GLOBE Program, which seeks to promote the teaching and learning of science and promote scientific discovery amongst K-12 students
2017	Co-led an Adobe Illustrator workshop with Purdue's Women in Science Program
2016-2017	Co-organized Earth Science Passport Day, a community outreach event at the local children's science center that drew 150+ visitors